Design and Optimization of Two-dimensional Molybdenum Disulfide Field-effect Transistor: Density Functional Theory Study and Characterization

by

Junsen Gao

A thesis submitted in partial fulfillment of the requirements for the degree of

Doctor of Philosophy

in

Photonics and Plasmas

Department of Electrical and Computer Engineering
University of Alberta

Abstract

The Moore's law predicts that the number of integrated circuits Integrated Circuits (ICs) on a chip doubles every two years [1]. The global IC market size was USD 452.5 billion in 2021, and it is expected to grow from the USD 483.00 billion in 2022 to USD 893.10 billion in 2029 [2]. However, the IC industry is faced with challenges of following the Moore's law. During the scaling process of ICs, issues such as gate leakage [3], source-drain tunneling [4], short-channel effects [5] and etc have become the major obstacle. Showing great stacking ability, flexibility and functionality, two-dimensional Two-Dimensional (2D) materials have become promising candidates for solving the existing issues of the IC scaling. Among the 2D materials, MoS_2 and other transition metal dichalcogenide monolayers Transition Metal Dichalcogenide (TMDC) family members are considered as suitable 2D channel materials for their tunable non-zero bandgap energy. Thus, designing high-performance flexible MoS_2 electronic devices such as 2D MoS_2 field-effect transistors Field-Effect Transistors (FETs) is the main focus of this work.

2D FET design includes the contact and channel design. To design high-performance MoS_2 FETs, it is crucial to find good Schottky/Ohmic contacts. In this work, a comprehensive computational study based on the density functional theory Density Functional Theory (DFT) has been performed. The projected local density of states Projected Local Density of States (PLDOS) analysis is employed to extract the Schottky barrier height of optimized Au-(monolayer Monolayer (ML))MoS_2, W-(ML)MoS_2 and Mo-(ML)MoS_2 contacts. The simulation results demonstrate that Mo tends to form the best Schottky contact with ML MoS_2 for the vertical Schottky barrier of

0.13 eV, lateral Schottky barrier of 0.1915 eV and built-in potential of 0.0793 eV. As compared to Mo, Au forms a high-resistance Ohmic contact with the ML MoS_2, with a large vertical barrier height of 0.63±0.075 eV. It is observed that forming Schottky contact with metal materials introduces doping to the intrinsic ML MoS_2, which creates strong metallization. This effect affects the carrier mobility and designed functionality of the devices, which also impacts the controllability of the device fabrication.

To overcome the metallization issues of the metal contacts, Van der Waals contact TiS_2 has been investigated using DFT techniques. It is observed that TiS_2 contact adds 3.85E-17 $cm^{-}3$ p-type doping to the ML MoS_2 while the graphene contact tends to introduce n-type doping. TiS_2 can be utilized as Ohmic contact material if the ML MoS_2 is p-type doped. While the ML MoS_2 is n-type doped, the Schottky barrier height of TiS_2-(ML)MoS_2 contact ranges from 0.3 to 1.35 eV, which is based on the doping concentration of the ML MoS_2. The simulation results also demonstrate that, TiS_2 contact is able to preserve the bandgap of the ML MoS_2 after forming the contact, while the traditional metal contacts tend to metalize the MoS_2. For this reason, 2D semi-metallic materials like TiS_2 can be applied in the 2D electronics as pristine contacts in the future.

As it is difficult to fabricate TiS_2 contact, we have used Au contacts. Au-MoS_2 contacts are designed and fabricated to verify our computational works. By using microscopy-assisted mechanical exfoliation technique, MoS_2 flakes with the thickness of 4L, 89L, and 55L are deposited onto the Au electrodes with optimized comb patterns. The annealing process greatly reduces the series resistance and improves the contact quality. The I-V characterization results prove that the well-defined thermionic model and series-resistance model fail to extract correct I-V parameters of the fabricated back-to-back Au-MoS_2 contacts. Using the novel image-force model, the two contacts in the Au-(4L)MoS_2 back-to-back Schottky diodes show Schottky barrier height of 0.134 eV and 0.137 eV respectively. The I-V characterization demon-

strates that the reverse-biased contact in the back-to-back Schottky diodes determine the I-V characteristics. The extracted experimental Schottky barrier height is within the prediction of our simulation.

2D material properties change with monolayer stacking. It is essential to study the stacking-dependent electronic properties of MoS_2 as it is difficult to deposit MoS_2 samples with uniform orientation angle. DFT is employed to study the effective mass variation of 2-10L AA and AB stacking MoS_2. The simulation reveals that AA stacking MoS_2 shows the smallest effective mass while the AB stacking MoS_2 shows the largest effective mass. The Mulliken population Mulliken population (MP) method, electron density Electron Density (ED) and electrostatic differential potential Electrostatic Differential Potential (EDP) simulations demonstrate that the MoS_2 lattice with AB stacking orientation shows stronger in-plane scattering effect on the carriers than AA stacking MoS_2, leading to larger carrier effective mass in AB stacking MoS_2. Since the mobility of the carriers is inversely proportional to the effective mass, it can be concluded that AA-stacking MoS_2 shows larger carrier mobility than AB-stacking MoS_2.

Finally, to explore the channel structure beyond MoS_2, DFT simulations have been performed to investigate the emergent properties of ML TMDC heterojunctions. The band shifting and bandgap modification of the constituent layers of the TMDC heterojunctions show a strong correlation with the interface electron orbital coupling, revealed by ED and projected bandstructure projected Bandstructure (PBS) simulation. Type I and Type II heterojunctions can be formed by ML semiconducting TMDC materials, while the ML WTe_2 is able to form n-type or p-type Schottky contacts with other ML TMDCs. These heterostructure-introduced emergent properties lead to novel designs and applications.

In this work, a systematic optimization has been performed on both the contact and channel designs of 2D MoS_2 FETs. For contact optimization, the DFT work predicts that Mo forms better Schottky contact with ML MoS_2 than W and Au.

Preserving the semiconducting properties of MoS_2 channel, TiS_2 forms either Schottky/Ohmic contact with ML MoS_2, dependent on the channel doping type. The I-V extraction by using the novel image-force model demonstrates that low-barrier-height Au-MoS_2 contact can be achieved by annealing. As for channel optimization, DFT simulations show that AA-stacking MoS_2 possesses largest carrier mobility. TMDC heterojunctions including Type I, Type II and n-type/p-type Schottky heterojunctions will lead to new applications of 2D devices. Our work has conducted systematic optimizations towards 2D MoS_2 FETs and solved some of the existing issues, which will make a contribution to the advance of next-generation electronics.

Preface

The work of this thesis was conducted in the Department of Electrical and Computer Engineering of University of Alberta, from September 2015 to July 2022. The original research idea of this work is provided by Dr. Manisha Gupta. Dr. Manisha Gupta also supervised all the fabrication, characterization and simulation work.

The literature survey in chapter 1, chapter 2 and chapter 3 is the original work of Junsen Gao.

The DFT simulation work of metal-MoS_2 contacts in chapter 4 and TiS_2-MoS_2 contact in chapter 5 are performed using Atomistix ToolKit Atomistix ToolKit (ATK) [6] software. The chapter 4 has been published as Junsen Gao, Dipanjan Nandi and Manisha Gupta "Density functional theory projected local density of states based estimation of Schottky barrier for monolayer Molybdenum Disulphide," Journal of Applied Physics 124, 014502 (2018). The geometry optimization analysis was conducted by Junsen Gao and Dipanjan Nandi. The rest part of the simulation and data analysis was conducted by Junsen Gao. The manuscript was written by Junsen Gao. Dr. Manisha Gupta edited the manuscript and supervised the data analysis.

The chapter 5 has been published as Junsen Gao, Manisha Gupta "Titanium disulfide as Schottky/Ohmic contact for monolayer molybdenum disulfide," npj 2D Materials and Applications, (2020) 4: 26. The original idea was provided by Dr. Manisha Gupta. The simulation, data analysis and the manuscript writing were conducted by Junsen Gao. Dr. Manisha Gupta edited the manuscript and helped the data analysis.

In chapter 6, the fabrication of Au electrodes and the exfoliation of MoS_2 were

conducted by Junsen Gao. The Raman Spectrum of the MoS_2 was measured by Dipanjan Nandi. The atomic force measurement was conducted by Andres Forero Pico. Dhanini Gudi performed the annealing process. The I-V characterization and data analysis were carried out by Junsen Gao.

The work presented in chapter 7 and chapter 8 followed the original idea provided by Dr. Manisha Gupta. The DFT simulation and data analysis are the original work of Junsen Gao. Dr. Manisha Gupta guided and provided valuable suggestions to the simulation and data analysis. The ATK software and workstation are sponsored by Dr. Manisha Gupta.

Acknowledgements

First and foremost, I would like to express my most sincere gratitude and appreciation to my mentor and supervisor Dr. Manisha Gupta. She has provided me a valuable chance to start my research adventure. Her wisdom and passion in research has consistently motivated me through my Ph.D program. She is not only a good guider in research but also a good advisor in daily life. When I bump into difficulties, she is always willing to lay on a helping hand. I am especially thankful for all her patience, support and guidance, which let me improve and achieve.

Many thanks to my colleagues and friends: Dipanjan Nandi, Andres Forero Pico, Dhanvini Gudi, Jiaxin Fan, Payel Sen, Seongdae Kang, Michael Facchini-Rakovich, Darren Majak, and Yuchen Shao, for creating a positive and friendly atmosphere in research and all kinds of help and support. Here I would like to thank Dipanjan Nandi, Andres Forero Pico, and Dhanvini Gudi for their collaboration in my research. I will always miss the coffee, lunch, group picnic and all the happy time we spent together.

Here I would like to thank my parents. Who always provide me with finance and mental support. Many thanks for the patience and freedom they have provided with me, which allows me to chase my dream. I am so thankful to their encouragement and care during my Ph.D journey.

I would like to acknowledge the financial supports the University of Alberta. I would also like to acknowledge the MNT financial assistance for the fabrication and characterization costs provided by CMC Microsystems.

Table of Contents

List of Tables

List of Figures

Chapter 1

Introduction

1.1 Motivation

In the past few decades, the modern electronic industry has become more and more important in our economy. In 2022, it is expected that the global semiconductor chip industry will reach US$483.00 billion [2]. Following the Moore's law [1], the transistors have been scaling, this scaling process greatly reduces the cost of the fabrication and improves the circuit efficiency [7].

However, the scaling of the metal-oxide-semiconductor ICs is becoming challenging. On the one hand, it has been reported that, while fabricating the metal-oxide-semiconductor field-effect transistors Metal-Oxide-Semiconductor Field-Effect Transistors (MOSFETs) in smaller size, issues such as gate leakage [3], source-drain tunneling [4], short-channel effect [5] and etc emerge. The novel designs of the FETs such as fin field-effect transistors Fin Field-Effect Transistors (FinFETs) [8] could partially solve these issues. On the other hand, the material issues limit the fabrication techniques of the traditional semiconductors with three-dimensional Three-Dimensional (3D) crystalline structures (3D materials). For example, while the device is small in size, to dope the source and drain becomes difficult because of the irregular dopants distribution [9]. It is also challenging to achieve distinct heterojuntions with atomic thin films of the traditional semiconductors, which is as a result of the alloy issue and interface defects generated by lattice mismatch [10, 11]. These material

issues also make the scaling of traditional MOSFETs challenging.

The 2D materials are crystalline materials with layered structures. With interlayer valence bonding and intralayer Van der Waals bonding, 2D materials can be exfoliated into monolayer/multilayer thin films [12]. Also, the absence of the dangling bonds on the 2D interface and weak interlayer Van der Waals bonding grant 2D materials superior ability of stacking [13]. Thus 2D materials can form heterostructures with each other without the concern of lattice mismatch [14]. Thus, using 2D materials as the channel/dielectrics/contacts to fabricate 2D FET has been considered as a promising solution to solve some of the challenges of the IC scaling. Among 2D materials, graphene has attracted great attention for its superior mobility, which could reach 200000 $cm^2/(V \cdot s)$ as reported [15]. However, the absence of bandgap and zero bandgap energy limit the optical and electronic application of graphene. Compared to graphene, Molybdenum disulfide (MoS_2), which is a member of TMDC family, possesses non-zero bandgap. As reported, monolayer MoS_2 shows a direct bandgap of 1.2 eV [16], while bulk MoS_2 shows an indirect bandgap of 1.8 eV [17]. Besides the non-zero bandgap, MoS_2 also possesses good flexibility [18] and an adequate mobility (200 $cm^2/(V \cdot s)$ [19]). These advantages make MoS_2 a competitive candidate for the channel materials of 2D FETs.

In the 3D MOSFETs, the N-P-N or P-N-P doped semiconductor chunks act as the source-body-drain configurations. However, the same technique can not be applied on the 2D FETs directly. It is difficult to perform partial doping or graded doping on 2D channels of 2D FETs [20, 21]. Also, the defects generated by the doping greatly reduces the channel mobility [22]. New doping methods such as chemical doping [23] are still under development. For these reasons, instead of applying N-P-N or P-N-P structures, in the 2D FETs, the Schottky contacts play the role of the source and drain [24, 25]. In this case, the performance of the MoS_2 2D FETs is highly dependent on the MoS_2 Schottky contacts.

In the past few years, efforts have been devoted to find suitable metals for MoS_2

Schottky/Ohmic contacts [26–28]. However, forming a good MoS_2 Schottky/Ohmic contact is still a big challenge. It has been demonstrated that the Schottky-Mott law [Naturwiss. 26, 843 (1938); Cambridge Philos. Soc. 34, 568 (1938)] is a well-defined tool to predict the Schottky barrier height of the Schottky contacts of 3D materials. According to the reported results, the Schottky-Mott law fails to predict the Schottky barrier heights of the MoS_2 Schottky contacts [27, 28]. In this case, it is an urgent need to find another effective way to make the prediction of the MoS_2 Schottky contacts. Besides, the contact introduced doping is also a big challenge of the metal-MoS_2 Schottky contacts. It has been reported that, the metal contacts tend to add doping to the MoS_2 channels and modify its electronic structure [26–29]. This phenomenon greatly impact the performance of the metal-MoS_2 Schottky contact. The Van der Waals contacts can partially solve this issue.

Normally, Van der Waals contacts (2D contacts) refer to the contacts formed by 2D materials which are metallic/semi-metallic. Compared with traditional metal contacts, firstly, Van der Waals contacts form Van der Waals bonding with MoS_2 at the Schottky interface, which creates less defects and reduce the introduced doping to the MoS_2 channel. Secondly, the absence of the dangling bonds at the surface of the 2D contacts reduces the charge scattering in the channel, which improve the carrier mobility of the MoS_2 channel. Thirdly, 2D contacts could be fabricated in atomic thickness, which helps the scaling of the FETs. The great flexibility of the Van der Waals contacts greatly improve the flexibility of the 2D MoS_2 devices, making them more competitive for the flexible electronic applications. Right now, only a few 2D contacts for MoS_2 Schottky contacts have been studied, such as graphene contact [30]. More investigation is needed to explore new Van der Waals contacts. However, the Schottky-Mott law is not applicable to predict the Schottky barrier height of these 2D Schottky contacts. Thus, it is important to develop an effective prediction method.

Fabricating prototype MoS_2 Schottky contacts and conducting the characterization is a reliable way to evaluate the performance of the contact. But it is expensive and

time consuming to develop valid fabrication flow for each potential candidate. The density functional theory has proven itself to be an effective way to predict the barrier height of MoS_2 Schottky contacts. By carefully setting up the simulation methods and building the proper geometry configurations, the simulated results could match the experiments well [27]. After predicting the Schottky barrier height, it is important to fabricate prototype MoS_2 Schottky contacts and extract their characteristics to demonstrate the validity of the simulation. Normally, the well-defined thermionic emission model [31] is used to describe the current-voltage behavior of the Schottky contacts. For single Schottky diode with less defects, this model can match the measured I-V well by employing ideality factor n [32, 33]. However, in most of the cases, the fabricated MoS_2 Schottky contacts are back-to-back Schottky diodes. In this case, the TE model is no longer valid and a new model is required.

In the 2D FETs, the channel also plays an important role in the functionality of the devices. As reported, the electronic properties of semiconducting 2D materials such as MoS_2 and other TMDC family members show dependence on the geometry factors like stacking orientation [34], film thickness [35], neighboring layers [36] and etc. To achieve a good controllability of the device fabrication, it is important to gain a comprehensive understanding of how the geometry factors impact the performance of the channel material. It has been reported that, the different stacking orientations of MoS_2 such as AA stacking and AB stacking show different carrier effective mass and optical properties [37, 38]. During the deposition of MoS_2 thin films, these orientations and their mixture are avaliable by controlling the growth conditions [38]. Thus it is important to conduct DFT simulations on different MoS_2 structures to predict their electronic properties.

The emergent properties are defined as the properties which only exist in the heterostructures. Each constituent material alone does not possess these properties [39]. The reported emergent properties of the 2D heterostructures include bandgap/band-structure [40], carrier mobility [41], intrinsic doping [42], photoluminescence [43] and

etc. The emergent properties of 2D heterostructures not only broaden the functionality and application field of the 2D devices, but also bring about new challenges. It has been reported that it is impossible to predict the band alignment of 2D heterojunctions by well-defined Anderson's rule [44]. In this case, to explore new possibility of 2D devices based on MoS_2 and other TMDC materials, developing an effective way to predict the emergent properties of 2D heterostructures is an urgent need. Multiple groups have reported their own prediction on TMDC heterostructures by using DFT simulations, but the results are still under debate [44, 45]. A comprehensive and systematic DFT study on TMDC heterostructures is still required.

The goal of this work is to design and optimize high-performance two-dimensional field-effect transistors (2D FET) that can be used in the field of electronics and optical electronics. The properties of the Schottky contacts and 2D channels in 2D FETs are the two major factors determining the performance of the devices. For this reason, our work is divided into two sub-goals: optimize the Schottky contacts of the 2D FET, and optimize the electronic properties of the 2D channels.

The MoS_2 is chosen as the channel material for its non-zero bandgap energy. Firstly, the traditional bulk metal contacts such as gold (Au), tungsten (W) and molybdenum (Mo) are investigated by the DFT method. By extracting the density of states Density of States (DOS), projected density of states Projected Density of States (PDOS) and PLDOS of metal-MoS_2 contacts, the variation of the bandstructure before and after forming the contact is sketched out intuitively, and the built-in potential and Schottky barrier height have been extracted. To further investigate the performance of metal-MoS_2 contacts and verify the simulation results, the Au-(multilayer/bulk)MoS_2 back-to-back Schottky diodes have been fabricated. Because that the conventional current-voltage Current-Voltage (I-V) analysis methods could not be used to extract Schottky barrier height of the back-to-back diodes, a novel I-V analysis method based on image force model has been developed. As mentioned, the metal contacts tend to introduce defects and metallization to the 2D channel,

which will affect the functionality of the 2D FETs. To address this issue, novel 2D semi-metallic material TiS_2 is considered as a promising candidate for forming Van der Waals Schottky contact with MoS_2. A comprehensive and detailed DFT analysis is performed to investigate the TiS_2-(ML)MoS_2 contacts.

The electronic properties of MoS_2 show dependence on the stacking orientation and thickness of the MoS_2 films. To gain a comprehensive understanding on the effective mass variation of the carriers in terms of the MoS_2 stacking orientation, a systematic DFT study has been conducted on the 2-10L of MoS_2 with AAA, ABA and hybrid stacking orientations. TMDC materials show non-zero bandgap and advantages of stacking with other, thus they are chosen to form 2D heterostructures. Since the Anderson's law could not predict the band alignment of the 2D heterostructures, a DFT simulation study including projected bandstructure simulation and electron density simulation has been performed to study the emergent properties of the TMDC heterostructures. The work conducted here would pave the path to next generation electronic and optical applications.

1.2 Outline

This thesis is organized into 9 chapters, beginning with the motivation of this work in chapter 1.

Chapter 2 is the background chapter. In this chapter, the existing challenges of traditional MOSFETs, the structure and working principle of 2D FETs, the progress and existing issues of MoS_2 FETs, the working principle of MoS_2 Schottky contacts, the concept of Van der Waals contacts and the remaining challenge of finding good MoS_2 Schottky contacts are introduced with relevant references.

Chapter 3 is the methodology chapter. This chapter includes two parts: the simulation methods and experimental methods. In the first half of the chapter, the DFT concepts and the simulation parameter set-ups are introduced and explained. In the second half, the characterization methods and tools are presented.

Chapter 4 reports the DFT simulation of metal-MoS_2 Schottky contacts. To find good Schottky/Ohmic contacts for MoS_2, three metal contacts gold (Au), molybdenum (Mo) and tungsten (W) are investigated. The Schottky barrier height of these contacts are extracted by PLDOS. The density of states, Mulliken population, electron density and average binding energy are simulated to explain the extracted Schottky barrier height. By using DFT method, we have conducted a systematic investigation on the interfacial properties of the metal-MoS_2 contacts and extracted their barrier heights. The chapter 4 has been published as Junsen Gao, Dipanjan Nandi and Manisha Gupta "Density functional theory projected local density of states based estimation of Schottky barrier for monolayer Molybdenum Disulphide," Journal of Applied Physics 124, 014502 (2018).

Chapter 5 presents the optimized TiS_2-MoS_2 2D contacts to solve the metallization issue of the metal-MoS_2 contacts. The interlayer bonding condition is presented by electron density, average binding energy, electrostatic differential potential and Mulliken population simulation. The projected local density of states reveal the Schottky barrier height variation in terms of the doping concentration in the ML MoS_2 of the contact. By using the DFT method, we have extracted the barrier height of the TiS_2-MoS_2 contact with different doping concentrations of the monolayer MoS_2. We also propose the novel 2D MoS_2 FET structure with asymmetric 2D contacts in this chapter. The chapter 5 has been published as Junsen Gao, Manisha Gupta "Titanium disulfide as Schottky/Ohmic contact for monolayer molybdenum disulfide," npj 2D Materials and Applications, (2020) 4: 26.

Chapter 6 reports our experimental results of the Au-MoS_2 back-to-back Schottky diodes. To verify the simulation results, we have fabricated back-to-back Au-MoS_2 contacts and extracted their barrier height. The first half of the chapter introduces our experiment methods, including the fabrication of optimized Au electrodes, optimized exfoliation process, annealing and thickness characterization. Three I-V analysis methods are employed to extract Schottky barrier height: ideal I-V model based

on thermionic-emission Thermionic-Emission (TE) model, series-resistance Series-Resistance (SR) model and the image-force Image-Force (IF) model developed by us. We have successfully extracted the barrier height of the back-to-back contacts using the novel image-force model. The validity of the image-force model has also been demonstrated in this work.

Chapter 7 demonstrates the geometry dependence of the carrier effective mass of MoS_2 thin films using DFT simulation. The deposited MoS_2 thin films tend to have different stacking orientations. To demonstrate the correlation between the electron mobility and stacking orientation of MoS_2 thin films, a comprehensive investigation has been conducted on 2-10L MoS_2 thin films with AA, AB and hybrid stacking orientations. The electron effective mass of the samples are extracted using band-structure analysis. The projected density of states, electrostatic differential potential and Mulliken population simulations are adopted to gain a good understanding of the extracted results. Our simulation demonstrates the geometry-dependent electron mobility variation and reveals the its physical mechanism.

Chapter 8 determines the emergent properties of ML TMDC heterostructures. The band alignment of these heterostructure are presented. The bandstructure and projected bandstructure simulations reveal the electronic structure modification of the constituent layers and its mechanism. The electron density analysis is also adopted to explain the emergent properties. The band alignments and heterojunction types of the samples have been well defined by our computational work.

Chapter 9 summarizes the primary outcomes and expounds the future perspectives of this thesis.

Chapter 2

Background

2.1 The Structure and Working Principle of Metal - Oxide - Semiconductor Field - Effect Transistors

Following the Moore's law, the rapid development and flourishing of the electronic manufacturing in the past few decades makes it the foundation stone of the modern industry and society. By making the transistors and their interconnects smaller in size, more circuits could be fabricated on one silicon wafer, which makes large-scale manufacture possible and lowers the cost of the electronic devices. On the other hand, the scaling of the electronic components makes the integration of numerous functions within one device possible, leading to a variety of designs of electrical appliances such as computers, mobile phones, televisions and etc.

Among all kinds of electronic devices, the MOS ICs play an essential role in a wide

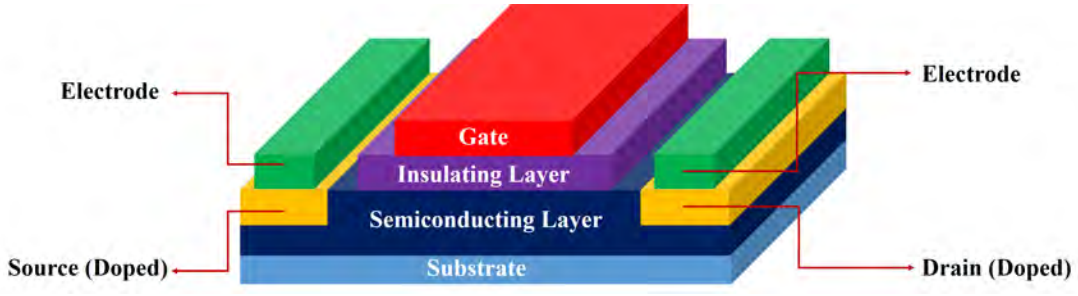

Figure 2.1: Schematic Figure of Traditional 3D Metal-Oxide-Semiconductor Field-Effect Transistors

range of applications such as computing, entertainment, communication, sensing, automotive and etc. The MOSFETs are the main functional units in the MOS ICs. After decades of development, the traditional MOSFETs based on 3D crystalline material bulks have evolved into well-defined structures [46]. As shown in fig-2.1, a typical 3D MOSFET consists of five major components: the doped source and drain (colored by yellow), semiconductor body (colored by dark blue), metallic gate (colored by red) and the insulating layer (colored by purple) which separates the channel and the gate. To achieve a good on/off current ratio, the source and drain are of the same doping type, while the body is of the opposite doping type to the source and drain. For example, if the MOSFET is n-channel (while the device is on, the channel is n-type), the source and drain should be heavily n-type doped while the body is p-type doped. Separated from the semiconductor body by the insulating layer, the metallic gate is designed to control the channel charge concentration. In order to assure the introduction or depletion of the inversion charges could extend all the way from the source to drain, while designing traditional 3D MOSFETs, it is significant to make the MOSFET gate overlap slightly or align with the edge of the source and drain contacts to achieve a good gate controllability. The general structure of the 3D MOSFET could be seen as the metal-oxide-semiconductor capacitor plus the source and drain terminals. Thus the working state of MOSFETs is based on the charge concentration modulation controlled by the MOS capacitance between the metallic gate and semiconductor body.

The working mechanism of the 3D MOSFETs has been explained in many works [46]. To control the on and off state of the device, the inversion charges could be introduced into or purged from the channel region by applying different gate bias. While under the suitable gate bias, the adequate amount of charges with opposite polarity to the body doping will be driven to the body-insulator interface, and a channel linking source and drain will be form. In this case, when applying source-drain bias, the current will flow through the MOSFET. For MOS capacitors, the

onset of the strong inversion is defined in terms of a threshold voltage V_T [46]. As mentioned above, the MOS capacitor formed by gate, oxide and body controls the inversion charge population in the channel of the MOSFET. Thus, analogous to MOS capacitors, the on and off states of MOSFETs could be defined by the threshold voltage V_T. When a gate-source bias V_{GS} larger than the V_T is applied to the MOSFET, the MOSFET is at the above-threshold conducting state. In this case, when a source-drain bias V_{DS} is applied to the device, the channel electron sheet density, channel conductance and device current could be altered by modifying the V_{GS}. While $V_{GS}<V_T$, the channel region of the MOSFET will be at the weak inversion or depletion mode, the MOSFET is at the off state. While a certain V_{GS} larger than V_T is applied on the device, applying a source-drain bias V_{DS} will generate source-drain current I_{DS} through the channel. At small V_{DS}, the I_{DS} exhibits a linear response to the increase of V_{DS}. After $V_{DS}>V_{Saturate}$, here the $V_{Saturate}$ is the saturation voltage of the V_{DS}, the I_{DS} remains the same no matter how the V_{DS} increases. In this case, the MOSFET is working under the saturation mode. The MOSFET is in saturation when $V_{GS}>V_T$ and $V_{DS}>V_{GS}-V_T$. Under the saturation mode, the I_{DS} could be given by the equation:

$$I_{DS} = \frac{K}{2}(V_{DS} - V_T)^2 \tag{2.1}$$

Where the I_{DS} (A) is the source-drain current, V_{DS} (V) is the source-drain bias and V_T (V) is the threshold voltage. In the equation 2.1, the parameter K is defined as:

$$K = \frac{W}{L}\mu C_{ox} \tag{2.2}$$

Where the W (cm) is the channel width, L (cm) is the channel length, μ ($cm^2/(V \cdot s)$ is the electron effective mobility and C_{ox} (F) is the oxide capacitance of the MOSFET.

2.2 The Mechanism and Challenges of the Metal - Oxide - Semiconductor Field - Effect Transistors Scaling

To advance towards large scale integration industry, the device scaling tech has become the most effective way to achieve faster operation speed and more compact integration of MOSFETs. After the scaling of an IC, its packing density and speed increase while the power consumption decreases [47].

Generally, two types of strategies are used to achieve the device scaling, which are Constant Field Scaling Constant Field Scaling (CFS) and Constant Voltage Scaling Constant Voltage Scaling (CVS). The CFS method is defined as: when all the dimensional parameters and voltages are downscaled by a factor S, the doping concentrations and charge densities of the devices are increased by equal factor S at the same time. Thus the electric fields in the transistor remain unaffected [48]. In this case, the circuit speed of the device is increased with the factor S while the circuit density is increased with S^2 [48]. Compared with CFS method, CVS method decreases all the dimensions of the device by a factor S, while the terminal voltage and power supply remains the same. By applying CVS, the device speed is increased by S^2, but the power consumption and the electric field are increased by S, which may cause the reliability problems of the device [48]. The mechanisms and the effects of the two scaling methods are shown in table-2.1.

The past few decades have witnessed the success of the device scaling. But it is becoming more and more difficult to develop new generations of electronic devices with smaller size and higher efficiency to meet the Moore's law. The Fig-2.2 shows that, measured by the gate length of MOSFETs, after decades of development the scaling of the ICs has dramatically slowed down in the past few years. The scaling of MOSFETs nowadays is faced with challenges, since the systematic scaling process demands the simultaneous reduction of several critical dimensional parameters of the

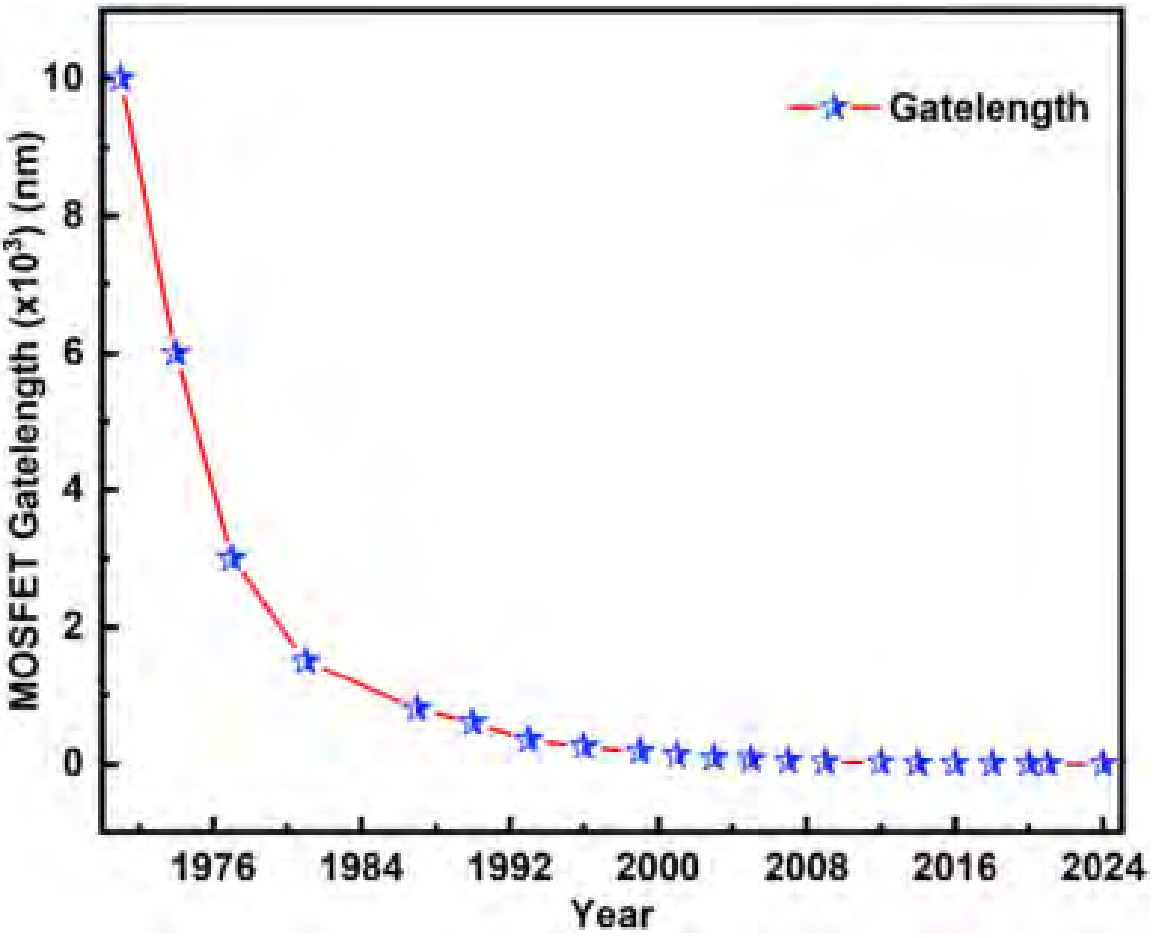

Figure 2.2: The Year Wise Gate Length Reduction in Very-Large Scale Integration (VLSI) Technology [47].

Table 2.1: The Comparison Between CFS and CVS Method

Parameter	Symbol	CFS	CVS
Gate Length	L	1/S	1/S
Gate Width	W	1/S	1/S
Field	ε	1	S
Oxide Thickness	t_{ox}	1/S	1/S
Substrate Doping	N	S^2	S^2
Gate Capacitance	C_g	1/S	1/S
Oxide Capacitance	C_{ox}	S	S
Transit Frequency	f_r	S	S^2
Voltage	V	1/S	1
Current	I	1/S	S
Power	P	$1/S^2$	S

MOSFET, instead of simply reducing one dimensional parameter only, as shown in table-2.1.

Multiple issues have emerged during the MOSFET scaling. For example, to reduce the gate size but also maintain a good gate control over the channel, the channel length of the MOSFET needs to be reduced at the same time. A shorter channel may cause short-channel effects including source-drain tunneling [4], drain induced-barrier lowering [49], velocity saturation [50], quantum confinement [51] and hot carrier degradation [52]. With the reduction of channel length, an appropriate reduction of the insulating layer thickness is also needed. An insulating layer with smaller thickness can lead to the gate-oxide tunneling, causing the increase of the gate leakage [3].

The issues mentioned above can be partially solved by introducing new designs of the FET structures, such as finFETs [8]. However, besides of the structural issues, the material issues and the resulting fabrication challenges also limit the scaling of the 3D FET devices. For traditional 3D MOSFETs, when the devices hitting

atomic dimension, the doping of the source and drain becomes very difficult because of the randomness of the dopants distribution [9]. The adoption of the traditional semiconductors with 3D crystalline structures also limits the layer thickness of the MOSFET. While depositing layers of 3D materials in small thickness, the issues such as the increasing impact of the defects generated by the lattice mismatch [11] and alloy effects (thin films of the 3D materials tend to mix with each other) [10] occur. At the same time, the existence of the dangling bonds at the surfaces of the 3D materials also causes the oxidization to happen easily, which results in the degradation of the devices.

2.3 Two - Dimensional Materials: The Solution to Scaling Challenges of Field - Effect Transistors

2D materials are a category of crystalline materials with layered structures. In the 2D materials, atoms in the same plane/layer are covalently or ionically bonded with their neighbors, while the layers are held together by Van der Waals coupling. The weak interlayer Van der Waals bonding and the strong intralayer covalent/ionic bonding in the 2D materials make them easy to exfoliate and obtain monolayer/multilayer thin films [12]. Since the first identification of the graphene in 2004 [53], the study of the 2D materials has led to the most extensive researches. After the discovery of graphene, many new 2D materials, such as TMDCs [54], MXenes, borophene [55] and hexagonal boron nitride (h-BN) [56], have been explored for different applications, as shown in fig-2.3. These 2D materials include semiconductors, semimetals and insulators.

The 2D materials provides us with a promising solution to the structural issues and material issues emerging in the scaling process of the MOSFET. As mentioned above, either by exfoliation or deposition, 2D materials are able to form more chemically stable thin films with monolayer or a few monolayers thickness. Thus by applying 2D materials as the layers of the FET, it is possible to scale down the layer thickness

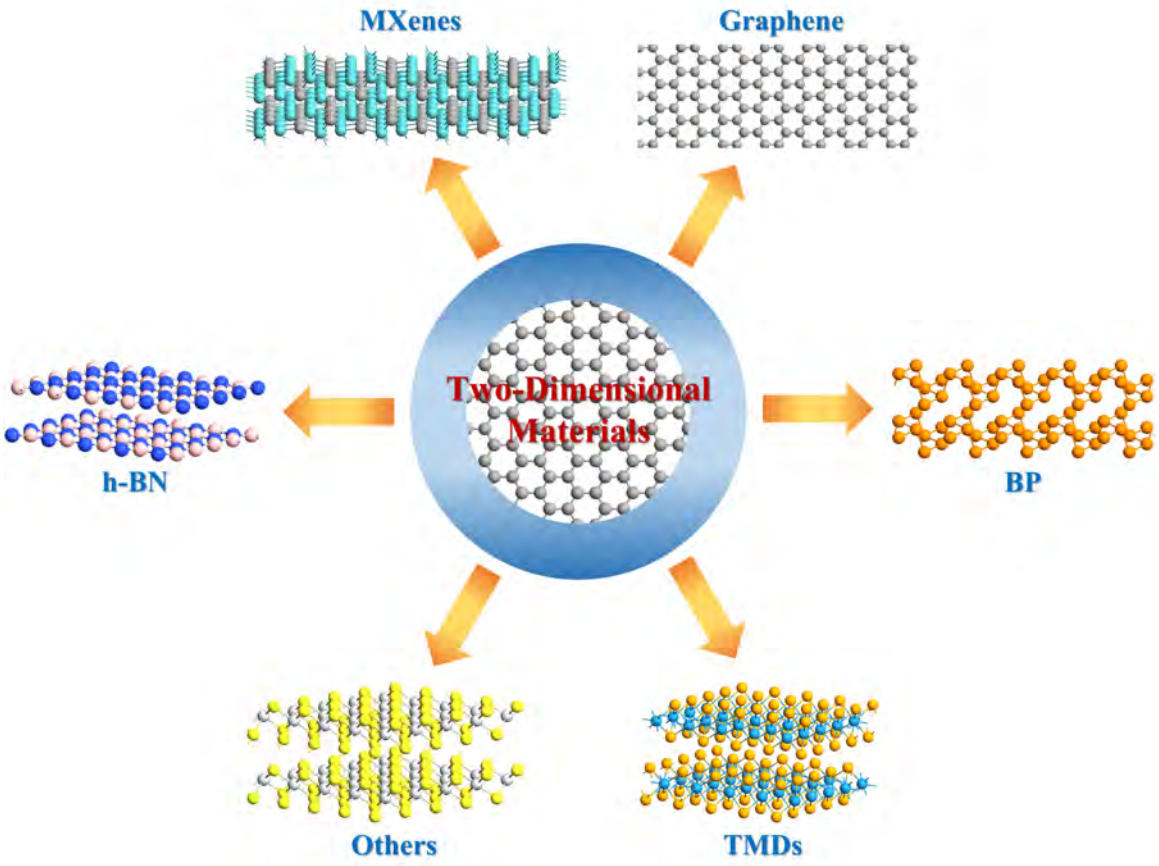

Figure 2.3: The Family Members of 2D Materials.

to even monolayer. By adopting the 2D materials as the channel materials, the reduction of the channel thickness will improve the gate controllability of the devices. The gate size could be further reduced to a smaller size while keeping the channel length the same. It has been demonstrated that, in the 2D FET, the 2D channel is able to work properly under the control of a small gate [57]. Another advantage of the 2D materials is their superior stacking ability. The unique features of the 2D materials like the weak Van der Waals interaction between layers, and the absence of the interfacial dangling bonds, allow materials to be able to be stacked on top of each other without the concern of lattice mismatch and alloy issues. The lack of the interfacial dangling bonds also help improve the interface quality. The high-quality interfaces between the 2D channel and other layers will increase the channel carrier mobility. The stacking ability of the 2D materials makes the fabrication of pure 2D FETs possible. By using semiconducting 2D materials as the channel, metallic 2D materials as the gates and contacts, and insulating 2D materials as the insulating layer, the FETs totally based on 2D materials could be fabricated and functionalized. On the other hand, some 2D materials such as Molybdenum Disulfide (MoS_2) have shown tunable properties dependent on structural factors (such as film thickness, stacking and strain) [58–60]. It is possible to adjust the electronic properties of the 2D thin films in the FETs by structure engineering. Besides the structure engineering, the stacking ability of the 2D materials have boosted the research of 2D heterostructures. It has been revealed that, the heterostructures composed of two or more types of 2D materials possess inherently higher degree of complexity and functionality, and the novel emergent properties arise from these hybrid structures [40–43]. By selecting the 2D constituents of the 2D heterostructures, the band structure tailoring could be realized, paving the roads towards multiple front-line optical, electronic and quantum information applications.

2.4 Two - Dimensional Field - Effect Transistors

2.4.1 The Structure of the Two - Dimensional Field - Effect Transistors

To provide an overall solution to the existing scaling issues and afford new routes towards next-generation high-performance electronics, the concept of 2D FET has been proposed [24]. Compared with 3D MOSFETs, as shown in fig-2.4, the biggest novelty of the 2D FETs is the design of 2D channels. In some ambitious designs, even the source, drain, gate, and the insulating layer are replaced by 2D metals and insulators respectively [30, 61]. There are two reasons for adopting the Schottky contacts as the source and drain. Firstly, the mature doping technology for 3D MOSFETs cannot be applied to 2D FETs at present. Conducting efficient partial doping or graded doping for 2D materials is extremely tough [20, 21]. Traditional ion implantation doping method tends to generate large amount of defects in the 2D thin films, which can easily cause the degradation of the channel [62]. As alternative choices, newly developed doping methods such as chemical doping are still under investigation [23], which cannot be put in commercial application right now. Secondly, adopting the Schottky barrier field-effect transistor Schottky Barrier Field-Effect Transistor (SB FET) design coincides with the requirements of the scaling. The SB FET design simplifies the FET structure by removing the heavily doped source and drain, and the scaling issues of the source and drain could be fully solved. It has been demonstrated that the SB FET structure shows the advantage in gate controllability [63]. By applying SB FET structure, for the 2D FET devices, a smaller gate size could be achieved.

Two typical designs of 2D FET are shown in fig-2.4 (a) and (b). If the 2D semiconductor is previously deposited onto the substrate before depositing the electrodes, the metallic electrodes will be deposited onto the 2D channel and cover it partially. The Schottky junctions formed on the two sides of the channel act as the source and drain region. Two gate designs are widely used in the 2D FETs: the top-gate design

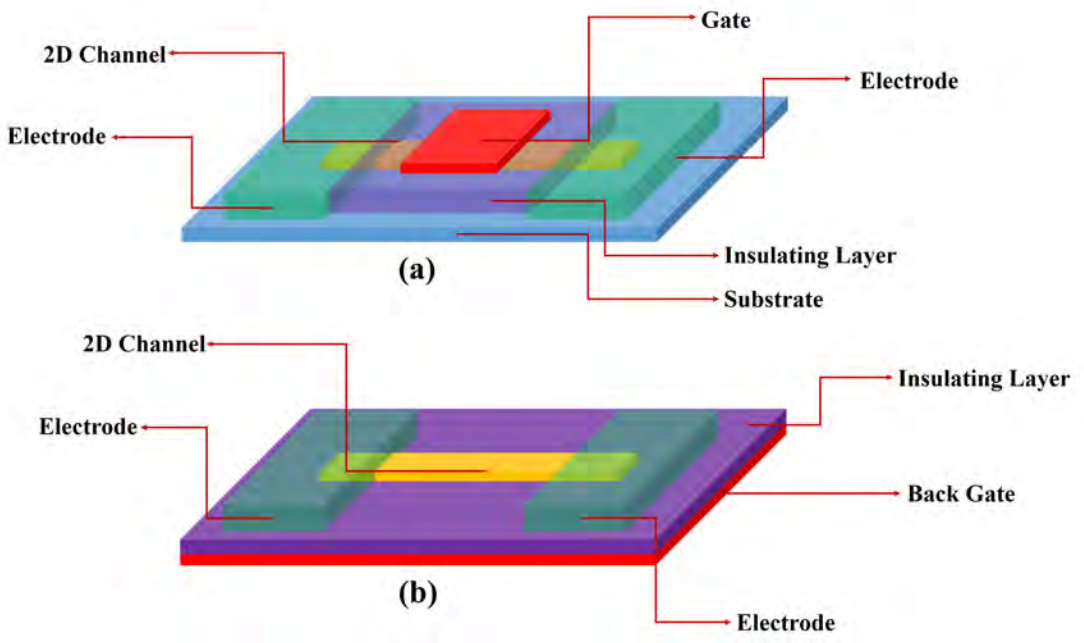

Figure 2.4: Schematic Figure of 2D SB FETs. (a) 2D SB FET with Top Gate. (b) 2D SB FET with Back Gate.

(shown by fig-2.4 (a)), and the convenient back-gate design (shown by fig-2.4 (b)). In the top-gate design, after the deposition of the electrodes, the insulating layer will be deposited on the top of the fabricated structure, then a metallic gate will be added onto the insulating layer. As for back-gate design, the insulator such as SiO_2 or Si_3N_4 is deposited onto heavily doped silicon (Si) wafer (normally it is p+ Si) as the insulating layer while the Si layer serves as the back gate. After that, the 2D thin films can be deposited onto the insulating layer. Before the deposition of 2D materials, using an annealing process to treat the silicon-insulator wafer would slightly improve the surface condition of the insulating layer, hence improving the bonding condition between the 2D semiconductor and the insulating layer. This annealing process would slightly increase the carrier mobility [64]. After depositing the 2D semiconductor, similar to the top-gate devices, the metal electrodes can be patterned and deposited onto the 2D layer.

Compared with the top-gate 2D FETs, the fabrication of the back-gate 2D FETs skips the step of depositing the insulating layer onto the 2D semiconducting materi-

als. Directly depositing the insulating layer onto the 2D semiconductor may introduce defects and geometry distortion, which cause the scattering of the carriers and reduce the carrier mobility. For example, right now, for MoS_2 based 2D SB FETs, normally back-gate devices show higher carrier mobility than top-gate devices [65–68]. However, although the back-gate 2D FETs show higher mobility than the normal top-gate 2D FETs, the existence of the large back gate in the back-gate devices will be a huge obstruction in the roadmap of the scaling. It is very hard to etch the back gate of the 2D FETs efficiently. As a result, most of the reported back-gate devices play the role of the prototype devices for investigating the characteristics of the 2D materials, rather than the practical commercial electronic devices. As for the top-gate devices, to improve the carrier mobility, several methods are under development, such as adopting the high κ materials like Hafnium Oxide (HfO_2) as the insulating layer [69], using 2D materials to encapsulate the 2D channel (encapsulation technique) [70], using 2D metal contacts like graphene [30], and etc. These new techniques reduce the surface polarization charges, thus reduce the unwanted carrier scattering to improve the carrier mobility. On the other hand, some approaches such as encapsulation method significantly complicate the fabrication process of the devices, which will definitely increase the manufacture cost and difficulty. Briefly speaking, both top-gate and back-gate designs have their advantages and disadvantages. In terms of the future application, top-gate devices would be the best choice. But there is still a long way to go before realizing its commercial applications.

2.4.2 The Working Principle of the Two - Dimensional Field - Effect Transistors

As mentioned above, 3D MOSFETs adopt the N-P-N or P-N-P doped semiconductor chunks as the source-body-drain configurations, while the Schottky contacts in the 2D FETs act as the source and drain. For this reason, the I-V characteristics of the 2D FETs under certain gate bias are determined by the Schottky barrier height of

the contacts.

To explain the working mechanism of the 2D FETs, let's take the n-type 2D FET (the channel is n-type) as an example. The working mechanism of the n-type 2D FET is shown in fig-2.5. The band diagrams depict different operating regimes. In the plots, the applied gate bias is denoted as V_g. As shown in fig-2.5 (a), while the V_g=0, the device is off. The energy barrier for the electrons is exactly the Schottky barrier between the metal contact and the 2D channel. The energy barrier for the holes is composed of the intrinsic energy barrier of the contacts and the built-in potential arising from the metal/semiconductor interface. Since the surface potential resulting from the gate also contributes to the effective hole barrier, thus it needs to be taken into the consideration as well. The source-drain current is very small while the V_g is zero, because of the large energy barrier for both electrons and holes.

If the V_g is increased to a certain value (because the channel is n-type, a negative gate bias is applied in our discussion), as shown in fig-2.5 (b), the charge polarity in the channel is reversed from n-type to p-type. As a result, the built-in potential of the device is eliminated. The energy barrier for the electrons remain the value of the contact Schottky barrier height Φ_{SBH}, while the energy barrier for holes is largely reduced because of the absence of built-in potential. The FET is at the flat-band state. Under the circumstance, the device is at the onset of the strong inversion, and the applied gate bias could be defined as the threshold voltage V_T. When the device is at the threshold and above-threshold state ($V_g \geq V_T$), according to the thermionic emission model [31], if a source-drain bias V_{ds} is applied to the device, the source-drain current could be written as:

$$I_{ds} = A \times \ A^* \times \ T^2 \times \exp\left(-\frac{q\Phi_{peff}}{kT}\right)\left(1 - \exp\left[\frac{qV_{ds}}{kT}\right]\right) \tag{2.3}$$

Where I_{ds} (A) is the source-drain current; Φ_{peff} (eV) is the energy barrier for holes, V_{ds} (V) is the source-drain bias, A (m^2) is the junction area, A^* ($A/(m^2 \cdot K^2)$) is the effective Richardson constant, q (e) is the charge of electron, k ($m^2 \cdot kg/(s^2 \cdot K)$) is

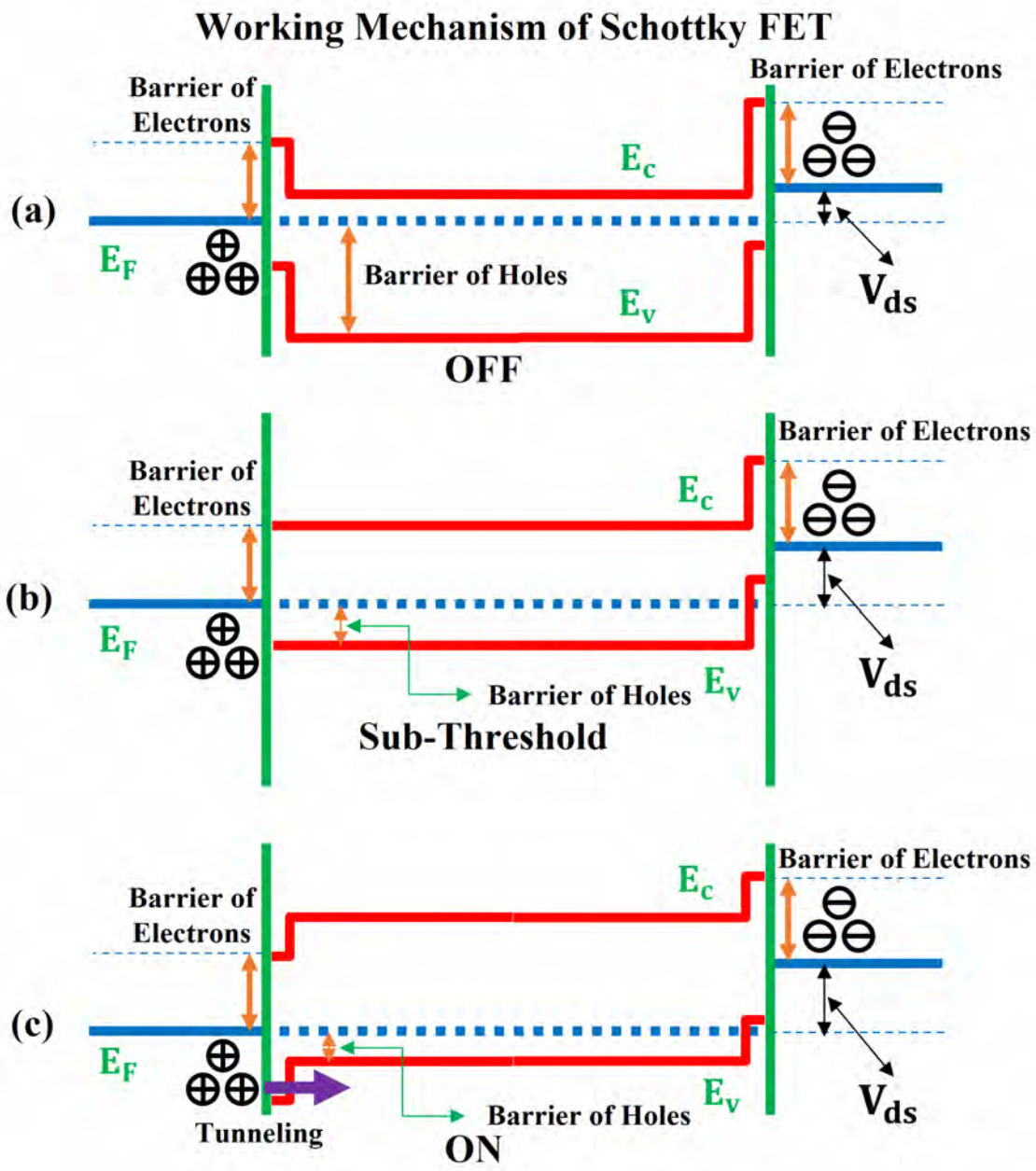

Figure 2.5: The Working Mechanism of N-Type 2D FET. (a) The Band Structure of the n-type 2D FET at Small Gate Bias. (b) The Band Structure of the n-type 2D FET at Sub-threshold State. (c) The Band Structure of the n-type 2D FET at Large Gate Bias.

the Boltzmann's constant and T (K) is the temperature.

If the applied gate voltage is further increased, as shown in fig-2.5 (c), it will cause the bands to bend up. In this case, the channel is at the strong inversion. The energy barrier for the holes is becoming thinner and thinner. When the applied gate bias increases to a certain value, the holes will start to tunnel through the barrier either directly or with the help of the thermal energy. The tunneling mechanism [31] will predominate the I-V characteristics of the FET instead of the thermionic model.

In brief, the sub-threshold condition of 2D FETs is determined by the Schottky barrier height and relative built-in potential. The charge polarity of the channel could be controlled by the applied gate bias, which is the same as 3D MOSFETs. For 3D MOSFETs, by modifying the channel charge polarity, the channel conductance could be put under control, thus the on/off states of the device could be defined. For 2D FET, applying the gate bias is mainly to modify the built-in potential, thus to control the energy barrier height for the charge carriers. By lowering/lifting the energy barrier for the electrons or holes, the 2D FET could be set as on or off. The working principle of 2D FETs clearly shows that, to get a precise prediction and evaluation of the device performance of 2D FETs, it's necessary to conduct a comprehensive study on the Schottky contacts of 2D materials.

2.4.3 Schottky Contacts in Two - Dimensional Field - Effect Transistors

The Geometry of Two - Dimensional Schottky Contacts

Schottky contact is the contact formed at the interface between the metallic and semiconducting materials. For 3D materials, only the abrupt metal-semiconductor interface needs to be considered while analyzing the Schottky contact. It has been reported that, differing from the 3D Schottky contacts, in metal-2D material Schottky contacts (2D Schottky contacts), more than one interface requires investigation while modelling the I-V of the devices [26, 27, 29]. Here we take metal-ML/multilayer

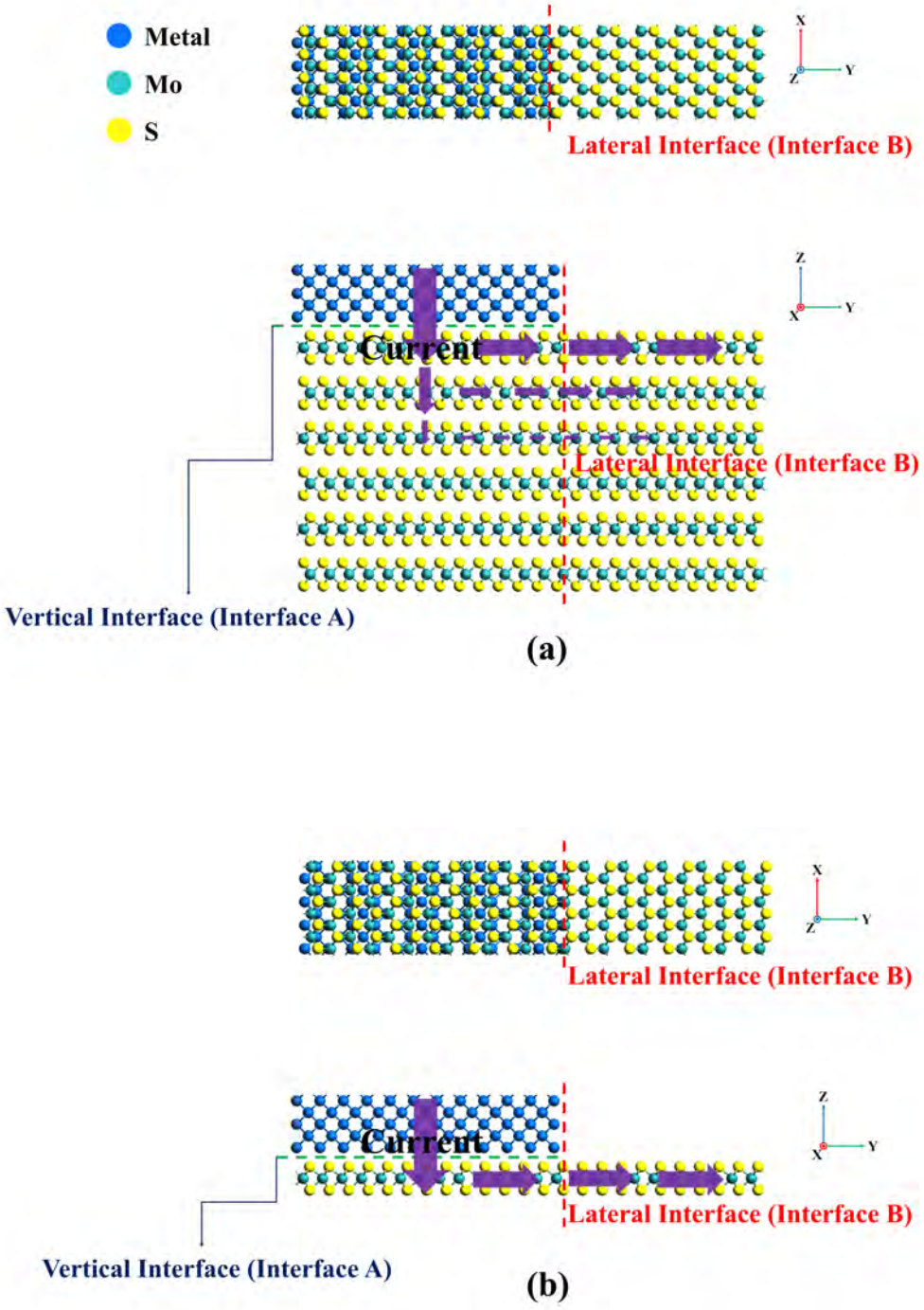

Figure 2.6: The Schematic Figure of the Geometry Configuration of Metal-MoS_2 Schottky Contacts. (a) 3D MoS_2 Schottky Contact. (b) ML MoS_2 Schottky Contact.

MoS_2 Schottky contacts as an example. As shown in fig-2.6 (a) and (b), both the ML and multilayer MoS_2 Schottky contacts consist of two interfaces: the vertical interface, which is denoted as interface A, and the lateral interface, which is denoted as interface B. As shown in fig-2.6, the interface A lies between the contact and the 2D channel. Because of the layered structure of 2D materials, the channel material at the interface A won't be depleted like 3D semiconducting materials in 3D Schottky contacts. In this case, the energy barrier which prevents carriers from injecting into the channel plane vertically is abrupt. The interface B lies between the contact-channel overlapping region and the central channel. In contrast with the absence of the depletion region at the interface A, a depletion region will be created at the interface B and extends into the central channel region, if this is an energy barrier. Thus the behavior of the energy barrier at the interface B is the same as the Schottky barrier between 3D materials.

In 2D FET, the I-V mechanism at the interface A varies in terms of the channel thickness and doping concentration. For ML MoS_2 Schottky contact, as shown by fig-2.6 (a), if the channel region overlapping with the contacts is metalized, the impedance of the interface A could be ignored [26, 27], In this case, only the Schottky barrier at the interface B needs to be investigate. If the doping concentration of the MoS_2 channel is small, a tunneling barrier will be formed at the interface A and blocks the charge transport. For multilayer MoS_2 Schottky contact, as shown in fig-2.6 (b), at the interface A, the energy barrier will be zero if the channel is metalized. The tunneling barrier will be non-zero if the doping in the channel region is small. After the charge carriers injecting into the first layer of the channel, the carriers will travel downwards to the deeper MoS_2 layers, forced by the applied bias. Under small applied bias, the channel current transport would not involve all the MoS_2 layers. Since the carriers will be impeded by the interlayer Van der Waals barriers between the MoS_2 layers, the current will only exist in the first few layers of the MoS_2. At large bias, the current will pass through all the MoS_2 layers. Since the depletion region and built-in

potential only exists at the interface B in the metal-2D material contacts, the barrier height at the interface B determines the rectification of the 2D contacts. If the energy barrier at the interface B is zero, then the 2D contact shows Ohmic I-V characteristics. If the energy barrier at the interface B is non-zero, the 2D contact is Schottky. The energy barrier height of the interface B depends on the doping concentration of the 2D channel. By doping the channel with p-type or n-type doping, the energy barrier height of the interface B could be either reduced or enhanced.

The Current - Voltage Relationship of Two - Dimensional Schottky Contacts

The current-voltage characteristics are the most import features to describe the electronic properties of the 2D Schottky contact. This is the main focus of the experimental part of this thesis.

To model the I-V of a Schottky contact, the TE model [31] based on thermionic emission theory has been brought up for many decades, and it has become the most successful and widely used model to describe the charge transport of Schottky junctions. It points out that, at high temperature and low field, the variations of the emitted current across the Schottky barrier is mainly due to the temperature dependence of the carrier density. In this case, the thermionic emission over the Schottky barrier predominates, and the current can be expressed by equation [31]:

$$\mathrm{J} = \mathrm{A}^{*}\ \mathrm{T}^{2} \exp\left(-\frac{\phi_{\mathrm{b}}}{\mathrm{kT}}\right) \exp\left(\frac{\mathrm{qV}}{\mathrm{nkT}}\right) \times \left[1 - \exp\left(-\frac{\mathrm{qV}}{\mathrm{kT}}\right)\right] \tag{2.4}$$

Where Φ_{b} (eV) is the barrier height, k ($\mathrm{m}^2 \cdot \mathrm{kg}/(\mathrm{s}^2 \cdot \mathrm{K})$) is the Boltzmann constant, q (e) id the electronic charge, T (K) is the absolute temperature, and A^* ($\mathrm{A}/(\mathrm{m}^2 \cdot \mathrm{K}^2)$) is the Richardson constant. The Richardson constant could be given by:

$$\mathrm{A}^{*} = 4\pi \mathrm{m}^{*} \mathrm{qk}^{2}/\mathrm{h}^{3} \tag{2.5}$$

Where m^* is the effective mass of the carriers and h ($\mathrm{m}^2 \cdot \mathrm{kg}/\mathrm{s}$) is the Planck's constant.

However, for many cases, the I-V equation of TE mode could not be applied to the ML/multilayer 2D Schottky junctions/contacts directly. As mentioned, the geometry of 2D Schottky junctions differs from the traditional planar 3D Schottky junction. For 2D Schottky contacts, both the two interfaces: interface A and B in the junctions will affect the current across the junction area. For 2D Schottky junction with weak ionization effects, the Van der Waals barrier exists at the interface A and causes the voltage drop across the interface [29]. The charge transport through the energy barrier at the interface A could be seen as tunneling, and the possibility of the carriers tunneling through the energy barrier T_B can be written as:

$$T_B = \exp\left(-4\pi \frac{\sqrt{2\ m\Delta V}}{h} W_B\right) \tag{2.6}$$

Where the T_B (eV) is the tunneling possibility, ΔV (eV) is the barrier height, h ($m^2 \cdot kg/s$) is the Planck's constant, m (kg) is the electron rest mass and W_B (m) is the barrier width. However, neither the ΔV nor the W_B could be extracted easily from the experiments. For this reason, a more convenient model is employed to correct the existing TE model.

The obstruction of the tunneling barrier existing at the interface A could be considered as the equivalent series resistance added to the system. For 2D Schottky contacts with large interfacial Van der Waals barrier, the series resistance model could provide correction to the error generated by the voltage drop through the equivalent series resistance of the interface A. To model effects of the series resistance of the system, the applied bias V in the equation 2.7 is replaced by V-IR_s, where IR_s represents the voltage drop due to the series resistance. After correction, the I-V equation could be given by:

$$J = A^*\ T^2 \exp\left(-\frac{\Phi_b}{kT}\right) \exp\left(\frac{q\,(V - IR_s)}{nkT}\right) \times \left[1 - \exp\left(-\frac{q\,(V - IR_s)}{kT}\right)\right] \tag{2.7}$$

It has been demonstrated that, the well-defined TE model and its series-resistance correction are adequate to describe the I-V behavior of most of 2D Schottky devices

[31, 71]. However, as mentioned above, the contact-channel-contact structure of 2D Schottky FETs forms a back-to-back Schottky system. While the barrier height of the Schottky contact is large, the equation 2.7 is invalid to describe the I-V behavior of the back-to-back system. In this case, the TE model needs to be corrected.

2.5 Molybdenum Disulfide Two - Dimensional Field - Effect Transistors

2.5.1 Why Molybdenum Disulfide

As mentioned in the previous paragraphs, the 2D channel plays an essential role in the functionality of 2D FETs. To design and fabricate high-performance 2D FETs, it is important to choose the proper 2D material as the channel material at first.

Many 2D materials have been studied for their unique 2D properties since their discovery. Among these materials, graphene has become the most popular 2D material [53]. The main reason why the graphene is so attractive is that the graphene possesses extremely large carrier mobility, which could reach 200000 $cm^2/(V \cdot s)$ as reported [15]. However, due to the zero bandgap of graphene [72], the usage of graphene in the electronic and optical applications is significantly limited. Not only the graphene, but the absence of bandgap of other metallic or semi-metallic 2D materials restricts their application as the channel materials in 2D FETs. For this reason, to find good 2D channel materials, people turn their attention towards semiconducting 2D materials. Molybdenum disulfide (MoS_2), which is a member of TMDC family, has attracted interest in the recent years.

MoS_2 is known as one of the layered TMDCs. Structurally, as shown in fig-2.7 (a), bulk MoS_2 is a stack of planes where covalently bonded S-Mo-S atoms are closely packed in a hexagonal arrangement, while the adjacent planes are held together by Van der Waals interactions. Each layer of MoS_2 is 0.65 nm thick [73]. Like other 2D materials, the layered structure of the MoS_2 crystal makes mechanical exfoliation

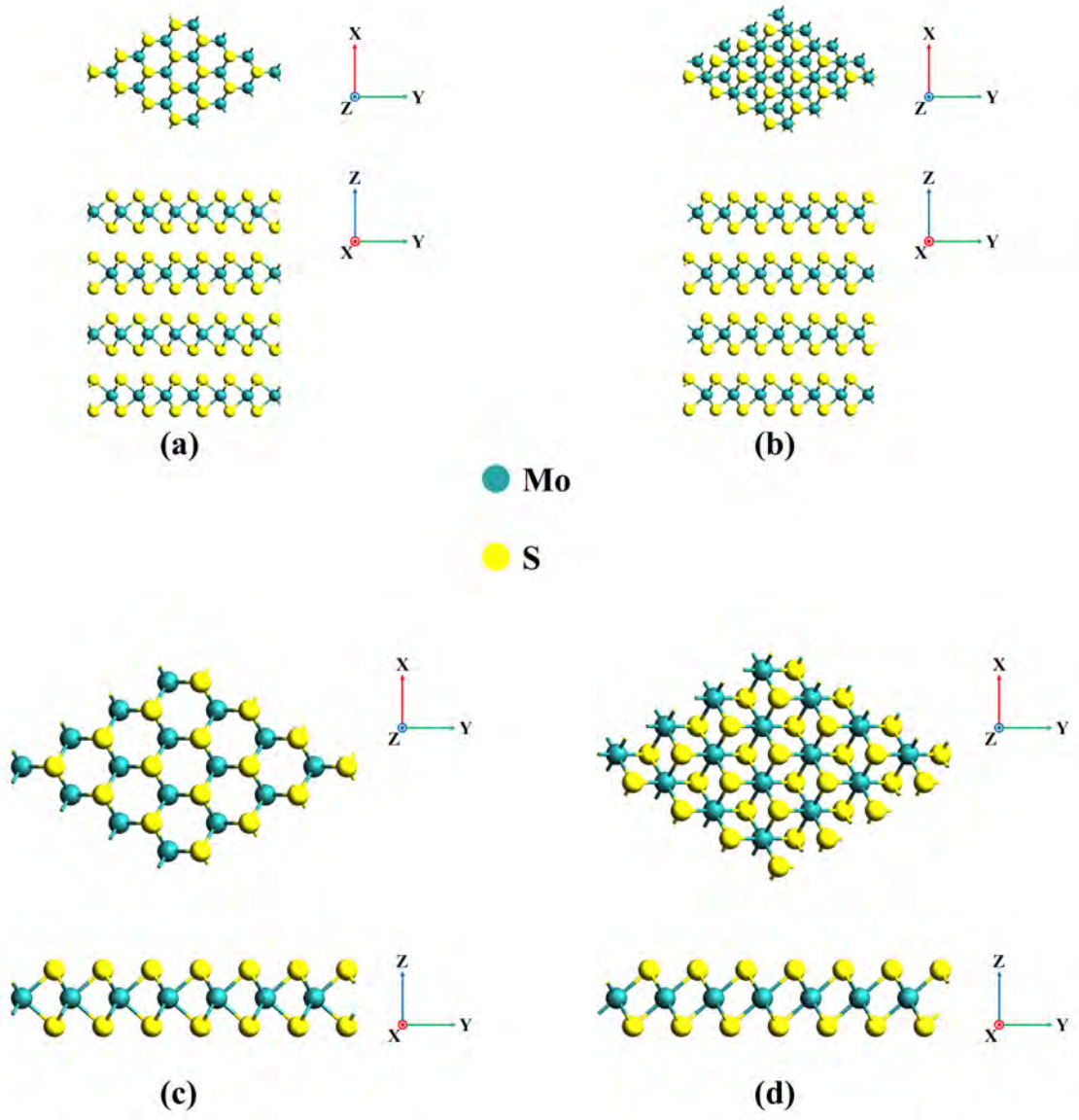

Figure 2.7: The Geometry of MoS_2. (a) Bulk MoS_2 with AA Stacking. (b) Bulk MoS_2 with AB Stacking. (c) ML MoS_2 in 2H Phase. (d) ML MoS_2 in 1T Phase.

possible [12]. Multilayer MoS_2 has two stacking orientations [38], one is AA stacking, as shown by fig-2.7 (a), and the other is the AB stacking, as shown in the fig-2.7 (b). In AA stacking MoS_2, the S atoms are at the on-top sites of the Mo atoms. Compared with AA stacking, in AB stacking MoS_2, there will be a 60° twist angle between adjacent layers, and each hollow site of the superlattice will be filled with one S atom. For multilayer MoS_2 with 3 or more monolayers, the stacking orientation of the crystal will be a combination of both AA and AB stacking [74]. As shown in fig-2.7 (c), the ML MoS_2 with trigonal prismatic geometry is found to be semiconducting (which is referred to 2H), while fig-2.7 (d) shows the ML MoS_2 of octahedral configuration (referred to as 1T) is metallic [75]. Normally, ML MoS_2 is in 2H phase, since the 1T phase is not chemically stable [75].

Bulk MoS_2 has an indirect band gap of 1.2 eV [16], while ML MoS_2 exhibits a direct band gap of 1.8 eV [17]. A non-zero bandgap with moderate bandgap energy makes MoS_2 more suitable to be adopted as the 2D channel than graphene. Theoretically, ML MoS_2 shows a mobility which is more than 400 $cm^2/(V \cdot s)$ [76]. The estimated theoretical mobility for multilayer MoS_2 ranges from 200 $cm^2/(V \cdot s)$ to 300 $cm^2/(V \cdot s)$ [77]. In experiments, the observed carrier mobility for MoS_2 is much lower than the theoretical values. Compared with some other 2D materials such as black phosphorus, the MoS_2 is very stable in air. The MoS_2 is only attacked by the aggressive reagents and shows high thermal stability. The great flexibility and mechanical strength of ML MoS_2 is also advantageous for high performance flexible 2D devices. It is reported that, flexible ML MoS_2 devices show unchanged performance even under the 1.5% strain [78]. MoS_2 is mechanically flexible with a Young's modulus of 0.33 ± 0.07 TPa [79], which is very similar to graphene.

2.5.2 Progress of the Molybdenum Disulfide Field - Effect Transistors

MoS_2 FETs previously showed low carrier mobility less than 10 $cm^2/(V \cdot s)$ [76]. B. Radisavlijevic et al. (2011) proposed a single-layer MoS_2 transistor with a Hafnium Oxide (HfO_2) layer as the gate dielectric layer [19], which indicates the ML MoS_2 works well in the environment of high-κ dielectric materials (HfO_2 has a κ of 23 [80]). The reported mobility hits 200 $cm^2/(V \cdot s)$. This work demonstrates that ML MoS_2 can be used to fabricate 2D FETs with large carrier mobility. In the recently reported experiments, the bulk/multilayer MoS_2 FETs show a carrier mobility ranging from 50 $cm^2/(V \cdot s)$ to 200 $cm^2/(V \cdot s)$ [81–83]. Compared with ML MoS_2 FETs, without the optimization of high κ dielectrics and encapsulation, the devices based on a few monolayer of MoS_2 or bulk MoS_2 show larger carrier mobility than ML MoS_2 devices [84–86]. This is because that ML MoS_2 is more sensitive to the interface conditions [85, 86]. By adopting high κ dielectrics like HfO_2 and conducting annealing and encapsulating, the interface conditions of the MoS_2 FET is improved and the experimental mobility of ML MoS_2 FETs exceed bulk MoS_2 devices [19, 87, 88]. Both the ML MoS_2 and bulk/multilayer MoS_2 devices show good on/off current ratio, which is around 10^6 for bulk MoS_2 [82], and 10^8 for ML MoS_2 [85]. The subthreshold swing of the reported MoS_2 FETs is near-ideal, which is around 70 to 80 mV per decade [82].

2.6 Optimization of Molybdenum Disulfide Two - Dimensional Field - Effect Transistors

MoS_2 FETs have shown great potential in the future applications. To improve the device performance, quite a lot of research has been conducted on different aspects to optimize the device.

2.6.1 Substrate Material Optimization

The choice of the substrate material greatly impacts both of the fabrication process and the performance of 2D MOSFET devices. Due to the lack of reliable etching technique for 2D materials, to obtain large-scale high-quality MoS_2 flakes, micro mechanical exfoliation tech or other wet exfoliation techs are still the best choice. It has been demonstrated that, the type of the substrate material, as well as the substrate thickness, determine the goodness of the adhesion between the MoS_2 crystal and the substrate [89]. For back-gate devices, the substrate consists of highly doped Si and the insulating layer. Only the insulating layer contacts with the MoS_2 channel directly. Under this circumstance, the dielectric material for the insulating layer affects both the adhesion and the gate efficiency. For this reason, the typical configuration of the back-gate devices may come up with such kind of issue: the insulating material which is suitable for optimizing the interface conditions of the channel region, will lose its competitiveness because of its poor adhesion with the MoS_2 flakes.

For both top-gate and back-gate MoS_2 FETs, silicon dioxide (SiO_2) and silicon nitride (Si_3N_4) are the most widely used substrate dielectric materials for fabrication. The SiO_2 has a dielectric constant of 3.9 [90], while Si_3N_4 has a dielectric constant of 7.5 [91]. It has been reported that, dielectric materials with higher κ could provide better charge screening to the MoS_2 channel, and reduce the carrier mobility loss due to the scattering effect generated by interfacial charge [92]. However, at present, for the reported back-gate MoS_2 FETs, the Si_3N_4 substrates show no advantages in carrier transport as compared with SiO_2 substrates.

The adhesion of the 2D flakes on the substrate could be defined by the adhesion energy. To quantize this matter, in 2002, the Volinsky's group demonstrated that, based on the thermodynamics, the adhesion energy could be given by [93]:

$$\mathrm{W} = \gamma_f + \gamma_s + \gamma_{fs} \tag{2.8}$$

Where the W (eV) is the work required to separate the 2D flake and the substrate,

the γ_f (eV) is the surface energy of the flake, the γ_s (eV) is the surface energy of the substrate and the γ_{fs} (eV) is the adhesion energy for the film-substrate interface. The normalized adhesion energy of SiO_2-MoS_2 and Si_3N_4-MoS_2 interfaces has been extracted by using the wrinkled MoS_2 thin films [89]. For SiO_2-MoS_2 interface, the adhesion energy is 0.170 ± 0.033 J/m^2, and for Si_3N_4-MoS_2 interface, the adhesion energy is 0.252 ± 0.041 J/m^2. The Si_3N_4 substrate shows better adhesion to MoS_2 films than SiO_2.

For back-gated MoS_2 FETs, high-κ materials like HfO_2 have attracted people's attention. They are considered as superior candidates for the substrate material compared with silicon-based dielectrics [92, 94]. The experimental studies have confirmed that, using HfO_2 as the substrate insulating layer for back-gate MoS_2 FETs could dramatically increase the carrier mobility of MoS_2 channel by more than 10 times [94]. The experimental results show that, high-κ dielectrics could provide strong charge screening to the MoS_2 channel and shield the carriers from the scattering [92]. For this merit, high-κ insulators has become promising candidates for the insulating layer and the coating layer of the substrate.

2.6.2 Insulating Layer Optimization

Insulating layer directly contacts with the 2D channel and separate the channel and gate. The material selection of the insulating layer has a direct impact on the charge transportation of the MoS_2 channel.

As mentioned, SiO_2 and Si_3N_4 are the most common insulating materials applied in MoS_2 FETs. While using the SiO_2 as the insulating layer, owing to the charge trapping at the insulator-channel interface, the 2D MoS_2 FETs suffer from hysteresis effect and charge scattering issue [95–97]. It has also been confirmed that the trapped charges in the SiO_2 layer of the device could be the dominant source of the potential fluctuations [98]. Compared with SiO_2, Si_3N_4 shows a much better performance while acting as the insulating layer of MoS_2 FETs [99]. The reported experimental

results demonstrate that, depositing Si_3N_4 layer onto SiO_2 substrate to form a charge screening layer, could largely eliminate the hysteresis [100]. According to the reference [100], after depositing the 30nm Si_3N_4 passivating layer onto the substrate, for the tested MoS_2 FET, the channel conductivity is increased by 100 times.

Besides Si_3N_4, several other dielectrics have been proved to be able to improve the interface conditions. One group adopted Al_2O_3 to passivate the 300 nm SiO_2 insulating layer of a back-gate MoS_2 FET. The mobility of the device was increased from 4 $cm^2/(V \cdot s)$ to 125 $cm^2/(V \cdot s)$ [101]. A MoS_2 FET with 45 nm Al_2O_3 back-gate dielectric was reported in 2015 [102]. The device performance was improved by the enhancement of dielectric screening effect. Obviously, the Al_2O_3 dielectric shows a better performance than SiO_2. However, the dielectric constant of the Al_2O_3 is still not high enough, which is 7.8 [103]. For this reason, HfO_2, which has a dielectric constant of 23 [80], is attracting more and more attention. With a large κ value, HfO_2 has proven itself as a good choice for the encapsulating passivating layer or the gate dielectric [94, 104, 105]. One group has reported that, by using the atomic layer deposition Atomic Layer Deposition (ALD) tech, 10 nm to 20 nm thick HfO_2 dielectric is deposited onto the multilayer MoS_2 flake to form a capsulation. The encapsulated device yields a carrier mobility of 42.1 $cm^2/(V \cdot s)$ [105]. Another group has exhibited a back-gate multilayer MoS_2 FET with a 10 nm thick HfO_2 gate dielectric layer deposited by ALD, showing a carrier mobility of 40 $cm^2/(V \cdot s)$ [94]. Compared with other designs, the MoS_2 FETs with HfO_2 gate dielectric show good carrier mobility and better on/off ratio [94, 104, 105]. By adopting high-κ dielectrics, the thickness of the insulating layer and passivating layer could be reduced, and the coupling between the gate and channel could be enhanced. A better gate control will further improve the on/off ratio of the devices.

2.6.3 Finding Good Metal Contacts for Molybdenum Disulfide Two - Dimensional Field - Effect Transistors

As mentioned, the performance of the MoS_2 FETs is highly dependent on the quality of the Schottky contacts. For this reason, great efforts of both experimental and computational works have been put on finding suitable metal materials for forming good Schottky/Ohmic metal-MoS_2 contacts [26–29]. Kaushik at et al. (2014) reported that, Au could form a low-barrier-height Schottky contact with MoS_2 thin films. The measured Schottky barrier height was 0.06-0.16 eV [28]. At the same time, the Palladium (Pd)-MoS_2 contact showed a much larger barrier height, which was 0.38-0.5 eV [28]. The high-performance Mo-MoS_2 Schottky contact has also been proposed [27]. It has been demonstrated that the Mo-MoS_2 contact exhibits a Schottky barrier height of 0.1 eV by both computational prediction and experiment [27]. Other electrode materials like Scandium (Sc), Chromium (Cr) and Titanium (Ti) are also used as contact materials to fabricate MoS_2 (SB) MOSFET [106–108], and most of them show low Schottky barrier heights and good conductivities.

2.6.4 The Application of Two - Dimensional Heterostructures in Molybdenum Disulfide Two - Dimensional Field - Effect Transistors

Two - Dimensional Van der Waals Contacts

Although the metal contact is the most popular choice to fabricate MoS_2 FETs, it has been observed that [26, 27, 29, 108], the metal contacts introduce metallization to the MoS_2 channel. On the one hand, the metallization adds states to the forbidden gap of MoS_2, which will reduce the bandgap energy of the MoS_2 and modify the MoS_2 electronic structures. These unwanted effects will largely impact the functionality of the devices, causing the device performance to diverge from the original design. On the other hand, the defects introduced by the metal contacts increase the charge scattering in the channel, reducing the mobility of the charge carriers. To overcome

the existing issues of the metal-MoS_2 contacts, the concept of the Van der Waals contact has been proposed and studied [30].

Normally, Van der Waals contacts denote the 2D metallic contacts consisting of monolayer/multilayer 2D metallic materials. Compared with the metal contacts, the Van der Waals contacts show several advantages. Firstly, the weak Van der Waals bonding between the MoS_2 and the Van der Waals contacts reduces the metallization effect introduced in the channel. The Van der Waals contacts may add doping to the overlapping region in the channel and cause the modification of the electronic structure there. Unlike the metal contacts, such kind of effects won't be extended to the rest of the channel region. Instead, a depletion region will be created at the interface B. Compared with metals, the unwanted metallization created by Van der Waals contacts is small and localized. This merit makes the Van der Waals contacts able to preserve the intrinsic properties of the 2D channel and improve the controllability of the fabrication process. Secondly, replacing the metal contacts with the 2D Van der Waals contacts helps the FET scaling. By applying ML/multilayer 2D channel and contacts, the fabricated devices could be extremely small in size. The flexible 2D contacts also greatly improve the flexibility of the MoS_2 FETs.

Right now, only a few 2D metallic materials have been studied for forming MoS_2 Schottky contacts. The graphene-MoS_2 Schottky contact has been reported and tested by Joon Young Kwak's group [30]. In the reported work, an asymmetric structure with graphene-MoS_2 and Ti-MoS_2 contacts is fabricated. The experimental results show that, the concentration of the donors added to the MoS_2 by graphene contact is only $3.57\times11\text{cm}^{-2}$, which is much smaller compared with metal contacts. The Schottky barrier height of graphene-MoS_2 contact is 0.23 eV, which is acceptable. The MoS_2-black phosphorus heterojunction has also been proposed [109, 110]. In the presented work [109], the I-V characteristic of the MoS_2-black phosphorus heterojunction shows gate tunability. By applying different gate bias, the junction could be either n-n or p-n type. However, the black phosphorous could be oxidized in the

air easily, which limits its application.

Two - Dimensional Capsulation

Besides the high-κ materials such as HfO_2, a type of 2D insulating materials, hexagonal baron nitride (h-BN), provides another option for gate dielectric layer and encapsulation. The h-BN is the hexagonal form of the baron nitride, with a bandgap energy of 5.2 eV [111]. The dielectric constant of h-BN is anisotropic, and can be divided into two groups: out-of-plane dielectric constant, ranging from 3.29 to 3.76, and in-plane dielectric constant, ranging from 6.82 to 6.93 [112]. Both the out-of-plane dielectric constant and in-plane dielectric constant has layer dependence. Compared with HfO_2, h-BN has its own advantages. The h-BN thin films show zero dangling bonds on the surface, which will largely reduce the interfacial charge populations while forming heterostructure with MoS_2. The weak Van der Waals bonding between h-BN and MoS_2 will protect the geometry configuration and intrinsic properties of the MoS_2 film. The h-BN thin films also possess high flexibility, which makes them available for flexible electronics. The experimental works have demonstrated that the h-BN encapsulation could largely improve the device performance. By forming h-BN-MoS_2-h-BN sandwich-like structure, the interfacial charges generated by the substrate and insulating layer could be screened efficiently. This will reduce the charge scattering of the carriers and improve the carrier mobility. Vu et al. (2018) reported a ML MoS_2 FET with h-BN encapsulation [70]. The device shows near-zero hysteresis (0.15% of the sweeping range of the gate bias), near-ideal subthreshold swing (69 mV/decade) and high on/off ratio (10^8). The carrier mobility of the device is 40 $cm^2/(V \cdot s)$, which has been improved by 4 times compared with the non-encapsulating cases. Lee et al. (2013) reported a MoS_2 MOSFET with h-BN as back-gate dielectric [113]. A few layers of h-BN was deposited onto the SiO_2/Si substrate by mechanical cleavage method before depositing the MoS_2. The device yields a carrier mobility of 45 $cm^2/(V \cdot s)$.

2.7 Remaining Issues of Molybdenum Disulfide Two - Dimensional Field - Effect Transistors

Although the study of how to fabricate high-performance MoS_2 2D FETs has made huge progress, however, many issues still remain (for both MoS_2 2D FETs and other 2D FETs).

2.7.1 Large - Scale Growth

In the past few years, a wide-range of methods have been developed for synthesizing large-area MoS_2 thin films. These methods include exfoliation methods [12], chemical vapor deposition Chemical Vapor Deposition (CVD) [114], molecular beam epitaxy Molecular Beam Epitaxy (MBE) [115], pulsed laser deposition Pulsed Laser Deposition (PLD) [116] and magnetron sputtering [117]. Although considerable efforts have been devoted to the exploration of the MoS_2 synthesis and valuable results have been generated, the experimental outcomes indicate that, there are still lot's of challenges for each deposition method respectively, and the journey towards the development of practical commercial MoS_2 deposition approach is still long. For the deposition methods mentioned above, multiple issues remain unsolved at present. Among all the mentioned deposition methods, the exfoliation method has been proved to be the most convenient and cost-effective method. However, it is impossible to gain a good control over the shape and thickness of the exfoliated MoS_2. Meanwhile, exfoliate MoS_2 thin films onto the prepared surfaces will cause lots of geometry defects and contamination, which would definitely affect the performance of the devices negatively. As for the other deposition methods, to fabricate scalable single- or multi-layer MoS_2 films, the thermal decomposition of ammonium thiomolybdate and low-pressure annealing are integrated into the PLD and CVD methods [118–121]. At the same time, the Mo precursors such as Mo and MoO_3 are applied to the CVD technique to get ML MoS_2 [122, 123]. However, these processes require multiple steps, high toxic precur-

sors, and treated substrates. The deposition process of these methods will generate lots of toxic chemical waste, which is not environmental friendly. Meanwhile, the as-produced films could be poly-crystalline or have grain boundaries [119, 124], while would significantly reduce the carrier mobility. All of these issues will greatly affect the commercial applications of these methods. The MBE method has been proved to be able to produce high-quality MoS_2 thin films [115]. But the cost of the MBE method is expensive. And the MBE process is complicated and time consuming. As for the other methods, most of the reported results show that the produced MoS_2 films are in morphologies, which do not meet the requirement of practical applications.

2.7.2 Etching Molybdenum Disulfide

To put MoS_2 FETs into large-scale manufacture, it is necessary to be able to make the fabricated devices reproducible. To meet this requirement, it is crucial to find an easy way to etch the MoS_2 films into the designed thickness and shape. After years of exploration, quite a few MoS_2 etching methods have been developed, including Gamma radiation etching, CF_4 plasma etching and Oxygen/Argon plasma etching [125–127]. The plasma-assisted methods could also be processed under the help of the deposited metallic mask (Au mask) [128]. Although these methods show controllability and selectivity, however, the experimental results show that, these etching methods tend to dope the MoS_2 by creating sulfur vacancies [125, 126]. After etching, the MoS_2 channel will lose it intrinsic properties, and the device performance will diverge from the design.

2.7.3 Forming High Quality Schottky/Ohmic Contacts

As mentioned in the previous parts, lots of studies have been conducted to find good Schottky/Ohmic contact for MoS_2, and some metal and metallic 2D materials have been demonstrated to be good choices. However, forming a good Schottky or Ohmic contact with MoS_2 is still a big challenge.

The biggest issue for exploring good contacts is the uncertainty of the Schottky barrier height after metal-MoS_2 contact formation. For 3D materials, we can predict the Schottky barrier height with well-defined Schottky-Mott law [129]. The Schottky-Mott law claims that the Schottky barrier height could be given by:

$$\phi_{\mathrm{SBH}} = \Phi_{\mathrm{M}} - \chi \tag{2.9}$$

Where the Φ_{SBH} (eV) is the Schottky barrier height, Φ_{M} (eV) is the workfunction of the metal and χ (eV) is the electron affinity of MoS_2. However, according to the references [26–29, 106–108], the Schottky-Mott method failed to predict the metal-MoS_2 Schottky barrier height in multiple cases. According to the reported studies [27, 28, 106–108], both low and high workfunction metals tend to covert the MoS_2 layer from intrinsic to n-type material, modifying the electronic structure of the MoS_2 by adding ionized doping. This causes the Schottky-Mott law unable to predict the Schottky barrier height of the MoS_2 Schottky contacts. These results also indicate that the MoS_2 Schottky contact is not only determined by the electron affinity and work function of materials, but also the interface properties. To solve the issue above, a new model is required to comprehensively explain the physical mechanism behind the formation of metal-MoS_2 Schottky contact, but such kind of model is still unavailable nowadays. Nowadays, the Schottky barrier height of metal-MoS_2 is still unpredictable before massive simulation and extensive experimental work. It is impossible to find good metal contacts for MoS_2 just by simply evaluating the metal work function and MoS_2 electron affinity.

As mentioned previously, the metal-introduced doping/ionization is also an issue for the 2D FETs based on the metal-MoS_2 contacts. It has been confirmed by both experiments and simulations that the metal contacts tend to introduce gap states to the MoS_2 channels [26, 27, 29]. After contacting with metal, the intrinsic MoS_2 channel will become either n-type or p-type and the bandgap energy of MoS_2 will be reduced largely [26, 29]. Sometimes the metal contacts could heavily dope the

MoS_2 [29]. The introduced doping is mainly generated by the defects in the MoS_2. These defects are generated by the strain [130, 131] or bonding [26, 29] at the vertical interface (interface A). These defects also add trap states in the forbidden gap and cause the reduction of the MoS_2 bandgap. This kind of doping is random and unpredictable because they are highly dependent on the interface conditions, which are related to the fabrication process. On the one hand, the metallization of the MoS_2 channel introduced by metal contacts eliminates the tunneling barrier at the interface A. On the other hand, the metallization creates interfacial charges, which will reduce the Schottky barrier height and affect the functionalization of the devices. The introduced defects in the MoS_2 channel also scatter the charge carriers and reduce their mobility significantly. Generally speaking, the uncontrollable metal-introduced doping of the MoS_2 channel affects the device performance negatively. Although the 2D contacts could solve the metallization issue, but a more comprehensive study is still an urgent need.

To solve the issues mentioned above, in this study, we have conducted a comprehensive study based on both experiments and computational works. We have conducted DFT simulations to find good Schottky/Ohmic contacts for MoS_2, using the traditional metals, and novel 2D semimetals. To verify the simulated results, we have fabricated and tested back-to-back Au-MoS_2 contacts. A novel mathematical model based on image-force correction has been developed to extract the Schottky barrier heights of the diodes. To optimize the MoS_2 channel, we have conducted a comprehensive DFT study on the effective mass variation of the MoS_2 thin films with different stacking orientations, and TMDC heterojunctions.

Chapter 3

Methodology

To achieve a better understanding of MoS_2 FETs, we have conducted a comprehensive study on the metal/TiS_2-MoS_2 contacts and TMDC heterostructures, which is based on both simulations and experiments.

3.1 Density Functional Theory

The simulation part is the main focus of this thesis, which has been conducted by using the well-defined DFT method. The DFT simulations in this thesis are performed by applying the DFT package provided by Quantumwise Atomistix ToolKit (ATK) Ver.16.2 [6].

3.1.1 Concept of Density Functional Theory

DFT is one of the most popular and successful quantum mechanical approaches [132]. It is nowadays widely applied on calculating the binding energy of molecules in chemistry and the band structure of solids in physics. Unlike the traditional Hartree-Fock Hartree-Fock (HF) method, which tries to solve a full dimensional Schrodinger equation to describe a many-electron system, the DFT method supposes that the properties of many-electron systems can be determined by using functionals. The functional is defined as the functions of another function. In this case, the functionals defined in the DFT theory is spatially dependent on the electron density of the system [132].

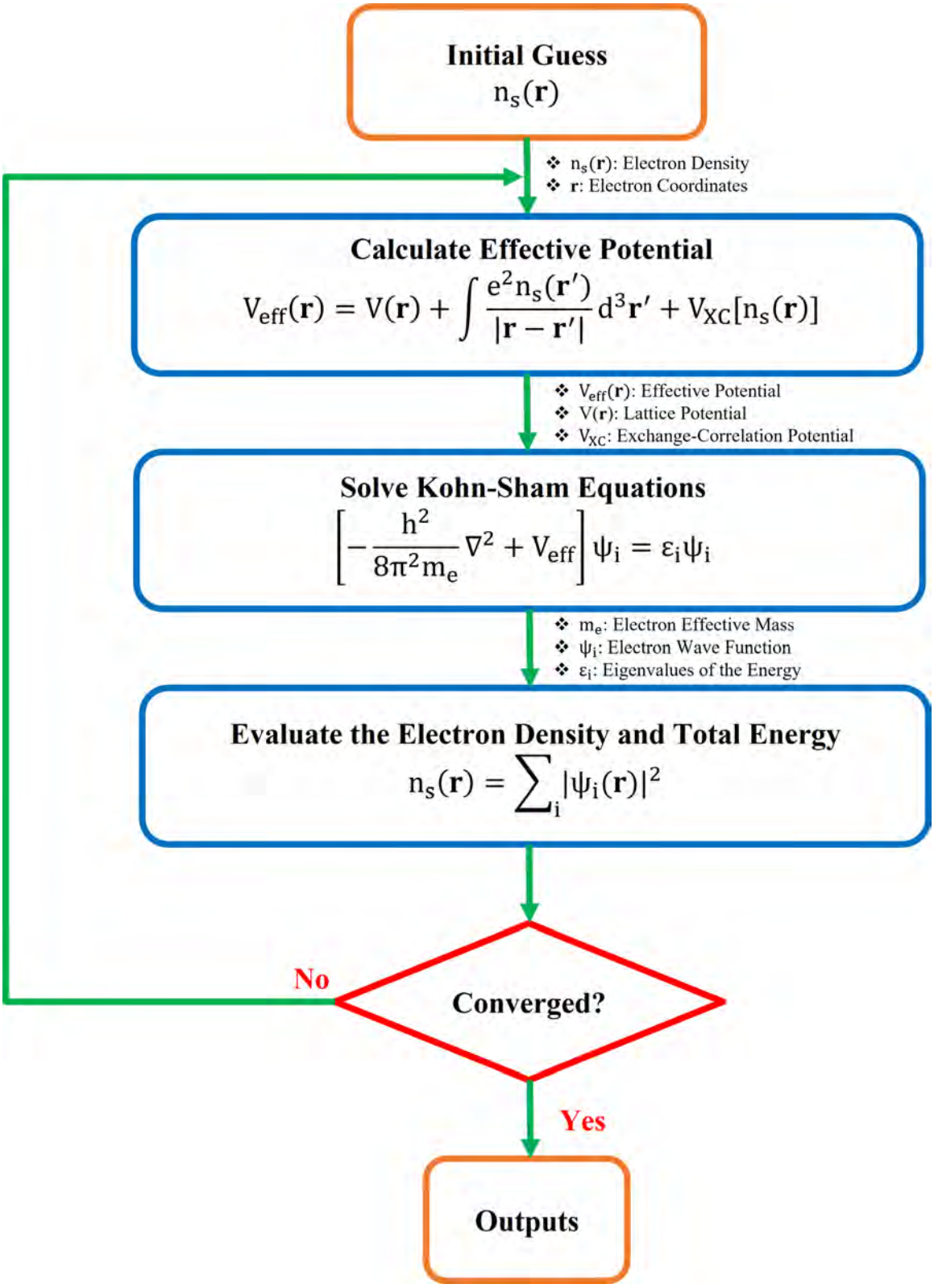

Figure 3.1: The Process Flow of Solving the Self-Consistent Kohn-Sham Equations.

In the DFT theory, while performing calculations for many-body electronic structure, the nuclei of the treated molecules or clusters is considered as fixed. This will generate a static external potential V, in which all the electrons are moving. The stationary electron states can be described by the wave function $\Psi(\overrightarrow{r_1}, \overrightarrow{r_2}, \ldots, \overrightarrow{r_n})$, which satisfies the many-electron time-independent Schrodinger equation:

$$\widehat{H}\Psi = [\widehat{T} + \widehat{V} + \widehat{U}]\Psi = E\Psi \tag{3.1}$$

Where, for the N-electron system, $\widehat{H}$ is the Hamiltonian, E is the total energy, $\widehat{T}$ is the kinetic energy, $\widehat{V}$ is the potential energy from the external field due to the positive charge of the nuclei, and $\widehat{U}$ is the electron-electron interaction energy. To solve this many-body Schrodinger equation, there are many sophisticated methods. However, applying these methods needs huge computational effort. This makes it virtually impossible to apply them efficiently to large, complex systems. For this reason, the DFT method is more appealing. The only key variable in DFT method is the electron density $\overrightarrow{n(r)}$, which can be given by the normalized electron wave function Ψ. The total energy E can be described by a functional:

$$E[n] = T[n] + U[n] + \int V(\overrightarrow{r})n(\overrightarrow{r})d^3r \tag{3.2}$$

Where, n is the electron density, the $\widehat{r}$ is the spatial vector, T[n] and U[n] are the universal functionals while V depends on the system being studied. The V can be expanded to a more detailed equation:

$$V_s(\overrightarrow{r}) = V(\overrightarrow{r}) + \int \frac{e^2 n_s\left(\overrightarrow{r'}\right)}{|\overrightarrow{r} - \overrightarrow{r}'|} d^3r' + V_{XC}\left[n_s(\overrightarrow{r})\right] \tag{3.3}$$

Where the V_s is the effective single-particle potential, and V_{XC} is the exchange-correlation potential. The second term is the so-called Hartree term, which describes the electron-electron Coulomb repulsion, while the last term is called exchange-correlation potential. To be noticed, once the V_{XC} is determined, the self-consistent equation 3.3 can be fully solved. The whole process is shown in figure-3.1. According

to the Kohn-Sham theory, the exchange-correlation energy V_{XC} is also a functional of electron density [132]. This fact gives great convenience to the DFT simulation since a pre-defined functional is possible to be defined for solving the many-body Schrodinger equation of the system.

3.1.2 Functionals

As mentioned, it is possible to define the exchange-correlation functional to solve the many-body Schrodinger equation of the system. Many exchange-correlation functionals have been invented. For the electronic structure calculation in the solid-state community, the local-density approximation Local-Density Approximation (LDA) [133] and generalized gradient approximation Generalized Gradient Approximation (GGA) [134] are normally applied for defining the exchange-correlation energy of the system. The LDA approximation assumes that the exchange-correlation energy functional of the DFT theory depends solely on the spatial distribution of the system electron density [133]. Since a homogeneous electron gas model is used to build the LDA method [133], the LDA tend to underestimate the exchange energy and overestimate the correlation energy of the system [135]. To improve the simulation accuracy, the GGA method has been brought up [134]. Compared with LDA, the GGA assume that the exchange-correlation energy is a functional of both the electron density and its gradient at each spatial point. In this case, the system is treated as a non-homogeneous electron gas system. In many applications, results obtained by GGA are confirmed to be accurate enough for interpreting experimental data or making prediction. What's more, the GGA are computationally cheap compared with the more sophisticated methods. However, it has been pointed out that, GGA may lead to results which are in very bad agreement with experiments. For example, the band gap of semiconductors and insulators can be severely underestimated or even be absent by using GGA [136]. To prevent such kind of issue, the Meta Generalized Gradient Approximation Meta Generalized Gradient Approximation (mGGA) functional [137] has been

invented to perform the band gap and electron transportation calculation.

The mGGA functional includes not only the local electron density and its gradient, but also the kinetic-energy of the electrons. At the same time, the Becke-Roussel Becke-Roussel (BR) potential is also employed by the mGGA method to model the Coulomb potential created by the exchange hole [138]. The mGGA could be expressed as [137]:

$$V_X^{TB} = cV_X^{BR}(\mathbf{r}) + \frac{3c-2}{\pi}\sqrt{\frac{4\tau(\mathbf{r})}{6\rho(r)}} \tag{3.4}$$

$$\tau(\mathbf{r}) = \frac{1}{2}\sum_{i=1}^{N}|\nabla\Psi_i(\mathbf{r})|^2 \tag{3.5}$$

Where the V_X^{TB} is the exchange potential given by Tran and Blaha [11], τ(r) is the kinetic energy density, Ψ_i(r) is the Kohn-Sham orbital, ρ(r) is the local electron density and V_X^{BR}(r) is the BR potential. The parameter c in the equation could be defined by:

$$c = \alpha + \beta\left[\frac{1}{\Omega}\int\frac{|\nabla\rho(\mathbf{r})|}{\rho(\mathbf{r})}d\mathbf{r}\right]^{\frac{1}{2}} \tag{3.6}$$

Where the Ω is the volume of the unit cell, the constant α equals to -0.012, and the β is 1.023 Bohr(1/2).

While applying the mGGA method, the first step is to find out the suitable c parameter for the semiconducting material simulated. By varying c, the bandgap energy will increase monotonically [139]. Normally, the bandgap obtained with c=1 is too small with respect to the experimental value. In most of the cases, the c parameter lies within the range of 1.1 to 1.3 for small-bandgap semiconductors. For large-bandgap semiconductors, the c could range from 1.4 to 1.7. An optimized fitting is required to obtain the c parameter which makes the simulation result a perfect agreement with the experiments. To extract the optimized c parameter, different predefined c parameters are adopted in the bandgap simulation to extract the respective bandgap energy. Then a linear fitting is conducted for extracting the c parameter against bandgap energy curve. After fitting, the c parameter which could give the

experimental value of the bandgap energy is the optimized c parameter for the simulated semiconductor. To be noticed, for both the ML and multilayer MoS_2, the reported ML MoS_2 bandgap is adopted for the c parameter optimization, and the given c parameter is 1.15.

Although the GGA method could not predict bandgap energy accurately, but it is still qualified for other simulations such as electron density and Mulliken population. The mGGA functionals contain the second derivative of the electron density. For this reason, mGGA could not be used in geometry optimization. As a result, GGA method would be a good choice for geometry optimization. Besides, mGGA is a type of DFT+U method. The artificial potential added to the Schrodinger equation may change the physics meaning of the system and add unwanted modification to the band structure of the system. By comparing the band structures of multilayer MoS_2 systems given by mGGA and GGA, the results intuitively shows that the positions of valence band maximum and conduction band minimum given by GGA is closer to the experimental data. For this reason, due to the band structure shape issue of mGGA with large c parameters, GGA is also a much better choice for effective mass and mobility simulations. In our simulations, both the GGA and mGGA are adopted to perform the DFT simulations to obtain the most accurate results.

3.1.3 Pseudo Potential

In our simulation, the linear combination of atomic orbitals Linear Combination of Atomic Orbitals (LCAO) basis set is employed for expanding the orbitals of the simulated system. The accuracy of the simulation using LCAO models highly depends on the choice of the pseudo potential. In our simulation, three types of pseudo potential: Trouiller-Martins type Trouiller-Martins Type Pseudo Potential (FHI) [140], Hartwigsen-Goedecker-Hutter type Hartwigsen-Goedecker-Hutter Type Pseudo Potential (HGH) [141] and SG-15 type [134] are adopted to meet different accuracy and computational resources requirements of the simulations. Among the three types of

pseudo potentials, the SG-15 pseudo potential has the best accuracy, but it will occupy lots of computational resources. As a result, SG-15 is suitable for simulating small scale systems. HGH pseudo potential works well in most of the cases with a medium accuracy. At the same time, HGH pseudo potential requires less memory and cores compared with SG-15. That makes HGH suitable for the systems with medium size. Due to the poor accuracy, FHI pseudo potential is only applied to the simulations requiring massive configurations such as PLDOS simulations.

For Different pseudo potentials, there are several choices of the basis sets provided by the ATK DFT package. For FHI pseudo potential, SingleZeta SingleZeta (SZ), DoubleZeta DoubleZeta (DZ), SingleZetaPolarized SingleZetaPolarized (SZP), DoubleZetaPolarized DoubleZetaPolarized (DZP) and DoubleZetaDoublePolarized DoubleZetaDoublePolarized (DZDP) are provided by the ATK package. For each occupied valence orbital of the atom, the SZ provides with one confined orbital. Here the confined orbital is the solution of the radial Schrodinger equation with a confined potential. DZ provides one confined orbital and one analytical-split orbital built by smoothing the base orbital, for each occupied valence orbital of the atom in the simulated system. SZP provides one confined orbital for each of occupied valence orbital of the atom and one polarization orbital for the first unoccupied shell of in the atom. The polarization orbitals are generated by perturbing the base orbital with an E field in the z direction. For DZP, the basis set uses one confined orbital and one analytical orbital to describe each occupied valence orbital. The DZP also uses one polarization orbital to describe the first unoccupied shell of the atom. In DZDP basis set, confined orbitals and analytical orbitals are applied to model the occupied valence orbitals, while the unoccupied shell is defined by the polarization orbitals and analytical orbitals. Generally speaking, for FHI pseudo potential, more orbitals the basis set consists of, the higher accuracy it has. For HGH, Tier-0 to Tier-8 basis sets are provided by ATK. Adopting higher tier will make the HGH pseudo potential softer. This may lead to better results of simulating the interfaces of the systems.

Table 3.1: The Δ-Test Results of Different Pseudo Potentials

	Mo	W	Au	Ti	S	Se	Te
FHI-SZP	81.91	63.88	8.24	32.25	-	41.28	25.48
FHI-DZP	75.97	32.69	5.97	21.49	-	24.96	4.77
HGH Tier-4	3.78	71.19	13.44	0.40	-	9.53	14.06
SG-15 Medium	1.32	2.74	5.50	1.27	3.43	1.06	8.54
SG-15 High	1.54	0.39	4.08	1.44	0.34	1.58	4.02
SG-15 Ultra	1.26	0.23	3.30	1.90	0.34	1.95	3.99

Normally HGH has a better accuracy than FHI. But adopting HGH will make the simulation become computationally heavy. For SG-15 pseudo potential, three basis sets: Medium, High and Ultra, are generated by FHI basis sets and avaliable in ATK package. Normally, Medium is sufficient for most simulations, while High and Ultra are mainly for the simulations requiring extremely high accuracy.

The optional basis sets and their accuracy on simulating the materials involved by the thesis are shown in table-3.1. Great efforts have been devoted on investigating the precision and efficiency of the pseudo potential. The Δ-test of each combination of pseudo potentials and basis sets on different elements is provided in open source [142, 143]. In the Δ-test, the Δ is defined as the root-mean-square energy difference between the equations of two solid state DFT codes, which are averaged over all the crystals in a purely elemental benchmark set. The Δ-test values of different pseudo potentials could be seen as an important criterion of their accuracy.

3.1.4 Other Parameters

There are other parameters which are crucial to the accuracy of the DFT simulations. Here, only the physics meaning and functions of these parameters will be introduced since the set-up of them is highly based on the simulated systems. For these reasons,

the detailed values of these parameters will be reported separately in the each chapters associated with DFT simulations.

Boundary Conditions

In our DFT simulation, the periodic boundary condition Periodic Boundary Condition (PBC) is employed to describe the extension of the superlattice. By adopting PBC, the superlattice will be repeated in x, y and z directions to create a bulk system. A 2D system can be created by adding a vacuum buffer. The PBC requires the electrostatic potential of the lattice decays softly at the boundary. To improve the convergence of the simulated system, a maximum interaction distance is defined for the atoms in the superlattice while using PBC. Normally, the maximum interaction distance should be larger than 2 to 3 times of the lattice constants. In our simulations, this value is about 5 times of the lattice constants.

Electron Temperature

Electron temperature is pre-defined in the simulation to help the smearing of the electron distribution. The electrons in the system tend to start occupying the lowest eigenstates to the energy level determined by Aufbau principle [144]. This kind of electron distribution corresponds to the Fermi-Dirac distribution (at absolute zero), and the distribution could be described as a step function. However, the DFT simulation will have convergence issue if there are degenerate states at the Fermi level. One way to avoid this issue is to smear the electrons. For smearing, a finite temperature will be assigned to the Fermi-Dirac distribution, and the electron distribution will no longer be a step function. In this case, the simulation could converge smoothly at the Fermi level. In our simulations, the electron temperature is set as 300 K.

Cut-off Energy

The expansion of the Schrodinger equation solution consists of an infinite sum of the basis sets. The cut-off energy defines the largest k that the sum will involve and

make the calculation practical. A small cut-off energy may cause the convergence issue of the simulation, while a very large cut-off will make the simulation resource demanding. A convergence test is required to determine the best cut-off energy of the simulation. In our research, the cut-off energy is set as 100 Ry.

K-Points Sampling

In our simulation, the Monkhorst-Pack mesh [145] is applied on Brillouin zone sampling. To apply the Monkhorst-Pack method, it is required to specify how many k points are going to be used in each direction of the reciprocal space. A moderate amount of the sampling points is preferred during the DFT simulation. A convergence test by calculating the total energy of the system with respect to different k point numbers has been performed to find out the best k-point sampling. The number of k points is verified in each direction, and the total energy of the system will fluctuate with the variation of k point sampling. After a certain k point number, the total energy will stop fluctuating and become a constant value. In this case, the k point number at the convergence could be considered as the optimized value for sampling. The number of k points depends on the size of the system. A larger system in real space will have a smaller cell in the reciprocal space, thus it requires a smaller k point number for sampling.

3.2 Fabrication Tech

Besides the DFT simulations, the experiments have also been conducted to demonstrate the properties of metal-MoS_2 contacts. At the same time, the I-V tests on fabricated MoS_2 diodes provide valuable data for modeling the I-V characteristics of the metal-MoS_2 Schottky contacts. Here, a summary of the techs and facilities adopted in the experiments is presented.

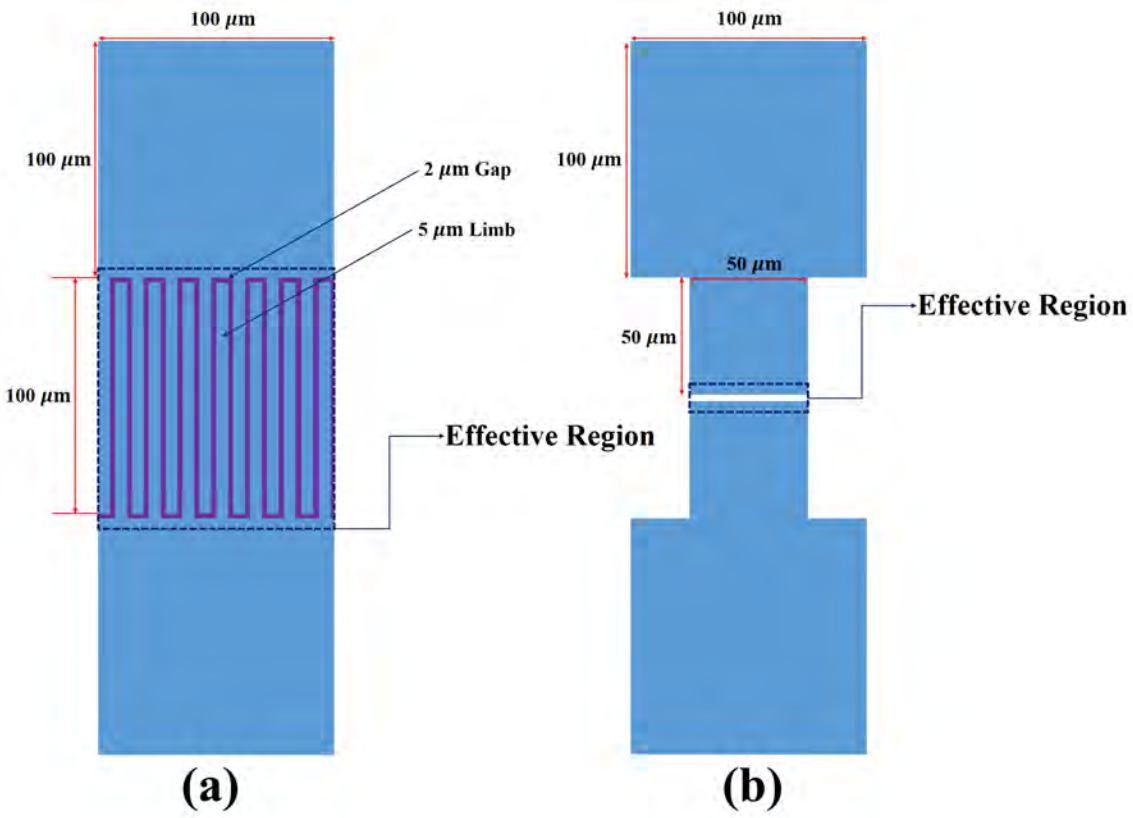

Figure 3.2: The Design of Electrodes. (a) Electrode with Comb Structure. (b) Electrode Consists of Simple Metal Pads without Limbs.

3.2.1 The Design of the Electrodes

To increase the yield of the exfoliation, the unique comb designs with limbs in different sizes are adopted to the patterning of the metal electrodes. The software Klayout v.0.24.10 is used to design the patterns of the electrodes. The electrode pads are set as 50(μm)×50(μm) and 100(μm)×100(μm) squares. The length of the limbs is set as 25μm, 50μm and 100μm respectively. The width of the limb is set as 5μm and 10μm. The gap between the limbs is set as 1μm, 2μm, 3μm, 5μm, 7μm and 10μm.

The comb structure design of the electrodes could improve the yields of the mechanical exfoliation by increasing the area of effective region. The effective region is defined as the region where a connection between two electrode pads could be formed when the MoS_2 flakes land on. As shown in fig-3.2 (a), take the electrode

with 100μm×5μm limbs as an example. In the plot, the two electrode pads are 100μm×100μm, and the gap between the limbs is set as 2μm. Suppose the deposited MoS_2 flake has a diameter of 7μm, which is obtainable by our mechanical exfoliation method. As shown in fig-3.2 (a), the area of the effective region, labeled with dark blue dash frame, is roughly 11,000 μm^2, while the single-limb design, as shown by fig-3.2 (b), has an effective area of 1200 μm^2. It is clear that, the comb design greatly improve the success rate of the exfoliation by increasing the effective area.

Although the comb structure could dramatically increase the yield of the exfoliation, however, there are some issues while using the comb design. First, the comb structure has lots of limbs. The zigzag gap between two limbs could create ripples on the MoS_2 surface, which will generate defects and reduce the carrier mobility. Secondly, the comb structure has a large effective region. After each exfoliation, multiple flakes may land within the effective region and link the two pads at the same time. This adds lots of difficulties to the modelling of the I-V since a system with multiple paralleled Schottky diodes has been created. For this reason, after exfoliation, only a few devices with single flake landing on are suitable for I-V modeling. Finally, the comb structures has a much higher requirement on the fabrication quality.

3.2.2 Lithography

To fabricate high-quality comb-structure electrodes, the process of the photolithography has been optimized. Before the deposition, the wafer is treated by a 15 min piranha process. Then the wafer is transferred to the YES oven (HMDS) for surface conditioning. This process is to improve the adhesion of the photoresist on the SiO_2 and Si_3N_4 wafers. The AZ5214 positive photoresist is adopted for the lithography. The reason of using positive photoresist is that, the positive photoresist is able to create an undercut below the photoresist after the developing, which helps the lift-off process after deposition. Besides, the undercut of the photoresist helps create high-quality electrodes without sharp edges, which benefits the exfoliation of MoS_2.

Table 3.2: The Set-Up of the Lithography Process of AZ5214 Photoresist

Process	Parameter
Spread	500 rpm/10 s
Spin	4000 rpm/40 s
First Bake	90 ℃/1 min
First Exposure	55.2 $W \cdot cm^{-2}$/2.8 s
Second Bake	115 ℃/40 s
Flood Exposure	30 s
Developing Time	35 s

For the AZ5214 photoresist, the optimized process in our study is: firstly spread at a speed of 500 rpm for 10 s then spin at a speed of 4000 rpm for 40 s. Then the wafer coated with photoresist is baked in the CEE 200CB coat-bake system at 90 ℃ for 1 min. After the first bake, the fist exposure is performed by using the mask aligner. The exposure power is 55.2 W/cm^2 and the exposure time is 2.8 s. Then a second bake is conducted at 115 ℃ for 40 s. After removing the mask from the mask aligner, a flood exposure of 30 s is conducted to the wafer. Finally, the pattern of the electrodes could be obtained after the 35s developing process. The recipe of the lithography is listed in the table-3.2.

3.2.3 Deposition

By using the sputtering system, Au is deposited onto the wafer, while the Mo and W are deposited by the electron-beam evaporation system. After the lift-off process, the patterned electrodes are ready for the mechanical exfoliation of the MoS_2.

The mechanical exfoliation is performed by using the homemade exfoliation aligner, as shown by fig-3.3. The aligner consists of standard optical setup parts. With the help of the X-Y stage and Z-axis adjuster, the sample holder of the system could move around in X, Y and Z direction by micron scale. Before the exfoliation, the Scotch-

Figure 3.3: The Homemade Mechanical Exfoliation Aligner.

3105-Magic tape is exfoliated onto a cleaned glass slide for 8 to 10 times to reduce the stickiness. This process helps reduce the glue residue created by the exfoliation. Then the commercial CVD grown MoS_2 is exfoliated by 6-8 times to obtain thin films. After the pre exfoliation of the MoS_2, the PARAFILM (BEMIS PM-992) is cut into 3(inch)×1(inch) rectangle and employed to cover the surface of glass slide. The MoS_2 flakes are transferred to the glass slide coated with PARAFILM. Then, the coated glass slide is loaded onto the sample holder of the aligner. By using the focus of the integrated microscope, the MoS_2 flakes are aligned with the desired electrode region and the exfoliation is conducted by lowering the stage.

3.2.4 Annealing

The annealing process is crucial for the performance of MoS_2 Schottky contacts. The annealing process helps clean the glue residue after the exfoliation, and restore the crystal structure of the MoS_2 film which may be damaged during the exfoliation process. An annealing process at high temperature could also improve the bonding condition between the MoS_2 and metal.

Our annealing process is conducted by using the vacuum chamber integrated with the MAPLE pulsed laser deposition system, which is provided by the PVD Products company, as shown in fig-3.4. The annealing temperature is set as 473 K (200 ℃) for Au-MoS_2 contacts, and the annealing time is 1 hr. The whole process is conducted at the high vacuum with a base pressure of 2.9E-7 Torr. The ambience of the chamber is also supplied with argon flow to prevent the MoS_2 oxidization. The flow rate of the argon is set as 40 standard cubic centimeters per minute. After annealing process, the load-lock is opened and the sample is transferred to the side chamber for cooling down. The side chamber is also at the high vacuum.

3.3 Characterization Techniques

3.3.1 Raman Spectroscopy

The two vibration modes in MoS_2: the interlayer vibrational mode (E^1_{2g}), which is related to the movement of the complete layers, and the intralayer vibrational mode (A_{1g}), which is related to the vibration inside the layer, have different layer dependence. While the number of layers of MoS_2 increases, the signature peaks of these two modes in Raman spectrum will shift to different wave numbers. This difference could help us to determine the thickness of MoS_2. The reported peak frequencies with various laser lines [146] are listed in the table-3.3 and table-3.4. After 5 layers, the multilayer MoS_2 becomes bulk, and the resolution of the differences between the two peaks could no longer support us to do any thickness investigation. The Raman spectroscopy is performed by using the Raman microscopy system provided by HORIBA Company, and the used laser wavelength is 532 nm.

3.3.2 Atomic Force Microscopy

The Raman spectroscopy is unable to figure out the thickness of bulk MoS_2 because of the reduction of the resolution of the difference of the shifting of the MoS_2 signature peaks as the number of layers of the MoS_2 increasing. The atomic force microscopy

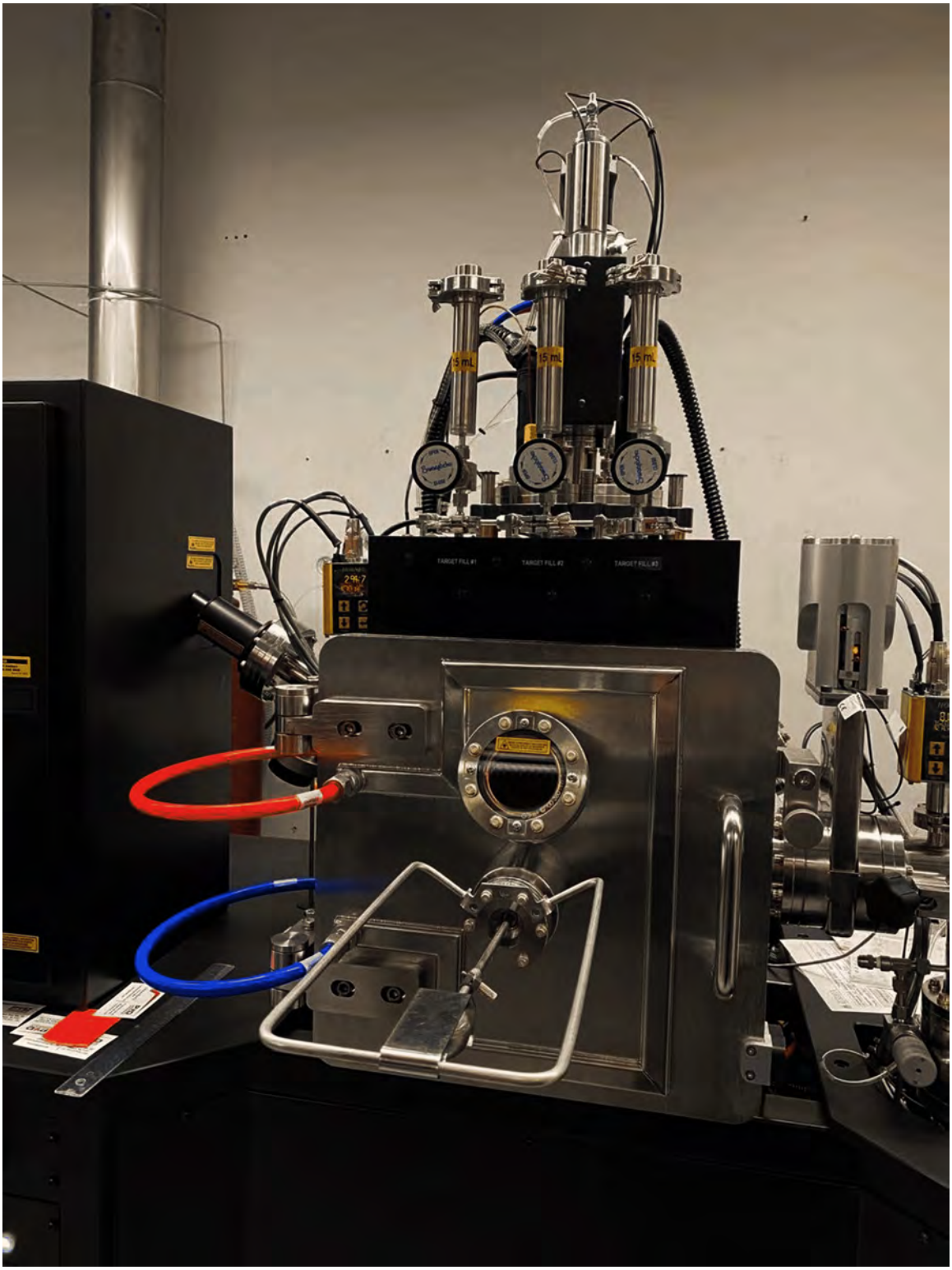

Figure 3.4: The Vacuum Chamber for Annealing.

Table 3.3: The Raman Peak Position of the E^1_{2g} Mode of the MoS_2 with Different Thickness

E^1_{2g} Peak Frequency (cm^{-1})					
Laser Line	1L	2L	3L	4L	Bulk
325 nm	384.2	382.8	382.8	382.7	382.5
488 nm	384.7	383.3	383.2	382.9	383
532 nm	384.7	382.5	382.4	382.4	383
632.8 nm	385	383.8	383.3	382.9	381.5

Table 3.4: The Peak Position of the A_{1g} Mode of the MoS_2 with Different Thickness

A_{1g} Peak Frequency (cm^{-1})					
Laser Line	1L	2L	3L	4L	Bulk
325 nm	404.9	405.5	406.3	407	407.8
488 nm	402.8	405.5	406.5	407.4	408
532 nm	402.7	404.9	405.7	406.7	407.8
632.8 nm	403.8	404.8	405	406	406.6

Atomic Force Microscopy (AFM) tech is adopted to investigate the topography of bulk MoS_2 devices. The AFM is a type of high-resolution scanning probe microscopy. By using a sharp tip supported by the cantilever, the AFM can scan the sample surface. The cantilever deflects while the tip contact the surface, and a detector will collect the data of the deflection motion. Then the signals will be processed and the surface information of the sample will be generated. Normally, two imaging modes are widely used during the AFM measurements: contact mode, and tapping mode. In our measurements, the tapping mode is used for measuring the thickness of the MoS_2 thin films. The AFM system adopted in our measurement is the Dimension Edge AFM provided by the Bruker Company.

3.3.3 Kiethley Current-Voltage Measurement

The Keithley 4200SCS semiconductor characterization system along with the Keithley 2612B dual channel sourcemeter are adopted to conduct the I-V measurement in this thesis.

Chapter 4

Density functional theory - projected local density of states - based estimation of Schottky barrier for monolayer Molybdenum Disulphide[1].

Junsen Gao[1], Dipanjan Nandi[1], Manisha Gupta[1,*]

*Address of correspondence mgupta1@ualberta.ca

[1]Department of Electrical and Computer Engineering, University of Alberta, Edmonton, Alberta T6G 2R3, Canada.

KEYWORDS: MoS_2*, Density Functional Theory, Schottky barrier height, built-in potential, electron density, PLDOS, Mulliken population.*

4.1 Abstract

One of the biggest challenges so far in implementing 2D materials in device applications is the formation of a high quality Schottky barrier. Here, we have conducted density functional theory (DFT) simulations and employed the projected local den-

[1]The chapter 4 has been published as Junsen Gao, Dipanjan Nandi and Manisha Gupta "Density functional theory projected local density of states based estimation of Schottky barrier for monolayer Molybdenum Disulphide," Journal of Applied Physics 124, 014502 (2018).

sity of states (PLDOS) technique to study the Schottky contact formation between monolayer (ML) MoS_2 with different metal electrodes (Mo, W, Au). Electrode formation on ML MoS_2 changes it from intrinsic to a doped material due to metallization, which creates issues in the formation of a good Schottky contact. Amongst the metals studied here, we observe that Mo tends to form the best Schottky barrier with ML MoS_2 based on both the vertical and lateral Schottky barrier heights (0.13eV for vertical Schottky barrier, 0.1915eV for lateral Schottky barrier) and the built-in potential (0.0793eV). As compared to Mo, Au forms a high-resistance ohmic contact with a much larger vertical barrier height of 0.63±0.075 eV and a negligible built-in potential. It is thus observed that ML MoS_2 is very susceptible to strain and pinning of the Fermi level due to metal junction formation. Thus, understanding both the vertical and horizontal Schottky barrier heights along with the built-in potential is critical for designing high performance 2D semiconductor devices.

4.2 Introduction

2D (two-dimensional) materials like MoS_2, WSe_2, and WS_2 are promising materials as one can tune their electronic and optical properties by changing the number of layers [147]. In the past few years, graphene has proved itself a prospective 2D material in the area of nanoelectronics with its high carrier mobility and flexibility [148]. However, due to zero bandgap, graphene exhibits semi-metallic property [149], and as a result, its application in complementary metal oxide semiconductor (CMOS) devices is limited. Thus, 2D materials beyond graphene have drawn great attention, and several categories of 2D materials with finite bandgap are being researched. Recently, transition metal dichalcogenides (TMDCs) such as MoS_2, $MoSe_2$, WS_2 and WSe_2 have shown significant promise owing to their unique tunable electronic, photoluminescence, spintronic and sensing properties [150–153]. Amongst them, MoS_2 is one of the promising materials due to its tunable Si-like indirect bandgap of 1.2 eV [154] in bulk which switches to a direct bandgap of 1.8 eV located at K, $K^{'}$ points in

the Brillouin Zone (BZ) for monolayer (ML) MoS_2 [155].

Metal contacts, both ohmic and Schottky, are essential to design good quality devices [156]. The metal-ML MoS_2 interface properties impact the carrier transport phenomena significantly [157], [26]. Earlier research has indicated [26, 27] that two Schottky barriers are formed at the metal semiconductor junction in field effect transistors (FET) based on ML MoS_2. The vertical Schottky barrier is the potential barrier at the interface between the metal contact and ML MoS_2 while the lateral Schottky barrier is formed between the contact region and the lateral ML MoS_2 channel. Both the vertical and lateral Schottky barriers are indicated in figure-4.1. The two Schottky barriers determine the current transportation in the devices. Furthermore, n or p type characteristics depend on the contact material selection. Previous studies have reported that both low (e.g., Sc, Ti) and high work function metals (Au, Ni and Pt) tend to convert the ML MoS_2 from intrinsic to n-type material [28, 29], which is quite different from the pinning effect mechanism applicable to traditional bulk metal-semiconductor junctions. This leads to challenges in fabricating a good quality Schottky barrier between the metal and ML MoS_2 and hence requires detailed understanding. Making a good quality Schottky contact for 2D materials still remains as one of the big hurdles in obtaining high-quality devices.

Quite a bit of effort has been devoted to fabricating high performance ML MoS_2 based electronic devices by utilizing both high and low-work-function metals [19, 158]. Both experimental and theoretical values for the vertical and lateral Schottky barrier heights have been reported by earlier studies [26, 28, 29]. The primary focus of our study is to understand the metal-ML MoS_2 interface not only by investigating density of states (DOS), band structure, Mulliken populations and Schottky junction properties using a density functional theory (DFT) approach [132], but also by applying a new method based on projected local density of states (PLDOS). By this method, the overall view of the device band diagram can be generated and a more detailed analysis is conducted. Here, we have chosen to study three different metals

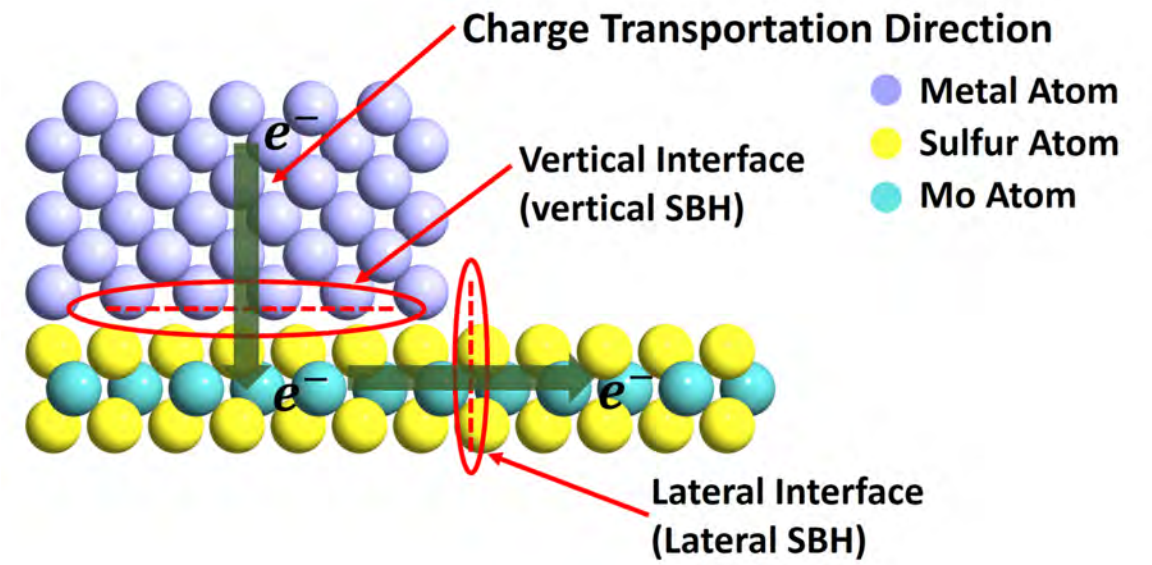

Figure 4.1: Schematic figure of a typical metal-MoS_2 interface in MoS_2 devices. The red circles along with the red dashed lines in the figure label the vertical Schottky barrier and lateral Schottky barrier out. The green arrows indicate the transportation direction of the carriers.

with two different crystal structures. We have chosen Mo and W, which have BCC structure and can form valence bonds with the S atoms, and Au which has an FCC structure. We have implemented two different device structures for the study – with one and two contacts (FET like structure) to extract both the vertical and lateral barrier heights for these metals, as shown in figure-4.2. The vertical Schottky barrier heights are determined by density of states and the projected device density of states analysis is performed using the Meta Generalized Gradient Approximation (Meta-GGA) functional [137], which gives an outline of the band structure along the lateral transportation direction. This reveals the distribution of the states and band bending due to the collective effect of the interface states, gap states and defects brought by the deformation of the original free-standing ML MoS_2 geometry configuration. The dramatic shift of the Fermi energy level and reported bandgap modification [159–161] have been observed and the lateral Schottky barrier heights are extracted. This work conducts a detailed band structure study across the whole Schottky device and ex-

tracts the Schottky barrier heights, which provide more insight about the metal-MoS_2 interface, which is an important component for high-performance devices.

4.3 Methodology

This computational work is a first-principles simulation study based on density functional theory (DFT). The calculations are performed using Atomistix ToolKit (ATK) [6].

A metal-MoS_2 junction based on ML MoS_2 is used to understand the electrode formation with Mo, W and Au and extract Schottky barrier height, shown in figure-4.2 (a). A series of supercells with different numbers of metal layers ranging from 1-7 layers are created to test the minimum number of metal layers which can represent the metal edge of the metal contact properly. It was observed that the atoms shift negligibly after 5 layers of metal and hence we assume 6 layers as bulk metal for the study. The supercell is constructed with intrinsic ML MoS_2 absorbed on the one side surface of the metal contact. The (001) surface is chosen for Mo and W to form a close-packed structure, while the (111) surface is chosen for Au with a mean absolute strain of 1.54%-5.84% due to the lattice mismatch, which is shown by figure-4.2 (d) to (f) and table-4.2. Because the number of atoms will affect the peak value of the density of states (a system containing a larger number of atoms will have higher peaks in the plot of the density of states), the adjusted ML MoS_2 contains 6 Mo atoms and 12 S atoms in one supercell for all three metals. To eliminate the interaction between the neighboring supercells such that the potential decays smoothly in z-direction, a periodic boundary condition (PBC) was applied with at least 20 Å vacuum in z-direction.

The GGA (Perdew-Burke-Ernzerhof variant of Generalized Gradient approximation) [134] is applied for the DFT calculation of the metal-MoS_2 junction case. HGH (Hartwigsen-Goedecker-Hutter) [141] basis set is adopted for geometry optimization and expanding the electron density. A DFT-D2 [162] correction is adopted to take

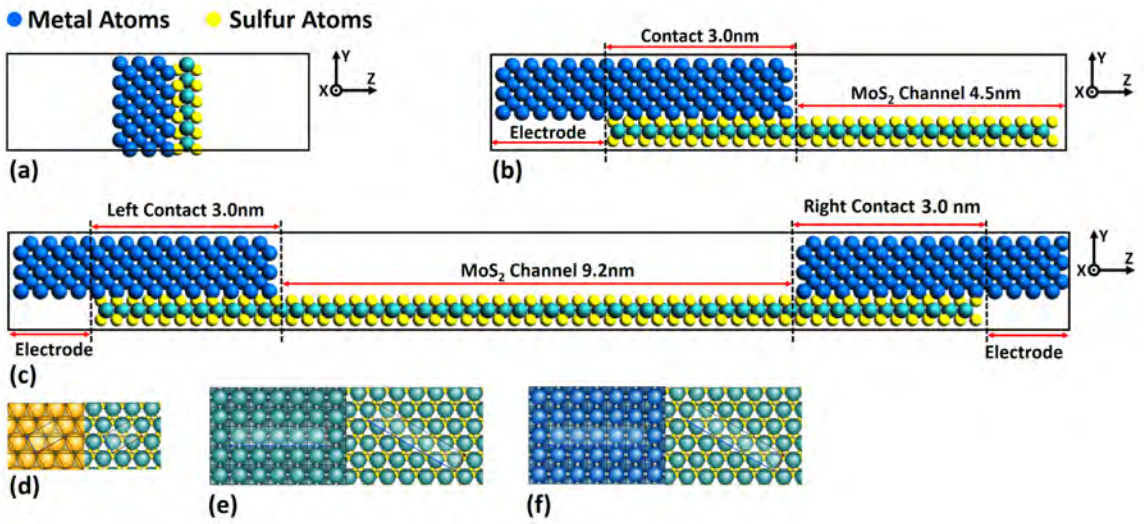

Figure 4.2: (a) Metal-MoS_2 junction, where the blue balls represent metal atoms Mo, W and Au while the yellow balls represent Sulfur atoms. (b) Metal-MoS_2 FET-like structure with one metal contact. (c) Metal-MoS_2 FET-like structure with two metal contacts. (d) Top view of (111) Au surface on monolayer (001) MoS_2 surface. (e) Top view of (001) Mo surface on monolayer (001) MoS_2 surface. (f) Top view of (001) Mo surface on monolayer (001) MoS_2 surface.

care of the van der Waals forces. The spin-orbital interaction is not taken into consideration in our simulation. 20×4×1 k points are used for the k sampling in the Brillouin zone (BZ), which has been tested by ensuring that the total energy is converged to less than 1.0E-5 eV. Using the convergence test, the energy cut-off is set as 200 Ry. For the geometry optimization, the temperature is set to be 300K and the maximum force is set to be 0.05 eV/Angstrom.

Two types of FET-like structures are set up to study the transport properties of the MS (metal-semiconductor) devices, which help to investigate the local density of states across the contact region and MoS_2 channel with or without the impact from the second metal contact. The first configuration consists of one metal contact and a MoS_2 channel, shown in figure-4.2 (b). This simulation is a zero-bias (0 V) simulation and no current transportation exists. The simulations conducted here have not optimized the electrode design and no current crowding effects have been studied. As a result, a MoS_2 contact without doping on the right side is acceptable and the

length is set to let the potential decay smoothly because of the employed Dirichlet boundary condition in the direction of transportation. The overlap between the metal and MoS_2 is 3 nm and the MoS_2 channel length is 4.5 nm. The second configuration consists of two electrodes and the ML MoS_2 channel, shown in figure-4.2 (c). Due to the limitation of the computational capacity, the length of the ML MoS_2 channel is chosen as 9 nm. The left and right contact regions formed by the metal-MoS_2 are set to the same length of 3 nm. For both configurations, the metal electrode contains 6 layers of metal atoms. Vacuum buffer is added in the y direction due to the PBC of the ATK. The device relaxation is done with the same settings of the metal-MoS_2 junction. The upper 4 layers of metal atoms are set as constrained since no noticeable change occurs after the first 2 layers near the interface according to the results of the test simulations, while the 2 layers which are near the metal-MoS_2 interface are not constrained. The transportation simulation is done by using the Meta-GGA method [137] along with the DZP basis sets (double zeta polarized) [163], which includes not only the local density and the gradient of the local density but also the kinetic energy to compute a more accurate bandgap. We have performed the c parameter optimization for our Meta-GGA simulations. As shown in table-4.1, DFT simulations were conducted for the different c parameter values until we obtained bandgap correction after fitting which matched the experimental value of the bulk MoS_2 bandgap [154]. This optimized value for the c parameter of 1.15 was used for the Meta-GGA approach to avoid convergence problems brought about by the vacuum buffer, and was tested with ML MoS_2 bandgap calculation, which gave us a value of 1.795 eV (matching the experimental value 1.8 eV [155]). The k sampling is $20\times1\times16$ to make sure that there are adequate k points in the transportation direction.

Also, though the GGA technique works well for ML MoS_2 [26, 27, 29], it adds error to the simulation for multi-layer MoS_2 [164, 165]. To maintain a consistent framework with our future work on multi-layer MoS_2, we have decided to use the Meta-GGA method for this study.

Table 4.1: The simulated values of Bulk MoS_2 bandgap under different c parameters.

c Parameter	Bandgap Energy (eV)
1.00	1.071
1.05	1.115
1.10	1.161
1.15	1.209
1.20	1.258

4.4 Discussion

The geometry optimization (GO) is conducted before the DOS analysis. After GO, the displacement values of the interfaces are obtained and shown in table-4.2. The total displacement is defined by the average shift of the interface atoms. The maximum displacement is observed for the Au-MoS_2 interface with the minimum displacement for the W-MoS_2 interface.

To investigate the bonding within the interface after GO, the electron density calculations, Mulliken population analysis [166] and bonding energy calculations for all three interfaces are performed. This provides an intuitive criterion to evaluate the electron bonding condition and the overlap of electron orbitals and partially reveals the formation of Schottky barrier at the MoS_2-metal interface. figure-4.3 shows the electron distribution in the yz cut planes. From the plot we can see that the electron population concentrates significantly at the metal-MoS_2 interface for Mo and W, which shows a very strong delocalization of valence electrons. However, the Au-MoS_2 interface does not exhibit delocalization of the valence electrons. The delocalization of the valence electrons indicates that the bond between the S atoms of the ML MoS_2 with Mo and W is much stronger as compared the one formed with Au. The 1D plots of the average electron density projected along the c-direction (which is the z-direction) are shown in figure-4.3. The peaks in the electron density vs. the frac-

tional coordinates in the c-direction indicate very high electron densities. The valleys indicate the bonding regions where the electron population is smaller. The valley at the interface is partly filled, indicating the existence of electron delocalization. A calculation of the average electron density based on the electron density plot has been done and the results are normalized. It shows that Au has the lowest average value 0.506/ $Å^3$ of electron density, while the values are 0.5206/ $Å^3$ for Mo and 0.547/$Å^3$ for W, respectively. This clearly indicates that Au has the lowest delocalized electron population in the interface region, and as a result, has the weakest bonding with S atoms compared to Mo and W. The bonding type of the existing bonds shown by electron density is defined by the Mulliken population for each metal-S bond (shown in figure-4.4) and the average bonding energy is shown by table-4.2. According to the Mulliken population method, a large value of the bond population indicates a covalent bond, while a small value indicates weak bonding (van der Waals bond) [166, 167]. Figure-4 shows that the bonding between Mo-S and W-S atoms is a combination of van der Waals and covalent interactions. The binding between W-S atoms consists of more covalent interaction as compared with Mo-S at the Mo-MoS_2 interface. Some W-S bonds demonstrate a stronger covalent interaction than the original Mo-S bonds in MoS_2 since they have higher bond populations, namely 0.35343 and 0.30939, compared to 0.26038 for Mo-S bonds in free standing ML MoS_2. The Mo-MoS_2 interface also contains some covalent bonds, but these are weaker than the Mo-S bonds in MoS_2. The calculation of binding energy provides further evidence for this conclusion and determine the bonding type of Au-MoS_2 interface. From DFT calculations, as shown in table-4.2, the binding energy for Mo-MoS_2 interface is 1.6992 eV per S atom. The binding energy for W-MoS_2 interface is 1.7793 eV per S atom and the binding energy for Au-MoS_2 interface is 0.3996 eV per atom, while the value is 0.7157 eV for the van der Waals bonds of the bilayer MoS_2. This reveals that the adhesion effect is strong in Mo-MoS_2 and W-MoS_2 systems while Au-MoS_2 interface shows a weak bonding effect, which indicates that the Mo-S and W-S bonds are much stronger than Au-S

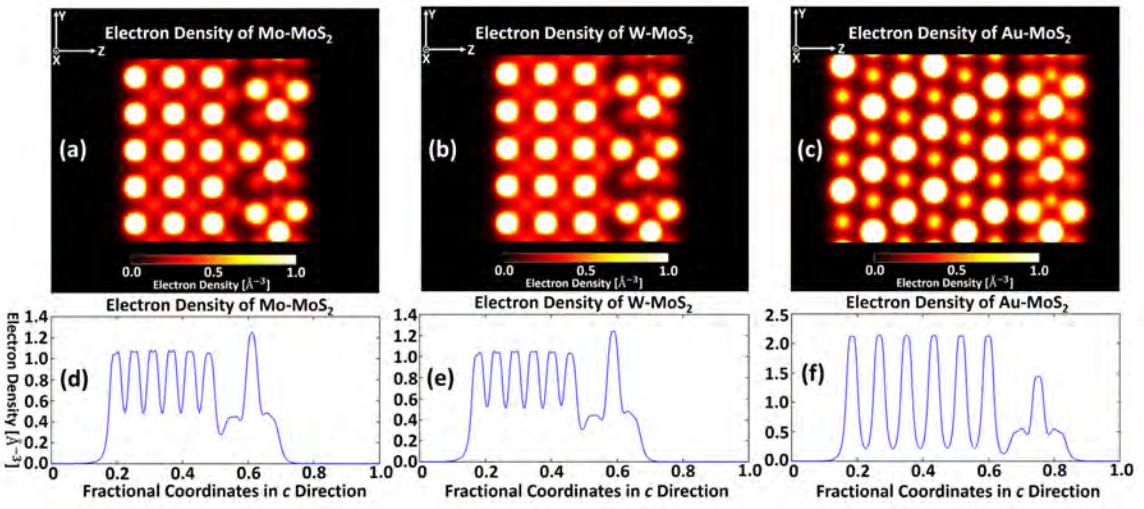

Figure 4.3: Electron density of metal-MoS_2 interface. (a) Electron density of the yz cut plane of the Mo-MoS_2 interface. (b) Electron density of the yz cut plane of the W-MoS_2 interface. (c) Electron density of the yz cut plane of the Au-MoS_2 interface. (d) Integral electron density along the c direction of the Mo-MoS_2 interface. (e) Integral electron density along the c direction of the W-MoS_2 interface. (f) Integral electron density along the c direction of the Au-MoS_2 interface.

bonds. By comparing the binding energy per S atom, the Au-S bond is defined as a weak van der Waals bond, which has been demonstrated by experimental work [168]. In other words, the Au-MoS_2 interface shows much weaker bonding effect compared to the other two interfaces, which supports our conclusion from electron density.

To obtain a better understanding of the Schottky barrier height (SBH) in both the vertical and lateral directions, the density of states of the three MoS_2-metal interfaces and the PLDOS of FET-like devices with one metal contact and two metal contacts are calculated. Prior to this, the basic electronic parameters of ML MoS_2, Mo, W and Au are extracted by DFT simulations. A comparison is also made between the SBHs extracted directly from the DOS and PLDOS and which are defined by the Schottky-Mott rule based on the simulated electronic parameters.

The band structure of MoS_2 is simulated not only to investigate the intrinsic MoS_2 properties but also to evaluate the validity of the method. To fix the issues of underestimating the bandgap of semiconductors [169], the Meta-GGA functional, which

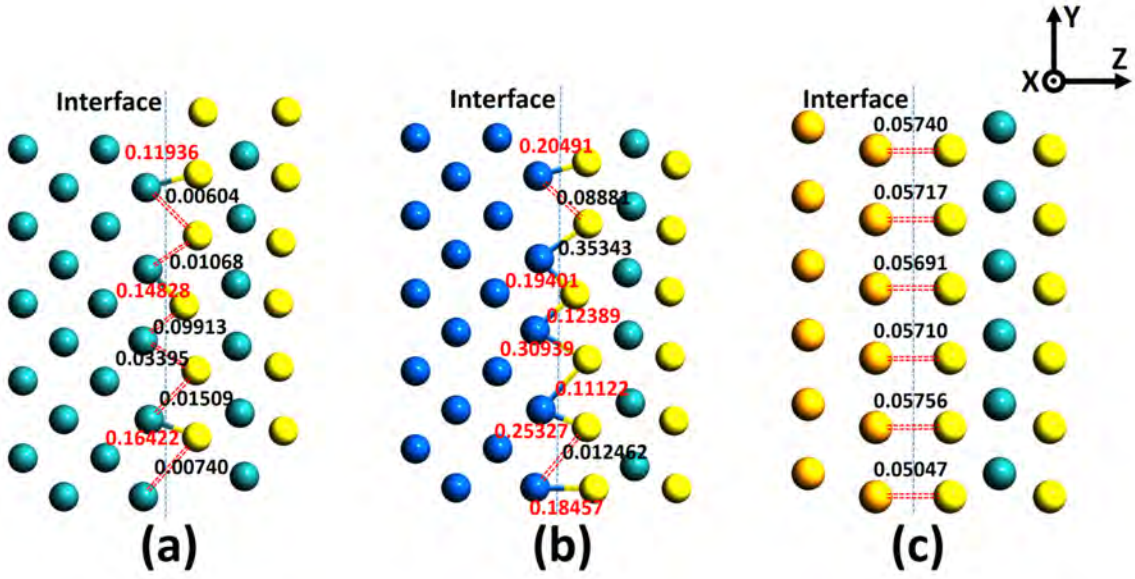

Figure 4.4: Mulliken Population of (a) Mo-MoS_2, (b) W-MoS_2 and (c) Au-MoS_2 interface. The red dashed double line represents the weak interaction (van der Waals bond) between the metal atoms of the metal contact and the sulfur atoms of the MoS_2 sheet. The valence bonds are drawn in the plot and their Mulliken populations are labeled by red color.

Table 4.2: Displacement, binding energy and related mean absolute strain of metal-MoS_2 interfaces.

Interfaces	Average Displacement (Å)	Binding energy per S atom (eV)	Mean Absolute Strain %
Mo-MoS_2	2.0720	1.6992	1.54
W-MoS_2	1.9684	1.7793	1.26
Au-MoS_2	2.6686	0.3996	5.84

belongs to the third rung of the Jacob's ladder of exchange-correlation functionals [137], is adopted to extract corrected band structures of all the configurations. Using the optimized c parameter of 1.15 and employing the Meta-GGA method, band structures of 1 to 5 layers and bulk free standing MoS_2 are generated. The ML MoS_2 sheet (see figure-4.5(a)) has a bandgap of 1.795 eV, which closely matches the reported simulation and experimental value of 1.8 eV [154]. As has been reported earlier, the bandgap changes significantly (from 1.795 eV to 1.219 eV) going from ML MoS_2 to bilayer (BL) (see figure-4.5 (a)-(e)). With the increase in the number of layers, the bandgap shrinks to the value of 1.203 eV until the MoS_2 system becomes a bulk system, shown in figure-4.5 (f). At the same time, degeneration occurs when the number of layers is modified. From figure-4.5, it is visible that the band splits into two for bilayer MoS_2 and splits to three for three-layer MoS_2 and so on, until the MoS_2 becomes bulk and the degeneration effect disappears. The degeneration effect has a dependence on the number of layers and is localized at the valley region in the Brillouin zone.

The electron affinity of MoS_2 and the work function of metals ϕ_M are calculated, and are shown in table-4.3. The electron affinity is defined by the calculation of the electrostatic potential of the free-standing ML MoS_2. A large volume of vacuum buffer is added to the supercell so that the potential of the monolayer MoS_2 is allowed to decay to the vacuum level. The calculated electron affinity of MoS_2 is 4.16 eV while an electron affinity for bilayer MoS_2 of 4 eV has been reported [170]. The work functions of metals for this work are generated by testing a metal slab which can be considered as bulk. The vacuum buffers for basis-set orbitals and potential decay are added and multi-grid solver as well as Dirichlet boundary condition are adopted. The calculated work function of Mo, W and Au are 4.38 eV, 4.74 eV and 5.43 eV, respectively. The error percentages reported in table-4.3 indicate that the divergence from experimental values is negligible and adopting the simulated values is valid for the analysis. The ideal SBH can be worked out by the Schottky-Mott rule by using

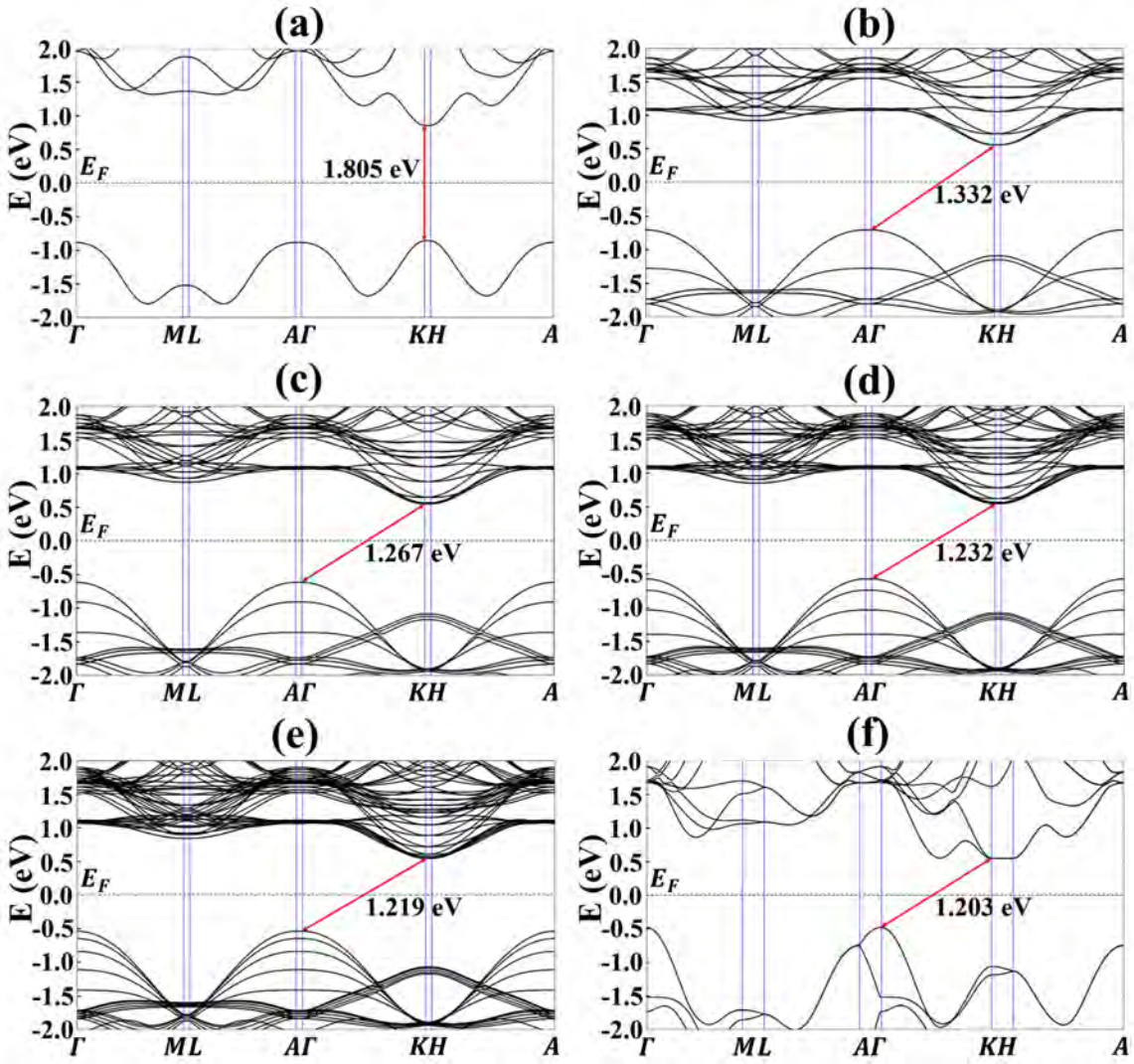

Figure 4.5: Band structure of MoS_2 with different layers. (a) Band structure of ML MoS_2, with a direct bandgap of 1.795 eV, which is denoted by the red line and located at K point in the first BZ; (b) band structure of bilayer MoS_2, with an indirect bandgap of 1.332 eV located between the Γ point of the valence band top and the K point of the conduction band bottom. (c)-(e) Band structure of 3 to 5 layers of MoS_2 and the corresponding bandgaps are 1.267 eV, 1.232 eV and 1.219 eV. The location of the bandgap remains the same as the bilayer MoS_2. (f) Band structure of bulk MoS_2. The bandgap is reduced to 1.203 eV and the location of the bandgap remains the same as the multi-layer cases.

Table 4.3: Calculated electronic parameters compared with experimental data. ϕ_M : metal workfunction. χ : electron affinity.

Material	Our Simulated ϕ_M (eV)	Experimental ϕ_M (eV)	Our Simulated χ (eV)	Experimental χ (eV)	Error
a	4.38	4.50 [171]	...	...	2.67%
b	4.74	4.63 [172]	...	...	2.38%
c	5.43	5.31 [173]	...	...	2.26%
d	...	...	4.16	4.00 [170]	4.00%

the equation: $\Phi_{SBH}=\phi_M-\chi$, where Φ_{SBH} is the Schottky barrier height, ϕ_M is the metal work function and χ is the electron affinity. The calculated ideal SBH Φ_{SBH-I} is shown in table-4.4. For Mo-MoS_2, Φ_{SBH-I} is 0.22eV and the Fermi level will pin towards the conduction band. For W-MoS_2, Φ_{SBH-I} is 0.58eV and the Fermi level pins towards the conduction band; the corresponding value is 0.53eV for Au-MoS_2 with pinning towards the valence band.

With the bandgap energy of MoS_2 and metal work function provided by the DFT simulation, the SBHs in the vertical direction can be extracted directly from the partial density of states (PDOS) of MoS_2 by excluding the overlap states contributed by the metal contact. Firstly, the first layer of metal atoms starting from the interface and the near-interface S atoms in MoS_2 are treated separately and the projections of the contributions by different electron orbitals are obtained. figure-4.6 (a) to (d) show the projected density of states contributed by the metal layer and S layer near the interface, which reveals the bonding conditions and metallization due to the coupling between the electron orbitals of S atoms in MoS_2 and metal atoms. figure-4.6 (a) and (b) show that the d orbitals of the valence electrons in metal layer contribute to the bonding most, while figure-4.6 (c) and (d) show that the p orbitals of the valence electrons in the MoS_2 interfacial S layer participate more than the other orbitals of this layer. figure-4.6(a) and (d) also show that for Mo and W, both the d orbitals

of interfacial metal layer and p orbitals of the interfacial S layer extend greatly into the gap region. The appearance of multiple gap states indicate the metallization of ML MoS_2. The conclusion that can be drawn is that the hybridization between the d orbitals of the interfacial metal layer and p orbitals of the interfacial S layer causes the metallization. Then, the PDOS of MoS_2 is calculated and shown in figure-4.6 (e). It is observed that several gap states are added to the original bandgap of MoS_2. The band structures of W-MoS_2 and Mo-MoS_2 have been filled, which means the original bandgap vanishes due to the large gap state population. The Au-MoS_2 interface reserves part of the intrinsic semiconducting properties of free standing ML MoS_2. The bandgap of MoS_2 prior to the junction formation can still be observed in the PDOS plots. For Mo-MoS_2 and W-MoS_2 interfaces, a distinguishable shift in Fermi energy can be observed in figure-4.6 (e). The Fermi level moves closer to the conduction band. From the PDOS results, the Fermi level shift can be extracted for Mo and W as 0.77 eV and 0.80 eV, respectively. Thus, the shift of Fermi level is similar for both Mo and W junctions. As compared to Mo and W, the Fermi level shift due to the Au interface with MoS_2 is 0.15 eV. Here, an assumption is made that the bandgap energy of the intrinsic ML MoS_2 won't change while applying metal contacts [174]. However, change in bandgap due to the strain created by the metal contact on ML MoS_2 has been reported earlier [150, 160, 161]. In this case, if the metal-introduced gap states are considered as the part of the conduction band, then there will be a change in the bandgap energy and the Fermi level will shift again. The modified Fermi level shift is still 0.77 eV for the case of Mo and 0.8 eV for the case of W, but it is 0.4 eV for the case of Au. From the results, it is observed that for Mo, W and Au, the metal-MoS_2 interfaces exhibit n-type behavior, although Au has a very high work function of 5.42 eV in this case, which should cause p-type behavior according to the Schottky-Mott rule [Naturwiss. 26, 843 (1938); Cambridge Philos. Soc. 34, 568 (1938)].

According to figure-4.6, there are gap states within the bandgap region. For Au,

Table 4.4: Calculated SBHs compared with ideal SBHs. Φ_{SBH-I} : ideal value of the Schottky barrier height. The Φ_V : vertical Schottky barrier height. $\Phi_{L_{1E}}$: lateral Schottky barrier height of one-electrode configuration. $\Phi_{L1_{2E}}$: the left lateral Schottky barrier height. $\Phi_{L2_{2E}}$: the right lateral Schottky barrier height, $\Phi_{L_{2E}}$: the average of the left and right lateral Schottky barrier height for the two electrode geometry.

	Ideal case (Schottky-Mott rule)	Vertical case	One-electrode	Two-electrodes		
Material	Φ_{SBH-I} (eV)	Φ_V (eV)	$\Phi_{L_{1E}}$ (eV)	$\Phi_{L1_{2E}}$ (eV)	$\Phi_{L2_{2E}}$ (eV)	$\Phi_{L_{2E}}$ (eV)
Mo	0.22	0.13	0.179 $\pm$0.013	0.167	0.216	0.1915
W	0.58	0.10	0.134 $\pm$0.062	0.137 $\pm$0.024	0.136 $\pm$0.026	0.1365 $\pm$0.025
Au	0.53	0.63 $\pm$0.075	0.092 $\pm$0.016	0.087 $\pm$0.018	0.087 $\pm$0.016	0.087 $\pm$0.017

the gap states are 10 times less than those present in the structures with W and Mo. This indicates that all the three metals at the metal-MoS_2 interfaces are metallizing the MoS_2 but to a different extent. The metallization due to Au is weaker as compared to Mo and W. The SBH in the vertical direction Φ_V is just the value of the $(E_c - E_f)$; here E_c is the conduction band bottom near the interface and E_f is the Fermi level. For Mo-MoS_2 interface, Φ_V is 0.13 eV, which is 0.10 eV for W-MoS_2 and 0.63$\pm$0.075 eV for Au-MoS_2. A clearer comparison can be made by comparing the SBH with the ideal values (obtained from the Schottky-Mott rule), which are given in table-4.4. It shows that the simulated SBHs diverge a lot from the ideal SBH. This points out that the vertical SBH is dependent mainly on the interface properties defined by the bonding condition between the metal and semiconductor, instead of the intrinsic properties of either metal or semiconductor. figure-4.6 can be used to explain the metal-introduced gap states and their occupation by electrons pin the Fermi level. Thus, SBH shows very little dependence on the value of the semiconductor or metal

work functions.

The projected local density of states (PLDOS) is a powerful tool to reveal the band structure along the transportation direction of diodes, which is difficult to obtain from experiments. The projected local density of states is a kind of projection in terms of the c direction (which is defined as the transportation direction in ATK-tool, as the potential which is added by the bias decays in this direction). The absolute values of the density of states are represented by different colors. These values represent the integration in a direction and b direction, just like the contour plot.

The PLDOS of one-contact devices are shown in figure-4.7, and the cross-section view of the geometry is also included (as explained in the section on Methodology). The plot shows that the PLDOS of all three metal-MoS_2 devices can be divided into three parts. On the left side is the metal electrode part with a high volume of density of states. In the middle is the metal-MoS_2 contact region, where the metal and MoS_2 overlap with each other. From figure-4.7 we observe that in the contact region, Au-MoS_2 shows distinct band bending, the original valence band is still easy to recognize (although the original conduction band is not clear), while the PLDOS of this region is more uniform in W-MoS_2 and Mo-MoS_2. This is also explained by the weaker metallization in Au-MoS_2 as compared to W and Mo. As a result, the intrinsic semiconducting properties are partly reserved in Au-MoS_2. The right region in the PLDOS is the MoS_2 channel. In this region we observe the initial MoS_2 semiconducting properties such as the band gap, valence band and conduction band. The black region indicates there is a band gap within this region. One interesting point to observe is that the band gap in Mo-MoS_2 is 1.73±0.04 eV, 1.71±0.06 eV in W-MoS_2 and only 1.10±0.05 eV for Au-MoS_2. This indicates that the gap states lead to the shrinking of the band gap. Thus, the electronic structure of MoS_2 by surface treatment can be tuned [**172 173**]. It means that tunable-gap devices can be fabricated based on this mechanism. From figure-4.7 (c) it can be observed that for Au-MoS_2 case isolated gap states are present near the valence band.

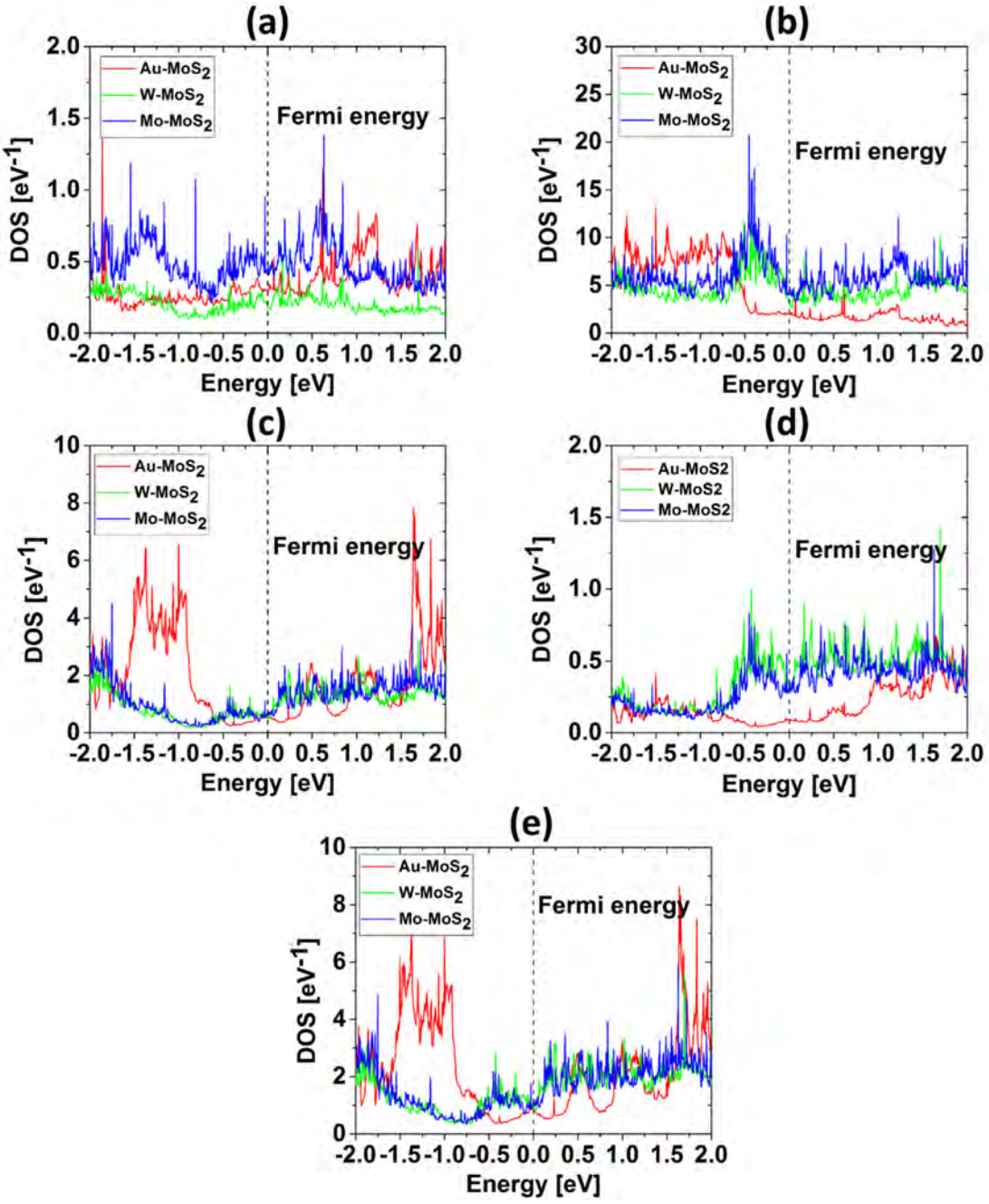

Figure 4.6: Partial density of states of the metal-MoS_2 (ML) junction. (a) Density of states contributed by the p orbitals and (b) density of states contributed by the d orbitals of the metal atoms nearest to the metal-MoS_2 interface. (c) Density of states contributed by the p orbitals and (d) density of states contributed by d orbitals of the Sulfur atoms of the ML MoS_2 which are nearest to the interface. (e) Density of states contributed by the MoS_2 of the junction.

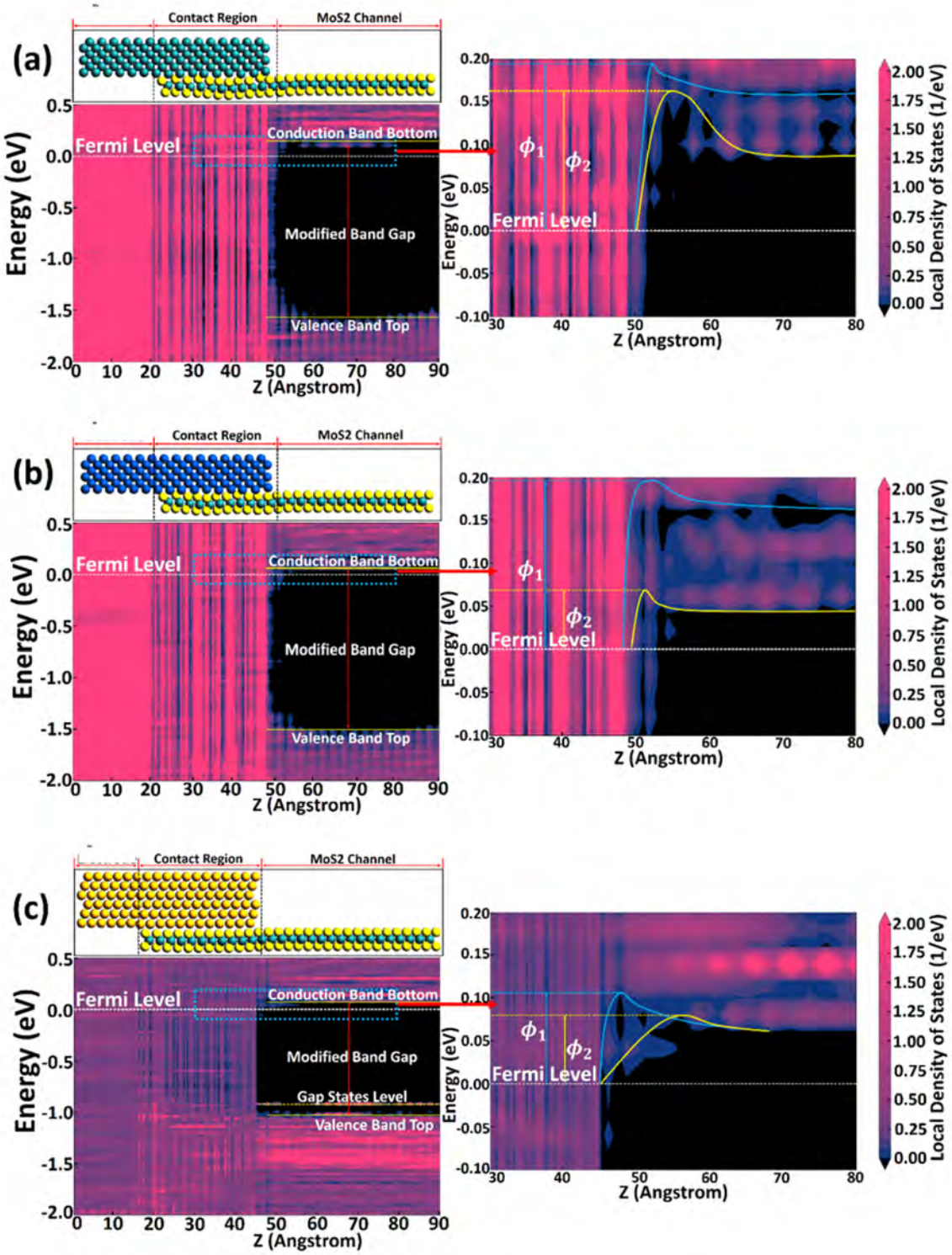

Figure 4.7: PLDOS (projected local density of states) of one-metal-contact MoS_2 devices. The blue dashed square frame means the location of the zooming region shown on the right side. (a) The PLDOS of the Mo-MoS_2 device with one metal contact. (b) The PLDOS of the W-MoS_2 device with one metal contact. (c) The PLDOS of the W-MoS_2 device with one metal contact. In (a)-(c), ϕ_1 indicates the upper limit of the peak value of conduction band bending while ϕ_2 is the lower limit.

We also observe a shift in the Fermi level of MoS_2 due to the addition of metal electrode. Due to the possible modification of the band gap, the shifting is impossible to define, but we observe that with all the three metals we obtain an n-type material (as the Fermi level moves closer to the conduction band). For Mo, the difference between conduction band bottom and Fermi level is 0.10 eV, which is 0.05 eV for W and 0.07 eV for Au. It has been reported that the geometry changing will cause doping-like effect on the ML MoS_2 which is observed from our results, too [27, 29, 158]. The impact of the metal contacts extends to the channel region and the geometry defects (compared with the original free-standing configuration) brought by this impact will make the MoS_2 channel n-type. The Fermi level position and band structure are also modified (pinning) due to the gap states created by the geometry defects.

The lateral SBH can be extracted by analyzing the PLDOS near the interface region. Two effects add to the difficulty of extracting the exact value of SBH. One is the gap states added to the channel region. It shows that gap states exist near the interface edge, which will mix the Schottky barrier with the surrounding background. Another challenge is the imaging-force effect caused by the dipoles created inside the metal-MoS_2 interface. The simulation of electron density distribution and Mulliken population analysis in our work indicates that the covalent bonding and van der Waals bonding consist of the interfacial interactions within the interfaces. The covalent bond may cause the polarization. The introduction of the metal contacts breaks the charge symmetry and the dipoles are created as a result. The delocalization of the metal and S valence electrons will also cause charge accumulation near the interface and the charge neutrality will be broken. Due to this, the imaging-force effect will be strong in these configurations. As result, the edge of the SBH becomes smooth due to the effect of the imaging force as shown in figure-4.7. We extract the value of SBH based on the average value of the local density of states. The upper limit Φ_1 and lower limit Φ_2 are decided by 2 different threshold values of the local density of states, which are 0.0001 eV^{-1} and 0.075 eV^{-1}. The lateral SBH can be

Table 4.5: Calculated built-in potential. $\phi_{\mathrm{bi}_{1\mathrm{E}}}$: built-in potential of the one-electrode configuration. $\phi_{\mathrm{bi}1_{2\mathrm{E}}}$: built-in potential on the left side of the two-electrode configuration. $\phi_{\mathrm{bi}2_{2\mathrm{E}}}$: built-in potential on the right side of the two-electrode configuration. $\phi_{\mathrm{bi}_{2\mathrm{E}}}$: built-in potential of the two-electrode configuration, which is the average of $\phi_{\mathrm{bi}1_{2\mathrm{E}}}$ and $\phi_{\mathrm{bi}2_{2\mathrm{E}}}$.

	One-electrode	Two-electrodes		
Material	$\phi_{\mathrm{bi}_{1\mathrm{E}}}$ (eV)	$\phi_{\mathrm{bi}1_{2\mathrm{E}}}$ (eV)	$\phi_{\mathrm{bi}2_{2\mathrm{E}}}$ (eV)	$\phi_{\mathrm{bi}_{2\mathrm{E}}}$ (eV)
Mo	0.0604±0.0128	0.0612	0.0947	0.0793±0.0181
W	0.0313±0.0029	0.0786±0.0284	0.0846±0.0280	0.0816±0.0282
Au	0.0186±0.007	0	0	0

defined by taking an average value of Φ_1 and Φ_2. The lateral Schottky barrier height $\Phi_{\mathrm{L}_{1\mathrm{E}}}$ for the three metals is: 0.092±0.016 eV, 0.179±0.013 eV and 0.134±0.062 eV for Au, Mo and W, respectively. It is interesting to observe that even though Au demonstrates the weakest bonding with MoS_2, $\Phi_{\mathrm{L}_{1\mathrm{E}}}$ is low for Au. This indicates that the electrical properties of 2D structures have strong dependence on the surface properties, and not only on the chemical properties. The built-in potential of the one-electrode configuration $\phi_{\mathrm{bi}_{1\mathrm{E}}}$ can also be extracted by calculating the bending of the conduction band. The calculation of $\phi_{\mathrm{bi}_{1\mathrm{E}}}$ is conducted using the same method as used for the lateral SBH. By using the same threshold values, two built-in potential values can be obtained and are averaged to obtain $\phi_{\mathrm{bi}_{1\mathrm{E}}}$. As shown in table-4.5, $\phi_{\mathrm{bi}_{1\mathrm{E}}}$ is 0.0604±0.0128 eV, 0.0313±0.0029 eV and 0.0186±0.007 eV for W, Mo and Au, respectively.

One issue still remains unsolved from the one-contact structure study. If an intrinsic MoS_2 electrode is adopted, after a certain distance away from the interface, the MoS_2 will become intrinsic again (depletion length), and the Fermi level pinning by the interface states will vanish. In this simulation, PBC is adopted. As a result, both the valence band and conduction band will go up, which will reduce the accuracy of the SBH extraction. This effect will become more pronounced when a longer channel is

adopted.

To fix this issue, two-contact configurations were used to conduct the simulation to verify the SBH results. For these simulations, two metal slabs were set on the left and right separately and contacting the MoS_2 ML with a top-contact form. The MoS_2 channel is set to be long enough to avoid the side effects from the short-channel effect. The PLDOS of all three two-contact devices are shown in figure-4.8. The lateral Schottky barrier heights are clearer than those of one-contact devices. The lateral Schottky barrier height can be directly extracted from the PLDOS plot of these simulations. Due the slight difference in geometry between the left part and right part after the geometry optimization, the lateral SBH on the left side is different from that of the right side. This issue cannot be avoided due to the flexibility of the ML MoS_2. If the constraint is applied on both sides of MoS_2 due to the metal contact, a distortion occurs and the distortion on each side is different from each other. This reveals that the band structure of MoS_2 devices is sensitive to the geometry changing [158, 160, 161].

From the results shown in figure-4.8 and applying the same method as described for the one-electrode case, the lateral SBH and built-in potential are extracted for both left and right electrodes. The values for $\Phi_{\mathrm{L1}_{\mathrm{2E}}}$ and $\Phi_{\mathrm{L2}_{\mathrm{2E}}}$, which are extracted lateral SBH for the right and left electrode, respectively, are shown in table-4.4. As can be observed from table-4.4, the left and right lateral SBH differ slightly for all the contacts. We think that this is due to the lattice mismatch differences between the left and the right junction and due to the slightly un-symmetric contacts. Thus, to obtain one value for the lateral SBH, we have taken an average, $\Phi_{\mathrm{L}_{\mathrm{2E}}}$, of the left and the right SBH values, shown in table-4.4. The built-in potential of the left side, $\phi_{\mathrm{bi1}_{\mathrm{2E}}}$, and the built-in potential of the right side, $\phi_{\mathrm{bi2}_{\mathrm{2E}}}$, are given in table-4.5. From the data in table-4.4 and table-4.5, it can be seen that the lateral SBH values extracted from one- and two-electrode configurations are very closely matched, which indicates the validity of the simulation. In other words, there is little difference between using

the one-electrode configuration or two-electrode configuration to evaluate the lateral SBH. Both the lateral SBH values generated by these two methods are similar in value and match other experimental results [27, 28].

From table-4.4 it can be observed that both Mo and W demonstrate small vertical SBH, indicating the interface will provide small resistance to flow of carriers. The lateral SBHs for Mo and W have values larger than 0.1 eV, which can provide decent rectification. Au contact (unlike Mo and W) demonstrates a vertical SBH of 0.63 eV as compared to a lateral SBH of 0.09 eV, which is in close agreement with the reported experimental values [28]. This clearly indicates that the Au contact does not form a rectifying contact with ML MoS_2, and the lateral SBH and vertical SBH depend on different mechanisms in the case of Au. The calculated built-in potential is another important criterion for analyzing the formation of the Schottky contact. Mo and W have non-zero built-in potentials, as shown in table-4.5. Combining the built-in potential values along with the lateral SBH, it can be concluded that both Mo and W form a good Schottky contact with ML MoS_2. The built-in potential for Au-MoS_2, as shown in table-4.5, is close to zero, which indicates an ohmic contact with a small potential barrier height, although the contact may have large resistance due to the large vertical SBH.

table-4.6 shows a comparison of our simulation results with previous studies. It can be clearly seen that for Au, our results match the simulated and experimental results [26, 28, 29, 168]. For Mo, the vertical Schottky barrier height reported in our results are very similar to other computational work reported in the literature [12]. The biggest difference is the lateral Schottky barrier height, which is 0.1915 eV according to our simulation while a value of 0.1 eV has been reported earlier [13]. To the best of our knowledge, we have not found any study with W as a contact with ML MoS_2 and our results strongly reflect that this may form a good Schottky barrier. In the near future, we will conduct an experimental study to confirm our simulated results.

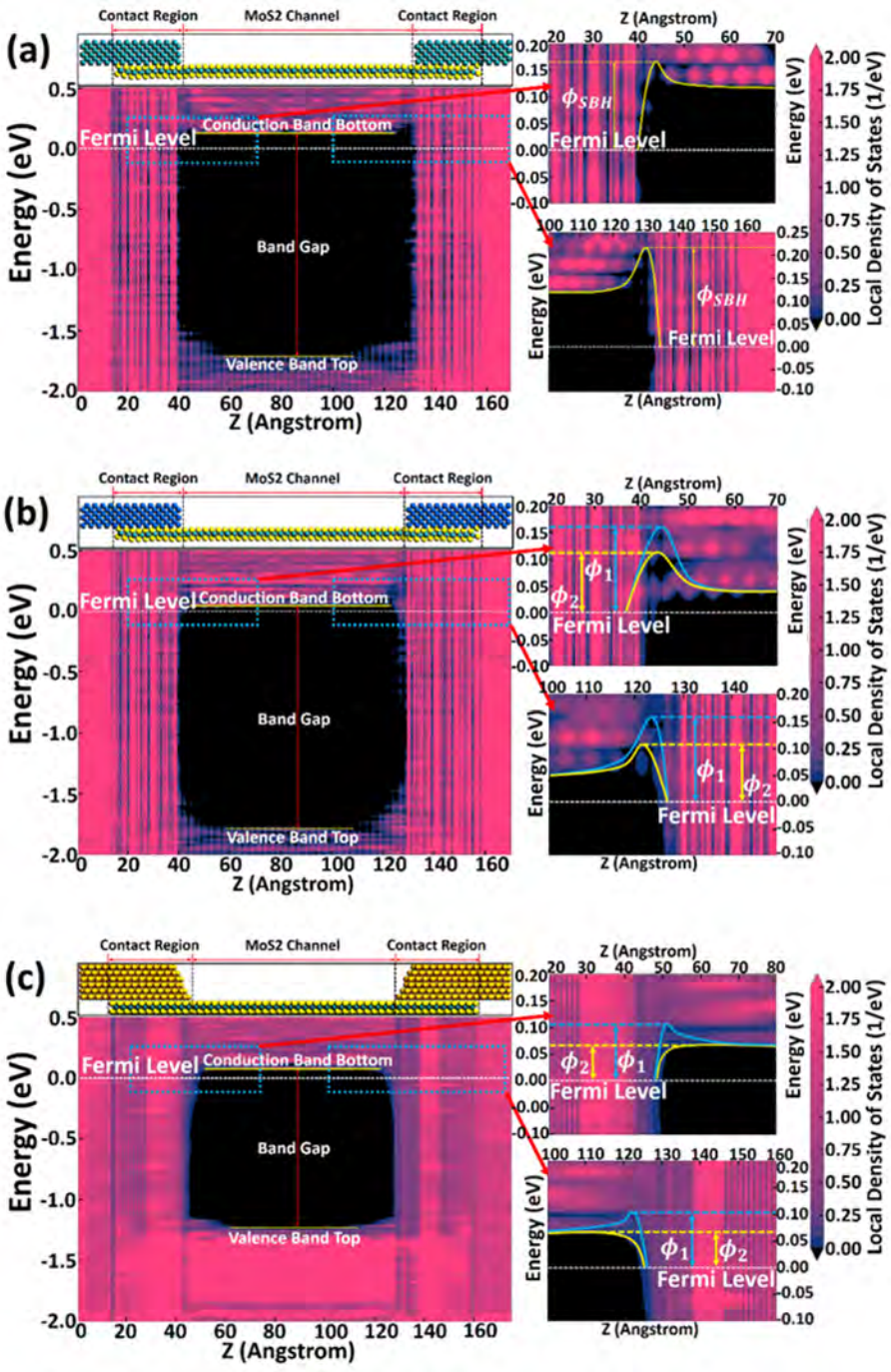

Figure 4.8: PLDOS (projected local density of states) of two-metal-contact MoS_2 devices. The blue dashed square frames mean the location of the zooming regions shown on the right side.(a) The PLDOS of the Mo-MoS_2 device with two metal contacts. (b) The PLDOS of the W-MoS_2 device with two metal contacts. (c) The PLDOS of the W-MoS_2 device with two metal contacts. In (a), Φ_{SBH} indicates the Schottky barrier heights of the left lateral interface and the right interface, for Mo. In (b)-(c), ϕ_1 indicates the upper limit of the peak value of conduction band bending while ϕ_2 is the lower limit.

Table 4.6: A comparison between the results in this study with the simulated or experimental results available in other references. In the table, Φ_V denotes the vertical Schottky barrier height while Φ_L denotes the lateral Schottky barrier height. There is only one Schottky barrier value given in experiments, so Φ_{SBH} indicates the Schottky barrier height extracted in the experimental work done by other groups.

	Our Results		Simulated Results in References		Experimental Results in References
Metal	Φ_V (eV)	Φ_L (eV)	Φ_V (eV)	Φ_L (eV)	Φ_{SBH} (eV)
Mo	0.13	0.1915	0.13 [26]	0.1 [27]	...
W	0.10	0.1365 $\pm$0.025	...	...	...
Au	0.63 $\pm$0.075	0.087 $\pm$0.017	0.62 [26], 0.667 [29]	0 [29]	0.06-0.16 [28], ohmic [168]

4.5 Conclusion

We have conducted a comprehensive study on Schottky barriers of metal-ML MoS_2 structures using DFT. Two different geometries with one and two electrodes were studied for three different metals (Mo, W and Au). We have implemented a new technique based on PLDOS to conduct a comprehensive study for extracting the vertical and lateral SBH along with the built-in potential. Both Mo and W demonstrated a larger built-in potential as compared to Au, which is important for rectification. The Mo- MoS_2 device has a very small vertical SBH in comparison to the Au- MoS_2 device. It is observed that the strong metallization due to the covalent bonds formed between metal and sulfur atoms lead to reduction of the vertical SBH in the case of Mo-MoS_2 and W-MoS_2. The weaker van der Waals bonding between Au atoms and sulfur atoms leads to a larger vertical SBH. From the DOS analysis, it is also concluded that the vertical SBH may not have a significant rectifying effect on the overall electron transportation, due to the existence of the gap states. The similarity in the lateral SBH values obtained from the one and two electrode cases shows

that the PLDOS method demonstrates validity for extracting lateral SBH along with the built-in potential. By comparing the vertical SBH, lateral SBH and built-in potential, it can be concluded that both Mo and W can form good Schottky contacts with ML MoS_2, with a suitable barrier height and adequate built-in potential, while Au cannot form a good contact with MoS_2 at the vertical interface and the contact at the lateral interface is ohmic, with zero built-in potential. From our study, it is very clear that the behaviour of ML MoS_2 is very strongly modified by introducing a metal contact, indicating great care is required in fabricating these devices to prevent interface states.

Chapter 5

Titanium disulfide as Schottky/Ohmic contact for monolayer molybdenum disulfide[1]

Junsen Gao[1], Manisha Gupta[1]

[1]Electrical and Computer Engineering, University of Alberta, Edmonton, Canada

*Corresponding author, mgupta1@ualberta.ca

5.1 Abstract

2D semiconductors like Molybdenum disulfide (MoS_2) still have issues in forming good metal electrode (Schottky and Ohmic) especially for mono layer (ML) to few layers thick due to strain and metallization issues. Here, we explore a 2D semi-metal, titanium disulfide (TiS_2), for making different types of contacts with ML MoS_2 using density functional theory (DFT). It is observed that ML TiS_2 induces ML MoS_2 to become p-type with a doping density of 3.85×10^{17} cm^{-3} which becomes larger with thicker TiS_2. Thus, TiS_2 can thus be utilized as a variable contact material ohmic if the MoS_2 is p-type and as Schottky if the MoS_2 is n-type with a Schottky barrier height ranging from 0.3 eV to 1.35 eV. One of the important results from the study is that compared to a traditional metal-MoS_2 in a TiS_2-MoS_2 contact the bandgap

[1]The chapter 5 has been published as Junsen Gao, Manisha Gupta "Titanium disulfide as Schottky/Ohmic contact for monolayer molybdenum disulfide," npj 2D Materials and Applications, (2020) 4: 26.

is preserved where in contrast, a traditional metal contact metalizes the monolayer MoS_2 and fill its bandgap with states. Hence, a clear path forward to make pristine contacts is to use 2D semi-metals in conjunction with 2D semiconductors.

5.2 Introduction

miconductors. Introduction In recent years, MoS_2, one of the Transition Metal Dichalcogenide Monolayers (TMDC), has attracted significant attention and has been explored for a variety of applications in a vast range of fields [19, 175, 176]. Interlayer van der Waals bonding of MoS_2 allows one to obtain monolayer thickness [177]. Due to its 2D nature, the monolayer (ML) MoS_2 shows planar structure without the presence of the dangling bonds. This gives ML MoS_2 perfect surface smoothness and helps reduce the surface trap states [178]. Compared to other 2D materials, MoS_2 has a non-zero layer-dependent bandgap, which is 1.2 eV indirect bandgap [154] for bulk MoS_2 and 1.8 eV direct bandgap [179] for ML MoS_2. This unique property enables ML or multilayer MoS_2 to act as a semiconductor and thus broadens the application of MoS_2 in the field of electronics and photonics. MoS_2 also has other merits like good flexibility [180], adequate mobility [181] and availability of large-scale thin films (synthesis) [182]. For these reasons, MoS_2 is fast becoming a promising candidate for the 2D semiconducting channel of the next-generation field effect transistors (FET). Although many MoS_2 FET have been reported [183–185], obtaining a good contact for MoS_2 FET is still an important issue. To find both good ohmic and Schottky contacts, extensive research has been conducted to investigate metal-(ML) MoS_2 contacts [26–29, 186] via both computational and experimental work. However, it is observed that the covalent bonds forming between the metal and MoS_2 introduce defects and metallization effect the MoS_2 structure [28, 186], which can be seen in figure-5.1 (a). After creating a contact, the defects generated lower the charge mobility [28]. To overcome this issue, some groups have utilized encapsulation technique, the MoS_2 mobility can be preserved by using h-BN (hexagonal boron nitride) nano

sheets to enclose the MoS_2 sheet [70, 187]. This encapsulation technique though increases the fabrication complexity of the devices which add difficulty for large-scale manufacturing.

To overcome the existing issues of the metal-MoS_2 contact, the concept of van der Waals contact based on 2D metals and semimetals has been studied earlier [188]. In recent years, many MoS_2 devices integrated with 2D contacts have been fabricated [189–191]. Compared with traditional metal contacts, these contacts show higher mobility, smaller structural changes in MoS_2 and smaller metallization is added to MoS_2 along with higher flexibility. The h-BN encapsulation can also be used for these contacts with its deposition by chemical vapor deposition (CVD) or exfoliation to further increase the device mobility [191, 192]. Thus, utilizing 2D materials as a electrode material improves the scalability of the devices. It has been shown that smoothness, absence of dangling bonds, and the ultra-thin layer of the 2D contact enables shorter channel devices in 2D MoS_2 FET [192]. Obtaining good and reliable ohmic and Schottky contacts for MoS_2 will speed up the development of high-performance 2D heterostructure devices.

It is thus essential to explore and understand 2D materials suitable for electrode formation with MoS_2. There are quite a few 2D metallic materials and we consider titanium disulfide (TiS_2 for the electrode here. TiS_2 is also a member of TMDC family, but there is a small overlap between the conduction band and valence band of TiS_2 [193]. Some references have claimed that TiS_2 has a narrow bandgap of 0.2 eV [194] exhibiting semi-metallic properties. As a semi-metallic material, TiS_2 has already been employed as electrode material of lithium ion batteries and solar cells due to its high electric conductivity (1×10^4 S/m) [195–201]. However, compared with graphene, to the best of our knowledge no study detailed study has been conducted. Hence, we have conducted a systematic computational study on the 2D TiS_2-MoS_2 (ML) contacts by using first-principles simulation. We found that the intrinsic structure of ML MoS_2 is well preserved after forming a contact with TiS_2. As shown in figure-(b)

and (c), the TiS_2 contact induces ML MoS_2 to demonstrate p-type behavior, while graphene contact induces it to become n-doped [42]. Another interesting finding from our study is that the Schottky barrier height for the TiS_2 contact and ML MoS_2 changes by varying the doping type and concentration of MoS_2. By using the projected local density of states analysis (PLDOS), we have extracted the barrier heights of TiS_2-MoS_2 (ML) contacts at different doping type and concentrations along with different TiS_2 thickness. We found that, for intrinsic and n-type doped ML MoS_2, TiS_2 forms a Schottky contact whereas for p-type ML MoS_2, TiS_2 forms an ohmic contact. Thus, we can use TiS_2 to obtain high quality ohmic and Schottky contacts for ML MoS_2 for fabrication of high-quality devices.

5.3 Results

The methods section describes the DFT techniques used for this research. The contact formation between TiS_2-MoS_2 leads to two interfaces as seen in figure-5.2 (d). To confirm this, two geometries are adopted to investigate the contact, which are shown in figure-5.2 (a) and (b). A group of TiS_2-MoS_2 junctions are used to test the electron transport from TiS_2 contact to the ML MoS_2 sheet at the lateral interface (interface A in figure-5.2 (d)). Another group of FET-like TiS_2-MoS_2 heterostructures (TiS_2-MoS_2 FET-like junctions) are used to simulate the electron transportation from the contact region to semiconducting channel region at the vertical interface (interface B in figure-5.2 (d)).

For TiS_2-MoS_2 FET-like junction, the projected local density of states (PLDOS) is calculated for revealing the band structure after the contacting of 1-4 layers of TiS_2 and ML MoS_2 sheet. The configuration after geometrical optimization (GO) is shown by figure-5.2 (d). The overlap of 1-4 layers of TiS_2 and ML MoS_2 is 2.5 nm. Due to the limitation of computational capability, the ML-MoS_2 channel is set as 8 nm. To increase the accuracy in the transportation direction, the k-point sampling is changed to $10\times1\times40$. For each of 1-4 layers of TiS_2 simulations, The MoS_2 channel doping

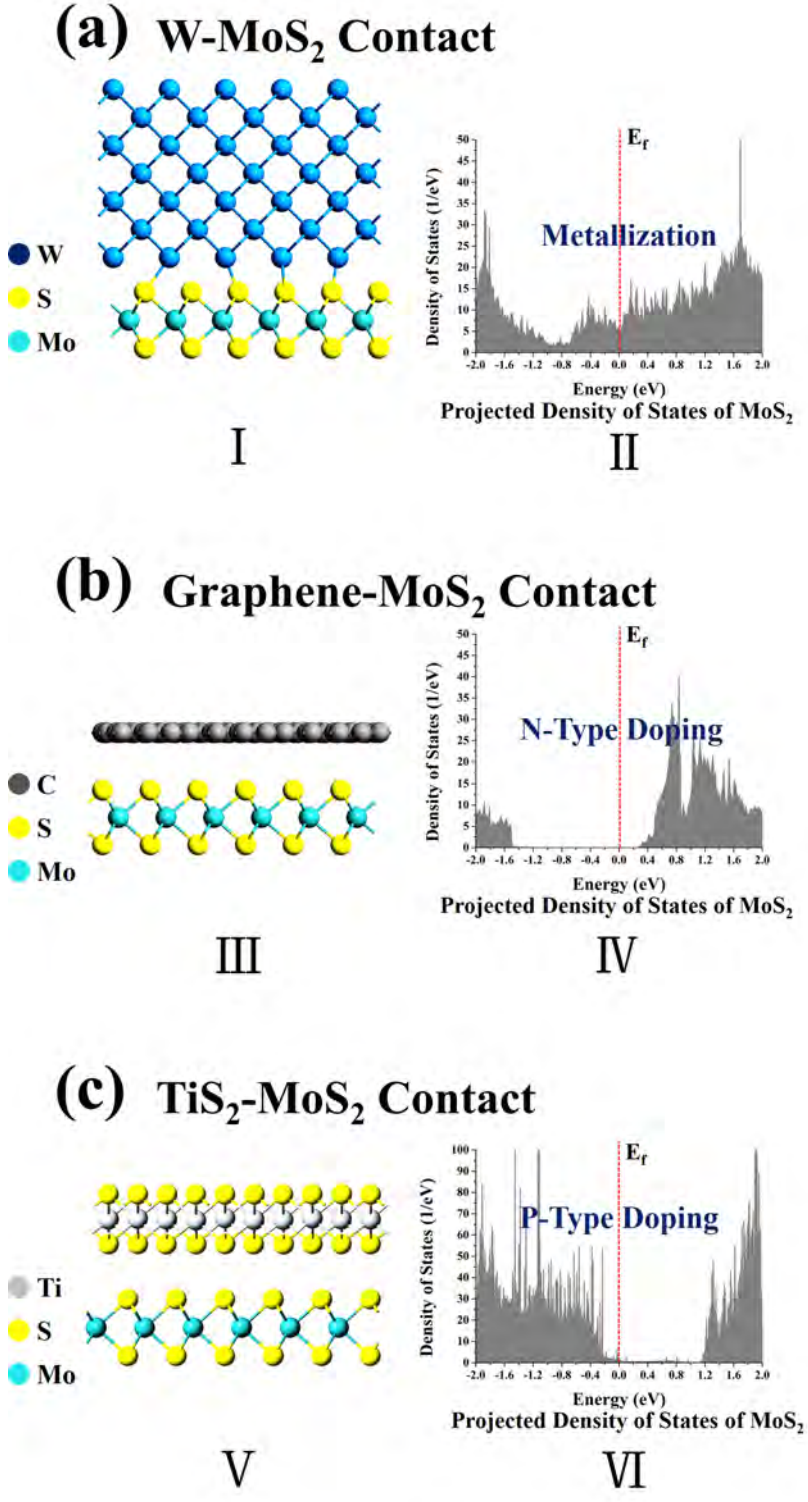

Figure 5.1: ML MoS_2 Contact Formation with Metal, W, Graphene and TiS_2 indicating the Difference in the Type of contact. Contact geometry is shown in (a), (b) and (c) along with respective PLDOS shown (d), (e) and (f) for Tungsten(W) – ML MoS_2 contact, Graphene-ML MoS_2 contact and TiS_2- ML MoS_2 contact.

Figure 5.1: The results for metal-contact [29, 186] and graphene contact are obtained by our simulations and in agreement with the reported experimental data [28, 42, 186]. It indicates that metal contact adds metallization to ML MoS_2 and bandgap of MoS_2 vanishes. Graphene and TiS_2 contacts preserve the bandgap, due to the van der Waal forces, of ML MoS_2 but add n-type and p-type doping respectively.

is varied to understand the type of electrode formation as 5×10^{18} cm^{-3} (3.25×10^{11} cm^{-2} for ML MoS_2) n-type doping, 1×10^{19} cm^{-3} (6.5×10^{11} cm^{-2} for ML MoS_2) n-type doping, 5×10^{19} cm^{-3} (3.25×10^{12} cm^{-2} for ML MoS_2) n-type doping and 5×10^{18} cm^{-3} (3.25×10^{11} cm^{-2} for ML MoS_2) p-type doping. Thus, we obtain a n_i) value of 1.4×10^{4} cm^{-3} for ML MoS_2. We chose the doping concentration carefully to meet the calculated upper and lower limits: a large doping concentration will lead to degenerate behavior of the channel and a small doping concentration will cause the depletion length to exceed the length of channel creating artificial results. The overlap region between the TiS_2 and MoS_2 is undoped. Only the uncovered ML-MoS_2 channel is doped with the chosen doping concentrations.

To investigate the charge transport and its mechanism through the interface A in figure-5.2 (d), the calculation of DOS, ED, average binding energy (EBE) and EDP are conducted after the GO.

After simulating the DOS of the optimized TiS_2-MoS_2 structure, the projected partial density of states (PDOS) is shown in figure-5.3. The PDOS of TiS_2 after making a contact with ML MoS_2 is defined as shown in figure-5.3 (a). It shows that, after making a contact with ML MoS_2, the TiS_2 DOS remains the same as the free-standing TiS_2. The only difference is that some trap states are added which shown as spikes in the figure-5.3 (a). These added states are created by the tiny displacement of the atoms in TiS_2 layer, which is of the order of 0.01 Angstrom. This indicates that the presence of ML MoS_2 has a negligible effect on the TiS_2 band structure. The situation of MoS_2 is different, as shown in figure-5.3 (b). The plot clearly demonstrates that the TiS_2 contact modifies the MoS_2 band structure significantly and adds a large

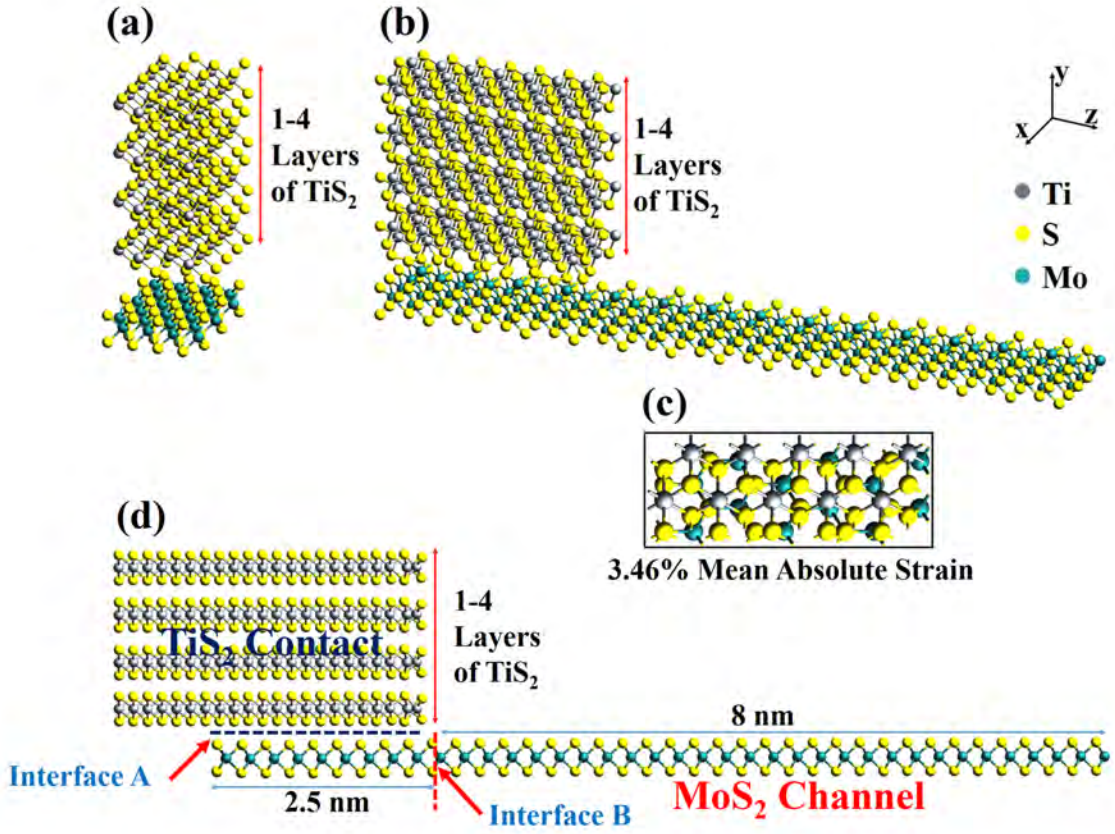

Figure 5.2: Geometry Set-up for TiS_2-MoS_2 Contacts. (a) TiS_2-MoS_2 junction, where the grey, blue and yellow balls represent Ti, Mo and S atoms respectively. (b) TiS_2-MoS_2 FET-like structure. (c) Top view of (001) TiS_2 surface on monolayer (001) MoS_2 surface. (d) Parameter set-up for (1 to 4 layers of) TiS_2-MoS_2 FET-like junctions. Here, the interface A shows the lateral interface, which lies between the TiS_2 contact and ML MoS_2. The interface B shows the vertical interface, which lies between the contact region and the MoS_2 channel.

amount of p-type doping to the ML MoS_2. In figure-5.3 (b), compared with the band structure and DOS of intrinsic ML MoS_2 on the left side, for all the cases of ML to 4-layer TiS_2 contacts, the PDOS of ML MoS_2 exhibits Fermi level pinning towards valence band. This shift of Fermi level ranges from 0.40 - 0.45 eV. Even though the 3 and 4-layer TiS_2 forming a contact with ML MoS_2 show a larger Fermi level shift the difference in Fermi level shift with change in number of TiS_2 layers is very small. The energy difference between the valence band and Fermi level is 0.05-0.1 eV. The energy difference between the Fermi level and valence band is defined by:

$$\Phi = E_f - E_V \tag{5.1}$$

where E_f and E_v are the Fermi level and the valence band top respectively. Knowing the Fermi level shift and Φ, the p-type doping concentration can be determined by calculating the effective density of states in the conduction band (N_c) and the valence band (N_v). As there are not too many reported values of N_c and N_v reported, we have calculated these to estimate what doping concentration we should use for our electrode simulations for ML MoS_2. Hence, the effective density of state values is required only for estimating the doping concentrations of MoS_2. After simulating the DOS, the energy difference between the quasi Fermi level and the valence band can be calculated. These two well-defined equations can be applied to determine N_c and N_v:

$$N_C = ne^{\frac{E_c - E_F}{kT}} \tag{5.2}$$

$$N_V = pe^{\frac{E_c - E_F}{kT}} \tag{5.3}$$

where n and p are the electron and hole concentrations, respectively. From the simulation, N_c and N_v for ML MoS_2 are calculated to be 2 $\times 10^{19}$ cm^{-3} (1.38×10^{12} cm^{-2}) and 1×10^{19} cm^{-3} (6.5 $\times 10^{12}$ cm^{-2}), respectively, which are similar to the reported ML and bulk MoS_2 values [202–205]. Using these values, the calculated doping concentration added to the ML MoS_2 by TiS_2 contacts with different number of layers ranges from 3.85×10^{17} to 2.63×10^{18} cm^{-3} (2.50×10^{10} to 1.71×10^{11} cm^{-2} for

ML MoS_2). Compared with metal-MoS_2 contacts [26–29, 186], although the ML MoS_2 is p-type doped after forming a contact with TiS_2, its bandgap is preserved as shown in figure-5.3 (b); in contrast, the metal contact will metalize the ML MoS_2 and fill its bandgap with states as shown in figure-5.1 (a). The TiS_2-MoS_2(ML) contact makes ML MoS_2 p-type as compared to the n-type in graphene-MoS_2 contact (figure-5.1 (b)).

Thus, the DOS simulation indicates that TiS_2-MoS_2 (ML) contact is a unique contact with less metallization and p-type behavior. It is necessary to conduct a comprehensive analysis on its interfacial bonding condition. ED and EBE are two important criteria to evaluate the bonding between TiS_2 and ML MoS_2. The average binding energy (EBE), E_B, can be defined as:

$$E_B = (E_T + E_M - E_{T-M})/N \tag{5.4}$$

where E_T is the total energy of the free-standing TiS_2, E_M is the total energy of the intrinsic ML MoS_2, E_{T-M} is the total energy of the TiS_2-MoS_2 (ML) contact after GO, and N can be considered as the number of interfacial Sulfur atoms on the MoS_2 side.

The ED of the TiS_2-MoS_2 junctions are shown by figure-5.4 (a). As seen in the plot, there is a clear gap between the TiS_2 layer and MoS_2 with no charge distribution in it. The electron gas overlap between TiS_2 and MoS_2 is very limited, according to the contour plot. The plot of the projected electron density in the y direction also clearly shows that the electron density overlap at the contact interface is very similar to those between TiS_2 layers, indicating that the bonding between TiS_2 and MoS_2 is not much stronger than interfacial bonding within TiS_2 layers. The buckling distance can also be extracted from both the ED plot and GO. For TiS_2-MoS_2 (ML) junctions, the optimized buckling distance for TiS_2-MoS_2 contacts are: 3.2282 Å for TiS_2 (ML)-MoS_2 (ML), 2.8112 Å for TiS_2 (2L)-MoS_2 (ML), 2.8069 Å for TiS_2 (3L)-MoS_2 (ML) and 2.7381 Å for TiS_2 (4L)-MoS_2 (ML). For comparison, the inter-layer distance for

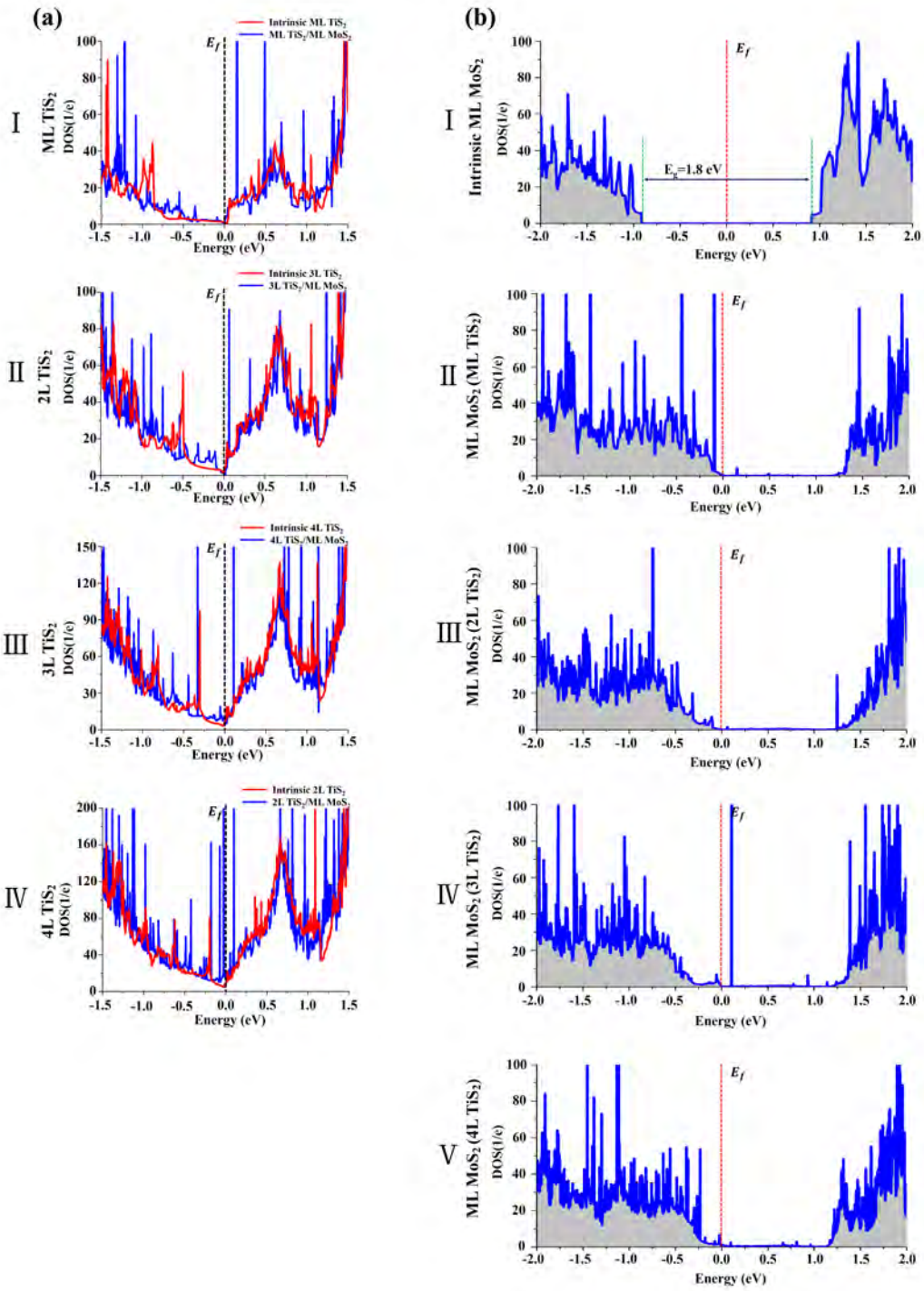

Figure 5.3: The Partial Density of States (PDOS) of TiS_2 and MoS_2 within TiS_2(ML to 4L)-MoS_2(ML) contacts. (a)PDOS of TiS_2 (from ML to 4L). In the plot, the dashed line indicates the position of Fermi level, which is set as zero point. The red line represents the DOS of free-standing TiS_2, as a comparison. (b) PDOS of ML MoS_2. On the top is the DOS of free-standing ML MoS_2, as a comparison. The Fermi level of each plot has been aligned to the same energy value. The label ML-TiS_2 to 4L-TiS_2 indicate the TiS_2 contact thickness.

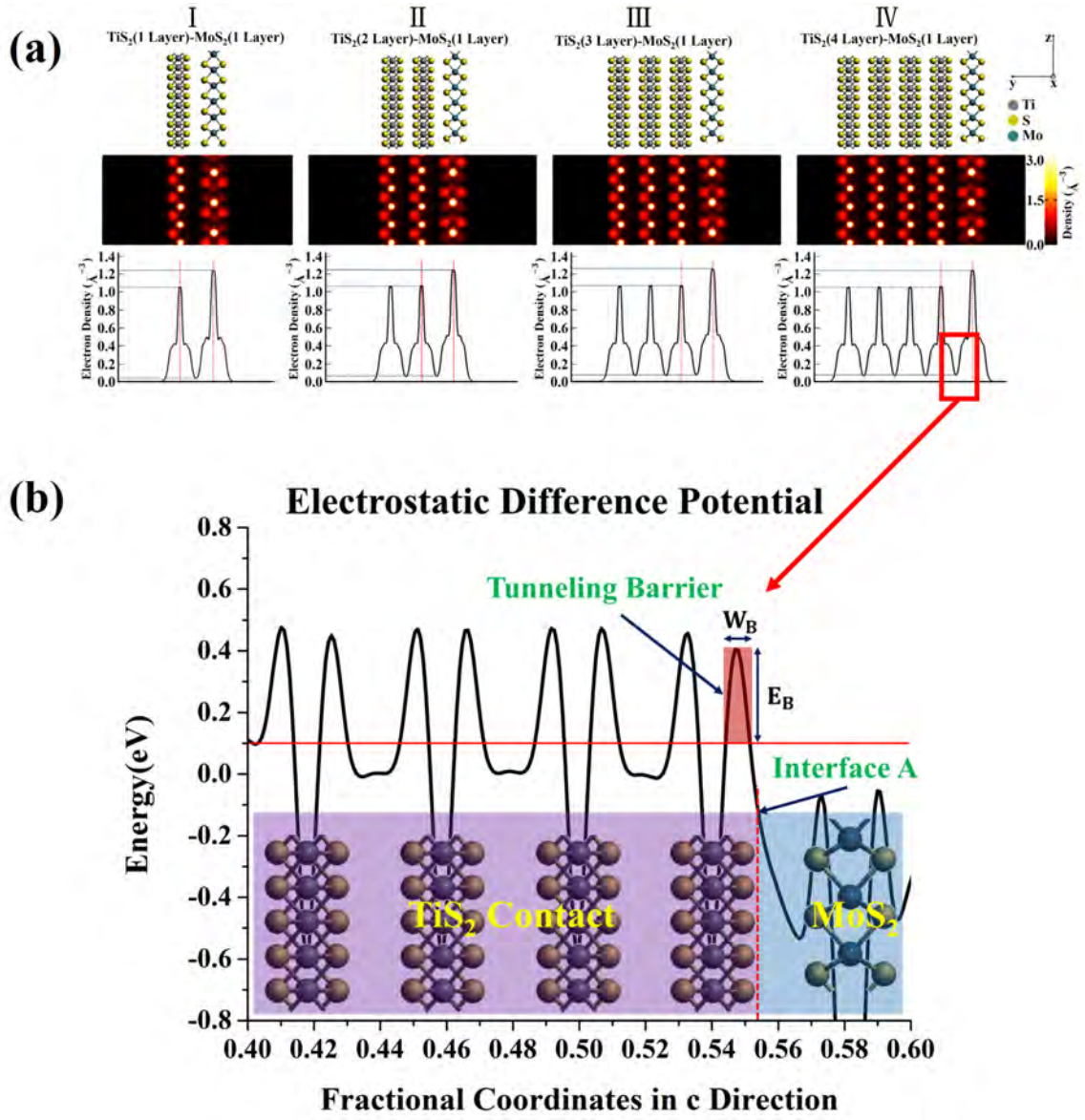

Figure 5.4: Electron Density (ED) and Electrostatic Difference Potential (EDP) of TiS_2-ML MoS_2 Junctions. (a) ED on the top is the configuration after GO. In the middle is the contour plot of the electron density in which brighter color indicates higher ED. The bottom plot is for the normalized ED projected on the y direction (vertical to the contact plane). (b) EDP, x axis is the fractional coordinates of the superlattice along the c direction with the length of superlattice as 8 nm. The geometry configuration is integrated in the plot, which is shown on the bottom. It shows that at the interface A, there is a small tunneling barrier. The barrier height E_B and barrier width W_B is labeled in the figure.

TiS_2 and MoS_2 is 2.8678 Å and 2.9754 Å, respectively. It is clear that thicker TiS_2 has larger attractive force to ML MoS_2 and leads to smaller inter-layer distance. These ED results reveal that the bonding between the TiS_2 contact and ML MoS_2 in TiS_2-MoS_2 (ML) junctions is Van der Waals bonding. Unlike the covalent bond, the delocalization of interfacial electron gas won't exist in these cases.

By using this definition, the EBE for TiS_2-MoS_2 (ML) interface is 0.7426 eV, while this value is 0.7157 eV for the Van der Waals bonds of bilayer MoS_2. This result further confirms the previous results and demonstrates that TiS_2-MoS_2 (ML) contact is a Van der Waals contact.

The tunneling barrier at the TiS_2-MoS_2 (ML) interface will determine the charge transport through the interface A. To evaluate the impedance to the current transportation added by the tunneling barrier, the electrostatic difference potential of the TiS_2-MoS_2 contact is simulated. As shown in figure-5.4 (b), the potential between the TiS_2 and MoS_2 is considered as the tunneling barrier. The shape of the potential barrier can be estimated as a rectangle. The tunneling probability, from the TiS_2 to the ML MoS_2 can be defined as, of carriers tunneling through the barrier, T_B:

$$T_B = \exp\left(-4\pi \frac{\sqrt{2\ m\Delta V}}{h} W_B\right) \tag{5.5}$$

where ΔV is the barrier height, which is defined by the length of the rectangle, h is the Planck constant, and W_B is the barrier width, which is defined as the half width of the rectangle. ΔV and W_B can be directly extracted from figure-5.4 (b): ΔV is 0.404620 eV and W_B is 0.35412 Å. By using these parameters and equation (4), we calculate T_B as 79.4%. A large T_B imdicates small impedance and a higher charge injection. It is very clear that even though the tunneling barrier at the interface A resists the charge transport vertically through the interface, the possibility of tunneling is high for carriers because of a very tiny barrier width (0.35412 Å). For this reason, the charge injection at the lateral interface can be ignored. However, the interfacial tunneling barrier within the TiS_2 contact may scatter the electrons and holes. This

scattering effect can be reduced by using a thinner TiS_2 film. Thus, we also address scaling down the thickness of TiS_2 contacts after meeting the stability requirement.

By analyzing the ED, EBE and GO for configuration for interface A, it can be concluded that TiS_2 tends to form Van der Waals bond with ML MoS_2, with thicker TiS_2 creating stronger bonding. The DOS in figure-5.3 shows that less metallization is created due to the weak Van der Waals bonding and the bandgap of ML MoS_2 is preserved. DOS results also show that TiS_2 will add p-type doping to the ML MoS_2. The EDP results in figure-5.4 show that the tunneling barrier is small at interface A, which means that the current injection won't be seriously impeded.

To understand the source-to-channel/channel-to-drain working mechanism for the TiS_2-MoS_2 (ML) contacts applied in 2D FET, the projected local device density of states (PLDOS) is adopted to sketch out the framework of the band structure at the interface B of the TiS_2-MoS_2 FET-like junctions. The PLDOS uses a contour plot to map the density of states projected onto the c axis, which is the transportation direction. The band structure can be determined by plotting the boundary between the states-filled region (bright region) and the no-states region (dark region). The extraction of the barrier height and contact type of TiS_2-MoS_2 contact can be achieved by evaluating the PLDOS. Two reasons let us dope the ML MoS_2. First, the intrinsic carrier concentration of ML MoS_2 is small; therefore, it is a good choice to dope the MoS_2 channel to improve the conductivity. For this reason, it is of great interest to investigate the contact consisting of doped ML MoS_2. Also, the channel length is set to 8 nm based on computational considerations, as mentioned earlier. An adequate amount of doping concentration is required to make sure that the depletion length is smaller than the channel length of the simulated configuration. Although the barrier height and contact type for the contact of intrinsic ML MoS_2 and TiS_2 cannot be extracted directly from the PLDOS, but the barrier height and contact type of doped cases can still be extracted accurately.

Four different doping concentrations: 5×10^{18} cm^{-3} n-type doping, 1×10^{19} cm^{-3}

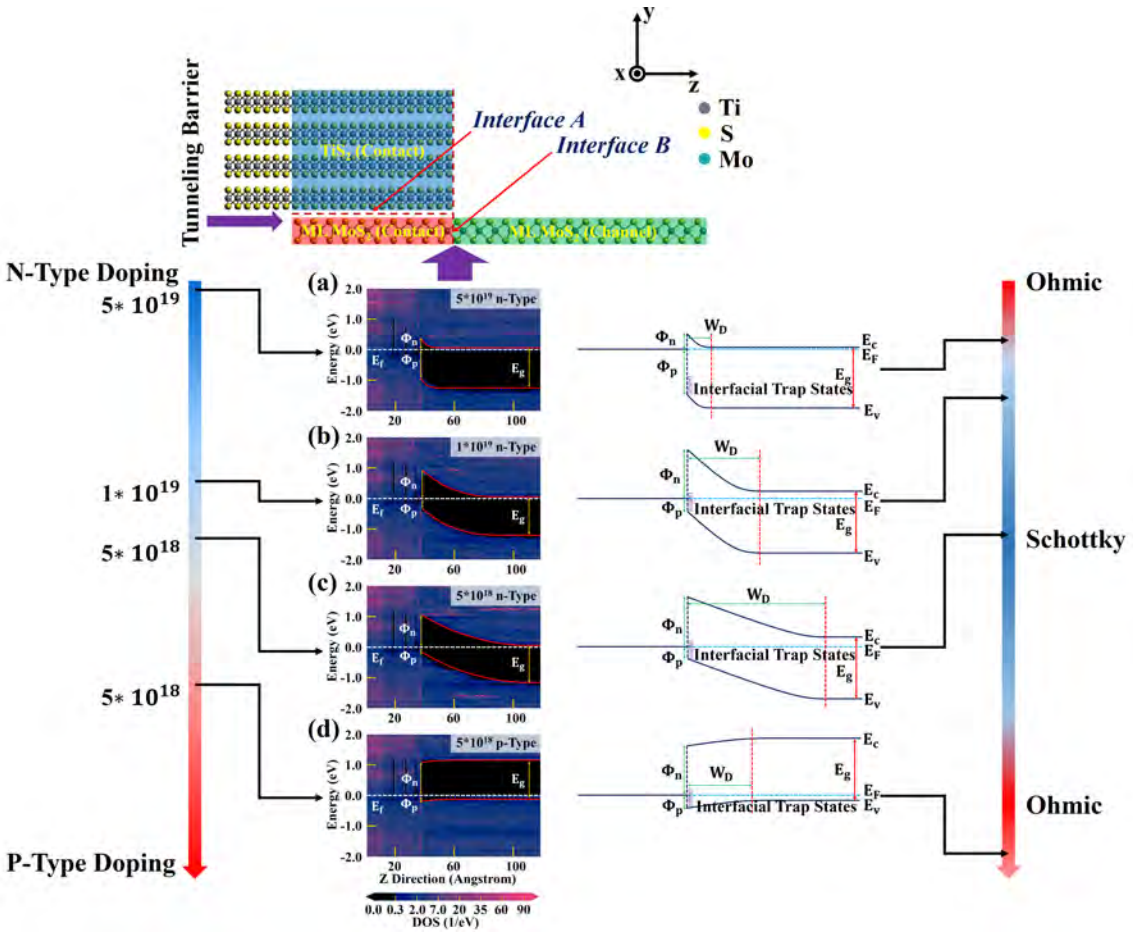

Figure 5.5: PLDOS of TiS_2-MoS_2(ML) FET-like Junctions Doped with Different Doping Concentration and the Variation of Band structure at Interface B. (a)-(d) The doping concentrations are: N=5×10^{19} cm^{-3}, N=1×10^{19} cm^{-3}, N=5×10^{18} cm^{-3}, and P=5×10^{18} cm^{-3}. The thickness of TiS_2 is 4 layers. On the right-side, the plot shows the variation of band structure under different doping concentration.

n-type doping, 5×10^{19} cm^{-3} n-type doping and 5×10^{18} cm^{-3} p-type doping is tested. The simulation results are shown in table-5.1. The figure-5.5 shows only the results of the TiS_2(4L)-MoS_2(ML) cases and the variation of the band structures with different doping concentrations.

For n-type doping concentrations smaller than N_c, the Schottky barrier height of the contacts are large: 1.03 eV-1.07 eV for 5×10^{18} cm^{-3}, and 0.88 eV-0.95 eV for 1×10^{19} cm^{-3}, as shown in table-5.1 and figure-5.5 (b), (c). The table-5.1 also clearly shows that for the cases with ML TiS_2, Φ_P of the contact is larger than Φ_P of 2L-4L cases with the same doping concentration. For the n-type doping concentration of 5×10^{18} cm^{-3}, Φ_P is 0.67 eV for ML but 0.21-0.25 eV for 2-4L. For n-type doping concentration of 1×10^{19} cm^{-3}, Φ_P is 0.7 eV for ML but 0.40-0.44 eV for 2-4L. By summing Φ_n and Φ_p, the modified E_g is 1.70 eV for the ML case doped n-type with concentration 5×10^{18} cm^{-3}, and for 2-4L cases doped with this concentration, E_g ranges from 1.26 eV to 1.32 eV. For n-type doping of concentration 1×10^{19} cm^{-3}, E_g is 1.65 eV for ML and 1.32 eV for 2-4L.

For a larger n-type doping concentration (5×10^{19} cm^{-3}), as shown in both table-5.1 and figure-5.5 (a), the Schottky barrier height is 0.30 eV-0.45 eV, which is much smaller than the cases with n-type doping concentrations of 5×10^{18} cm^{-3}) and 1×10^{19} cm^{-3}). This reduction in barrier height may be brought about by multiple causes. One possible reason is the imaging force created by the larger amount of excess charge, as a result of the larger doping concentration. It is observed that Φ_p increases compared with lower doping concentrations. Φ_p is 0.92 eV to 0.97 eV for the 1-4L cases. E_g for this concentration is 1.27 eV to 1.37 eV.

The simulation results and mapped band structures in figure-5.5 (a) to (c) for n-type doped TiS_2-MoS_2(ML) contacts show that, normally, n-type doped TiS_2-MoS_2(ML) contacts show a large barrier height, which is around 1.0 eV below a degenerate doping. Even though figure-5.5 shows that a larger doping concentration will reduce the barrier height for n-type carriers, it is obvious that, even for a doping

Table 5.1: Calculated Depletion Width W_D, Vertical Barrier Height for Electrons Φ_n, and Vertical Barrier Height for Holes Φ_p for the TiS_2 with different number of layers and ML MoS_2 junction.

Number of TiS_2 layers/ ML MoS_2 doping conc. and type.	Depletion width W_D (nm)	Vertical Barrier Height for Electrons Φ_n (eV)	Vertical Barrier Height for Holes Φ_p (eV)	Effective band gap after formation of junction E_g (eV)
1L, 5E18 p	...	1.35	0.13	1.48
2L, 5E18 p	...	1.18	0.05	1.23
3L, 5E18 p	...	1.18	0	1.18
4L, 5E18 p	...	1.18	0	1.18
1L, 5E18 n	6.4	1.03	0.67	1.70
2L, 5E18 n	6.3	1.05	0.21	1.26
3L, 5E18 n	5.8	1.07	0.25	1.32
4L, 5E18 n	5.8	1.03	0.23	1.26
1L, 1E19 n	3.6	0.95	0.70	1.65
2L, 1E19 n	4.9	0.92	0.40	1.32
3L, 1E19 n	4.6	0.90	0.42	1.32
4L, 1E19 n	4.8	0.88	0.44	1.32
1L, 5E19 n	1.6	0.35	0.95	1.30
2L, 5E19 n	1.5	0.45	0.92	1.37
3L, 5E19 n	1.2	0.30	0.97	1.27
4L, 5E19 n	1.2	0.30	0.97	1.27

concentration very close to degeneration, the Schottky barrier height is still larger for TiS_2- MoS_2(ML) contacts. The inference from figure-5.5 is that since the majority carriers in these n-type doped contacts are always faced with a large Schottky barrier height, the n-type doped TiS_2-ML MoS_2 Schottky diodes can probably act as high-power switches or Schottky barrier MOSFETs based on tunneling.

Unlike the n-type contacts, the p-type doped TiS_2-MoS_2 (ML) contacts shows zero barrier height when the p-type doping concentration reaches 5×10^{18} cm^{-3}). In figure-5.5 (d), it is observed that, at this doping concentration, the depletion width vanishes and the band is flat. The Schottky barrier at the interface shows both a small barrier height and a small built-in potential, which indicates the contact is an ohmic contact for ML MoS_2 doped p-type at a concentration 5×10^{18} cm^{-3}).

For the cases with p-type doping concentration of 5×10^{18} cm^{-3}), only the ML and 2L cases show a very small barrier height Φ_p (0.13 eV for ML and 0.05 eV for 2L). For the 3L and 4L cases, there is zero barrier height. Φ_n is 1.35 eV for ML and 1.18 eV for 2-4L, as shown in table-5.1. For the cases with p-type doping concentration of 5×10^{18} cm^{-3}), the bandgap shrinks to 1.48 eV for ML TiS_2 and 1.18 eV for 2-4L.

As inferred from figure-5.5 (d), when the doping is p-type with a concentration of 5×10^{18} cm^{-3}), the contact is ohmic for p-type carriers while the barrier for n-type carriers is still large. As mentioned earlier, the doping concentration P_c was added to the ML MoS_2 within the contact region ranges from 3.85×10^{17} cm^{-3}) to 2.63×10^{18} cm^{-3}). When the p-type doping of channel MoS_2 reaches the value of P_c, the band will become flat, and the contact becomes an ohmic contact. Thus, TiS_2 can be used as an either an ohmic or Schottky contact depending on the doping of the ML MoS_2.

5.4 Discussions

We propose a design for a ML MoS_2 with two different contacts namely TiS_2 on one side and graphene on the other to achieve tunable functionalities as shown in the schematic in figure-5.6. Since TiS_2 junction with ML MoS_2 induces p-type doping,

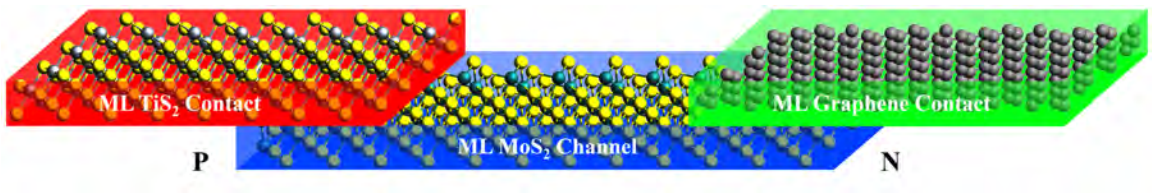

Figure 5.6: Schematic of TiS_2-MoS_2-graphene Heterostructure device. TiS_2 and graphene act as 2D contacts as the contact formation will induce p-type and n-type doping on the two sides of ML MoS_2 channel respectively.

while graphene contact induces n-type doping as reported [42]. The heterostructure shown in figure-5.6 consists of TiS_2 contact on the left side and graphene contact on the right with ML MoS_2 channel. The working principle of the device depends on the doping condition of the channel. If the channel is p-type doped, it tends to form Ohmic contact with graphene while forming a Schottky contact on the right side. This would flip if the channel is n-type. This device would turn on only if the Schottky barrier is overcome. In addition, if an oxide and gate are added to the MoS_2 to obtain better control over the channel. This device can be made using p and n-type ML MoS_2 doping using the same materials for electrode and obtain complementary devices. In addition, from our simulation studies, we observe that the covalent-bonding contacts add metallization to the MoS_2. Thus, for a good contact that preserves the doping concentration of the MoS_2 one would prefer a material which forms van der Waal bond with it although it will introduce some loss due to the inter-layer impedance. Hence, one can utilize 2D materials to obtain high performance devices.

Using the first-principle DFT simulation, a comprehensive and detailed study on TiS_2-(ML) MoS_2 contact has been conducted. The simulation shows that, unlike most other contact materials, it is unique that the presence of a TiS_2 contact adds p-type doping to the ML MoS_2 sheet. The Fermi level shift and smaller metallization effect in the contact region preserves the intrinsic nature of ML MoS_2. A tunneling barrier model is employed and we have extracted the transmission rate by using quantum mechanical calculations. The transmission rate T_B (79.4%) is very high at the interface. However, thinner contacts are necessary to reduce carrier scattering.

We thus observe that TiS_2 forms a n-type Schottky contact with intrinsic ML MoS_2 at the vertical interface, but the barrier heights for both electrons and holes are large. The barrier height for electrons (Φ_n) and the holes (Φ_p) at vertical interface can be reduced having either n-type or p-type doping in the channel region. The barrier height is small for p-type doped channels and TiS_2 can form either an ohmic contact or a Schottky contact with low barrier height, which depends on the p-type doping concentration of MoS_2. Thus, our simulation results demonstrate that TiS_2 is a promising 2D electrode material for ML MoS_2, because it does not distort the structure of the ML MoS_2 much as compared to the metals which metallize the MoS_2 strongly. This merit makes TiS_2 contact viable for a variety of applications for ML MoS_2 heterostructure devices like P-N hetero device. Also, in addition to its utility as a good electrode material TiS_2 also can be used as a p-dopant for MoS_2.

5.5 Methods

The computational study based on density functional theory (DFT) [132] has been conducted for this research using Atomistix ToolKit (ATK) [6]. For all the simulations, TiS_2-MoS_2 junctions and TiS_2-MoS_2 FET-like junctions, the thickness of the TiS_2 was chosen to range from ML to 4L (4 layers) to explore the impact created by the variation of the TiS_2 thickness, while the MoS_2 channel is set as ML. The mean absolute strain is set as 3.46% for the lattice mismatch between the TiS_2 layer and ML MoS_2 for the simulations. It means the $5\times\sqrt{3}$ unit cell of the Ti matches the $3\sqrt{3}\times2$ unit cell of ML MoS_2. The Ti atoms in the TiS_2 layer occupy both on-top sites and hollow sites of the MoS_2 layer. This combination gives a much smaller total energy compared with the pure on-top configuration (which is possible for TiS_2 and MoS_2 because both of them are TMDCs). Since the periodic boundary condition (PBC) is applied in the simulation, a vacuum buffer of 30 Å is added in vertical direction to both groups of configurations to let the electrostatic potential decay softly at the boundary.

GGA (Perdew – Burke - Ernzerhof variant of Generalized Gradient approximation) [134] is applied for the DFT calculation. For simulation, the HGH (Hartwigsen – Goedecker – Hutter) [141] basis set is adopted to expand the electron density (ED). A DFT-D2 [162] correction is applied to make a correction to the interfacial Van der Waals bonding. Since the spin-orbital interaction is not taken into consideration in our simulation no correction was applied for it. The k-point sampling for TiS_2-MoS_2 junction is 12×4×1 while it is 10×1×1 for TiS_2-MoS_2 FET-like junction. All the k-point samplings are defined after a convergence test, which ensures that the total energy is converged to less than 1.0×10^{-5} eV. By conducting the convergence test, the energy cut-off for the simulation is set as 200 Ry. The maximum force, which determines the convergence of the geometry optimization (GO), is set as 0.05 eV/Angstrom. The density of states (DOS), electron density (ED) and electrostatic difference potential (EDP) also have been conducted utilizing this set-up.

Chapter 6

Image - Force Model for Extraction of Experimental Barrier Height for Two - Dimensional Material Back - to - Back Schottky Devices

6.1 Introduction

As mentioned in the previous chapters, the Schottky-Mott law could not give a precise prediction to the Schottky barrier height of metal-MoS_2 interface. Although simulations such as DFT could provide cost-effective predictions, however, the only way to provide accurate estimation of the metal-MoS_2 Schottky barrier height Schottky Barrier Height (SBH) is the high-accuracy standard characterization of the prototype metal-MoS_2 contacts. Normally, people adopt the convenient TE model [31] to model the I-V of Schottky diodes. In most of the cases, while using the two-probe method to measure the source-drain current of metal-MoS_2 contacts at zero gate bias, a back-to-back Schottky diode system is created. In this case, the ideal TE model is not applicable. Besides, the image force lowering tends to reduce the SBH of the contacts, which requires a specific correction to the existing model.

We have performed the mechanical exfoliation method to deposit MoS_2 thin films onto the prepared Au electrodes. Several devices have been successfully fabricated. We have developed a novel image-force correction model to analyze the I-V character-

istics of the back-to-back Au-MoS_2 Schottky contacts. As compared to the TE and resistance-correction models, our image-force model can extract the Schottky barrier height of the back-to-back contacts directly. Motivated by the huge potential exhibited by the 2D MoS_2 devices, we hope our detailed analysis would build a standard I-V characterization method with high accuracy and shine some light to uncover the solution to the existing contact issues of MoS_2.

6.2 Fabrication and Characterization of Back - to - Back Gold - Molybdenum Disulfide Schottky Diodes

6.2.1 Fabrication

The Fabrication of the Electrodes

In this work, MoS_2 thin films are obtained by exfoliating the commercial CVD grown MoS_2 crystal and transferred to the prepared gold electrodes. Since the shape and quality of the Au electrodes is crucial for the yield of each exfoliation, a proper electrode design as well as an optimized fabrication process flow of the electrodes will definitely increase the experiment success rate. The process flow of the electrode deposition is shown by fig-6.1. Firstly, the 4-inch 200 nm Si_3N_4 wafer is cleaned using Piranha solution. Then the wafer is coated with AZ5214 photoresist. By using the negative AZ5214 photoresist, an undercut of the photoresist layer would be achieved after the developing. Thus, the Au electrodes would have no sharp edge after the lift-off process. This edge-less structure will protect the MoS_2 films during the transfer process. After lithography, the Au is deposited onto the patterned wafer via sputtering system. The exfoliated MoS_2 will be transferred to the substrate with deposited Au electrodes after the lift-off process.

The obtained lithography patterns and Au electrodes are shown in the fig-6.2. As shown by fig-6.2 (a)-(c), high-quality lithography has been performed, and the patterns after developing show no defects. The shadowed area near the pattern edge

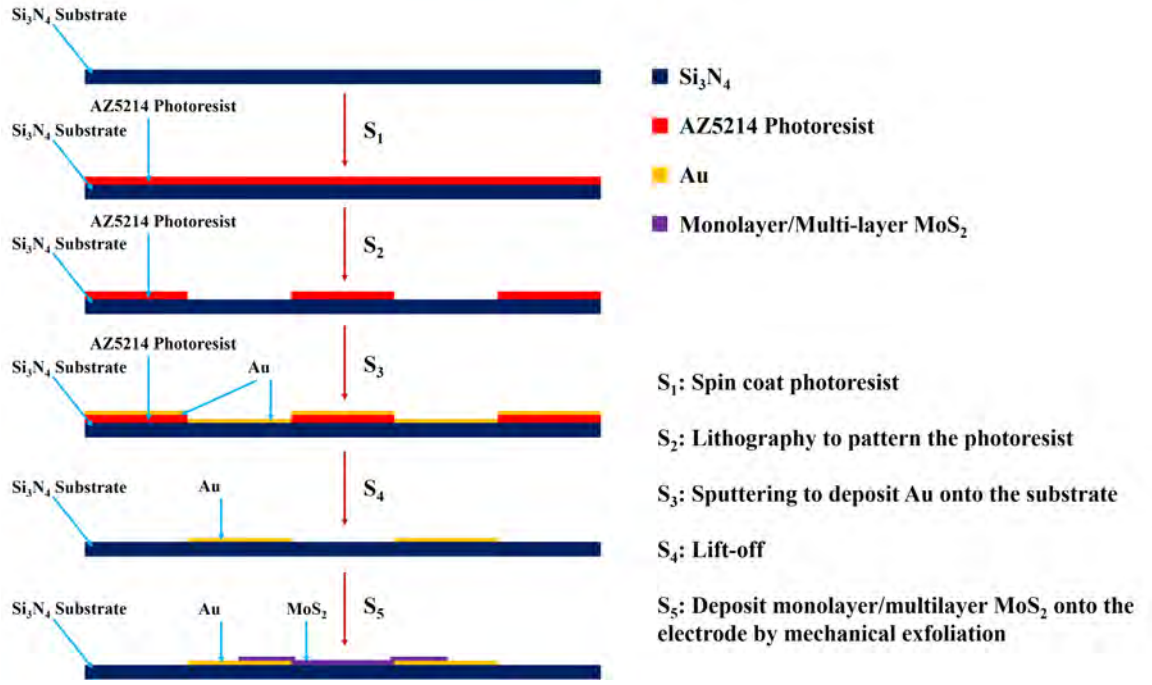

Figure 6.1: The Process Flow of the Device Fabrication. In the figure, the S_1 to S_5 denotes the step 1 to the step 5. The whole process includes: Piranha cleaning, pre-condition of the wafer, spin coating, lithography (bake, exposure and developing), sputtering of Au, lift-off, and the exfoliation and transfer of the MoS_2.

indicates the undercut of the photoresist. The Au electrodes after the deposition are shown by fig-6.2 (d)-(f). The electrodes are designed as comb structure to improving the success rate of the transfer process. If we take the exfoliation of MoS_2 as a needle throwing experiment, to improve the efficiency of each exfoliation, it is practical to increase the effective area for the exfoliation. The effective area can be defined as: once the MoS_2 flake lands within this region, it could form a close circuit with the Au electrodes. Since the size of the exfoliated MoS_2 flakes is uncontrollable, hundreds of exfoliation tests have been conducted to demonstrate the average size of the flakes. It has been determined that, by applying our exfoliation method, the median number of the flake diameters is around 3 μm. In this case, the gaps between the limbs of the electrodes are set as 1 μm, 2 μm, 3 μm, 5 μm, 7 μm, and 10 μm respectively. The width of the limb is set as 5 μm or 10 μm, and three different limb lengths are adopted: 25 μm, 50 μm and 100 μm. The Au electrode pad size is set as 100(μm) $\times$

100(μm). The efficiency of the electrodes η can be defined as:

$$\eta = \frac{S_{eff}}{s} \tag{6.1}$$

where the S (μm^2) is the total area, S_{eff} (μm^2) is the effective area. The S_{eff} can be given by:

$$S_{eff} = (l_1 + d) \times \left[\left[\frac{a}{l_2 + d}\right] - 1\right] \tag{6.2}$$

where the l_1 (μm) is the limb length, l_2 (μm) the limb width, α (μm) the side of the electrode pad and d the gap length between the limbs. For example, set l_1, l_2 and d as 50 μm, 10 μm and 3 μm respectively. The calculated S_{eff} is 954 μm^2, and the η is given as 3.77%. Due to the resolution of the mask aligner (exposure distance and UV light source), the electrode limb size is not exactly the same as the expected value. Normally there is an error ranging from 5% to 10%. While discussing the specific device in the next section, the dimensional parameters will be provided.

The Exfoliation of MoS_2

After the fabrication of the Au electrodes, the exfoliation of MoS_2 has been conducted systematically. As mentioned in the previous part, the layered structure of MoS_2 makes it possible to exfoliate MoS_2 thin films mechanically. As shown in fig-6.3 (a), it is obvious that, once the force between the substrate and bulk MoS_2 is larger than the MoS_2 interlayer Van der Waals bonding force, some MoS_2 flakes will be torn off by the exfoliation. In the fig-6.3 (a), the Van der Waals force within MoS_2 is represented by F_1, and the F_2 denotes the force between the substrate and the MoS_2. As reported, the scale of F_2 could be quantified by the adhesion energy between MoS_2 and the substrate materials [89]. It has been demonstrated that [89], among the silicon-based substrates, the Si_3N_4 substrate shows larger adhesion energy with MoS_2 thin films than other substrates such as SiO_2. On the other hand, a thicker and smoother substrate will also increase the adhesion energy. For these reasons, the 200 nm Si_3N_4 substrate is adopted in this work. Before processing the exfoliation, the substrate is

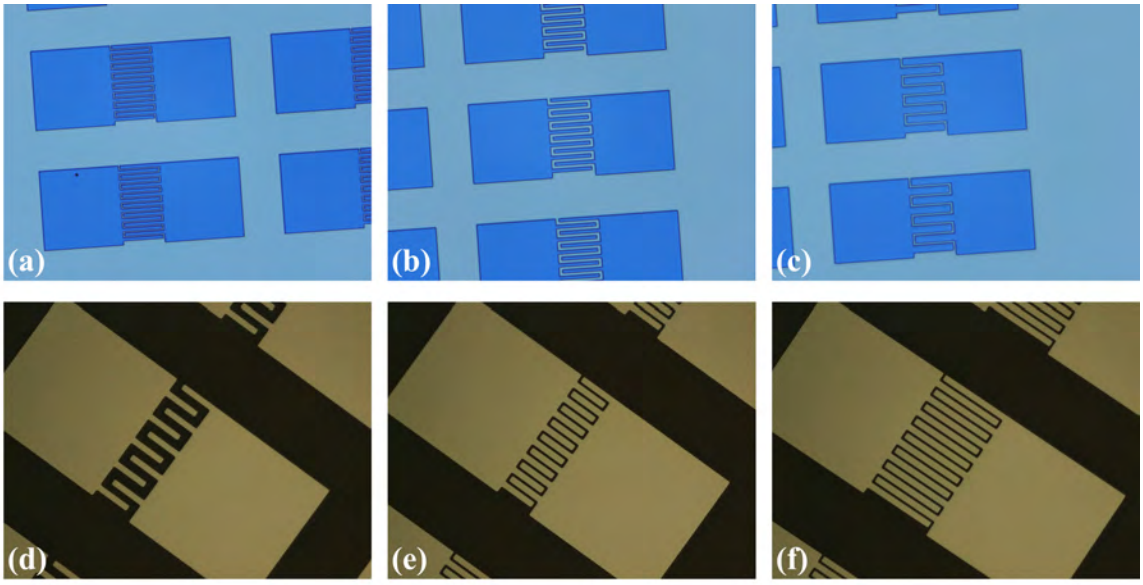

Figure 6.2: The Developed Photoresist Patterns and Deposited Au Electrodes. (a) The photoresist pattern of electrodes with 50(μm) $\times$ 5(μm) limbs and 1 μm gap. (b) The photoresist pattern of electrodes with 50(μm) $\times$ 5(μm) limbs and 3 μm gap. (c) The photoresist pattern of electrodes with 50(μm) $\times$ 10(μm) limbs and 2 μm gap. (d) The Au electrodes with 25(μm) $\times$ 5(μm) limbs and 5 μm gap. (e) The Au electrodes with 25(μm) $\times$ 5(μm) limbs and 1 μm gap. (f) The Au electrodes with 50(μm) $\times$ 5(μm) limbs and 1 μm gap.

treated with cold Piranha cleaning. This process removes the contamination on the wafer and improves the surface condition, thus enhancing the adhesion energy.

To land the MoS_2 flakes precisely, before the exfoliation, a transfer stage is set up by using standard optical setup parts. As shown in fig-6.3 (b), the homemade stage consists of a flexible holder, which could hold the glass slide carrying MoS_2 flakes. The stage could move up and down by adjusting the Z adjustment. The chunk which supports the holder could be calibrated in both X and Y direction by the adjustment located on the base. The fig-6.3 (b) intuitively shows that, the transfer stage is integrated with the microscope. By using the X, Y and Z adjustment, the calibration of the wafer and the glass slide could be realized in this way: first, adjust the glass slide within the focusing range of the microscope, and then lift it up. Then adjust the wafer to the focus plane by using the microscope stage. Finally, the glass slide is slowly lowered, move it to the focus but to a position which is slightly higher than the wafer, then by using the X and Y adjustment, move the chosen MoS_2 flake to the position which is exactly beyond the electrode's effective region. After lowering and pressing, some MoS_2 flakes will be transferred onto the electrodes.

The exfoliation of the MoS_2 follows the process flow shown by fig-6.3 (c). The first step is to exfoliate the MoS_2 before transferring it to the glass slide. To achieve a high quality transfer, it is important to reduce the stickiness of the scotch tape, because that the glue residual after the exfoliation will contaminate the glass slide and the wafer. This contamination will definitely affect the measurement and reduce the contact quality. Before exfoliation, the tape could be attached to a clean glass slide several times to reduce the stickiness. After that, the MoS_2 is exfoliated 5-6 times by the scotch tape to achieve lower thickness. To improve the success rate of the exfoliation, in the step 2, two strategies have been applied: one is to use thicker MoS_2 (with fewer times of exfoliation). The other way is to coat the glass slide with a layer of PMMA thin film, which is far less sticky than scotch tape and won't create much glue residual to the wafer. This coating layer will help improve the stickiness

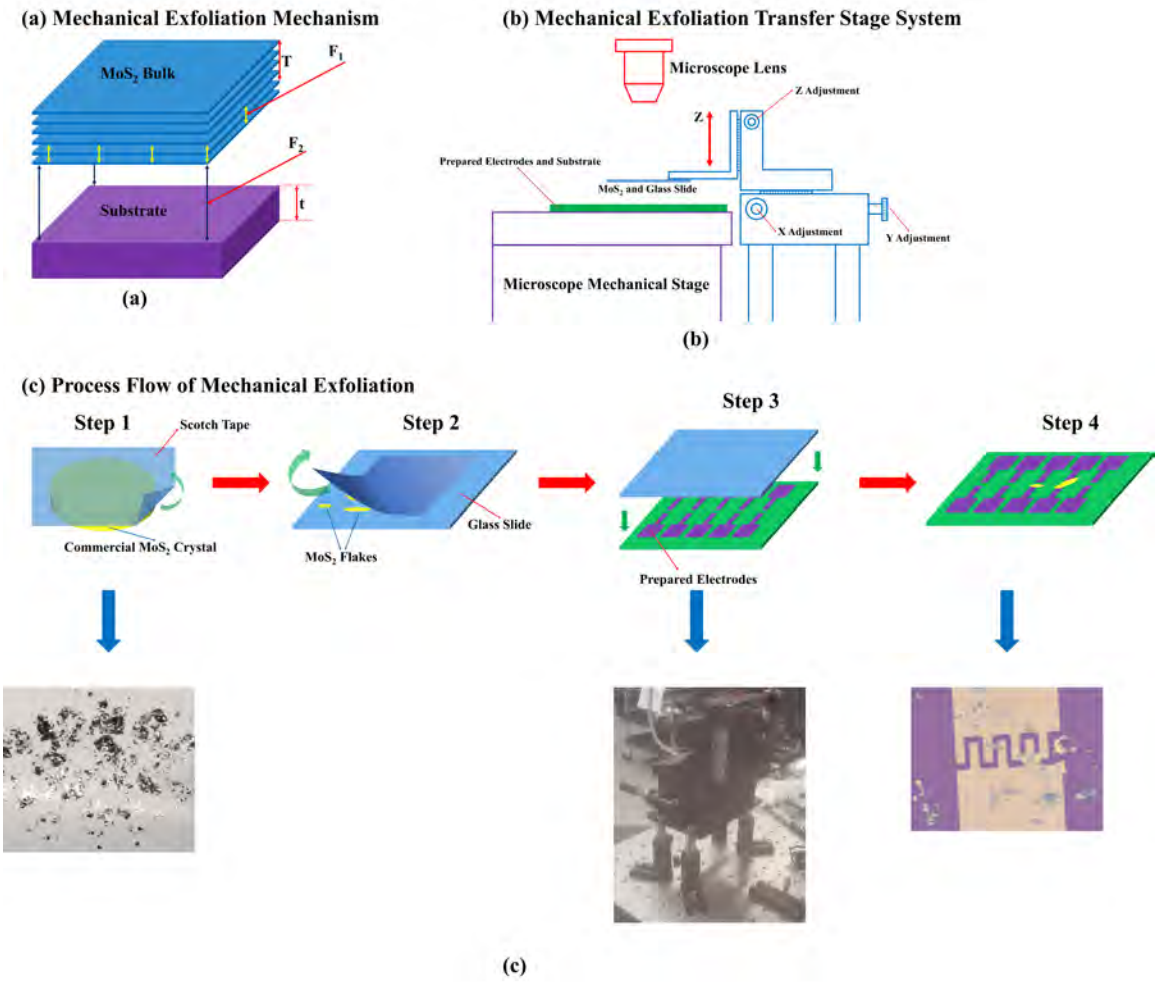

Figure 6.3: The Mechanism, Setup and the Process Flow of the Mechanical Exfoliation of MoS_2. (a) The mechanism of the mechanical exfoliation tech. In the figure, the blue layered structure denotes the MoS_2 bulk, the purple chunk represents the wafer. The Van der Waals force between outer layers of the MoS_2 is labelled as F_1. The adhesive force between the outer layers of MoS_2 and the wafer is labelled as F_2. The F_2 can be directly related to the adhesion energy. (b) The cross-section plot of the transfer system which consists of transfer stage, microscope and X, Y, Z adjustment. (c) The process flow of mechanical exfoliation of the MoS_2, which including: step 1, pre exfoliation of MoS_2; step 2, transfer MoS_2 flakes to the glass slide; step 3, calibration; and step 4, final exfoliation, transfer the MoS_2 flakes from the glass slide to the wafer and form contact. The figures below each step show the real look of the yields or setup.

of the glass slide surface and increase the amount of transferred MoS_2 flakes. After conducting the calibration in the step 3 by using the transfer stage, as shown in fig-6.3 (c), by pressing the glass slide onto the wafer for several seconds, the MoS_2 thin films will be transferred onto the Au electrodes. Under certain circumstance, multiple flakes connect the same electrode pads simultaneously. In this case, analyzing the I-V of the system would be impossible. Although these devices could still yield decent I-V data, but they won't be discussed in this work.

6.2.2 Thickness Characterization

Before the IV characterization, it is important to measure the thickness of the MoS_2 films in the devices. After the exfoliation, 3 prototype devices are chosen for the further analysis. Both Raman spectra analysis and atomic force microscopy (AFM) measurements are conducted to estimate the thickness of the MoS_2 channel.

Raman Spectroscopy

Raman spectra is considered as a powerful tool to determine the thickness of MoS_2 thin films with a few monolayers [146]. It is understood that two types of vibration modes exist in MoS_2: the intralayer mode and the interlayer mode. The intralayer mode refers to the vibrational modes inside layers, which is mainly related to the chemical composition of a layer and can be seen as the fingerprint of the material. In the Raman Spectra, the intralayer mode's peak frequency is slightly influenced by the MoS_2 thickness, while the interlayer mode's peak frequency is highly dependent on the number of layers. The measurement is conducted by using 532 nm laser. The two fingerprint peaks E^1_{2g} and A_{1g} are extracted from the spectra. As shown in fig-6.4, for device-1, the two peaks E^1_{2g} and A_{1g} are located at 382.74 cm^{-1} and 406.992 cm^{-1} respectively. For device-2, the E^1_{2g} peak is located at 382.57 cm^{-1}, while the A_{1g} peak is located at 408.278 cm^{-1}. The E^1_{2g} and A_{1g} peaks of the device-3 are located at 382.553 cm^{-1} and 408.33 cm^{-1}. According to the reported experimental data

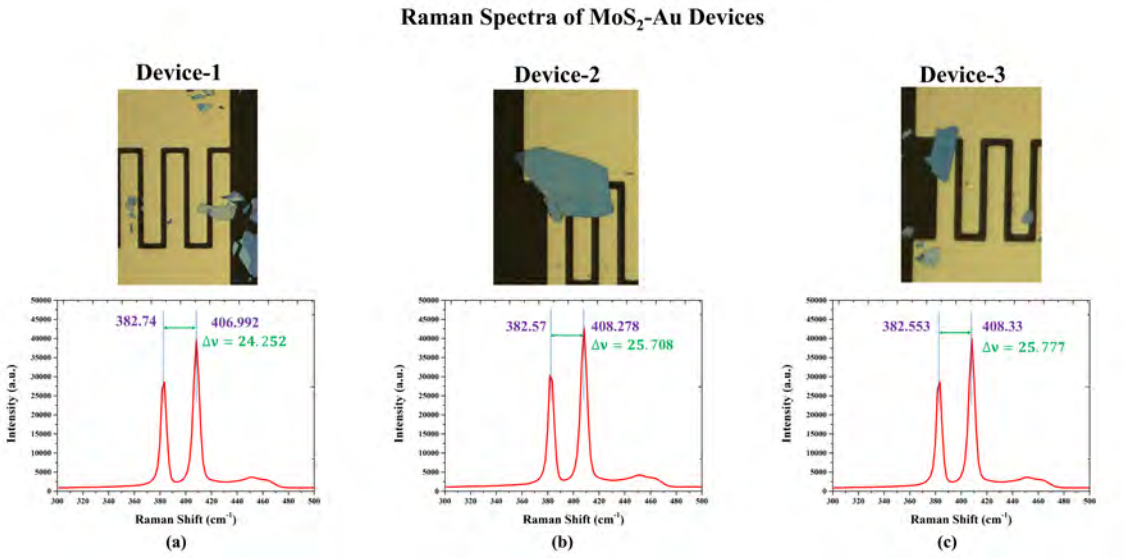

Figure 6.4: Exfoliated Devices and Raman Spectra. (a) The microscopy image and Raman spectra of devices-1. (b) The microscopy image and Raman spectra of devices-2. (c) The microscopy image and Raman spectra of devices-3.

[146], measured using 325 nm laser, as the thickness of MoS_2 increases, the E^1_{2g} mode originally at 384 cm^{-1} shifts to lower frequencies while A_{1g} mode shifts from 405 cm^{-1} to higher frequencies. As a result, the frequencies of the two peaks shift towards to the bulk value with increasing thickness, and the frequency difference varies in terms of the MoS_2 thickness. The frequency difference $\Delta\nu$ is 24.252 cm^{-1}, 25.708 cm^{-1} and 25.777 cm^{-1} for device-1, 2 and 3 respectively. Obviously, the MoS_2 film in device-2 and device-3 is bulk because their peak positions match the bulk value [146]. As for the device-1, according to the reported value [146], the MoS_2 thin film in the device is 4L.

Atomic Force Microscopy Measurement

The Raman spectra analysis shows that, the MoS_2 thin film in the device-1 is 4L. But for MoS_2, after 5 layers, the shift of the two fingerprint peaks converges. The Raman spectra alone could not help us figure out the thickness of the two bulk samples. To solve the issue, the AFM measurement has been applied to the device-2 and device-3. As shown by fig-6.5, the AFM tip scanning region is located at the contact region,

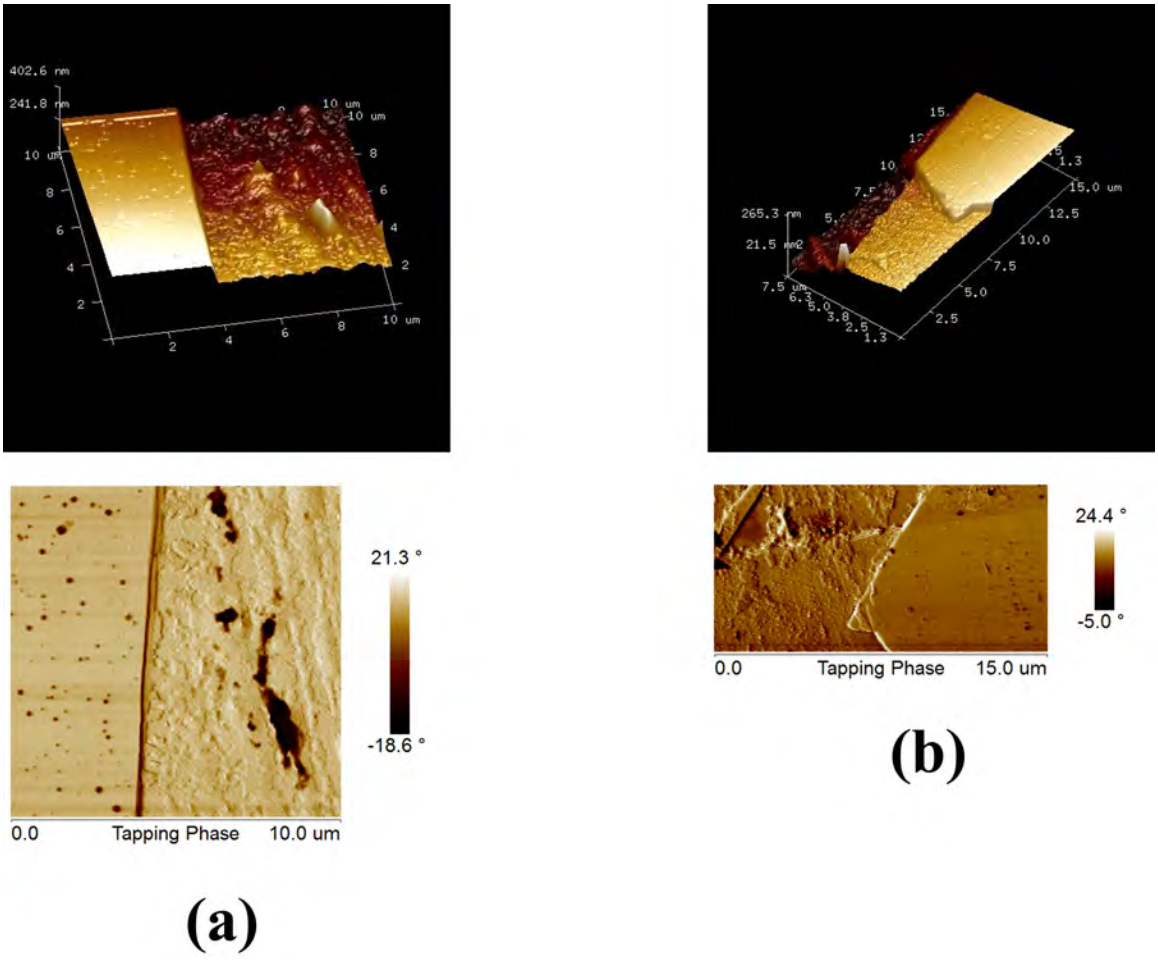

Figure 6.5: AFM Images for Device-2 and Device-3. (a) Three dimensional (3D) image and AFM topographic image of device-2. (b) 3D image and topographic image of device-3.

and the tapping mode is applied. Both the 3D images and the topographic images clearly show the border between the MoS_2 film and the gold contact. As shown by fig-6.5 (a) and (b), it is clearly, the exfoliated MoS_2 films have very smooth surfaces. Compared with MoS_2 flakes, Au contacts show much larger surface roughness. The measured MoS_2 thickness is 90 nm (146-147 layers) for device-2. The MoS_2 in the device-3 has a thickness of 55 nm (89-90 layers).

6.2.3 Current - Voltage Characterization

In order to explore the impact of the annealing, the I-V measurements have been conducted for all the three devices before and after the annealing process. All the I-V measurements are performed at the room temperature.

Mechanism of the Back - to - Back Schottky Diode Current - Voltage Relationship

Before presenting the I-V results, it is necessary to introduce the I-V mechanism of back-to-back Schottky diodes and the difficulty of extracting its I-V. As shown in fig-6.6 (a), for the normal single Schottky diode, when the metal forms a contact with the semiconductor, an energy barrier is formed at the interface of the two materials, which is called Schottky barrier. The value of the Schottky barrier height Φ_{SBH} of the interface determines the characteristics of the diode current transport. The fig-6.6 (a) shows the different working states of the normal n-type Schottky diode. In the plot, the applied bias is denoted as V_b and the E_{fi} is the Fermi level at the equilibrium. While a forward bias is applied to the n-type Schottky diode from left to the right (the direction from metal to the semiconductor), the quasi-Fermi level of the metal is lower than the E_{fi} by qV_b. As a result, the built-in potential at the interface is also reduced by qV_b. With the reduction of built-in potential, the forward current start to flow through the interface from the left side to the right side. As for reverse bias, when the reverse bias is applied form right to the left, the quasi-Fermi level of the metal is lifted by qV_b, and the built-in potential also increases by this value. The Schottky barrier at the metal-semiconductor interface now determine the charge injection from the metal to the semiconductor, and its barrier height Φ_{SBH} decides how large the reverse current is.

As shown in fig-6.6 (b), in the back-to-back Schottky diode, two Schottky contacts/interfaces with different Schottky barrier heights: Φ_{SBH1} and Φ_{SBH2} face to opposite directions. At forward and reverse bias, each of the two Schottky contacts contributes

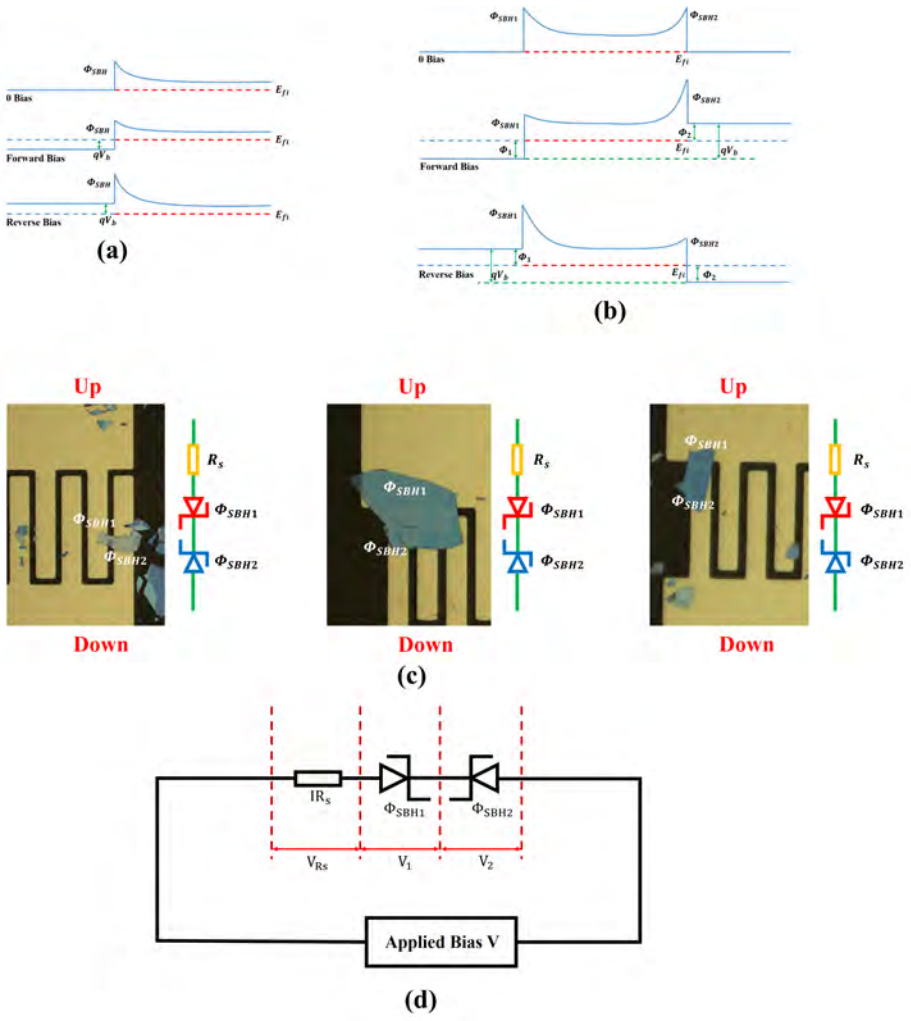

Figure 6.6: Schematic of the Working Mechanism of the Schottky Diode and Back-to-Back Schottky Diode. (a) The schematic of the working mechanism of normal single Schottky diode. (b) The schematic of the working principle of the back-to-back Schottky diode. (c) The definition of the applied bias direction and each Schottky contact interface in the back-to-back Schottky diode. In the figure, the top and the bottom of the photograph of each device is labelled by 'Up' and 'Down' to help define the polarity of the applied bias. The upper Schottky contact and its barrier height are denoted as schottky-contact-1 (in the main content) and Φ_{SBH1} respectively, while the schottky-contact-2 (in the main content) and Φ_{SBH2} are for the lower Schottky contact. If the applied bias drops from schottky-contact-1 to schottky-contact-2, the direction of the applied bias will be seen as 'from up to down'. (d) The equivalent circuit of the back-to-back Au-MoS_2-Au diodes. The voltage drop across the schottky-contact-1 is denoted as V_1, and the voltage drop across the schottky-contact-2 is denoted as V_2. The voltage drop due to the series resistance R_s is represented by V_{Rs}.

to the total voltage drop. In the forward-bias case, the bias direction is from the left to the right, and the quasi-Fermi level of the left-side metal bulk is Φ_1 below the E_{fi}, while the quasi-Fermi level of the right-side metal bulk is Φ_2 higher than the E_{fi}. Here the Φ_1 equals to qV_1 and the Φ_2 equals to qV_2, where V_1 is the voltage drop at the left-side Schottky contact and V_2 is the voltage drop at the right-side Schottky contact. Although the left-side contact's built-in potential is lowered, but the electron transport from the right side to the left side is still impeded by the Schottky barrier of the right-side contact. In this case, the Schottky barrier height of the right-side contact Φ_{SBH2} plays a predominant role in the I-V of the whole system. The reverse-bias case is quite similar to the forward-bias case, where the charge injection is mainly blocked by the left-side interface. In the reverse-bias case, the Schottky barrier height of the left-side Schottky contact Φ_{SBH1} dominates the reverse I-V.

For the convenience of the analysis, each of the interfaces in the fabricated devices is labelled in terms of its relative position. As shown in fig-6.6 (c), all the three fabricated Au-Φ_{SBH2} is labelled with 'Up' and 'Down'. The polarity of the applied bias will be defined using these labels. As for the back-to-back Schottky diodes, the upper Schottky contact of each device is defined as Schottky-contact-1 and its barrier height is denoted as Φ_{SBH1}. The lower Schottky contact is referred to as Schottky-contact-1, and its barrier height is labelled as Φ_{SBH2}.

The fig-6.6 (d) shows the schematic figure of the equivalent circuit of the back-to-back Schottky diodes, which will be adopted in the analysis part. The voltage drop due to the schottky-contact-1, schottky-contact-2 and series resistance are denoted as V_1, V_2 and V_{Rs} respectively. For applied bias V, the relationship between V and the voltage drops could be given:

$$V = V_1 + V_2 + V_{Rs} \tag{6.3}$$

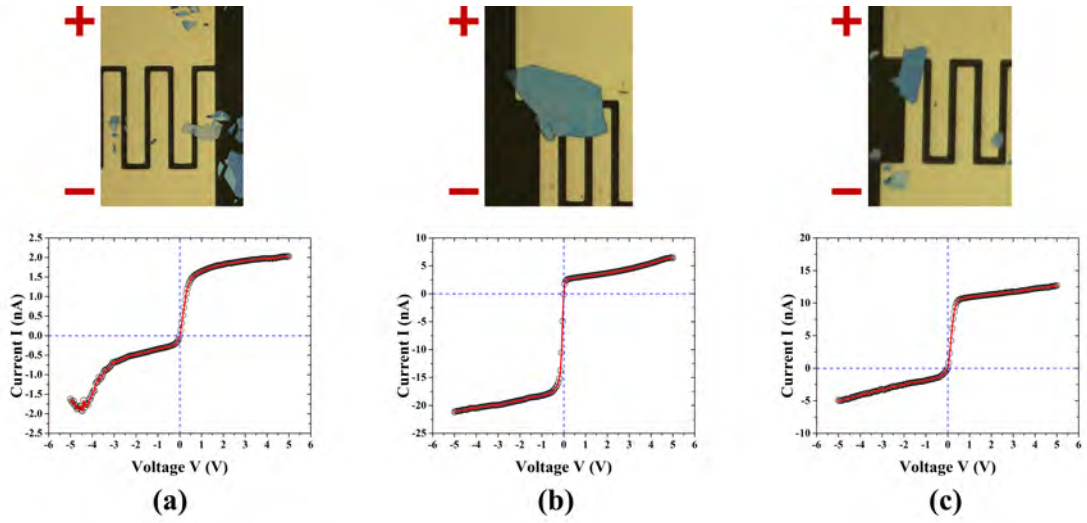

Figure 6.7: I-V Measurement Before Annealing. (a) The I-V of device-1. (b) The I-V of device-2. (c) The I-V of device-3. The applied bias direction is also labelled in the figure, which is from 'up' to 'down' (the forward bias direction). These measurements are conducted without the annealing process.

Current - Voltage Characterization before Annealing

The I-V measured before the annealing process is shown by the fig-6.7. The applied bias ranges from -5 V to 5 V. The positive forward bias direction is from 'up' to 'down'. The fig-6.7 (a)-(c) shows that, all the devices are not ON when the bias is applied. For device-1, under the reverse bias (bias direction is from 'down' to 'up'), the largest current is only -1.6205 nA. While under the forward bias, the largest current of device-1 is 2.031 nA. For device-2, the largest reverse and forward currents are -21.169 nA and 6.450 nA respectively. For device-3, the largest reverse current is -4.895 nA and the largest forward current is 12.717 nA. For all the three devices, without annealing, the current flow is only in nA scale, indicating large barrier heights at both the left-side and right-side interfaces of each device. This issue is probably generated by the poor interface bonding between the Au and exfoliated MoS_2.

Current - Voltage Characterization after Annealing

To improve the interface between metal-MoS_2, the annealing process has been performed. The Au-MoS_2 devices are annealed at 473K temperature for 1 hour in 1×10^{-7}

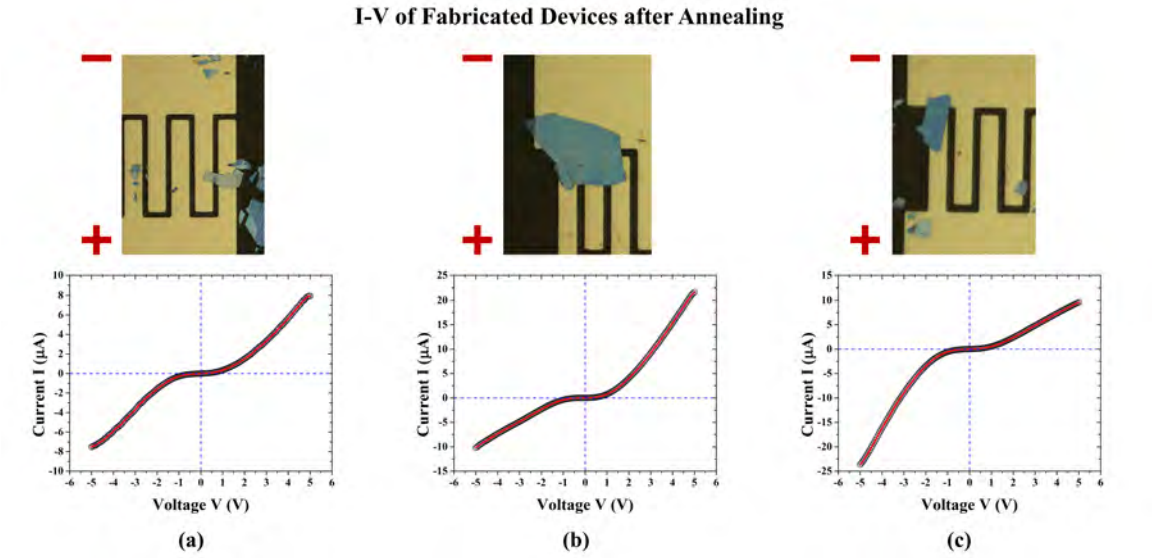

Figure 6.8: I-V Measurement after Annealing. (a) The I-V of device-1. (b) The I-V of device-2. (c) The I-V of device-3. The applied bias direction is also labelled in the figure, which is from 'down' to 'up' (the forward bias direction). These measurements are conducted after the annealing process.

Torr vacuum to prevent oxides.

The I-V measured after the annealing process is shown in the fig-6.8. Differing from the I-V measurements before the annealing process, the forward direction of the applied bias is from 'down' to 'up'. As shown in fig-6.8 (a), for the device-1, the largest reverse current is -7.5276 μA, while the largest forward current is 7.9474 μA. For the device-2, the largest reverse current is -10.2142 μA and the largest forward current is 21.7032 μA, as shown in fig-6.8 (b). The fig-6.8 (c) shows that, for the device-3, the largest reverse and forward currents are -23.6466 μA and 9.6032 μA. It is clear that, the annealing process greatly improves the performance of the devices. The working current of each device is increased by more than 1000 times. Since the MoS_2 thin film is exfoliated onto the prepared Au contact, the interfacial energy barrier could be very large due to the weak Van der Waals bonding between Au and MoS_2. It demonstrates that, the annealing process helps reduce the height of this energy barrier and improve the bonding condition between Au and MoS_2 surface.

6.3 Current - Voltage Analysis of Back - to - Back Gold - Molybdenum Disulfide Schottky Diodes

6.3.1 Junction Interface Area

The improvement of the device performance makes the systematic I-V analysis possible. Before analyzing the I-V, it is necessary to determine the dimensional parameters of the Au-MoS_2 back-to-back Schottky diodes. By using the pixel map technique, the dimensional parameters of the devices are extracted by the microscopy. The measured limb length and the gap width between the limbs of the devices are listed in the table-6.1. For the device-1, the limb length is 9.42 μm and the gap width is 2.58 μm. For the device-2, the limb length is 9.27 μm and the gap width is 3.73 μm. As for device-3, the limb length is 9.29 μm and the gap width is 3.71 μm. Compared with designed limb length, the extracted limb length of the three devices show an error ranging from 5.8% to 7.3%. The extracted gap width shows an error ranging from 23.7% to 29%. Considering the uniformity of the difference between the experimental dimensional parameters and the designed dimensional parameters, the dimensional parameter error is mainly due to the resolution issue of the mask aligner. The pictures obtained from the microscope are enlarged by graphic editing software (such as Photoshop), and the length each pixel points account has also been calculated. The limb length of device-1, device-2 and device-3 occupies 39, 38 and 38 pixel points respectively, which indicates the side length of the pixel square is 0.24 μm. Then the area of each pixel square is also given as 0.0576 μm^2.

As mentioned before, there are two interfaces exist for 2D Schottky diodes: interface A and interface B. In this case, the interface A is considered as the overlapping region between Au and MoS_2. The interface B is the cross-section region located between the Au-MoS_2 overlapping region and the channel region. The area of interface B could be given by the side length of the overlapping region times the thin film thickness. For the Schottky-contact-1 and Schottky-contact-2 of each of the devices,

Table 6.1: The Measured Limb Width and Gap Distance of the Devices after the Deposition

	Limb Width (μm)	Error	Gap Distance (μm)	Error
Device-1	9.42	5.8%	2.58	29%
Device-2	9.27	7.3%	3.73	24.3%
Device-3	9.29	7.1%	3.71	23.7%

Table 6.2: The Number of Pixel Points for the Overlapping Region and Edge of Each Interface. In the table, the SC1 denotes Schottky-contact-1, and SC2 denotes the Schottky-contact-2.

	Overlapping Area	Edge Length
Device-1 SC1	418	21×1
Device-1 SC2	1144	26×1
Device-2 SC1	11813	267×1
Device-2 SC2	3719	171×1
Device-3 SC1	1040	48×1
Device-3 SC2	2263	105×1

Table 6.3: The Area of the Interface A and Interface B of Each Schottky Contact. In the table, the SC1 denotes Schottky-contact-1, and SC2 denotes the Schottky-contact-2.

	Interface A Area (μm^2)	Interface B Area (μm^2)
Device-1 SC1	24.98	0.0124
Device-1 SC2	68.38	0.0154
Device-2 SC1	706.06	5.77
Device-2 SC2	222.28	3.69
Device-3 SC1	62.16	0.633
Device-3 SC2	135.26	1.386

the numbers of pixel points occupied by the Au-MoS_2 overlapping region and its edges are listed in table-6.2. As shown in table-6.2, for device-1, the overlapping region of the Schottky-contact-1 occupies 418 pixel squares, and its area is calculated as 24.08 μm^2. The edge of the overlapping area of the Schottky-contact-1 occupies 21×1 pixel squares, and the side length of the edge is 5.04 μm. Since the Raman spectra demonstrates that the thickness of the MoS_2 in device-1 is 4 monolayers (2.48 nm), for device-1, the obtained area of the interface B in the Schottky-contact-1 is 0.0125 μm^2, while the area of the interface A is 24.08 μm^2. The dimensional parameters and the areas of the other interfaces are listed in table-6.2 and table-6.3.

6.3.2 Thermionic - Emission Model

Normally, people use two mathematical models to describe the I-V features of the metal-MoS_2 Schottky contacts. One model is the well-defined thermionic-emission model which is based on thermionic-emission theory [31]. The other model is the series-resistance correction (SR) model, which adds a correction of the series-resistance voltage drop to the TE model [71].

The TE model is derived by assuming that the barrier height is much higher than the value of kT, where the k is the Boltzmann constant. At the same time, the existence of the net current flow does not affect the equilibrium at the interface [31]. Considering these assumptions, the TE model is applicable when the applied bias is small and the measurement temperature is not high. The I-V relationship based on the TE model could be given by the equation:

$$I = A^* A T^2 \exp\left(-\frac{q\Phi_B}{kT}\right) \times \left[\exp\left(\frac{qV}{kT}\right) - 1\right] \tag{6.4}$$

Where the Φ_B (eV) is the Schottky barrier height, V (V) is the applied bias, and the A^* ($A/(m^2 \cdot K^2)$) is the Richardson constant. The value of the Richardson constant could be given by the equation:

$$A^* = \frac{4\pi q m^* k^2}{h^3} \tag{6.5}$$

Where is h is the Planck's constant, k is the Boltzmann constant, and the m^* is the effective mass of the electrons in the MoS_2. For multilayer and bulk MoS_2, the Richardson constant could be taken as 54 $A/(m^2 \cdot K^2)$. The equation given is the ideal I-V equation based on TE model. For normal cases, to describe the deviation of the I-V relationship from the ideal I-V relationship, an ideality factor n is added to the ideal I-V equation:

$$I = A^* A T^2 \exp\left(-\frac{q\Phi_B}{kT}\right) \times \left[\exp\left(\frac{qV}{nkT}\right) - 1\right] \tag{6.6}$$

Generally, n ranges from 1 to 2. While there is no tunneling current or depletion-layer recombination, the n will be close to unity.

To extract the ideality factor, the I could be written as:

$$I = I_s \times \left[\exp\left(\frac{qV}{nkT}\right) - 1\right] \tag{6.7}$$

Where the I_s is the saturation current and it is defined by equation:

$$I_s = A^* A T^2 \exp\left(-\frac{q\Phi_B}{kT}\right) \tag{6.8}$$

By taking the nature logarithm (Ln) on the both sides, the ideality factor n could be given by the slope of the Ln(I)-V curve. The Schottky barrier height Φ_B of the device needs to be extracted from the I_s-T relationship. However, the MoS_2 could be oxidized easily under heating. In our case, the Φ_B could only be extracted from the linear part of the Ln(I)-V curves.

The Ln(I)-V curve of the device-1 is shown by fig-6.9. At the forward bias (from 'down' to 'up'), the Schottky-contact-2 of the device-1 is considered as the contact under the measurement while applying the TE model. At the reverse bias (from 'up' to 'down'), the Schottky-contact-1 of the device-1 is considered as measured contact according to the TE model. The fig-6.9 (a) and (d) shows that, the Ln(I)-V curve of the device-1 is not linear, which is diverse from the TE model. The linear region (which is more linear compared with other regions) of the curve is used to extract

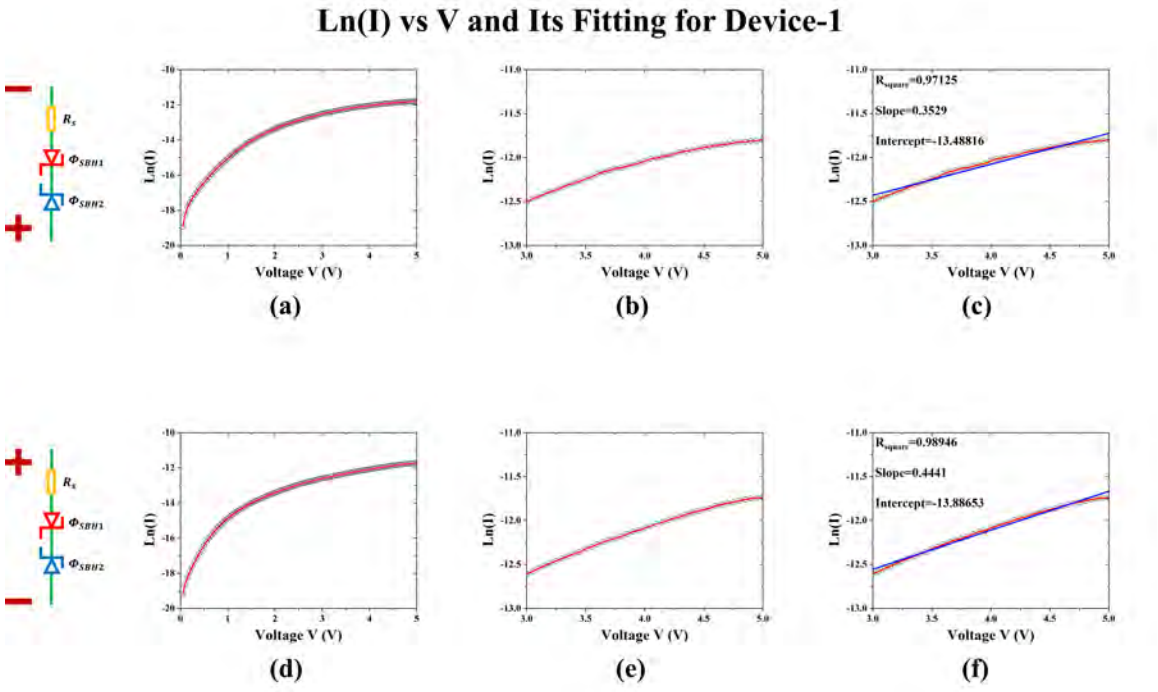

Figure 6.9: The Ln(I)-V Curves of the Device-1. (a)-(c), the Ln(I)-V curve under the forward bias, in which case the TE and SR model considers the Schottky-contact-2 is under measuring. (a) shows the Ln(I) vs V from 0V to 5.0 V, while (b) is the zoom-in figure of (a), ranging from 3.0 V to 5.0 V. (c) is the linear fitting of the Ln(I)-V curve, and the fitting range is 3.0 V to 5.0 V. (d)-(f), the Ln(I)-V curve under the reverse bias, in which case the TE and SR model considers the Schottky-contact-1 is under measuring. (d) shows the Ln(I) vs V from 0V to 5.0V, while (e) is the zoom-in figure of (d), ranging from 3.0V to 5.0 V. (f) is the linear fitting of the Ln(I)-V curve, and the fitting range is 3.0 V to 5.0 V.

the ideality factor. For both the Schottky-contact-1 and Schottky-contact-2 in the devices, the data points from 3.0 V to 5.0 V are picked for the fitting. The fitting results are shown by fig-6.9 (c) and (f). For the Schottky-contact-2, as shown in fig-6.9 (c), the slope of the Ln(I)-V is 0.3529, yielding an ideality factor of 13.573. The y-intercept of the Ln(I)-V is -13.48816, and the extracted I_s is 1.387 μA. For Schottky-contact-1, the slope is 0.4441 and the intercept is -13.88653. The extracted ideality factor n and saturation current I_s is 17.081 and 0.931 μA. The goodness of the fitting is given by the R_{square}. Normally, the closer the R_{square} is to 1, the better the fitting is. The calculated R_{square} of the forward and reverse I-V is 0.97125 and 0.98946 respectively, which is acceptable.

The ideality factor and saturation current of the device-2 and device-3 have also been extracted by TE model, as shown in fig-6.10 and fig-6.11. The fig-6.10 (c) shows that, the slope and the intercept of the curve after fitting are 0.42987 and -12.83102. The extracted ideality factor n and saturation current I_s of the Schottky-contact-2 for the device-2 are 16.533 and 2.676 μA. The R_{square} of the fitting is 0.99034. For the Schottky-contact-1, as shown by fig-6.10 (f), the extracted ideality factor is 13.991 since the fitting slope is 0.36376. The intercept is -13.2925, for that the given I_s is 1.687 μA. The R_{square} of the fitting is 0.99664. As shown in fig-6.11 (c) and (f), the given n and I_s is 13.012 and 1.841 μA for the Schottky-contact-2 in the device-3, and the R_{square} of the fitting is 0.9883. For the Schottky-contact-1 in the device-3, the n, I_s and R_{square} are 18.773, 2.219 μA and 0.98704 respectively.

The extracted ideality factors and saturation currents of each interface are listed in table-6.4. From the table we can see that, the given ideality factors are much larger than 2, which may indicates a large resistance of the devices in this case. To get optimized results, the SR model is brought up based on the TE model.

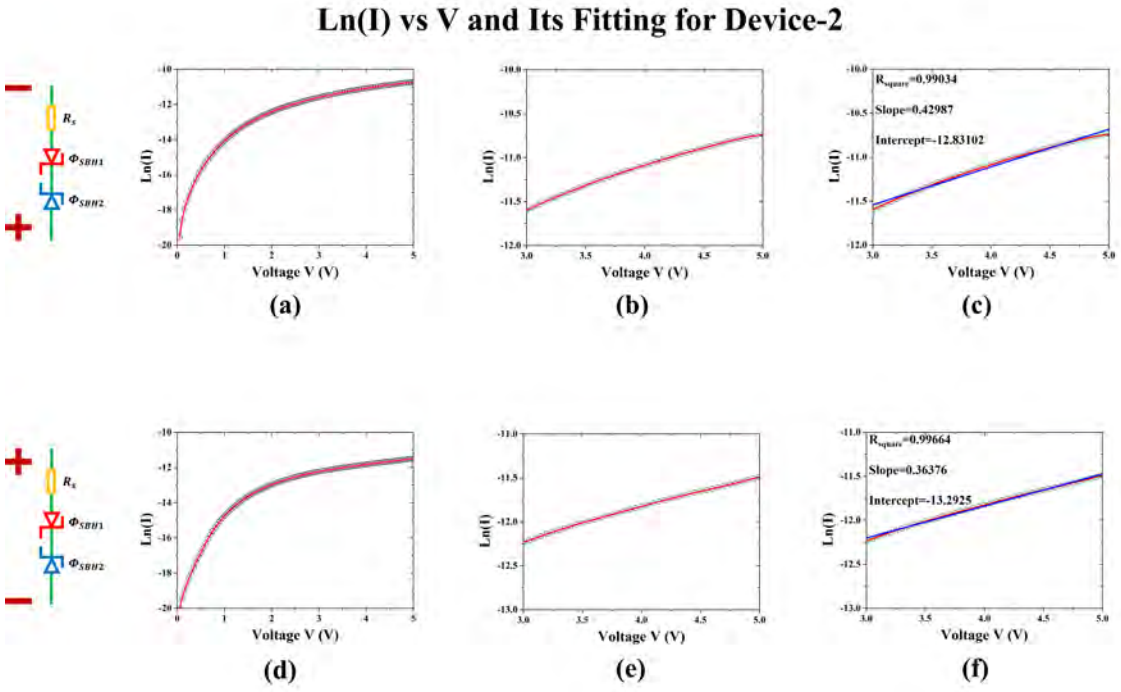

Figure 6.10: The Ln(I)-V Curves of the Device-2. (a)-(c), the Ln (I)-V curve under the forward bias, in which case the TE and SR model considers the Schottky-contact-2 is under measuring. (a) shows the Ln (I) vs V from 0 V to 5.0 V, while (b) is the zoom-in figure of (a), ranging from 3.0 V to 5.0 V. (c) is the linear fitting of the Ln (I)-V curve, and the fitting range is 3.0 V to 5.0 V. (d)-(f), the Ln(I)-V curve under the reverse bias, in which case the TE and SR model considers the Schottky-contact-1 is under measuring. (d) shows the Ln(I) vs V from 0 V to 5.0 V, while (e) is the zoom-in figure of (d), ranging from 3.0 V to 5.0 V. (f) is the linear fitting of the Ln (I)-V curve, and the fitting range is 3.0 V to 5.0 V.

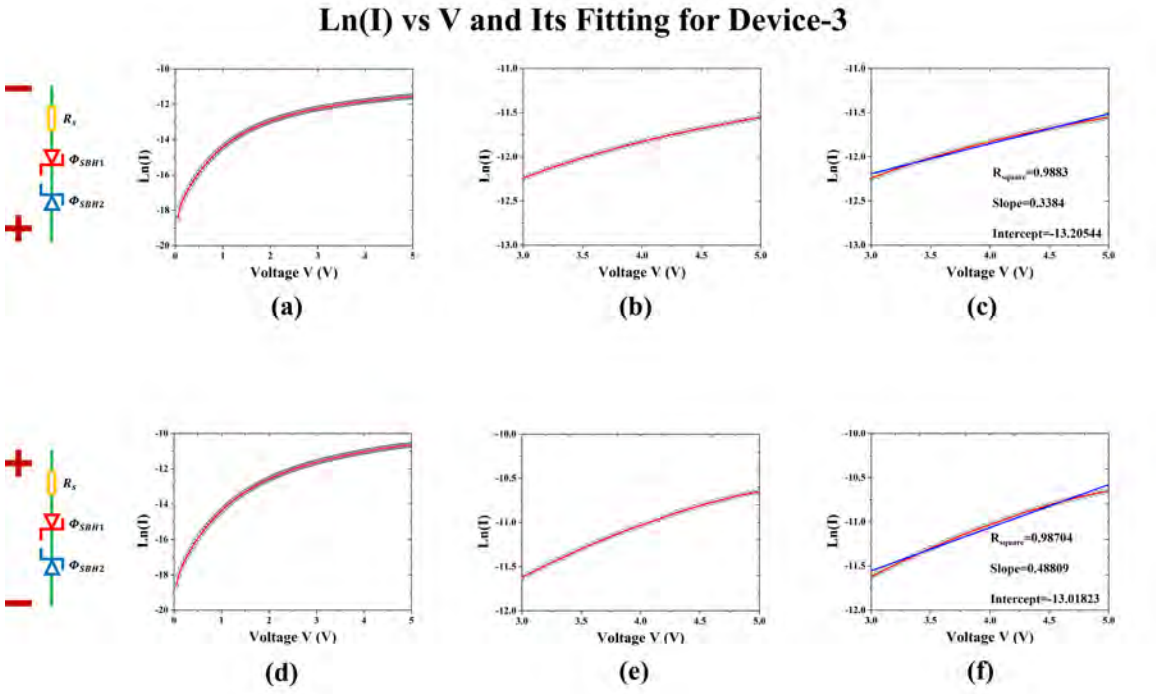

Figure 6.11: The Ln (I)-V Curves of the Device-3. (a)-(c), the Ln (I)-V curve under the forward bias, in which case the TE and SR model considers the Schottky-contact-2 is under measuring. (a) shows the Ln (I) vs V from 0 V to 5.0 V, while (b) is the zoom-in figure of (a), ranging from 3.0 V to 5.0 V. (c) is the linear fitting of the Ln (I)-V curve, and the fitting range is 3.0 V to 5.0 V. (d)-(f), the Ln (I)-V curve under the reverse bias, in which case the TE and SR model considers the Schottky-contact-1 is under measuring. (d) shows the Ln (I) vs V from 0 V to 5.0 V, while (e) is the zoom-in figure of (d), ranging from 3.0 V to 5.0 V. (f) is the linear fitting of the Ln(I)-V curve, and the fitting range is 3.0 V to 5.0 V.

Table 6.4: The Ideality Factor and Saturation Current Extracted by Ideal TE Model for Each Schottky Contact. In the table, the SC1 denotes Schottky-contact-1, and SC2 denotes the Schottky-contact-2. The n is the ideality factor and the I_s is the saturation current.

	n	I_s (μA)	R_{square}
Device-1 SC1	17.081	0.931	0.98946
Device-1 SC2	13.573	1.387	0.97125
Device-2 SC1	13.991	1.687	0.99664
Device-2 SC2	16.533	2.676	0.99034
Device-3 SC1	18.773	2.219	0.98704
Device-3 SC2	13.012	1.841	0.98830

6.3.3 Series - Resistance Model

The only difference between the SR model and TE model is that the SR model considers the voltage drop contributed by the series resistance and replaces the applied bias V in the TE model by V-IR_s. Now the I-V equation is written as:

$$I = I_s \times \left[\exp\left(\frac{q\,(V - IR_s)}{nkT}\right) - 1\right] \tag{6.9}$$

Where the R_s (Ω) is the series resistance of the system. To obtain the ideality factor, the nature logarithm is taken on the both sides of the equation and it could be written as:

$$Ln(I) - Ln\,(I_s) = \frac{q\,(V - IR_s)}{nkT} \tag{6.10}$$

By moving all the terms except applied voltage V to the left side, the equation 6.10 could be written as:

$$\frac{nkT}{q}Ln(I) - \frac{nkT}{q}\,Ln\,(I_s) + IR_s = V \tag{6.11}$$

By taking a derivative with respect to Ln(I) on the both sides of the equation 6.11, it yields:

$$\frac{nkT}{q} + \frac{dI}{dLn(I)}R_s = \frac{dV}{dLn(I)} \tag{6.12}$$

Since:

$$\mathrm{dLn(I)} = \frac{1}{\mathrm{I}}\mathrm{dI} \tag{6.13}$$

Finally, the equation 6.12 could be written as:

$$\frac{\mathrm{nkT}}{\mathrm{q}} + \mathrm{IR_s} = \frac{\mathrm{dV}}{\mathrm{dLn(I)}} \tag{6.14}$$

Here the series resistance could be extracted by calculating the slop of (dV)/d(Ln(I)) vs I, and the ideality factor n could be extracted by the y-intercept.

The fig-6.12 shows the V vs Ln(I) and (dV)/d(Ln(I)) vs I curves of the Schottky-contact-1 and the Schottky-contact-2 in the device-1. The fig-6.12 (b) and (f) shows that, the (dV)/d(Ln(I)) vs I curve of the device-1 is not linear at large-current region (which refers to the high-bias region). For this reason, the investigation and fitting is only conducted at small-current region (which refers to the low-bias region). As shown in fig-6.12 (c) and (d), the current region ranging from 0.0 A to 2×10^{-6} A is considered as linear, which is adopted for the fitting of (dV)/d(Ln(I)) vs I curve. The slope of the fitting is 391679, giving a series resistance of 391679Ω, and the intercept of the curve is 0.33306, indicating an ideality factor of 12.81. The $\mathrm{R_{square}}$ is 0.98917 for the fitting. For the Schottky-contact-2 in the device-1, as shown by fig-6.12 (h), the slope of the fitting curve is 470336, and the intercept is 0.22844, with a $\mathrm{R_{square}}$ of 0.97895. The extracted ideality factor and series resistance are 8.786 and 470336Ω respectively.

The ideality factor n and series resistance $\mathrm{R_s}$ of the other contacts have been extracted. As shown in fig-6.13 (b) to (d), for the Schottky-contact-1 in the device-2, the linear region of the (dV)/d(Ln(I)) vs I Plot ranges from 0.0 A to 1.25×10^{-5} A. The extension of the linear region indicates that the Schottky-contact-1 in the device-2 has better interfacial condition. The calculated slope and intercept are 135858 and 0.28144 for the Schottky-contact-1. The extracted n is 10.825 and the $\mathrm{R_s}$ is 135858Ω. The $\mathrm{R_{square}}$ of the fitting is 0.99656. As for the Schottky-contact-2, the fitting region is from 0.0 A to 5×10^{-6} A. The extracted ideality factor n is 8.786 and the $\mathrm{R_s}$ is

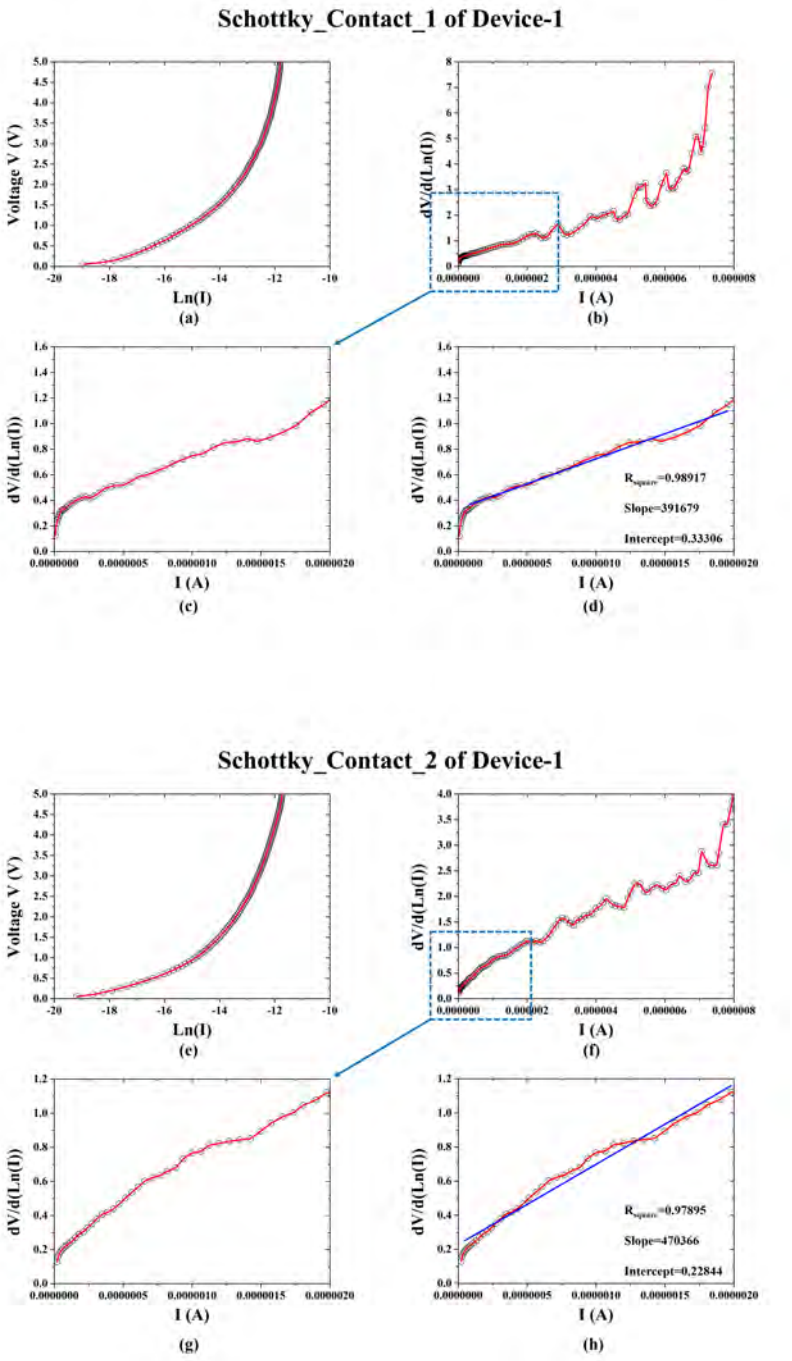

Figure 6.12: The V vs Ln(I) and (dV)/d(Ln(I)) vs I Plots of the Device-1. (a) the V vs Ln(I) plot of the Schottky-contact-1 of the device-1. (b) the (dV)/d(Ln(I)) vs I plot of the Schottky-contact-1. (c) the zoom-in plot of the (dV)/d(Ln(I)) vs I plot of the Schottky-contact-1, the range of I is from 0.0 A to 2×10^{-6} A. (d) the fitting of (dV)/d(Ln(I)) vs I zoom-in plot of the Schottky-contact-1. (e) the V vs Ln(I) plot of the Schottky-contact-2 of the device-1. (f) the (dV)/d(Ln(I)) vs I plot of the Schottky-contact-2. (g) the zoom-in plot of the (dV)/d(Ln(I)) vs I plot of the Schottky-contact-2, the range of I is from 0.0 A to 2×10^{-6} A. (h) the fitting of (dV)/d(Ln(I)) vs I zoom-in plot of the Schottky-contact-2.

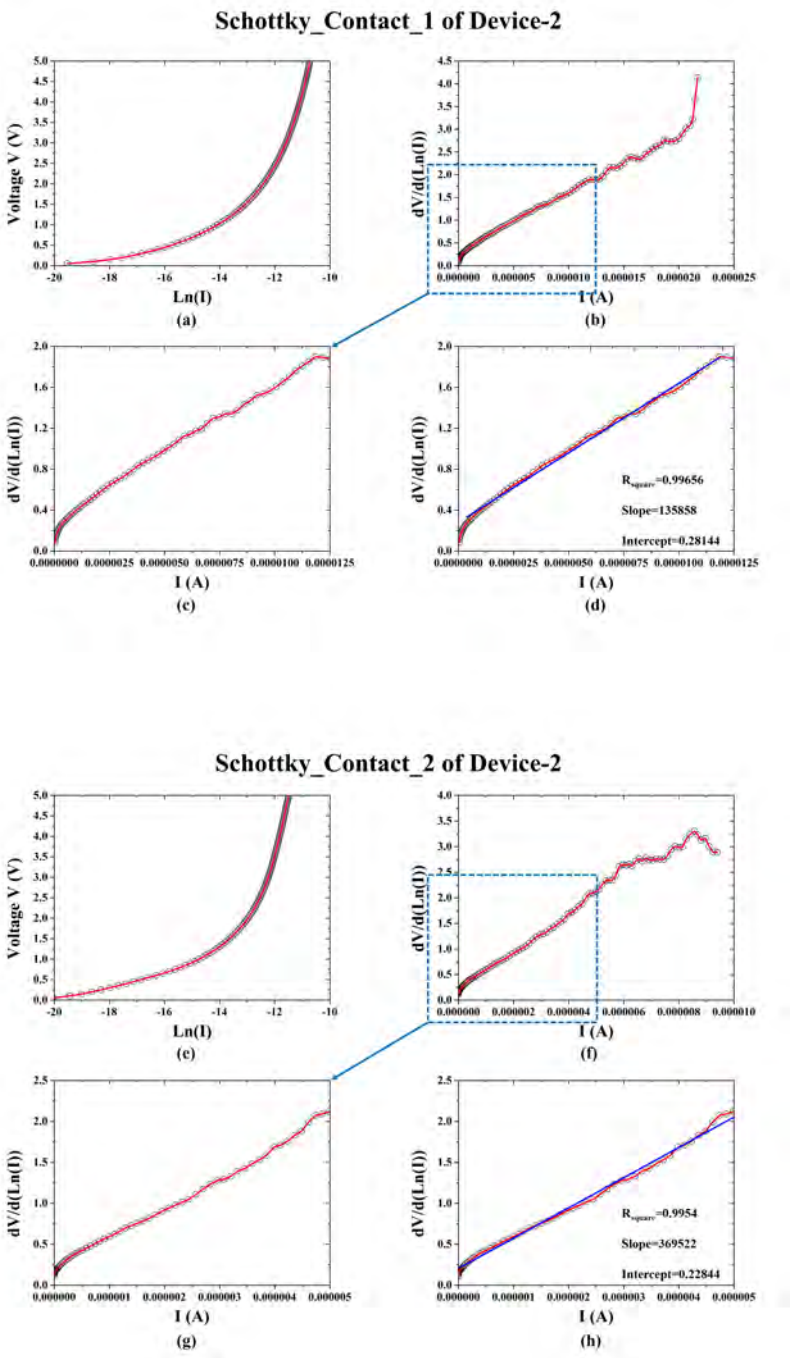

Figure 6.13: The V vs Ln(I) and (dV)/d(Ln(I)) vs I Plots of the Device-2. (a) the V vs Ln(I) plot of the Schottky-contact-1 of the device-2. (b) the (dV)/d(Ln(I)) vs I plot of the Schottky-contact-1. (c) the zoom-in plot of the (dV)/d(Ln(I)) vs I plot of the Schottky-contact-1, the range of I is from 0.0 A to 1.25×10^{-5} A. (d) the fitting of (dV)/d(Ln(I)) vs I zoom-in plot of the Schottky-contact-1. (e) the V vs Ln(I) plot of the Schottky-contact-2 of the device-2. (f) the (dV)/d(Ln(I)) vs I plot of the Schottky-contact-2. (g) the zoom-in plot of the (dV)/d(Ln(I)) vs I plot of the Schottky-contact-2, the range of I is from 0.0A to 5×10^{-6}A. (h) the fitting of (dV)/d(Ln(I)) vs I zoom-in plot of the Schottky-contact-2.

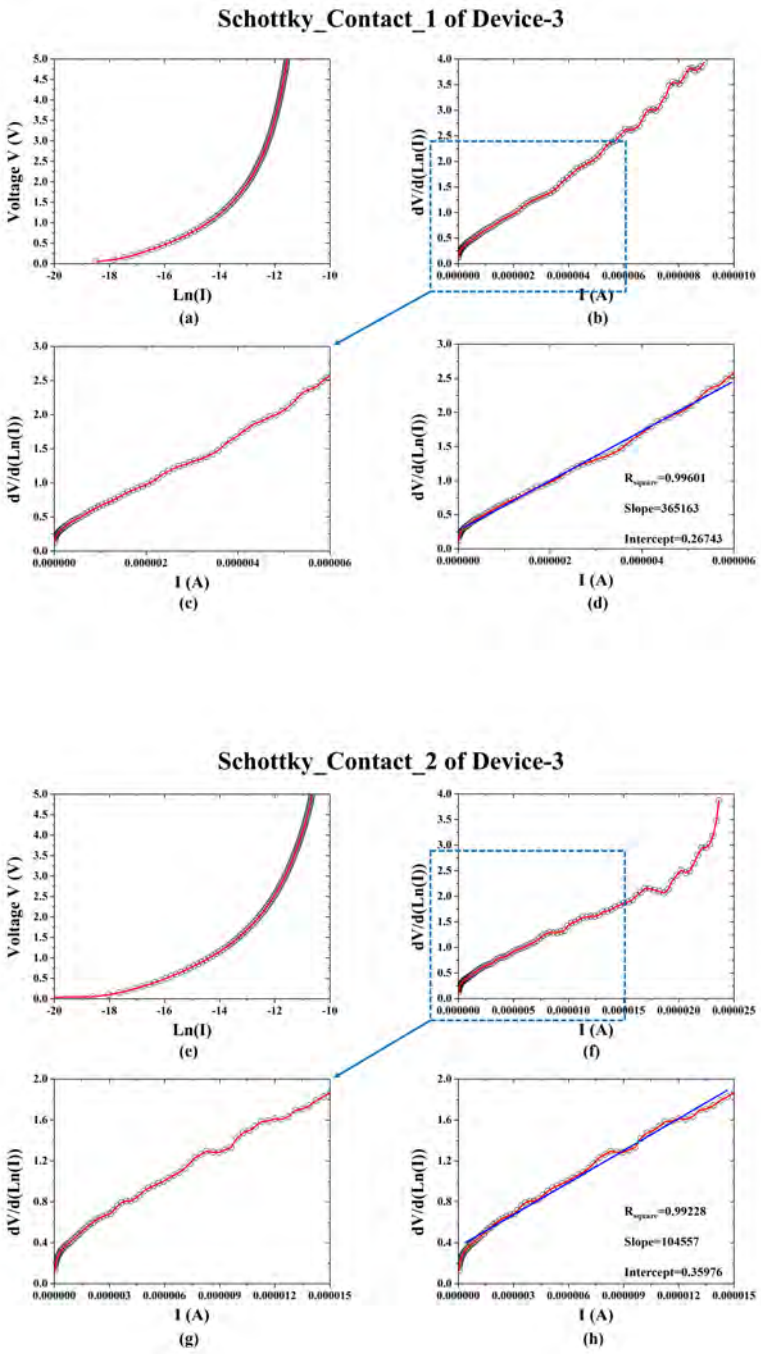

Figure 6.14: The V vs Ln(I) and (dV)/d(Ln(I)) vs I Plots of the Device-3. (a) the V vs Ln(I) plot of the Schottky-contact-1 of the device-3. (b) the (dV)/d(Ln(I)) vs I plot of the Schottky-contact-1. (c) the zoom-in plot of the (dV)/d(Ln(I)) vs I plot of the Schottky-contact-1, the range of I is from 0.0 A to 6×10^{-6} A. (d) the fitting of (dV)/d(Ln(I)) vs I zoom-in plot of the Schottky-contact-1. (e) the V vs Ln(I) plot of the Schottky-contact-2 of the device-3. (f) the (dV)/d(Ln(I)) vs I plot of the Schottky-contact-2. (g) the zoom-in plot of the (dV)/d(Ln(I)) vs I plot of the Schottky-contact-2, the range of I is from 0.0A to 1.5×10^{-5} A. (h) the fitting of (dV)/d(Ln(I)) vs I zoom-in plot of the Schottky-contact-2.

Table 6.5: The Ideality Factor and Series Resistance Extracted by SR Model for Each Schottky Contact. In the table, the SC1 denotes Schottky-contact-1, and SC2 denotes the Schottky-contact-2. The n is the ideality factor and the R_s is the saturation current.

	n	R_s (Ω)	R_{square}
Device-1 SC1	12.810	391679	0.98917
Device-1 SC2	8.786	470336	0.97895
Device-2 SC1	10.825	135858	0.99656
Device-2 SC2	8.786	369522	0.99540
Device-3 SC1	10.286	365163	0.99601
Device-3 SC2	13.837	104457	0.99228

369522Ω, as shown by fig-6.13 (h). The R_{square} of the fitting is 0.9954. For the Schottky-contact-1 in the device-3, as shown in fig-6.14 (b) and (c), the linear region ranges from 0.0 A to 6×10^{-6} A. The fig-6.14 (d) shows that, the calculated n of the Schottky-contact-1 is 10.286 and the R_s is 365163Ω. The R_{square} of the fitting is 0.99601. For the Schottky-contact-2 inf the device-3, as shown in fig-6.14 (f) and (g), the linear region for fitting is set as 0.0 A to 1.5×10^{-5} A. The fig-6.14 (h) shows that, the extracted n, R_s and the R_{square} is 13.837, 104557Ω and 0.99228 for the Schottky-contact-2 of the device-3.

The values of the ideality factor n and series resistance R_s extracted by SR model are listed in table-6.5. The extracted R_s and n are still much larger than 2, indicating that the SR model still needs further corrections. Besides, both the TE model and SR model could not be used to extract the Schottky barrier height of the Au-MoS_2 contacts directly. To extract the barrier height of the devices by using TE and SR model, a Richardson constant against inverse temperature plot is required. However, heating the Au-MoS_2 devices up in the air will cause oxidization of the devices. There is no convenient solution to this issue.

What's more, the TE and SR model could not be applied on the Au-MoS_2 back-to-

back Schottky diodes directly to analyze the forward-bias I-V features since there will always be a diode under the reverse bias while the other diode is at the forward bias, no matter the direction of the applied bias. By using the TE and SR model to extract the parameters from the I-V, the forward-bias I-V features are under investigation, while the diode which is at the forward bias is considered determining the I-V. This probably works for the Schottky contacts with very small Schottky barrier height. However, while the contacts in the back-to-back Schottky diode system have sufficiently large Schottky barrier height, the methods mentioned in the previous part did not work. Because in this case, the contact under the reverse bias will predominate in the I-V mechanism of the system.

To solve the existing issues mentioned above, we propose a novel method to extract the Schottky barrier height of the Au-MoS_2 back-to-back Schottky diodes. The detailed description and explanation of the mechanism of this model will be discussed systematically in the following parts.

6.3.4 Image - Force Model

To model the I-V of the Schottky contact under the reverse bias in the back-to-back system, we apply the image force correction to describe the reverse current of the diode. In this case, the I-V relationship with the image force correction could be written as:

$$\mathrm{I} = \mathrm{A}^{*}\mathrm{AT}^{2} \exp\left(-\frac{\mathrm{q}\Phi_{\mathrm{B}}}{\mathrm{kT}}\right) \tag{6.15}$$

Where the Φ_{B} is given by:

$$\Phi_{\mathrm{B}} = \Phi_{\mathrm{B0}} - \sqrt{\frac{\mathrm{qE}}{4\pi\varepsilon_{\mathrm{s}}}} \tag{6.16}$$

Where the Φ_{B0} (eV) is the Schottky barrier height before the image-force lowering effect, the ϵ_{s} (F/m) is the permittivity and E (V/m) is the maximum electric field at the junction region. The E is given by:

$$\mathrm{E} = \sqrt{\frac{2\mathrm{qN_D}}{\varepsilon_{\mathrm{s}}}\left(\mathrm{V} + \phi_{\mathrm{bi}} - \frac{\mathrm{kT}}{\mathrm{q}}\right)} \tag{6.17}$$

Where V (V) is the applied bias, N_D (m^{-3}) is the doping concentration and ϕ_{bi} (V) is the built-in potential (at the equilibrium). To extract the Schottky barrier height Φ_{B0} (eV) before lowering, the nature logarithm is taken on the both sides of the equation 6.17:

$$Ln(I) = Ln\left(A^*AT^2\right) - \frac{q\Phi_B}{kT} \tag{6.18}$$

Setting the A_1=Ln (A^*AT^2), the equation 6.18 be written as:

$$Ln(I) - A_1 = -\frac{q}{kT}\left(\Phi_{B0} - \sqrt{\frac{qE}{4\pi\varepsilon_s}}\right) \tag{6.19}$$

$$Ln(I) - A_1 + \frac{q}{kT}\Phi_{B0} = \frac{q}{kT}\sqrt{\frac{qE}{4\pi\varepsilon_s}}\Bigg) \tag{6.20}$$

$$\frac{k^2\ T^2}{q^2}\left(Ln(I) - C_1\right)^2 = \frac{qE}{4\pi\varepsilon_s} \tag{6.21}$$

Where the C_1 is given by:

$$C_1 = A_1 - \frac{q}{kT}\Phi_{B0} \tag{6.22}$$

$$\frac{4\pi\varepsilon_s}{q}\frac{k^2\ T^2}{q^2}\left(Ln(I) - C_1\right)^2 = E = \sqrt{\frac{2qN_D}{\varepsilon_s}\left(V + \phi_{bi} - \frac{kT}{q}\right)} \tag{6.23}$$

Set:

$$C_2 = \frac{4\pi\varepsilon_s}{q}\frac{k^2T^2}{q^2} \tag{6.24}$$

then the equation 6.23 could be written as:

$$C_2{}^2\left(Ln(I) - C_1\right)^4 = \frac{2qN_D}{\varepsilon_s}\left(V + \phi_{bi} - \frac{kT}{q}\right) \tag{6.25}$$

The equation 6.25 could be expanded as:

$$\begin{aligned} C_2^2\left(Ln(I) - C_1\right)^4 &= C_2^2\left((Ln(I))^4 - 4C_1(Ln(I))^3 + 6C_1^2(Ln(I))^2 - 4C_1{}^3\,Ln(I) + C_1^4\right. \\ &= C_3\ V + C_4 \end{aligned} \tag{6.26}$$

Where the constant C_3 is given by:

$$C_3 = \frac{2qN_D}{\varepsilon_s} \tag{6.27}$$

And the constant C_4 is defined as:

$$C_4 = \frac{2qN_D}{\varepsilon_s}\left(\phi_{bi} - \frac{kT}{q}\right) \tag{6.28}$$

Let's go back to the I-V relationship of the back-to-back Schottky diodes. For certain applied bias, if the V vs Ln (I) curve could be expanded into the format:

$$V = \text{ Intercept } + B_1\,Ln(I) + B_2(Ln(I))^2 + B_3(Ln(I))^3 + B_4(Ln(I))^4 \tag{6.29}$$

By comparing the equation 6.26 and equation 6.29, the relationship between the C_1, C_2, C_3, B_3 and B_4 could be extracted as:

$$\frac{{C_2}^2}{C_3} = B_4 \tag{6.30}$$

and

$$\frac{C_2^2}{C_3}(-4C_1) = B_3 \tag{6.31}$$

then the C_1 can be given by

$$-4C_1 = \frac{B_3}{B_4} \tag{6.32}$$

and

$$\Phi_{B0} = \frac{kT}{q} \times \frac{\frac{B_3}{B_4} + 4\ A_1}{4} \tag{6.33}$$

Before applying the image-force model, the relationship between the Ln(I) and $V^{1/4}$ need to be verified. If the Ln(I) vs $V^{1/4}$ curve is linear, then the model is valid.

The fig-6.15 shows the Ln(I) vs $V^{1/4}$ plots of all the interfaces in the fabricated devices. For all the contacts, the Ln(I) vs $V^{1/4}$ is not linear at low bias region. That is because the applied bias equals to the sum of the voltage drop at the Schottky-contact-1: V_1, and the voltage drop at the Schottky-contact-2: V_2. For example, while applying forward bias (from 'down' to 'up'), the Schottky-contact-1 is reversely biased and the Schottky-contact-2 is under the forward bias. While the applied bias is small, the built-in potential of the Schottky-contact-2 is still large and impede the transport of the carriers. In this case, both the V_1 and V_2 need to be considered

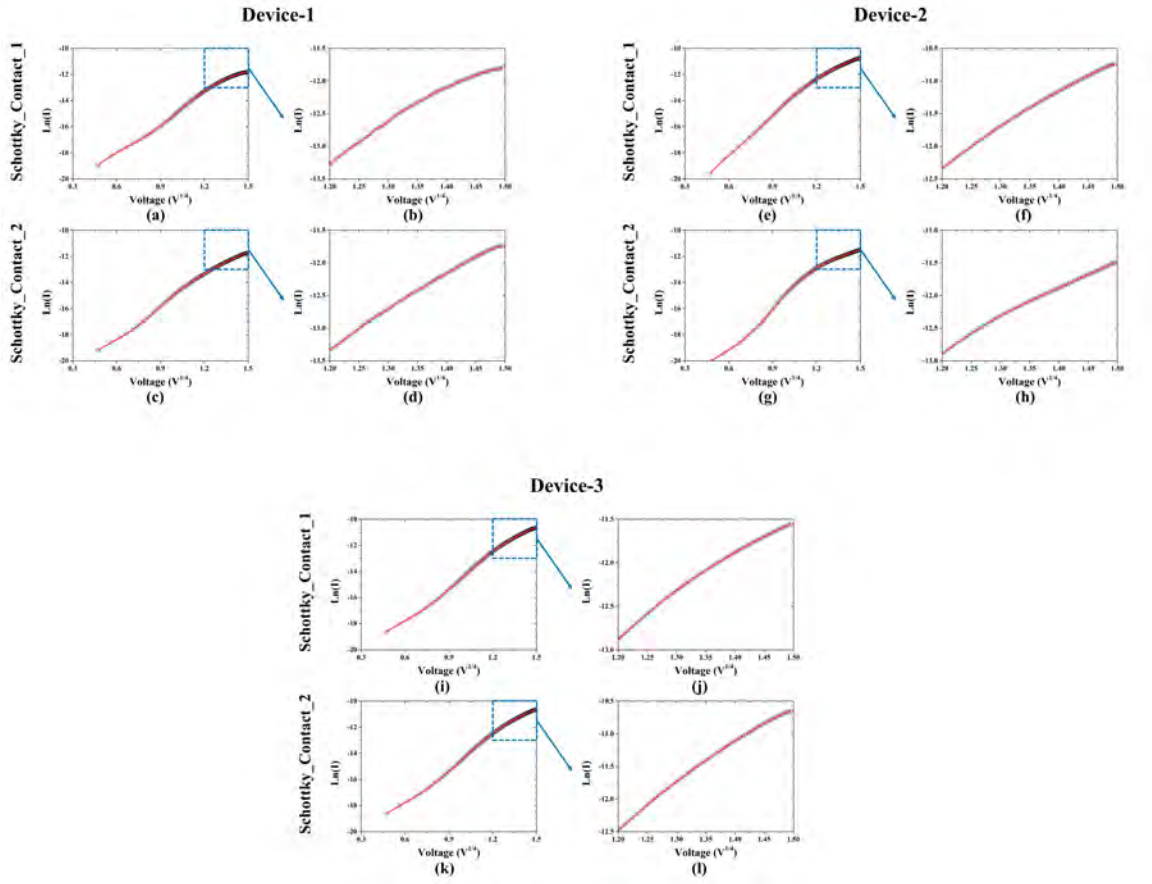

Figure 6.15: the Plot of Ln(I) vs $V^{1/4}$. (a), (b) the Ln(I) vs $V^{1/4}$ plot and its zoom-in plot of the Schottky-contact-1 in the device-1. (c), (d) the Ln(I) vs $V^{1/4}$ plot and its zoom-in plot of the Schottky-contact-2 of the device-1. (e), (f) the Ln(I) vs $V^{1/4}$ plot and its zoom-in plot of the Schottky-contact-1 in the device-2. (g), (h) the Ln(I) vs $V^{1/4}$ plot and its zoom-in plot of the Schottky-contact-2 in the device-2. (i), (j) the Ln(I) vs $V^{1/4}$ plot and its zoom-in plot of the Schottky-contact-1 of the device-3. (k), (l) the Ln(I) vs $V^{1/4}$ plot and its zoom-in plot of the Schottky-contact-2 in the device-3. For all the zoom-in plots, the voltage range is set and 2.0 V to 5.0 V and the $V^{1/4}$ ranges from 1.2 to 1.5 correspondingly.

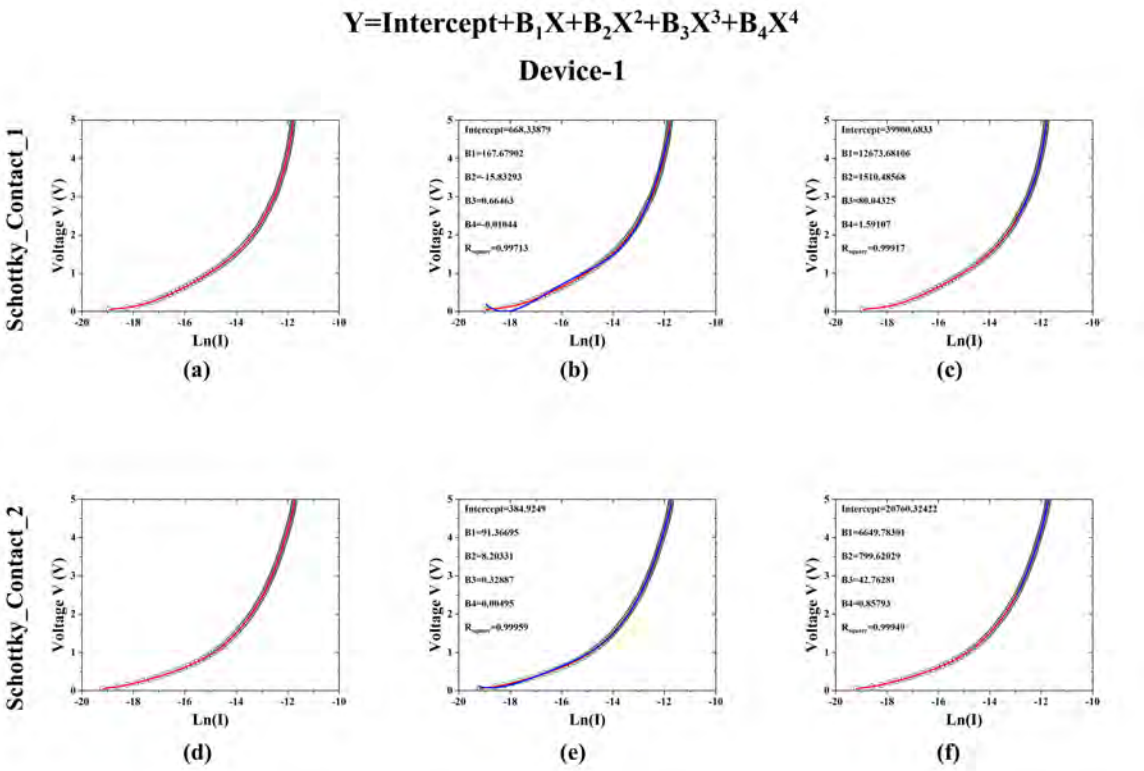

Figure 6.16: The Voltage V vs Ln(I) Plot and Its Fitting of the Device-1. (a) the V vs Ln(I) plot of the Schottky-contact-1 of the device-1. (b) the full-range fitting of the V vs Ln(I) plot of the Schottky-contact-1 of the device-1. (c) the fitting of the V vs Ln(I) plot of the Schottky-contact-1 at large-bias region (2.0 V to 5.0 V). (d) the V vs Ln(I) plot of the Schottky-contact-2 of the device-1. (e) the full-range fitting of the V vs Ln(I) plot of the Schottky-contact-2 of the device-1. (f) the fitting of the V vs Ln(I) plot of the Schottky-contact-2 at large-bias region (2.0 V to 5.0 V).

for analyzing the I-V. When the applied bias becomes larger, the built-in potential of the Schottky-contact-2 will be fully overcome, and the voltage drop across the Schottky contact under the forward bias (Schottky-contact-2 in this case) can be ignored. Meanwhile, the Schottky contact which is reverse biased will determine the I-V characteristics. If the applied bias is continuously increasing, after a certain point, the carriers will start to tunnel through the Schottky contact under the reverse bias and the voltage drop of the series resistance needs to be considered for analysis. For this reason, as shown in fig-6.15, the linear region of the Ln(I) vs $V^{1/4}$ plot is located between the 1.2 (2.0 V) and 1.5 (5.0 V). After 5.0 V, the curve starts to bend.

To extract the Schottky barrier height, the order-4 polynomial fitting has been

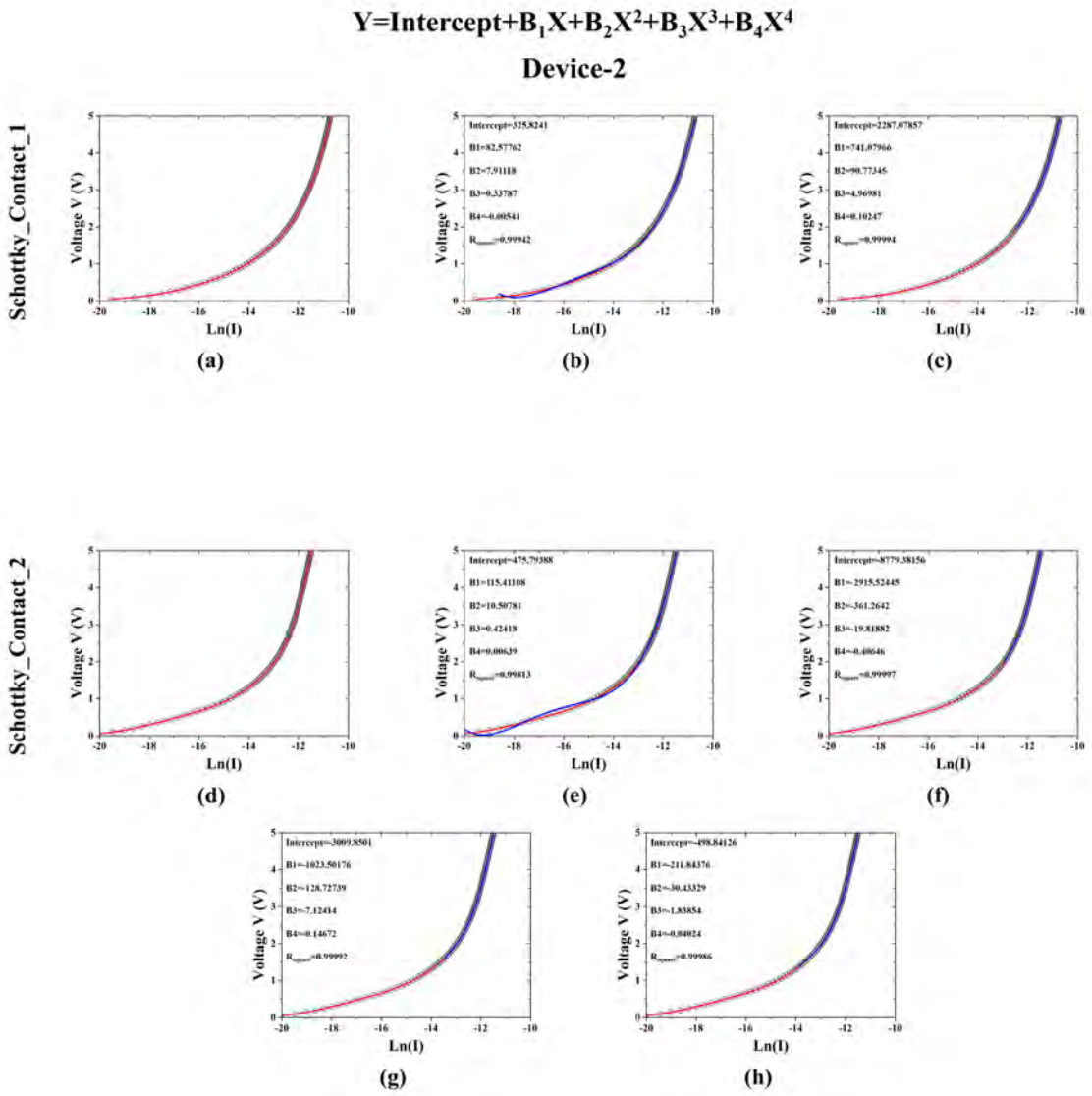

Figure 6.17: The Voltage V vs Ln(I) Plot and Its Fitting of the Device-2. (a) the V vs Ln(I) plot of the Schottky-contact-1 of the device-2. (b) the full-range fitting of the V vs Ln(I) plot of the Schottky-contact-1 of the device-2. (c) the fitting of the V vs Ln(I) plot of the Schottky-contact-2 at large-bias region (2.0 V to 5.0 V). (d) the V vs Ln (I) plot of the Schottky-contact-2 of the device-2. (e) the full-range fitting of the V vs Ln(I) plot of the Schottky-contact-2 of the device-2. (f) the fitting of the V vs Ln(I) plot of the Schottky-contact-2 at large-bias region (2.0 V to 5.0 V). (g) and (h) extended fitting of the V vs Ln(I), for Ln(I), the fitting range is extended from [-13, -11.5] to [-13.5, -11.5] and [-14, -11.5] respectively.

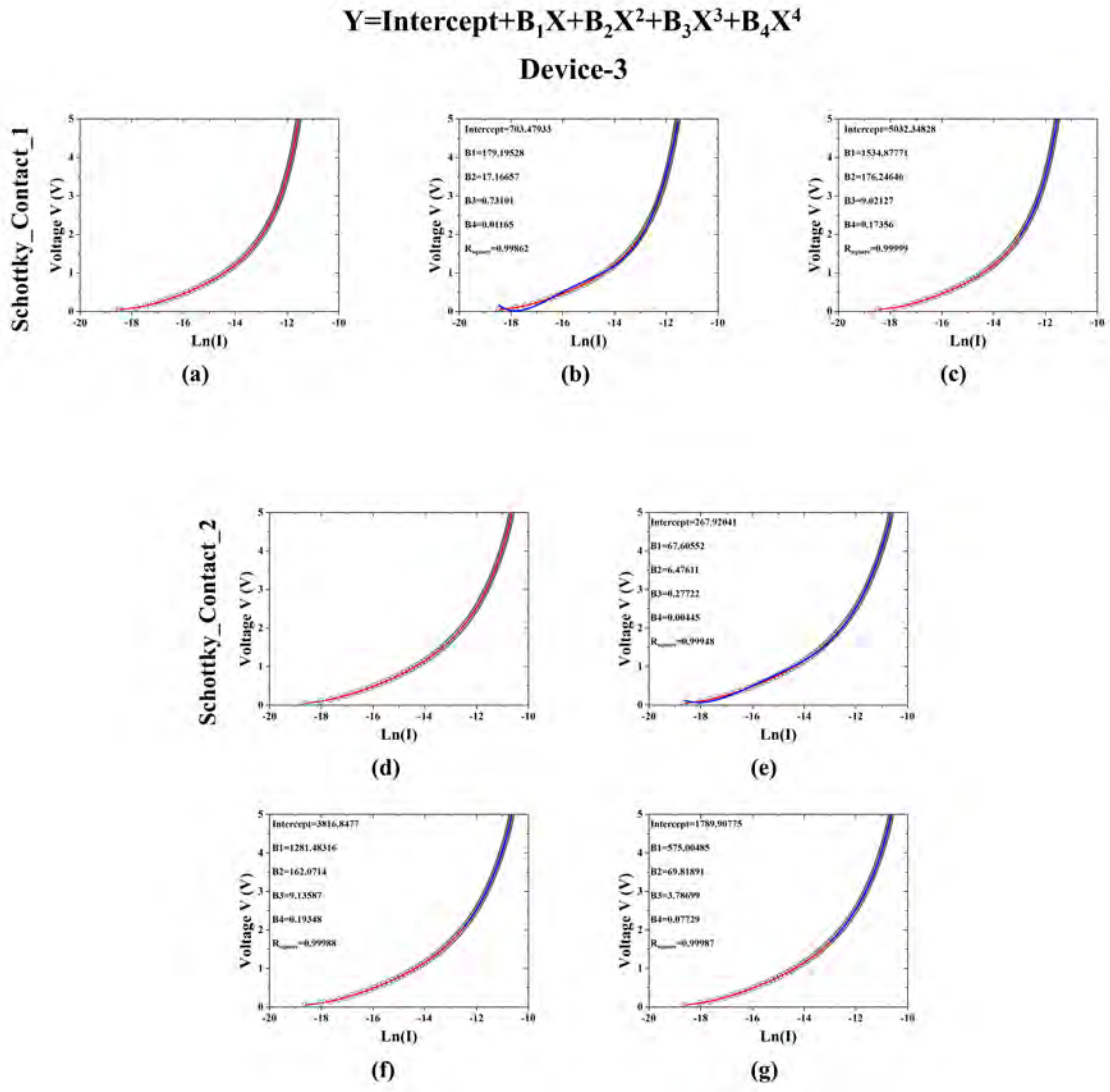

Figure 6.18: The Voltage V vs Ln(I) Plot and Its Fitting in the Device-3. (a) the V vs Ln(I) plot of the Schottky-contact-1 of the device-3. (b) the full-range fitting of the V vs Ln(I) plot of the Schottky-contact-1 in the device-3. (c) the fitting of the V vs Ln(I) plot of the Schottky-contact-2 at large-bias region (2.0 V to 5.0 V). (d) the V vs Ln(I) plot of the Schottky-contact-2 of the device-3. (e) the full-range fitting of the V vs Ln(I) plot of the Schottky-contact-2 in the device-3. (f) the fitting of the V vs Ln(I) plot of the Schottky-contact-2 at large-bias region (2.0 V to 5.0 V). (g) extended fitting of the V vs Ln(I), for Ln(I), the fitting range is extended from [-12.5, -10.6] to [-13, -10.6].

conducted to all the V vs Ln(I) plots. As shown in fig-6.16 (b) and (c), both the fitting over full voltage range and large-bias region has been conducted. For full-range fitting, the B_3 is 0.66463 and the B_4 is -0.01044. A negative SBH of the Schottky-contact-1 will be extracted by using these values, which is impossible. It demonstrates that the proposed model may not work if the small-bias region is included in the fitting. To fix this issue, the fitting over the large-bias region of the V vs Ln(I) curve has been conducted for all the contacts. As shown by fig-6.16 (c), the B_3 is 80.04325 and the B_4 is 1.59104. Here if we consider the interface A is the transport interface, the junction area is $24.98\mu m^2$. The calculated Schottky barrier height for the Schottky-contact-1 in the device-1 is 0.332 eV, which is much larger than the reported values [29]. If we consider the interface A is the transport interface, the junction area is $0.0124\mu m^2$. The given Schottky barrier height is 0.134 eV, which is comparable with the reported experimental work [29]. As for the Schottky-contact-2 in the device-1, if we take interface A as the transport interface, the given Schottky barrier height of the Schottky-contact-2 in the device-1 is 0.41 eV, while the given barrier height is 0.137 eV if the interface B is taken as the transport interface.

As shown in fig-6.17 and fig-6.18, the same techniques is also applied to the device-2 and device-3, and all the fitting data and extracted results are listed in the table-6.6. For the Schottky-contact-1 in the device-2, the extracted Schottky barrier height is 0.407 eV if the interface A is taken as the interface. If the interface B is considered as the contact interface, the extracted Schottky barrier height of the contact is 0.282 eV. As for the Schottky-contact-2 in the device-2, multiple fittings with different fitting ranges have been conducted. For the fitting with the Ln(I) ranging from -13 to -11.5, as shown in fig-6.17 (f), if we consider the interface A as the junction interface, the extracted Schottky barrier height is 0.379 eV. While the interface B is adopted, the extracted Schottky barrier height is 0.272 eV. If the fitting range of the Ln(I) is set as -13.5 to -11.5, the extracted Schottky barrier height is 0.377 eV for the interface A, and 0.270 eV for the interface B. When the fitting range of the Ln (I) is set as

Table 6.6: The Schottky Barrier Height Extracted by Image-Force Model for Each Schottky Contact. In the table, the SC1 denotes Schottky-contact-1, and SC2 denotes the Schottky-contact-2. The SBH-A is the Schottky barrier height of the contact while the interface A is considered as the junction interface. The SBH-B is the Schottky barrier height of the contact while the interface B is considered as the junction interface.

	Fitting Range (Ln(I))	SBH-A (eV)	SBH-B (eV)	R_{square} (Ω)
Device-1 SC1	[-13 to -11.8]	0.332	0.134	0.99917
Device-1 SC2	[-13 to -11.7]	0.410	0.137	0.99949
Device-2 SC1	[-12.5 to -10.7	0.407	0.282	0.99994
Device-2 SC2	[-13 to -11.5]	0.379	0.272	0.99997
	[-13.5 to -11.5]	0.377	0.270	0.99992
	[-14 to -11.5]	0.359	0.252	0.99986
Device-3 SC1	[-13 to -11.5]	0.367	0.247	0.99999
Device-3 SC2	[-12.5 to -10.6]	0.356	0.237	0.99988
	[-13 to -10.6]	0.367	0.248	0.99987

-14 to -11.5, the extracted Schottky barrier height is 0.359 eV considering interface A as the junction interface, and it becomes 0.252 eV if the interface B is taken as the junction interface.

For device-3, as shown in fig-6.18 and table-6.6, the Schottky barrier height of the Schottky-contact-1 is 0.367 eV if the interface A is the junction interface. The extracted Schottky barrier height value would become 0.248 eV if the interface B is taken as the contact interface. For the Schottky-contact-2 in the device-3, two different fitting ranges of Ln(I) are adopted to fit the V vs Ln(I) curve, which are [-12.5, -10.6] and [-13, -10.6]. The extracted Schottky barrier height for the case where the interface A acts as the junction interface is 0.356 eV and 0.367 eV. In the case where the interface B is seen as the junction interface, the extracted Schottky barrier height is 0.237 eV and 0.248 eV, respectively.

It intuitively shows that, the extracted results considering interface B as the junction interface are much closer to the reported experimental values [29] compared with interface A. This indicates that, the interface B should be the junction interface of the 2D metal-MoS_2 Schottky contact, which coincides with the conclusion of the DFT simulations in the previous part. The extracted results also shows that device-1 has much smaller Schottky barrier height than the device-2 and device-3. But this could not be simply explained as a matter of the thickness of the MoS_2 since lots of factors could affect the Schottky barrier height of metal-MoS_2 contacts. To verify this, more devices need to be fabricated and tested.

The fitting results shown in fig-6.16, fig-6.17 and fig-6.18 indicate that the fitting coefficients such as B_3 and B_4 will change as the fitting range changes. To investigate the impact of this variation to the Schottky barrier height extraction, a fitting test is conducted on the Schottky-contact-2 in the device-2 since its V vs Ln(I) curve shows a larger linear region compared with other contacts. The fitting starts with 60 data points (data point 40 to data point 100) and then the fitting region shrinks by 5 data points for each step. The smallest fitting region contains 25 data points (data point 75 to data point 100). As shown in table-6.7, and fig-6.19 (a) and (b), the variation of the B_3 and B_4 is very large at high bias region (data point 60 to data point 100). The largest given B_3 is -837.791, extracted from the fitting over the region from data point 75 to data point 100 (labelled by [75, 100]), while the B_3 given from the fitting starting at data point 60 (labelled by [60, 100]) is only -9.50687. The B_4 extracted over [60, 100] is -0.190, while the B_4 calculated by the fitting over [75, 100] is -17.845. However, the large variation of B_3 and B_4 does not affect the value of B_3/B_4 and $B_3/4B_4$ much. As shown by fig-6.19 (c), the variation of B_3/B_4 and $B_3/4B_4$ is very small. For $B_3/4B_4$, which decides the value of the Schottky barrier height, the largest value in the fitting test is 13.44, and the smallest value is 11.74. As shown in table-6.7, the results of the fitting test show that, although the coefficients B_3 and B_4 varies largely in terms of the fitting region, but the value of B_3/B_4 and $B_3/4B_4$ is stable at

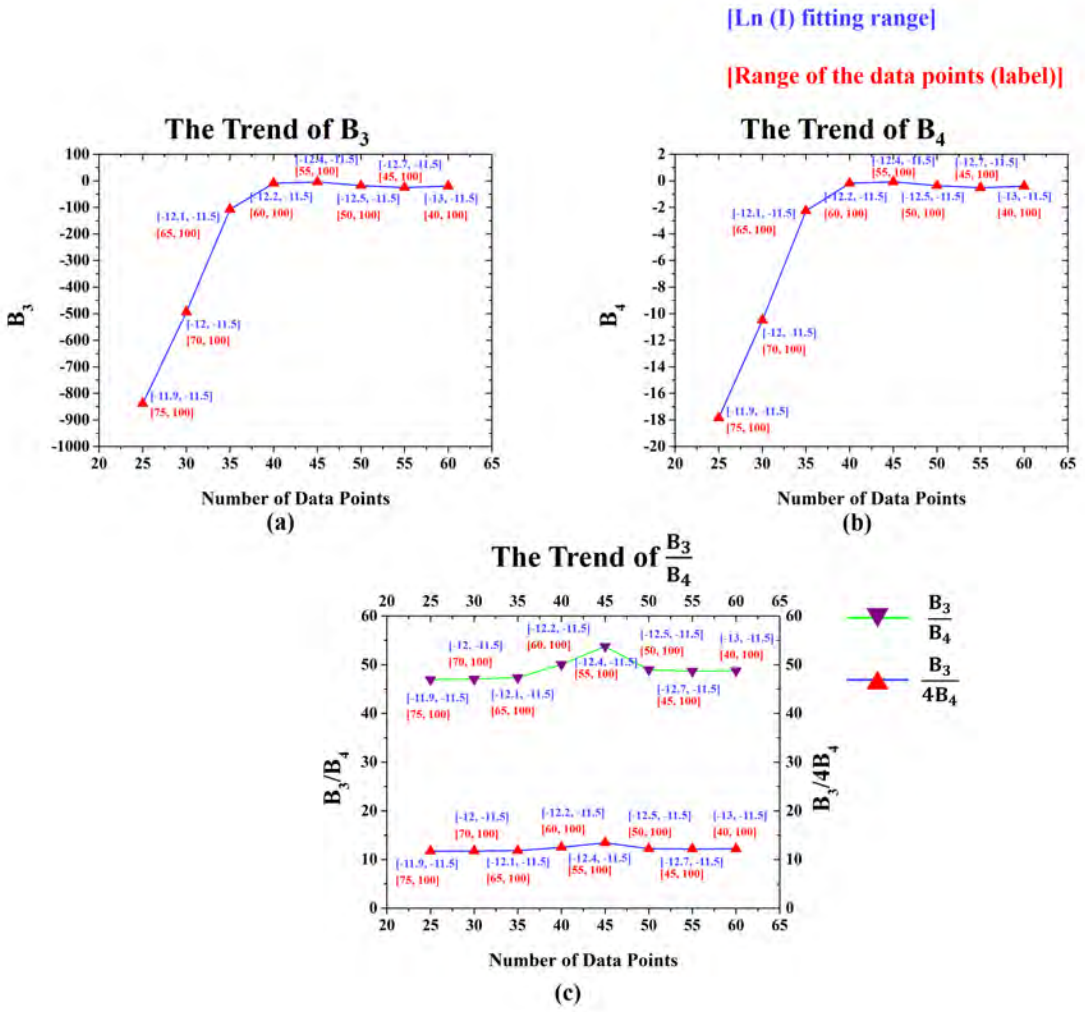

Figure 6.19: The Variation of B_3, B_4 and B_3/B_4 of Different Fitting Range and Number of Data Points. (a) the trend of the changing of B_3 in terms of the variation of fitting range of Ln(I). (b) the trend of the changing of B_4 in terms of the variation of fitting range of Ln(I). (c) the trend of the changing of B_3/B_4 and $B_3/4B_4$ in terms of the variation of fitting range of Ln(I). In the plot, the data points range and the Ln(I) range selected for fitting is labelled by red bracket and blue bracket repectively.

Table 6.7: The Fitting Test of the Image-Force Model on the Schottky-Contact-2 of the Device-2

Data Point Range	Number of Data Points	Ln(I) Range	B_3	B_4	B_3/B_4	$B_3/4B_4$
[40, 100]	60	[-13, -11.5]	-19.819	-0.406	48.76	12.19
[45, 100]	55	[-12.7, -11.5]	-25.206	-0.518	48.67	12.17
[50, 100]	50	[-12.5, -11.5]	-17.857	-0.365	48.99	12.25
[55, 100]	45	[-12.4, -11.5]	-4.320	-0.0804	53.76	13.44
[60, 100]	40	[-12.2, -11.5]	-9.507	-0.190	50.04	12.51
[65, 100]	35	[-12.1, -11.5]	-107.439	-2.268	47.37	11.84
[70, 100]	30	[-12.0, -11.5]	-493.708	-10.494	47.05	11.76
[75, 100]	25	[-11.9, -11.5]	-837.791	-17.845	46.95	11.74

the linear region of V vs Ln(I) plot. It means that the B_3/B_4 and $B_3/4B_4$ are mainly determined by the Schottky barrier height and the other characteristics of the Au-MoS_2 contact, not the applied mathematical tactics. This fitting test demonstrates the validity of the Schottky barrier height extraction. To be noticed, our proposed method is able to extract Schottky barrier height from the back-to-back Schottky contact I-V, but for other parameters like doping concentration of the MoS_2 channel, this model is not applicable since the variation of the relative fitting coefficients could not be explained right now.

6.4 Conclusion

To verify the previous DFT simulation results, we have fabricated three Au-MoS_2 back-to-back Schottky diodes and performed I-V characterizations. The Raman and AFM measurements demonstrate that the MoS_2 channel of the three back-to-back diodes are 4L, 146L and 90L. The annealing process after the exfoliation greatly improves the performance of the Schottky diodes. The peak current of the back-to-back

diodes are increased by more than 1000 times. Considering the forward-biased contact only and ignoring the voltage drop at the reversed-biased contact, the TE and SR models yield large ideality factor, which are 17.08 and 12.81. The TE and SR models can't be used to extract the Schottky barrier height of the fabricated diodes. To solve this issue, we have developed novel image-force model. Considering the reverse-biased contact only, the image-force model extracts reasonable Schottky barrier height values by analyzing the large-bias region with 4-order polynomial fitting. If consider the interface B as the junction interface, the extracted Schottky barrier height is more close to the reported values compared with interface A. The extracted Schottky barrier height with interface B as the junction interface ranges from 0.134 eV to 0.272 eV. Our model and the extraction of Schottky barrier height demonstrate that, the reversely biased diode within the back-to-back Schottky diode predominates over the I-V of the system, while under large applied bias. The variation of the current with the changing bias is mainly due to the image force lowering effect. The development of the novel image-force model and the relative I-V characteristic extraction of the fabricated Au-MoS_2 back-to-back Schottky diodes help us gain a better understanding of the mechanism of Au-MoS_2 Schottky contacts.

Chapter 7

The Mobility Variation Associated with the Stacking Orientation of Multi - layer Molybdenum Disulfide

7.1 Introduction

In the functionality of 2D MoS_2 devices, the MoS_2 channel plays an important role. To meet the requirement of certain electronic or optical applications, it is necessary to fabricate multilayer MoS_2 channels. According to the recent studies, the critical electronic/optical properties such as bandgap energy, carrier effective mass and refractive index of the MoS_2 thin film show a strong dependence on its stacking orientation [206]. Experimentally, it is challenging to obtain MoS_2 samples with uniform stacking order. Within one MoS_2 sample, different layers may show different orientation angles. According to the reported microscopy analysis [74], normally, the stacking order of the multilayer MoS_2 samples could be categorized in three groups. Firstly is the AA stacking. In AA stacking MoS_2 samples, the hexagonal lattice of each layer is parallel to each other, showing the same orientation angle. Secondly is the AB stacking. In AB stacking MoS_2 samples, the hexagonal lattice of one layer of MoS_2 exhibits a twisting angle of 60° to the adjacent layers. There is another stacking orientation, which is the mixture of AA and AB stacking [74]. For designing multilayer

MoS_2 devices, it is crucial to gain a fundamental understanding of how the stacking order of the MoS_2 films affects its electronic properties. For this reason, efforts have been devoted on exploring the relationship between the MoS_2 electronic properties and stacking orientation [35, 74, 206, 207]. Although these studies have revealed how the stacking orientation of the multi-layer MoS_2 impacts the device performance in all aspects. However, there are many unsolved issues. Most of the studies focus on very confined MoS_2 systems, such as 2 layers (L) and 3L MoS_2. The investigation over the MoS_2 beyond 4 layers is still a blank. Only a small portion of the possible stacking combinations have been investigated, and a more comprehensive study is required. The physic mechanism behind the stacking-associated variation of the MoS_2 electronic properties is still unknown.

To solve the issues mentioned above and optimize the device design of 2D MoS_2 FETs, we have conducted a comprehensive study based on DFT [132], focusing on investigating the correlation between the effective mass of electrons and MoS_2 stacking order. To obtain an overall view of the electron effective mass variation, the electronic structure of 2L to 10L AA and AB MoS_2 films are simulated. An enumeration of all the possible stacking order combinations of 4L to 6L MoS_2 is also adopted in this study. By evaluating the electronic properties of each possible combination carefully, we sketch out how the symmetric configuration affects the electron effective mass of the MoS_2. To obtain more accurate simulation results, we have optimized our simulation method by applying mGGA functional [137]. By simulating the Mulliken population and electrostatic differential potential, a detailed analysis is given to dig out the mechanism behind the stacking-controllable interlayer coupling of MoS_2. By gaining a better understanding of the interlayer coupling effects and how it will modify the electronic properties of the multi-layer MoS_2 devices, We hope that our work could give valuable prediction to optimize 2D MoS_2 devices and help exploit their future applications.

7.2 Methodology

7.2.1 Density Functional Theory Simulation Setup

The Atomistix ToolKit (ATK) [6] is adopted to perform the simulation. For geometry optimization Geometry Optimization (GO), the Perdew-Burke-Emzerhof variant of GGA [134] functional is applied. The basis set is set as HGH [141] basis set. A 16×16×1 Monkhorst-Pack k-point mesh is applied to all the simulations. The force tolerance of geometry optimization is set as 0.005 eV/ Å. The simulated a and b of the MoS_2 unit cell are 3.1857 Å, while the reported experimental value is 3.16 Å [208]. As what has been reported by other groups, GGA method could accurately predict the bandgap energy of ML MoS_2 and the bandstructure topology [26, 27], but the GGA method tends to underestimate the bandgap energy of multi-layer MoS_2 [136]. To solve this issue, in bandstructure and effective mass simulation, the mGGA functional [137] is adopted. After optimization, the c parameter of the mGGA is set as 1.15. On the one hand, the GGA functional is able to provide accurate results in MP and EDP simulations. On the other hand, the mGGA requires large amount of computational resource. For this reason, the GGA functional is adopted to perform the MP and EDP analysis in our work.

7.2.2 Geometry Setup of AA and AB Stacking Orientation

In our simulation, the AA MoS_2, as shown in fig-7.1 (a), refers to the MoS_2 with repeated piling with same orientation, where the Mo and S atoms in the one layer sits on the top of the S and Mo atoms in the neighbouring layers. The AB MoS_2, as shown in fig-7.1 (b), is the repeated piling with alternating orientations, where one S atom sits on the top of one hollow site. Mixed piling orientations of AA and AB MoS_2 also exist in multi-layer MoS_2. These stacking orientations will be discussed in the following content. To investigate the stability of the AA and AB configurations, the average binding energy has been simulated. In this study, the average binding

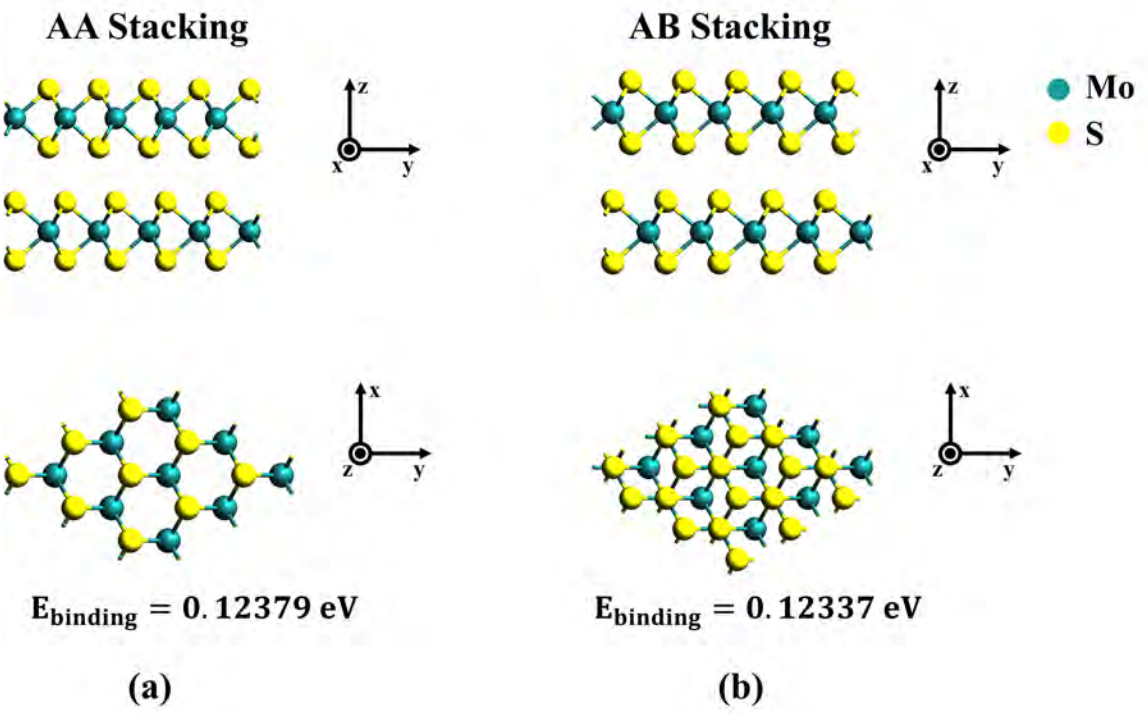

Figure 7.1: The Schematic Figure of the Configuration of AA and AB MoS_2. (a) AA MoS_2, which has an average binding energy $E_{binding}$ of 0.12379 eV. (b) AB MoS_2, which has an average binding energy $E_{binding}$ of 0.12337 eV.

energy is defined by the equation:

$$E_{binding} = \frac{E_{tot_2} - 2 \times E_{tot_1}}{N} \tag{7.1}$$

Where $E_{binding}$ (eV) denotes the average binding energy, E_{tot_2} (eV) is the total energy of AA or AB MoS_2, E_{tot_1} (eV) is the total energy of ML MoS_2, N is the number of sulfur atoms in the unit cell. A larger average binding energy indicates a more stable structure. The given average binding energy of AB and AA MoS_2 are 0.12337 eV and 0.12379 eV respectively. Obviously, the average binding energy of AA MoS_2 is very close to the AB. This may explain that why both AA and AB orientations exist in the multi-layer MoS_2 films after CVD deposition.

7.2.3 Effective Mass Extraction

Effective mass is a critical parameter to determine the carrier mobility of the devices. The effective mass of the carriers can be extracted from the the second order derivative of the energy(E)-wavevector(k) function E(k). At the conduction band minimum Conduction Band Minimum (CBM) and valence band maximum Valence Band Maximum (VBM), the E(k) could be written as:

$$E(k) = E_0 + \frac{h^2 k^2}{8\pi^2 m^*} \tag{7.2}$$

Where the E_0 is the ground energy, h is the Planck constant, k is the wavevector of the carriers, and m^* is the carrier effective mass. The equation 7.2 describes the E(k) by using a parabolic model, which is adopted in our analysis of the localized carrier effective mass at CBM. In our simulation, a sequence of k points around the specific CBM point is generated in the given direction, then the energy eigenvalues of these k points for the lowest conduction band are calculated. A numerical second order derivative D is then conducted on the band generated by these eigenvalues. The carrier effective mass in the given direction could be given by:

$$m^* = \frac{h^2}{(8\pi^2 D)m_0} \tag{7.3}$$

Where the D is the numerical second order derivative of the band mentioned above, h is the Planck constant, and m_0 is the free electron mass. In our study, we focus on analyzing the electron carrier behavior. Thus only the electron effective mass extraction and analysis are discussed in this chapter. To acquire the carrier effective mass for longitudinal and transverse directions, the electron effective mass in x direction m_{eff_x}, and y direction m_{eff_y} are calculated respectively. Then the total electron effective mass m_{eff} could be given by:

$$m_{eff} = \frac{2}{\frac{1}{m_{eff_x}} + \frac{1}{m_{eff_y}}} \tag{7.4}$$

Where the m_{eff} is the total electron effective mass, m_{eff_x} is the electron effective mass in x direction, and m_{eff_y} is the electron effective mass in y direction.

7.3 Bandstructure Simulation

The equation 7.2 and 7.3 indicate that the effective mass of the carriers is determined by the topography of the bandstructure of MoS_2. For this reason, a systematic study on the bandstructure of different MoS_2 configurations could help us understand the how the MoS_2 geometry affects the electronic properties of MoS_2.

7.3.1 Layer Dependence of the Bandstructures

As mentioned in the previous parts, the MoS_2 bandstructure varies according to the MoS_2 thickness. To verify this layer dependence of MoS_2 bandstructure, the bandstructure of 2-10L AA and AB MoS_2 films are simulated and analyzed. Both the GGA and mGGA methods are adopted to simulate the bandstructure of AA and AB MoS_2.

For AA MoS_2, the GGA bandstructures of 2L to 5L cases are presented in fig-7.2. The calculated GGA bandgap energy of 2L to 5L AA MoS_2 is 1.278 eV, 1.080 eV, 0.998 eV and 0.956 eV respectively, as shown in fig-7.2 (a) to (d). The bandgap energy of AA MoS_2 decreases while the MoS_2 thickness increases. As shown in fig-

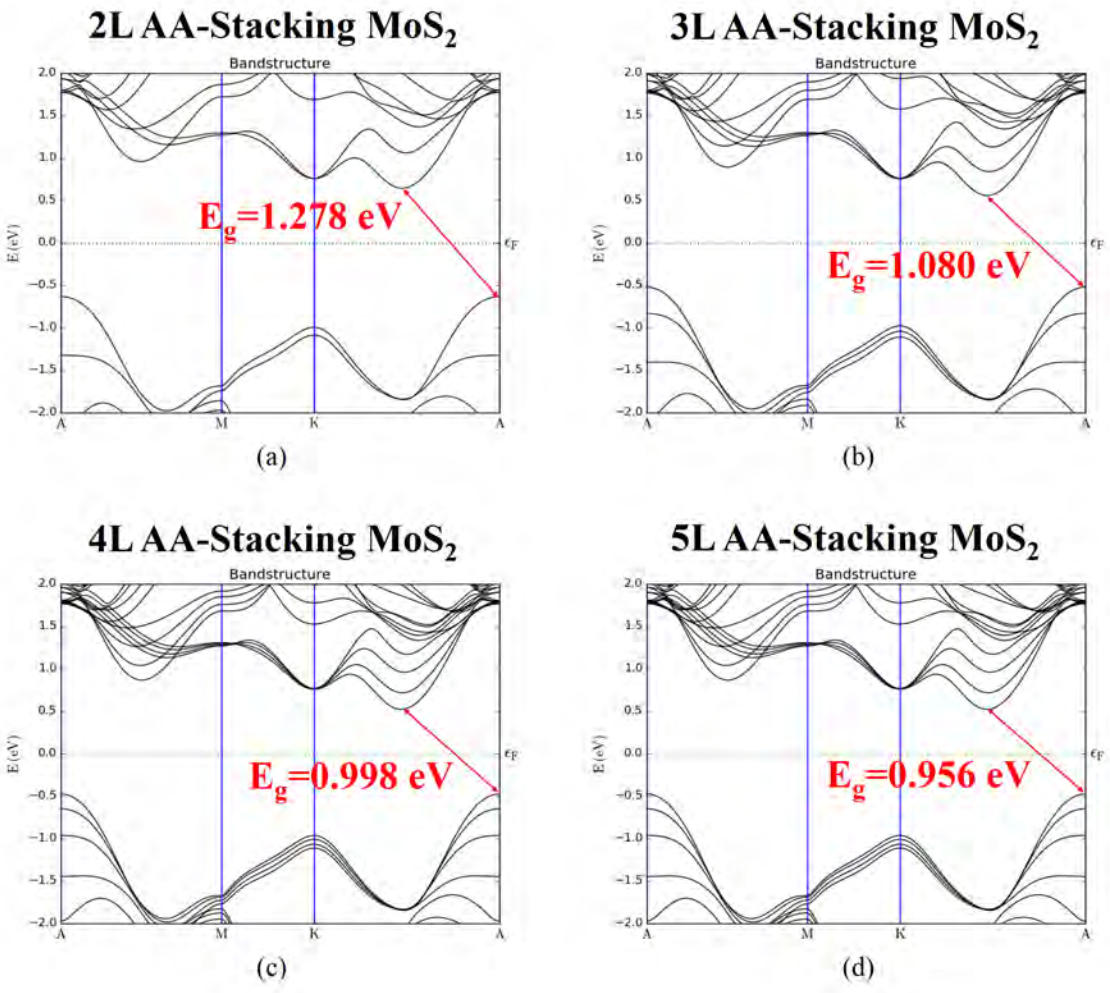

Figure 7.2: The Bandstructure of AA MoS_2 Simulated by GGA. (a)-(d), the bandstructure of 2-5 L AA MoS_2 calculated by GGA.

7.2 (b) to (d), the calculated GGA bandstructure matches the reported simulation results in terms of band shape [26, 34]. The CBM of the band lies between K and A point in the k space, while the VBM is located at A point. The studied MoS_2 samples possess indirect bandgap. The presented bandstructures clearly show layer-dependent degeneration. Starting from the K point, the conduction band tends to split into several branches. The number of the degenerate bands exactly equals to the number of MoS_2 layers. The valence band also shows layer-depended band degeneration. As for the valence band, the splitting of the degeneration bands starts at the valley point located between K and A. On the other hand, compared with experimental results [16, 17], the GGA method tends to underestimate the bandgap energy of AA MoS_2, especially for thicker samples. To solve this issue, the mGGA functionals are applied for our DFT simulation.

As shown in fig-7.3 (a) to (d), the calculated mGGA bandgap energy of 2L to 5L AA MoS_2 is 1.488 eV, 1.308 eV, 1.233 eV and 1.193 eV respectively. The mGGA bandgap energy shows the same trend as the GGA results. The CBM and VBM positions of mGGA bandstructure remain the same as GGA results.

The GGA and mGGA bandstructures of 2L to 5L AB MoS_2 are exhibited in fig-7.4 and fig-7.5. As shown in fig-7.4 (a) to (d), the GGA bandgap energy is 1.299 eV, 1.107 eV, 1.025 eV and 0.983 eV for 2L to 5L AB MoS_2. Meanwhile, the bandgap energy presented in fig-7.5 clearly shows that, the mGGA functionals solve the bandgap underestimation issue of GGA functionals. According to fig-7.5 (a) to (d), the calculated mGGA bandgap energy of 2L to 5L AB MoS_2 is 1.506 eV, 1.332 eV, 1.255 eV and 1.216 eV, which is closer to the experimental value compared with GGA results. The VBM and CBM position of AB MoS_2 is quite similar to the AA cases. As shown in fig-7.4 and fig-7.5, for both GGA and mGGA bandstructures of AB MoS_2, again the CBM of the band is between the K and A, while the VBM is located at A point. The degeneration of the AB MoS_2 bands shows different features from AA cases. In AA MoS_2 bandstructures, as shown in fig-7.2 and fig-7.3, the degenerate band branches

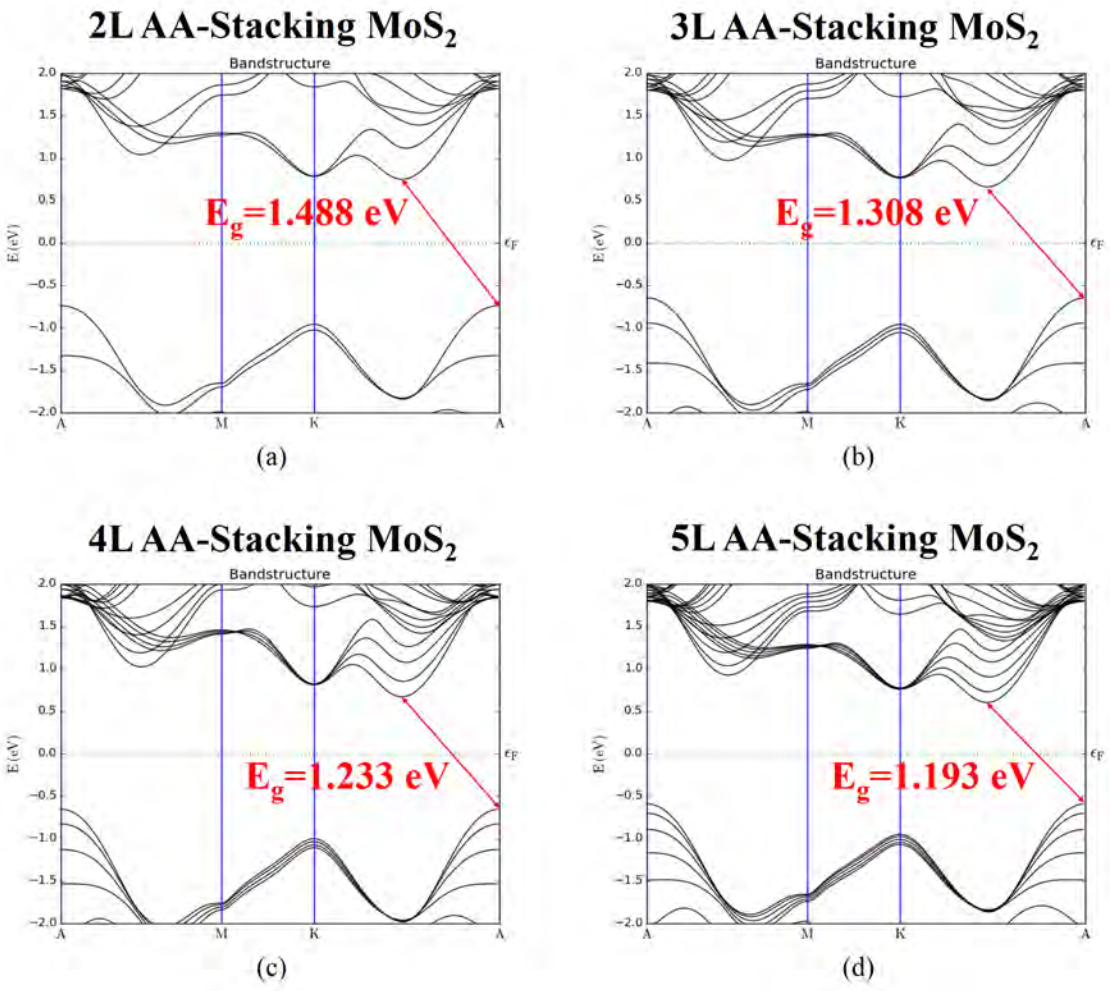

Figure 7.3: The Bandstructure of AA MoS_2 Simulated by Meta-GGA. (a)-(d), the bandstructure of 2-5 L AA MoS_2 calculated by mGGA.

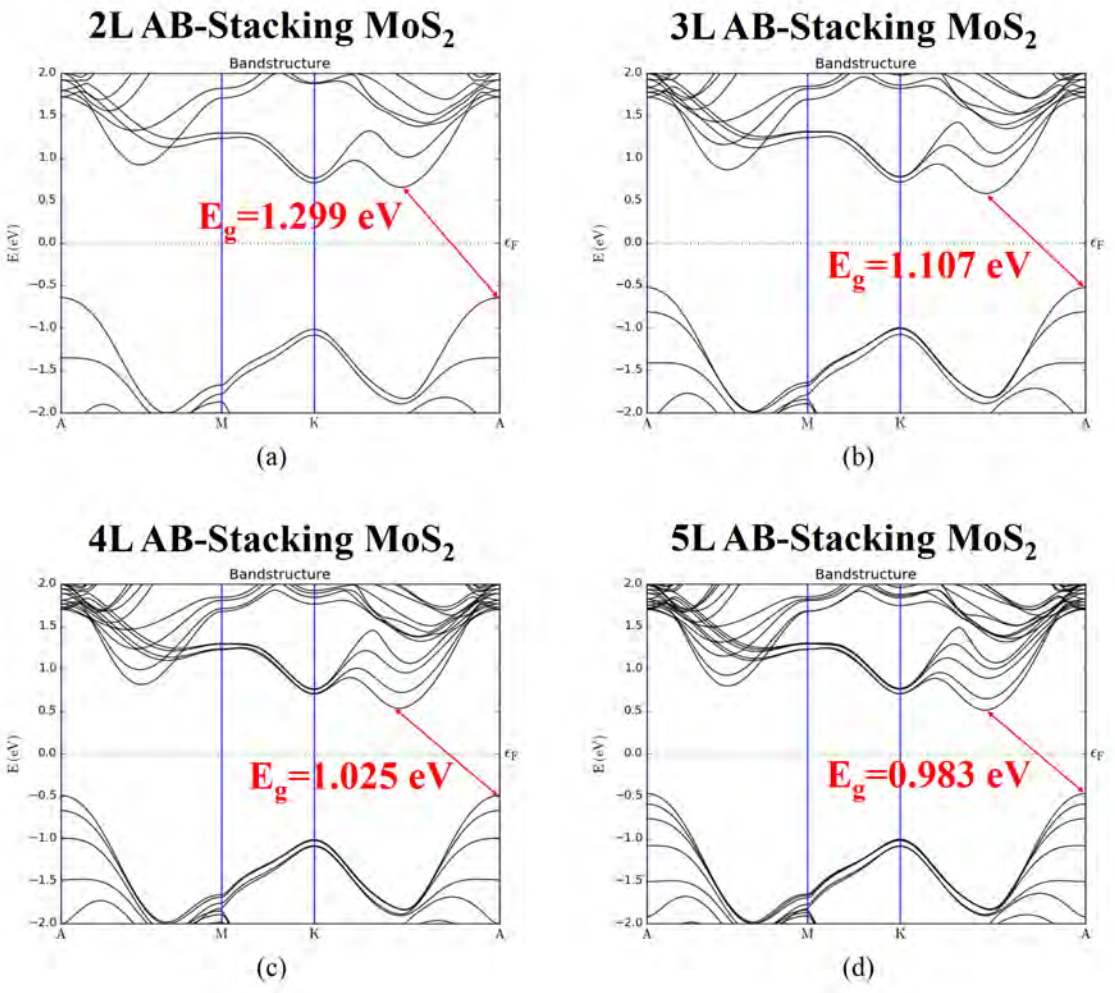

Figure 7.4: The Bandstructure of AB MoS_2 Simulated by GGA. (a)-(d), the bandstructure of 2-5 L AB MoS_2 calculated by GGA.

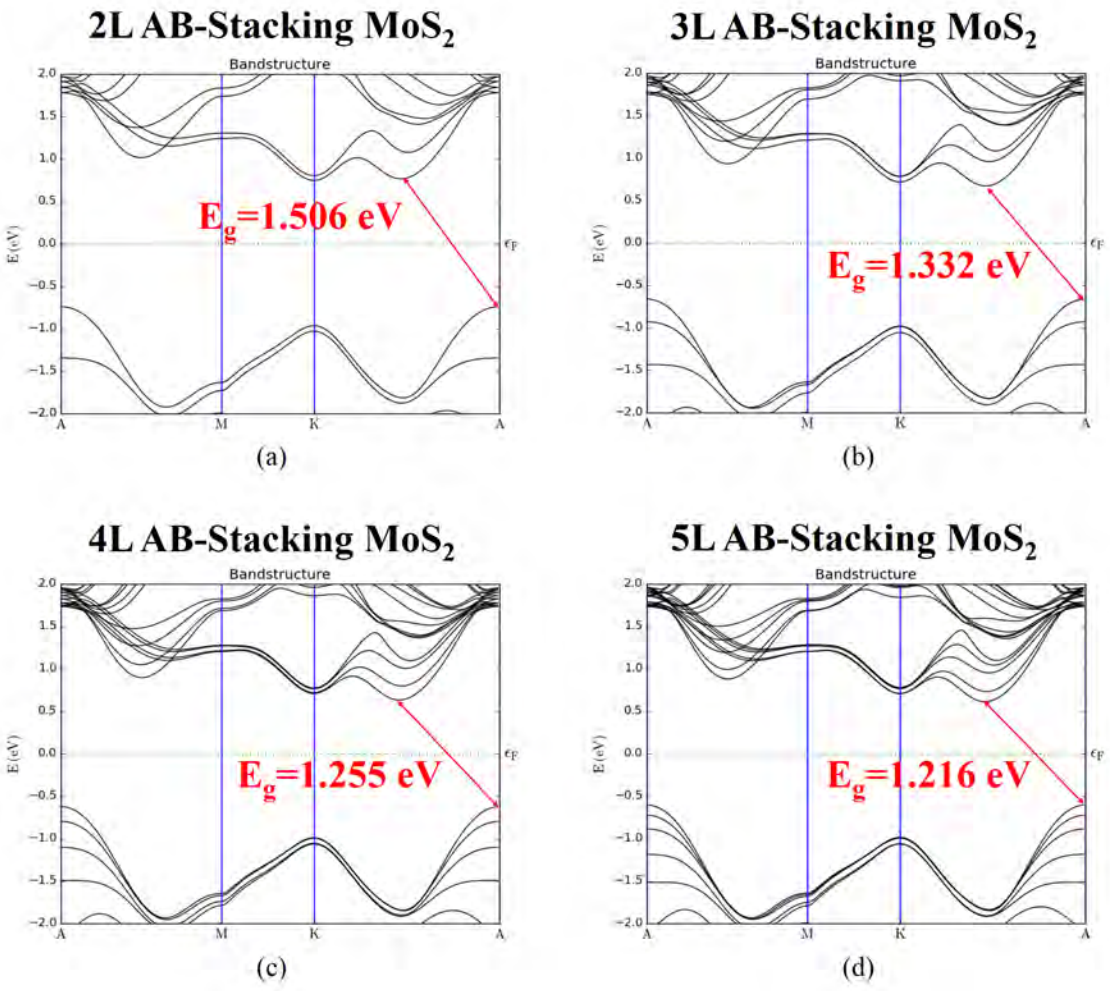

Figure 7.5: The Bandstructure of AB MoS_2 Simulated by Meta-GGA. (a)-(d), the bandstructure of 2-5 L AB MoS_2 calculated by mGGA.

start from a single joint. While the fig-7.4 and fig-7.5 intuitively show that, in AB MoS_2 bandstructures, the degenerate bands form two different groups and converge at two distinct joints. The different bandstructure degeneration features manifest that the broken symmetry of the MoS_2 affects its electronic structure.

7.3.2 Optimization of Bandstructure Simulation

A more detailed comparison between the GGA and mGGA bandstructures is provided and presented in fig-7.6 and fig-7.7.

As shown in fig-7.6 (a) to (d), for AA MoS_2, the CBM of the mGGA bandstructure is above the GGA CBM while the mGGA VBM is below the GGA VBM. The position of mGGA CBM and VBM remain the same as GGA in the k space. The energy difference ΔE between the mGGA and GGA CBM is 0.105 eV, 0.103 eV, 0.100 eV and 0.103 eV for 2L to 5L AA MoS_2 respectively, while the corresponding VBM ΔE is 0.108 eV, 0.127 eV, 0.135 eV and 0.135 eV. The AB cases show comparable energy shifting.

For 2L to 5L AB MoS_2, as shown in fig-7.7 (a) to (d), the CBM ΔE is 0.111 eV, 0.089 eV, 0.098 eV and 0.099 eV. The VBM ΔE is 0.096 eV, 0.135 eV, 0.133 eV and 0.134 eV. It is very clear that, compared with the GGA results, in general the mGGA conduction band tends to shift up while the valence band down. As a result, the mGGA bandgap energy is larger than the GGA. By investigating and comparing the topography of mGGA and GGA bandstructures, it clearly shows that, compared with GGA bandstructure, the shifting of the valley region of the bandstructure after applying mGGA functionals is negligible, While the energy difference is very evident at CBM and VBM positions. Thus the mGGA band is flatter than GGA band.

7.3.3 A Comparison Between AA and AB Bandstructure

It is of our great interest to figure out how the piling orientation affects the bandstructure of MoS_2. To investigate this matter, by comparing the bandstructure of

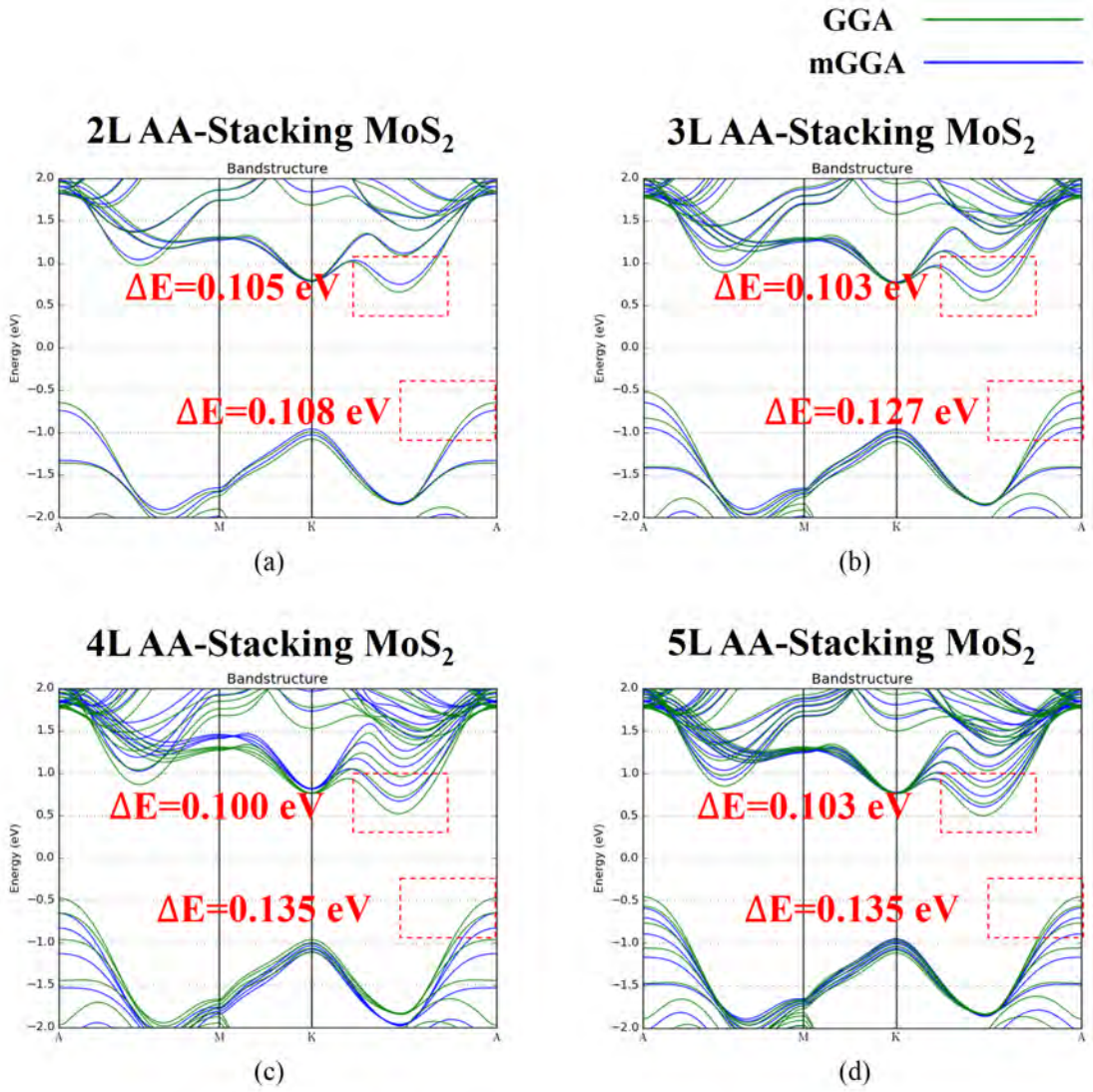

Figure 7.6: The Comparison between the GGA and Meta-GGA Bandstructure of AA MoS_2. (a)-(d), the comparison between the GGA and mGGA bandstructure of 2-5 L AA MoS_2, where the green line represents the GGA bandstructure and the blue line denotes the mGGA bandstructure. The energy difference ΔE (eV) is the energy difference between the GGA and mGGA bandstructure at the critical k points (labeled out by the red dashed frames).

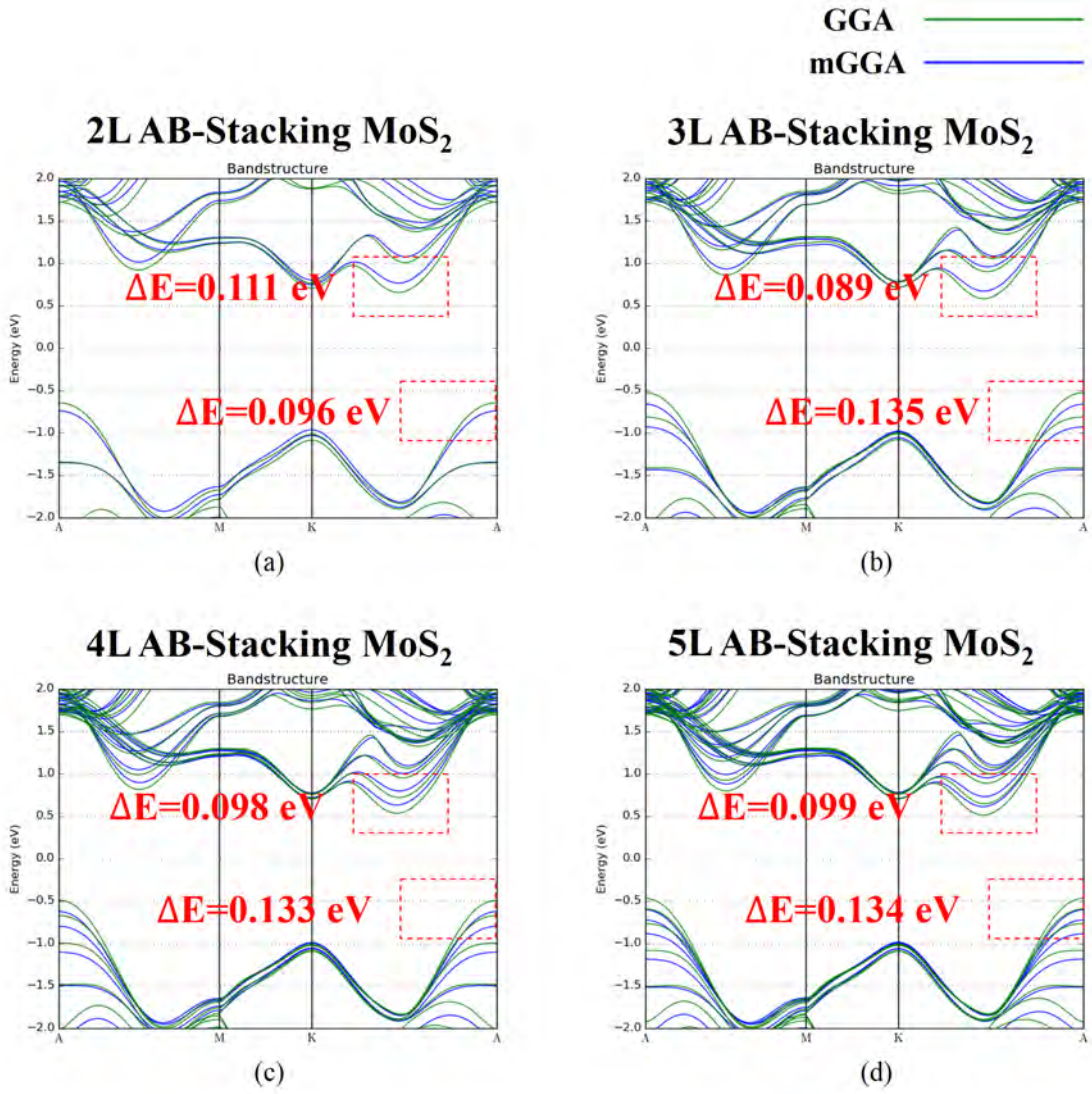

Figure 7.7: The Comparison between the GGA and Meta-GGA Bandstructure of AB MoS_2. (a)-(d), the comparison between the GGA and mGGA bandstructure of 2-5 L AB MoS_2, where the green line represents the GGA bandstructure and the blue line denotes the mGGA bandstructure. The energy difference ΔE (eV) is the energy difference between the GGA and mGGA bandstructure at the critical k points (labeled out by the red dashed frames).

AA and AB MoS_2, the energy difference ΔE located at CBM and VBM has been carefully calculated.

In fig-7.8 to fig-7.10, the Zoom-in plots at the critical k points are exhibited, which could give us a better view of the local ΔE. To determine whether the ΔE shows layer dependence, the 2L, 3L and 5L MoS_2 samples are investigated. The optimized bandstructure simulation results are provided by using the mGGA method. As shown in fig-7.8 (a), fig-7.9 (a) and fig-7.10 (a), the bandstructures of AA and AB MoS_2 samples do not show large mismatch. As shown in fig-7.8 (b) and (c), for 2L case, the CBM energy difference between AA and AB bandstructure is 0.017 eV, while the VBM energy difference is 0.001 eV. As shown in fig-7.9 (b) and (c), for 3L AA and AB MoS_2, the CBM energy difference is 0.010 eV, and the VBM energy difference is 0.013 eV. The CBM and VBM energy difference between 5L AA and AB MoS_2 is shown by fig-7.10 (b) and (c), which is 0.009 eV and 0.014 eV respectively. In general, considering the topography of AA and AB bandstructure, for both the AA and AB MoS_2, the CBM is located between K and A point, while the VBM lies at the A point. For AA stacking, in the conduction band, degenerate bands split from each other at the K point. The local CBM at the K point is the only joint for degenerate bands to diverge and converge. For AB MoS_2, the degenerate bands could be divided into two groups, and each group converges and diverges at its own joint at the K point. Compared with the original band position in AA cases, in AB bandstructures, one group of degenerate bands shift upwards while the other shifts downwards. This further degeneration by switching the MoS_2 stacking from AA to AB makes the conduction band edge in AB MoS_2 bandstructure shift towards the forbidden gap, which makes the local bands near the CBM of the AB MoS_2 bandstructure flatter than AA. This modification of the band edge slope will impact the electron effective mass greatly since it will reduce the second derivative of the band function, resulting a larger electron effective mass. The band shifting due to the degeneracy generated by AB piling orientation also occurs in the valence band, as shown in fig-7.8 (c), fig-

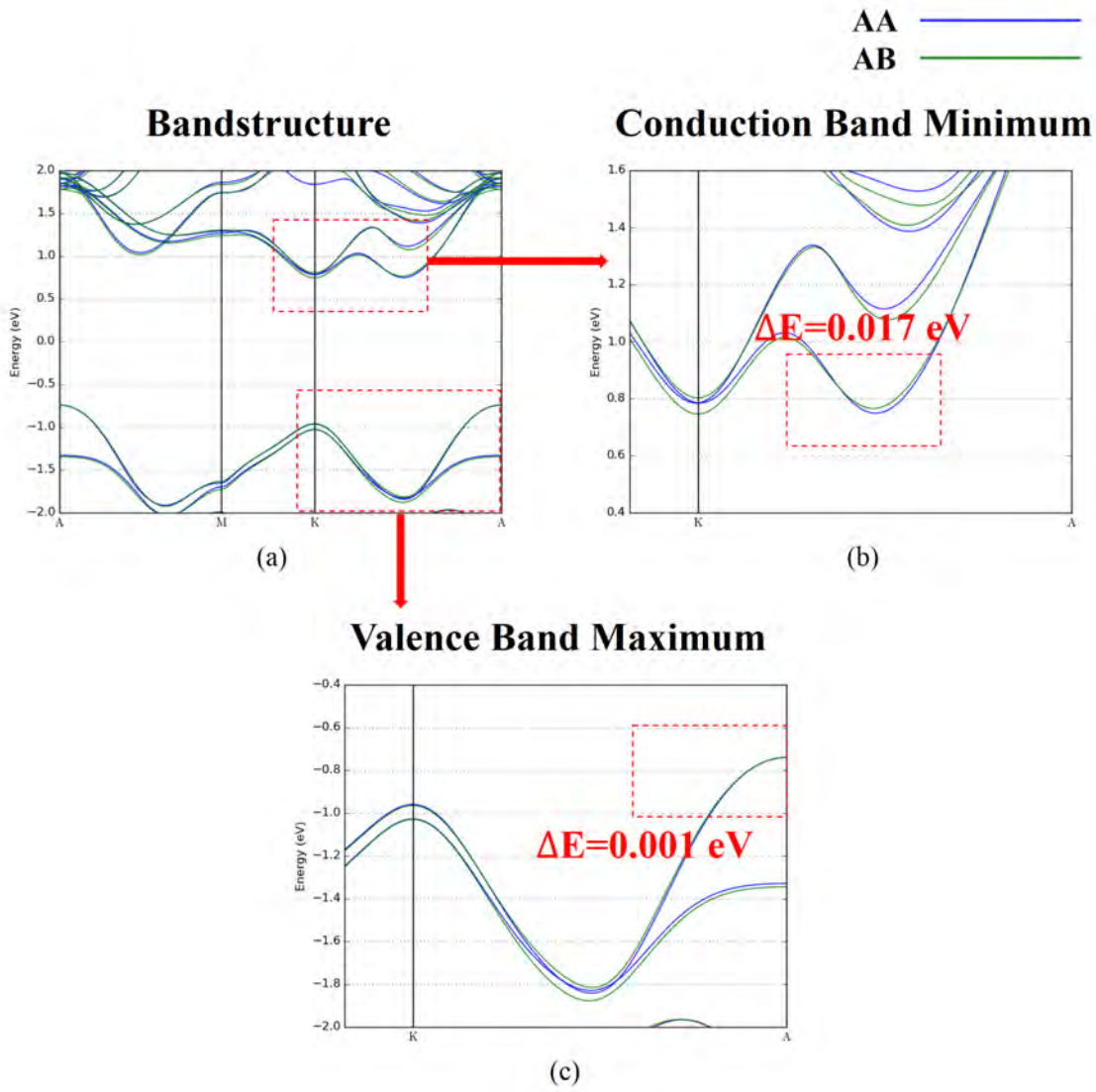

Figure 7.8: The Bandstructure Comparison between 2L AA and AB MoS_2. (a), the bandstructure of 2L AA and AB MoS_2. (b), the zoom-in plot of the CBM. (c), the zoom-in plot of the VBM. In (a)-(c), the green line represents the GGA bandstructure and the blue line represents the mGGA bandstructure. The energy difference ΔE (eV) is the energy difference between the AA and AB bandstructure at the critical k points (labeled out by the red dashed frames). The bandstructure is simulated by using mGGA.

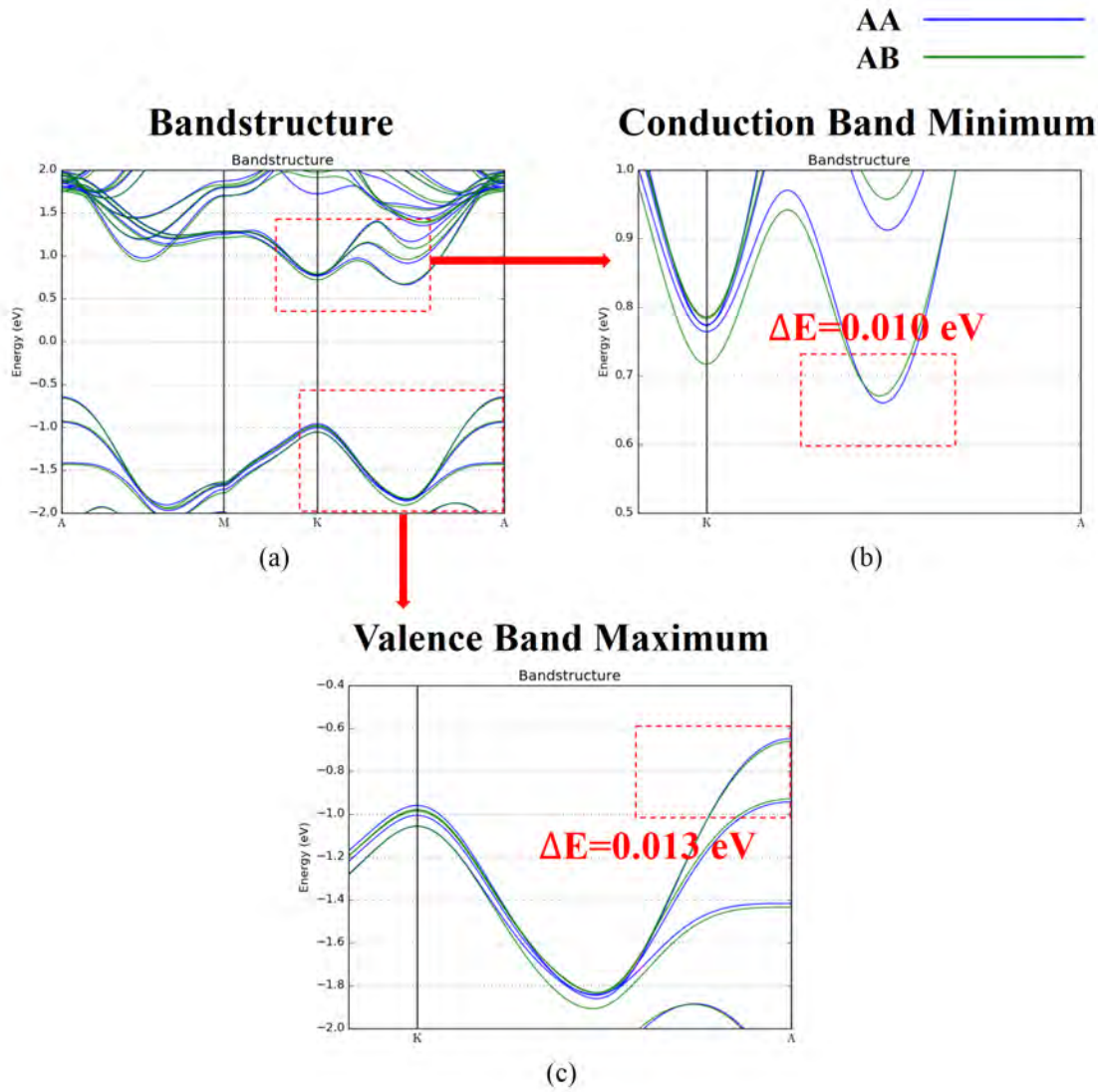

Figure 7.9: The Bandstructure Comparison between 3L AA and AB MoS_2. (a), the bandstructure of 3L AA and AB MoS_2. (b), the zoom-in plot of the CBM. (c), the zoom-in plot of the VBM. In (a)-(c), the green line represents the GGA bandstructure and the blue line represents the mGGA bandstructure. The energy difference ΔE (eV) is the energy difference between the AA and AB bandstructure at the critical k points (labeled out by the red dashed frames). The bandstructure is simulated by using mGGA.

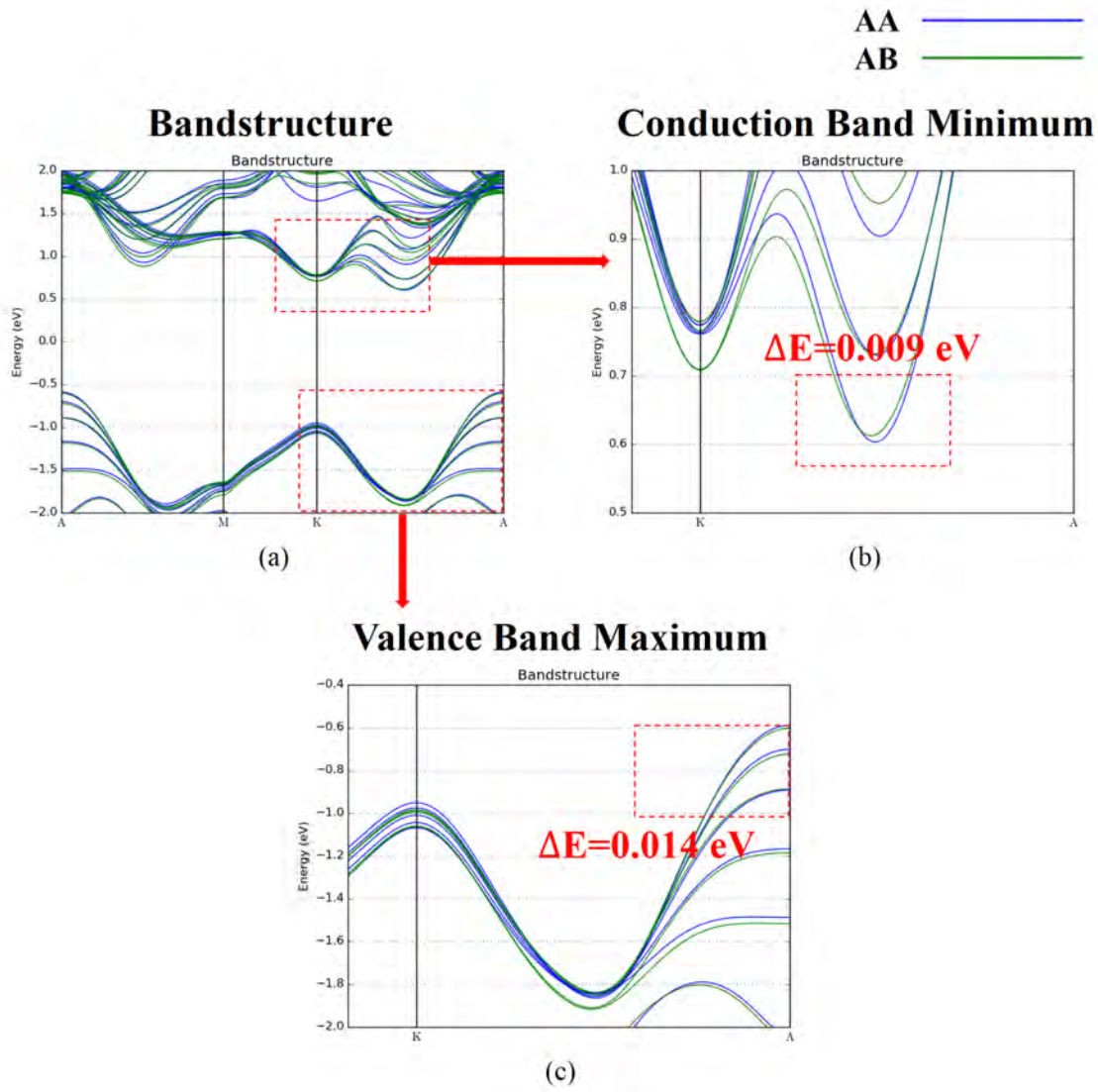

Figure 7.10: The Bandstructure Comparison between 5L AA and AB MoS_2. (a), the bandstructure of 5L AA and AB MoS_2. (b), the zoom-in plot of the CBM. (c), the zoom-in plot of the VBM. In (a)-(c), the green line represents the GGA bandstructure and the blue line represents the mGGA bandstructure. The energy difference ΔE (eV) is the energy difference between the AA and AB bandstructure at the critical k points (labeled out by the red dashed frames). The bandstructure is simulated by using mGGA.

Table 7.1: Bandgap Energy and the Position of CBM and VBM of AA MoS_2. In the table, ΔCBM denotes the difference between the mGGA method and GGA method of CBM, and ΔVBM denotes the difference between the mGGA method and GGA method of VBM. The E_g is the bandgap energy, and ΔE_g is the difference between the bandgap energy given by mGGA and GGA.

	CBM GGA (eV)	CBM mGGA (eV)	ΔCBM (eV)	VBM GGA (eV)	VBM mGGA (eV)	ΔVBM (eV)	E_g GGA (eV)	E_g mGGA (eV)	ΔE_g (eV)
2L	0.644	0.749	0.105	-0.632	-0.739	0.108	1.275	1.488	0.213
3L	0.558	0.660	0.103	-0.521	-0.648	0.127	1.078	1.308	0.230
4L	0.523	0.623	0.100	-0.475	-0.610	0.135	0.998	1.233	0.235
5L	0.500	0.603	0.103	-0.455	-0.590	0.135	0.955	1.193	0.238
6L	0.480	0.592	0.104	-0.443	-0.578	0.135	0.931	1.170	0.240
7L	0.480	0.585	0.105	-0.435	-0.571	0.136	0.915	1.156	0.241
8L	0.453	0.580	0.127	-0.409	-0.566	0.156	0.862	1.146	0.284
9L	0.470	0.622	0.152	-0.427	-0.603	0.175	0.897	1.225	0.327
10L	0.467	0.574	0.107	-0.425	-0.560	0.135	0.892	1.134	0.242

7.9 (c) and fig-7.10 (c). In AA MoS_2 bandstructure, one of the converge point of the degenerate bands in the valence band is located at the valley region between K and A point, and the other converge point is located at M point. In AB bandstructure, each converge point is degenerated into to two separate joints. The fig-7.8 (c), fig-7.9 (c) and fig-7.10 (c) intuitively show that, between the M and K point, the AB bands form two dispersed groups. In the plots, one group of the AB bands overlap with the AA bands, while the other group shifts downwards. In this case, the band shifting in the valence band does not modify the slope of the valence band edge largely.

7.3.4 Summary of Bandstructure Simulation

To provide a more comprehensive viewpoint, the calculated bandstructure parameters of 2L to 10L AA and AB MoS_2 are listed in the fig-7.11, table-7.1 and table-7.2 respectively. In general, as shown in fig-7.11 (a) and (b), both the AA and AB

Table 7.2: Bandgap Energy and the Position of CBM and VBM of AB MoS_2. In the table, ΔCBM denotes the difference between the mGGA method and GGA method of CBM, and ΔVBM denotes the difference between the mGGA method and GGA method of VBM. The E_g is the bandgap energy, and ΔE_g is the difference between the bandgap energy given by mGGA and GGA.

	CBM GGA (eV)	CBM mGGA (eV)	ΔCBM (eV)	VBM GGA (eV)	VBM mGGA (eV)	ΔVBM (eV)	E_g GGA (eV)	E_g mGGA (eV)	ΔE_g (eV)
2L	0.654	0.766	0.111	-0.645	-0.740	0.096	1.299	1.506	0.207
3L	0.582	0.671	0.089	-0.526	-0.661	0.135	1.108	1.332	0.224
4L	0.534	0.632	0.098	-0.490	-0.623	0.133	1.025	1.255	0.231
5L	0.513	0.613	0.099	-0.470	-0.603	0.134	0.983	1.216	0.233
6L	0.502	0.601	0.099	-0.456	-0.592	0.136	0.958	1.193	0.235
7L	0.494	0.594	0.100	-0.449	-0.585	0.136	0.943	1.179	0.236
8L	0.487	0.589	0.102	-0.445	-0.580	0.135	0.932	1.169	0.237
9L	0.484	0.586	0.102	-0.441	-0.577	0.136	0.925	1.162	0.238
10L	0.481	0.583	0.102	-0.438	-0.574	0.135	0.919	1.156	0.238

bandstructures show thickness dependence. The bandgap energy of AA or AB MoS_2 decreases when the thickness increases. This trend starts to saturate after 5 layers, which matches the criterion adopted to define the bulk MoS_2 in the previous chapter.

The fig-7.11 also shows that, the mGGA provides universal correction to the bandgap energy of 2L to 10L AA and AB MoS_2. Due to the exchange-correlation functional issue, the GGA method tends to underestimate the bandgap energy of MoS_2. The mGGA solves the issue by including the kinetic energy of the electrons and Becke-Roussel potential [138]. By applying mGGA, the average correction to the bandgap energy of 2L to 10L AA MoS_2 is 0.250 eV. The bandgap energy correction for 2L to 10L AB MoS_2 is 0.231 eV. To be noticed, as shown in fig-7.11, the calculated results for 9L AA MoS_2 is invalid. We will fix this issue in the future. It is very clear that, mGGA method includes more corrections to the bandgap energy of both AA and AB MoS_2. Thus in the following parts, only the mGGA results will be discussed for the bandstructure and effective mass analysis. By comparing the AA and AB bandstructure, it is intuitive that, the AB bandstructure does not differ from AA largely in terms of the energy level. But the broken symmetry of the AB MoS_2 structure generates further degeneration of both conduction and valence band. The band edge of the conduction band shifts and results in a flatter local band near the CBM. The impact of the band shifting on electron effective mass will be discussed in the following chapters.

7.4 The Effective Mass Analysis of AA and AB Molybdenum Disulfide

After the simulation of bandstructure, the calculation of electron effective mass has been performed for 2-10L AA and AB MoS_2. By applying the equation 7.2 and 7.3, the effective mass in X direction m_{eff_x}, and the effective mass in Y direction m_{eff_y}, are extracted by calculating the numerical second-order derivative of the band function. After that, the electron effective mass m_{eff} has also been calculated by using the

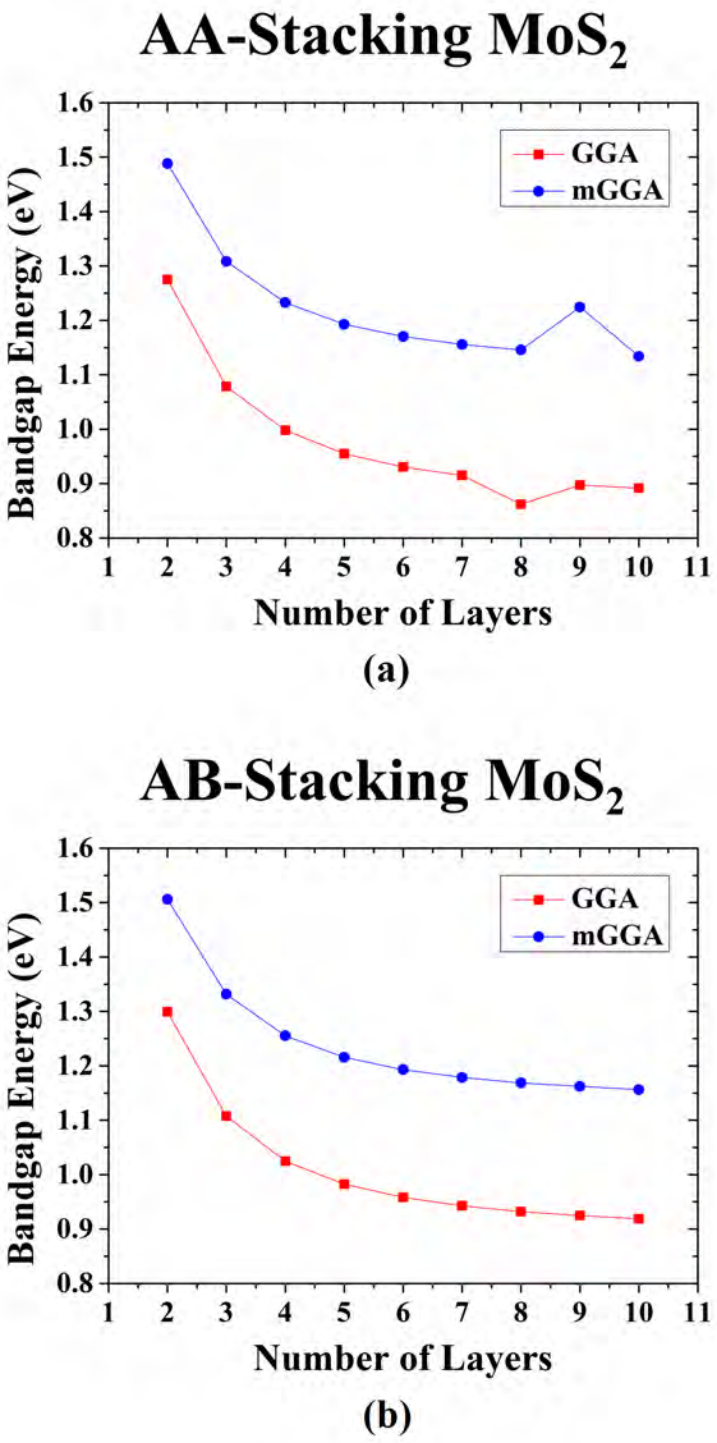

Figure 7.11: The Bandgap Energy of 2-10 L AA and AB MoS_2. (a), the bandgap energy of 2 to 10 L AA MoS_2. (b), the bandgap energy of 2 to 10 L AB MoS_2. In the plots, both the GGA and mGGA results are provided. The red line and squares denotes the GGA results while the blue line and dots refers to the mGGA results.

Table 7.3: Electron Effective Mass of AA MoS_2. In the table, the m_{eff_x} denotes the effective mass in x direction, the m_{eff_y} is the effective mass in y direction, m_{eff} is the effective mass. The unit m_0 is the electron rest mass, which is 9.10E-31 kg.

	m_{eff_x} GGA (m_0)	m_{eff_x} mGGA (m_0)	m_{eff_y} GGA (m_0)	m_{eff_y} mGGA (m_0)	m_{eff} GGA (m_0)	m_{eff} mGGA (m_0)
2L	0.589	0.654	0.854	0.978	0.697	0.784
3L	0.573	0.640	0.793	0.908	0.665	0.751
4L	0.565	0.634	0.769	0.880	0.651	0.737
5L	0.560	0.629	0.757	0.865	0.644	0.728
6L	0.557	0.626	0.750	0.856	0.639	0.723
7L	0.555	0.624	0.745	0.850	0.636	0.720
8L	0.534	0.623	0.788	0.847	0.637	0.718
9L	0.553	0.567	0.740	0.778	0.633	0.656
10L	0.552	0.621	0.739	0.842	0.632	0.715

equation 7.2.

For a few layers of MoS_2, the electron effective mass shows strong layer dependence. As shown in table-7.3, and fig-7.12 (a) to (c), for AA MoS_2, the m_{eff_x}, m_{eff_y}, and m_{eff} decrease while MoS_2 thickness increasing. For 2L AA MoS_2, the m_{eff_x}, m_{eff_y} and m_{eff} is 0.654 m_0, 0.978 m_0 and 0.784 m_0, while for 10L AA MoS_2, the corresponding effective mass decreases to 0.621 m_0, 0.842 m_0 and 0.715 m_0.

Compared with the effective mass of AA MoS_2, as shown in table-7.4, and fig-7.13 (a) to (c), the m_{eff_y} and m_{eff} of AB MoS_2 show similar layer dependence. The m_{eff_y} and m_{eff} of AB MoS_2 decrease with the number of layers increasing. When the AB MoS_2 thickness increases from 2L to 10L, m_{eff_y} and m_{eff} of AB MoS_2 decrease from 1.032 m_0 and 0.843 m_0 to 0.873 m_0 and 0.776 m_0 respectively. To be noticed, the 2L m_{eff_y} is larger than 1 m_0, which is comparable to the reported results calculated by other hybrid functionals [209]. The overestimation of electron effective mass by using hybrid functionals is a common issue. The m_{eff_x} of AB MoS_2 exhibits a different

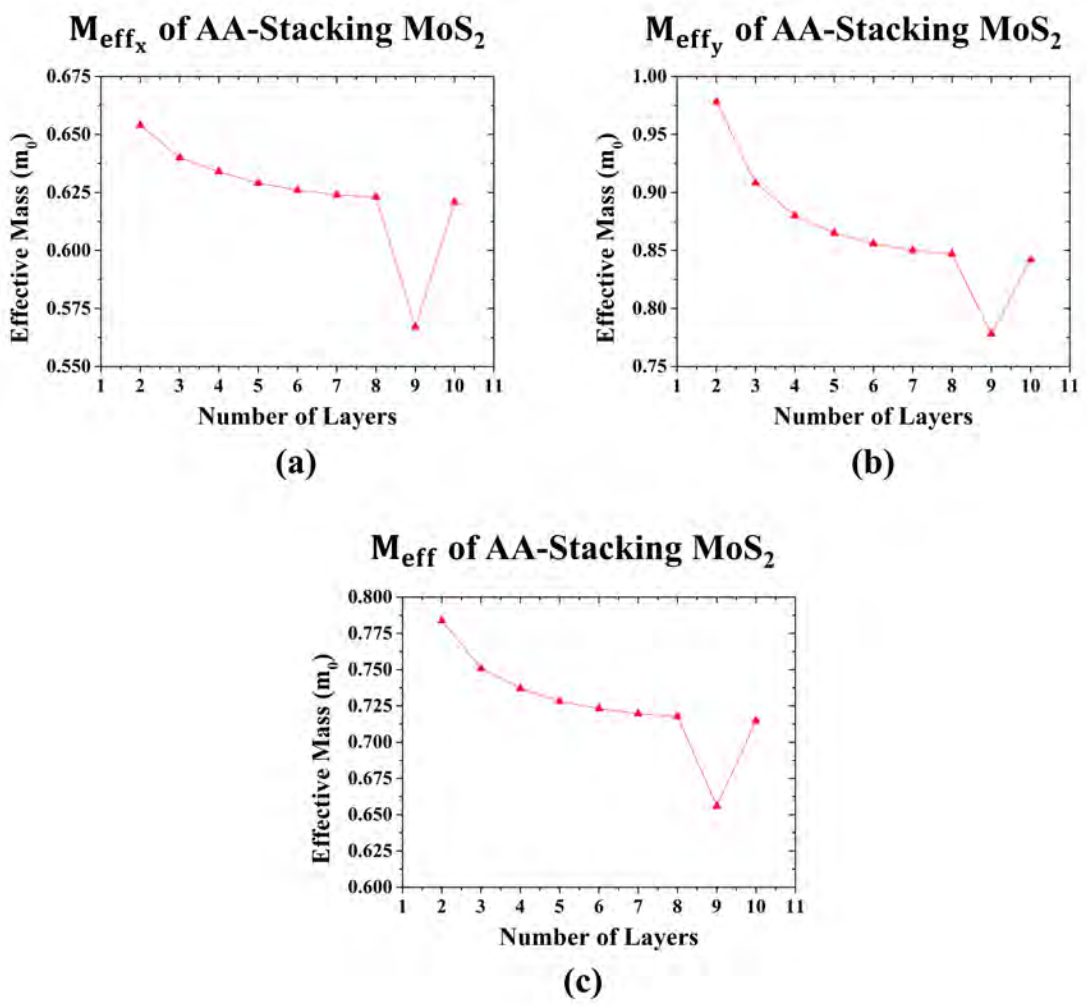

Figure 7.12: The Effective Mass of 2-10L AA MoS_2. (a), effective mass in x direction (transverse direction) m_{eff_x}. (b), effective mass in y direction (longitude direction) m_{eff_y}. (c), total effective mass m_{eff}. In the plots, for the m_{eff_x}, m_{eff_y} and m_{eff}, the unit m_0 is the electron rest mass, which is 9.10E-31 kg.

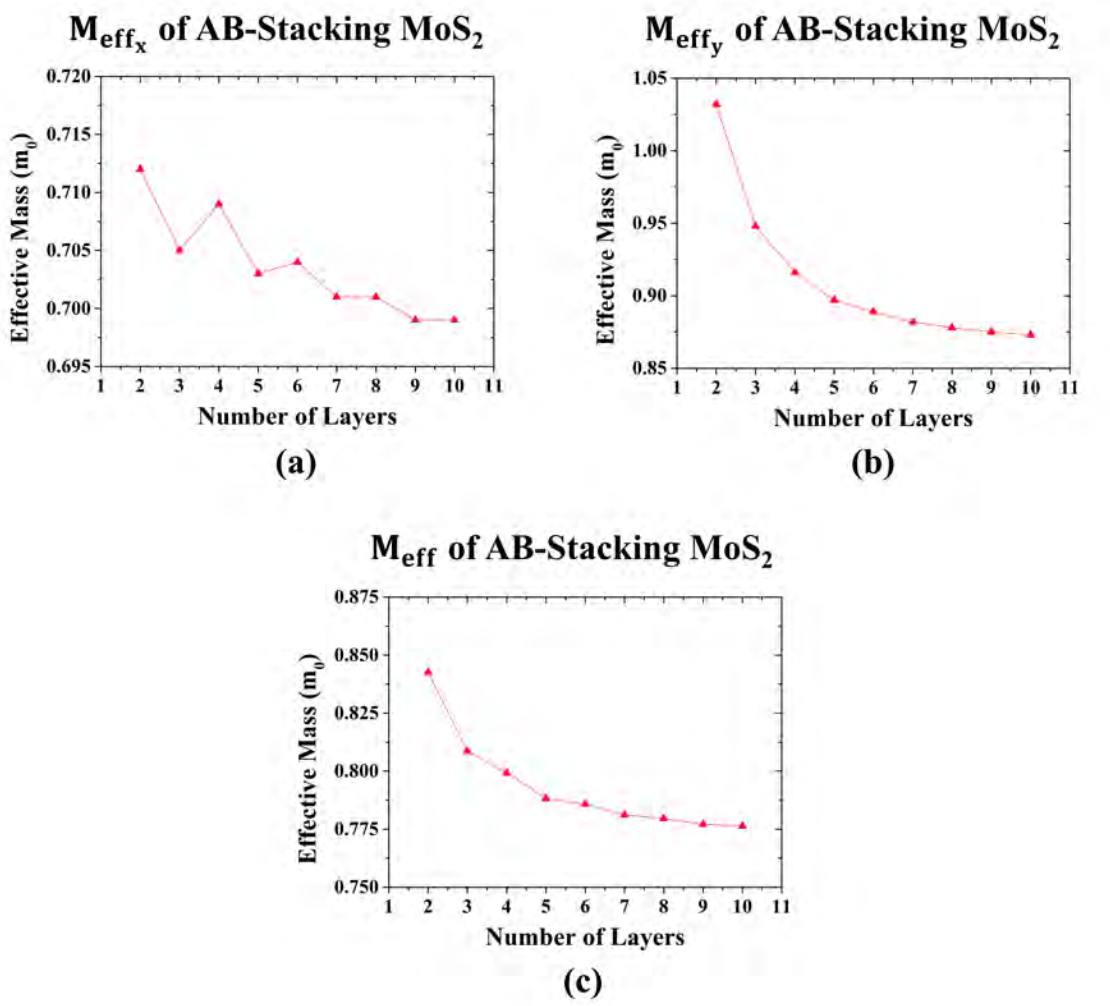

Figure 7.13: The Effective Mass of 2-10L AB MoS_2. (a), effective mass in x direction (transverse direction) m_{eff_x}. (b), effective mass in y direction (longitude direction) m_{eff_y}. (c), total effective mass m_{eff}. In the plots, for the m_{eff_x}, m_{eff_y} and m_{eff}, the unit m_0 is the electron rest mass.

Table 7.4: Electron Effective Mass of AB MoS_2. In the table, the m_{eff_x} denotes the effective mass in x direction, the m_{eff_y} is the effective mass in y direction, m_{eff} is the effective mass. The unit m_0 is the electron rest mass.

	m_{eff_x} GGA (m_0)	m_{eff_x} mGGA (m_0)	m_{eff_y} GGA (m_0)	m_{eff_y} mGGA (m_0)	m_{eff} GGA (m_0)	m_{eff} mGGA (m_0)
2L	0.642	0.712	0.903	1.032	0.750	0.843
3L	0.634	0.705	0.831	0.948	0.719	0.809
4L	0.642	0.709	0.811	0.916	0.717	0.799
5L	0.636	0.703	0.795	0.897	0.707	0.788
6L	0.638	0.704	0.788	0.889	0.705	0.786
7L	0.635	0.701	0.782	0.882	0.701	0.781
8L	0.636	0.701	0.779	0.878	0.700	0.780
9L	0.634	0.699	0.776	0.875	0.698	0.777
10L	0.634	0.699	0.774	0.873	0.697	0.776

correlation to the MoS_2 thickness from AA cases. As shown in fig-7.13 (a), the m_{eff_x} vs thickness curve of AB MoS_2 shows a zig-zag feature. While the main trend of the curve is that the m_{eff_x} decreases with the thickness of AB MoS_2 increasing, small fluctuations occur in the range of 2 to 7L. After 7L, the m_{eff_x} vs thickness curve starts to saturate.

The fig-7.14 (a) to (c) exhibits the electron effective mass comparison between 2-10L AA and AB MoS_2. For both AA and AB MoS_2, the trend of the curves in the fig-7.14 (a) to (c) clearly show that, while the thickness of the MoS_2 increasing, the effective mass of the MoS_2 will decrease. This trend is intuitive for 2L to 6L MoS_2. After 6L of MoS_2, the curves start to saturate to a constant value. This result indicates that, the electronic properties of few-layer AA and AB MoS_2, which is partially demonstrated by the carrier effective mass, is sensitive to the thickness variation. In this case, the thicker MoS_2 exhibits a smaller electron effective mass, thus a larger electron mobility. After 6 layers, the effective mass will be saturated very

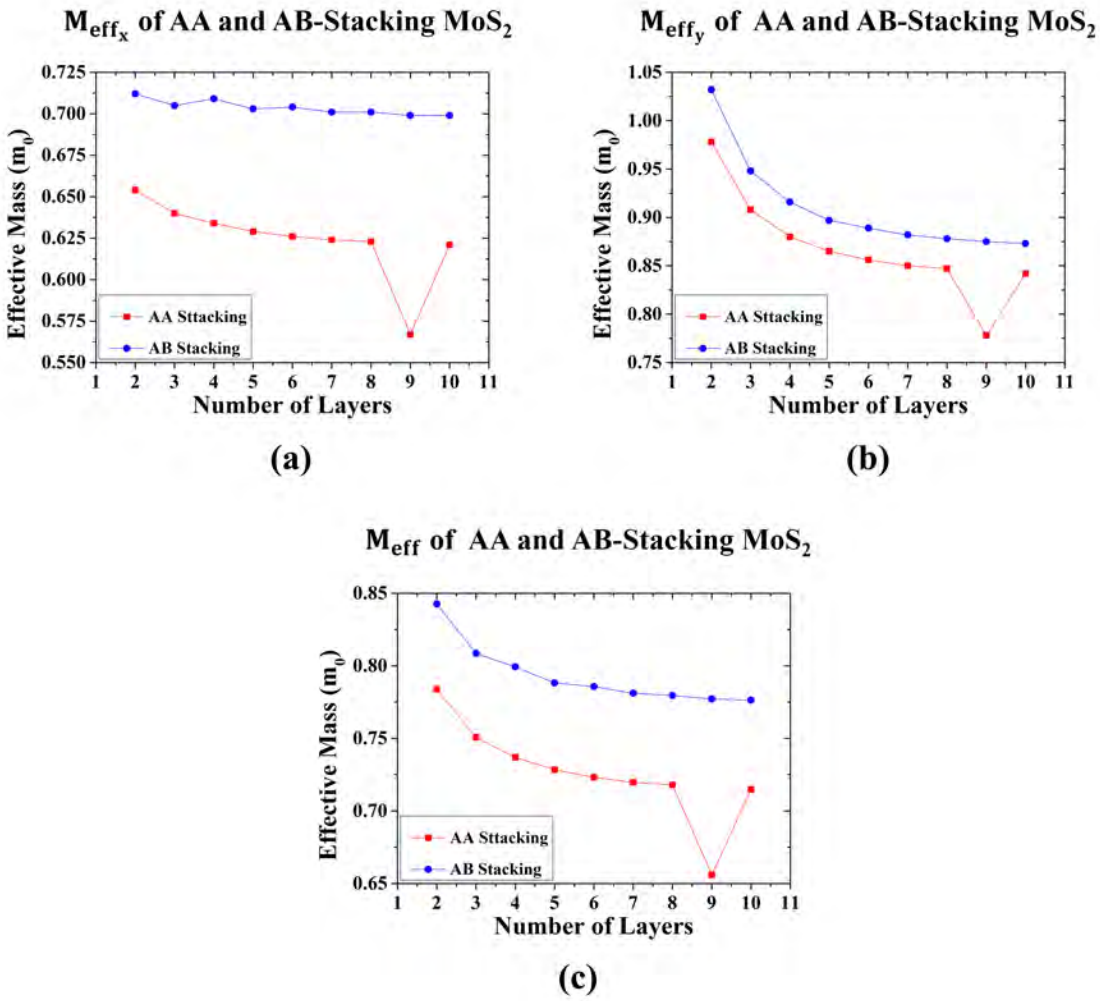

Figure 7.14: The Effective Mass of 2-10L AA and AB MoS_2. (a), effective mass in x direction (transverse direction) m_{eff_x}. (b), effective mass in y direction (longitude direction) m_{eff_y}. (c), total effective mass m_{eff}. In the plots, for the m_{eff_x}, m_{eff_y} and m_{eff}, the unit m_0 is the electron rest mass. The red line denotes the simulated effective mass for AA MoS_2, and the blue line denotes the simulated effective mass for AB MoS_2.

quickly since the MoS_2 start to become bulk configuration. On the other hand, the calculation identifies that, with the same thickness, the AB MoS_2 always show a larger effective mass than AA MoS_2. As what is mentioned in the previous chapter, the edge of the conduction band of AB MoS_2 bandstructure shifts towards the forbidden gap and causes a flatter CBM, compared with AA MoS_2 with same thickness. Considering the equation 7.2 and 7.3, a flatter CBM means a larger effective mass. Thus, the band shifting of AB MoS_2, which is generated by the modification of piling orientation, correlates with the larger electron effective mass AB MoS_2 possesses. As shown in fig-7.14 (a), the m_{eff_x} of AB MoS_2 shows a slower zig-zag decreasing, which is different from the trend of AA MoS_2. This is mainly due to the fact that the periodicity of the lattice structure of AB MoS_2 super lattice is different from AA MoS_2 in X and Z direction. As a comparison, the fig-7.14 (b) shows that the m_{eff_y} variation trend of AA MoS_2 is exactly the same as AB MoS_2. This result will be discussed and analyzed in details in the following chapters.

To be noticed, it is clearly that, the electron effective mass results for 9L AA MoS_2 are not valid. For this reason, the data points of 9L AA MoS_2 are excluded in the previous discussion. The solution of solving this issue will be included in our future work.

7.4.1 The Variation of the Effective Mass of Multilayer Molybdenum Disulfide with Different Piling Orientations

The previous chapters have shown that the morphology of the MoS_2 bandstructure shows great geometry dependence. To gain a comprehensive understanding of the designed MoS_2 devices, it is of great importance to investigate the effective mass variation in terms of the piling orientation changing. In this study, all the possible piling orientations of 4L, 5L and 6L MoS_2, including the AA stacking, AB stacking and mixed piling orientations, are created by exhaustive attack method Exhaustive Attack Method (EAM) and investigated. The naming system of the EAM cases is as

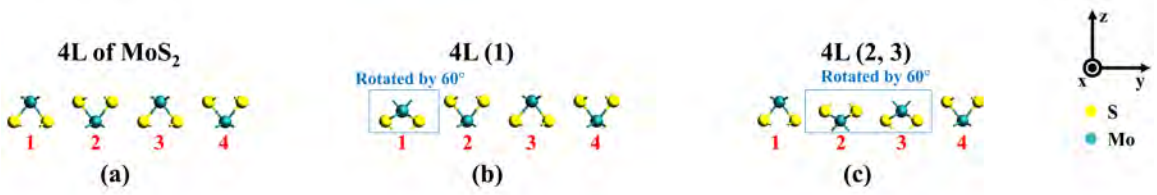

Figure 7.15: The Naming System for MoS_2 with Mixed Piling Orientations. Here we take 4L MoS_2 as an example. (a), 4L AA MoS_2. From left to right, the top layer of MoS_2 is labelled as layer 1, and the other layers are labelled as 2, 3, and 4 respectively. (b), the layer 1 of the 4L AA MoS_2 is rotated by 60°. The structure is denoted by 4L (1). (c), the layer 2 and 3 are rotated by 60°. In this case, the structure is denoted by 4L (2, 3).

shown in fig-7.15 (a)-(c). Take 4L MoS_2 as an example, as shown in fig-7.15 (a), each MoS_2 layer along the z direction is labelled as 1, 2, 3 and 4. As shown in fig-7.15 (b), if the layer 1 exhibits a rotation compared with the AA 4L MoS_2, this 4L MoS_2 structure is labelled as '4L (1)'. In fig-7.15 (c), the layer 2 and 3 in the 4L MoS_2 are rotated. This 4L MoS_2 configuration with mixed piling orientation will be referred to '4L (2, 3)'.

The equation 7.3 and 7.4 demonstrate that, the electron effective mass is highly dependent on the E-K function. In other words, the shape of the band located around the CBM point determines the electron effective mass. The comparison between the AA and AB MoS_2 bandstructure confirms that, compared with AB MoS_2, the AA MoS_2 configuration with a lower CBM also exhibits a steeper bandstructure and smaller electron effective mass. This result indicates that it is valid to correlate the the electron effective mass with the CBM position.

After conducting the electron effective mass analysis to all the EAM cases, the electron effective mass distribution in terms of the CBM position has been plotted. The CBM correlation of the m_{eff_x}, m_{eff_y} and m_{eff} are exhibited in fig-7.16, fig-7.17 and fig-7.18 respectively. In the plots, the m_{eff_x}, m_{eff_y} and m_{eff} data points are labelled by green, blue and red squares separately. By investigating and summarizing the fig-7.16 to fig-7.18 carefully, several laws could be extracted. Firstly, for 4L, 5L and

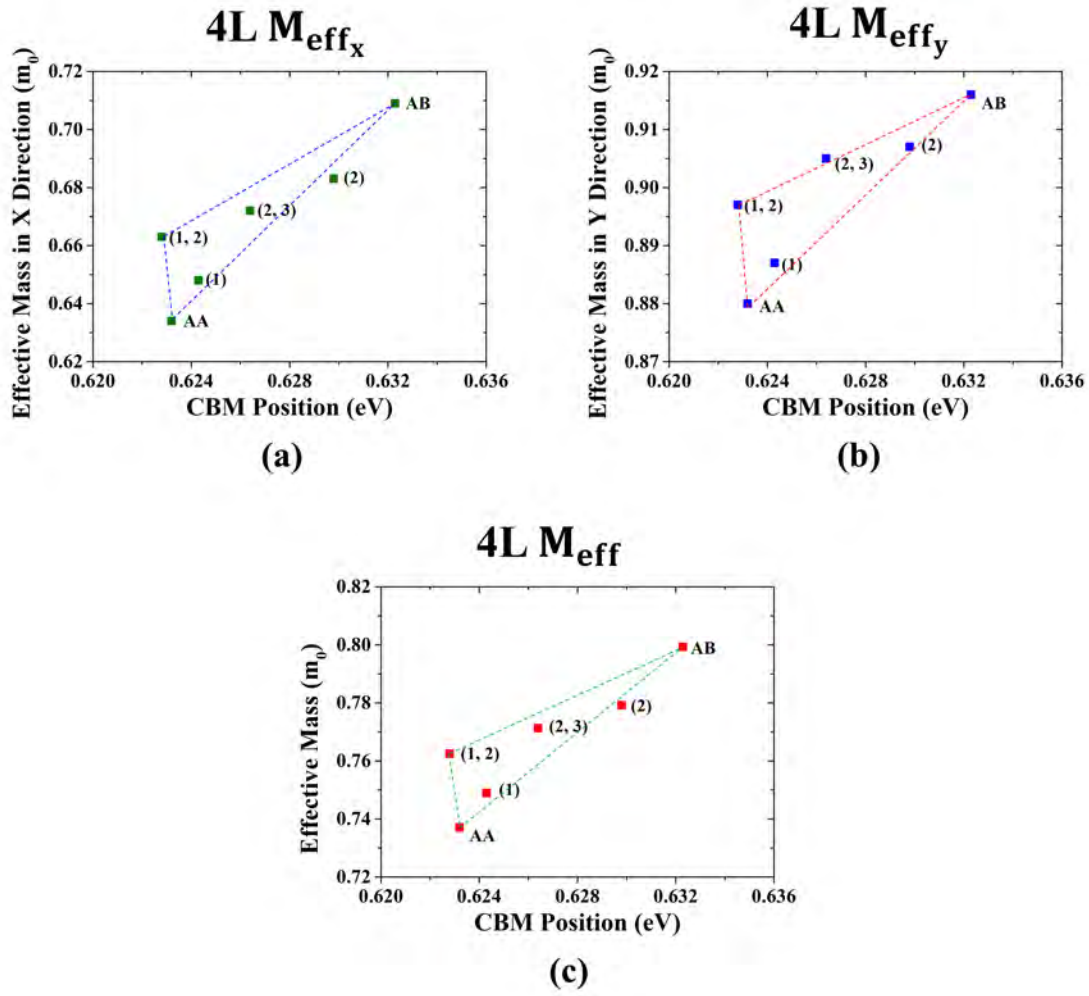

Figure 7.16: The Electron Effective Mass of All Possible Piling Orientations of 4L MoS_2. (a), the effective mass in X direction m_{eff_x}. (b), the effective mass in Y direction m_{eff_y}. (c), the total effective mass m_{eff}.

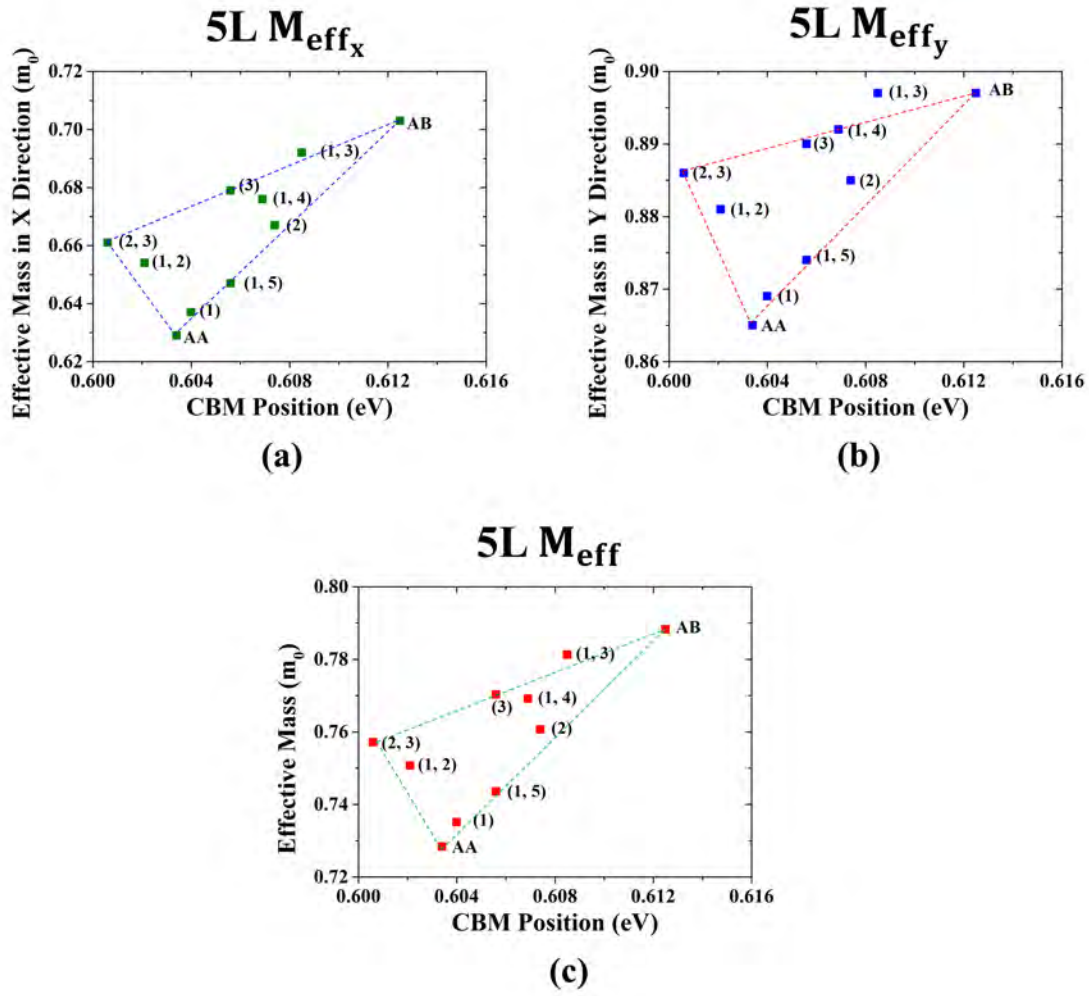

Figure 7.17: The Electron Effective Mass of All Possible Piling Orientations of 5L MoS_2. (a), the effective mass in X direction m_{eff_x}. (b), the effective mass in Y direction m_{eff_y}. (c), the total effective mass m_{eff}.

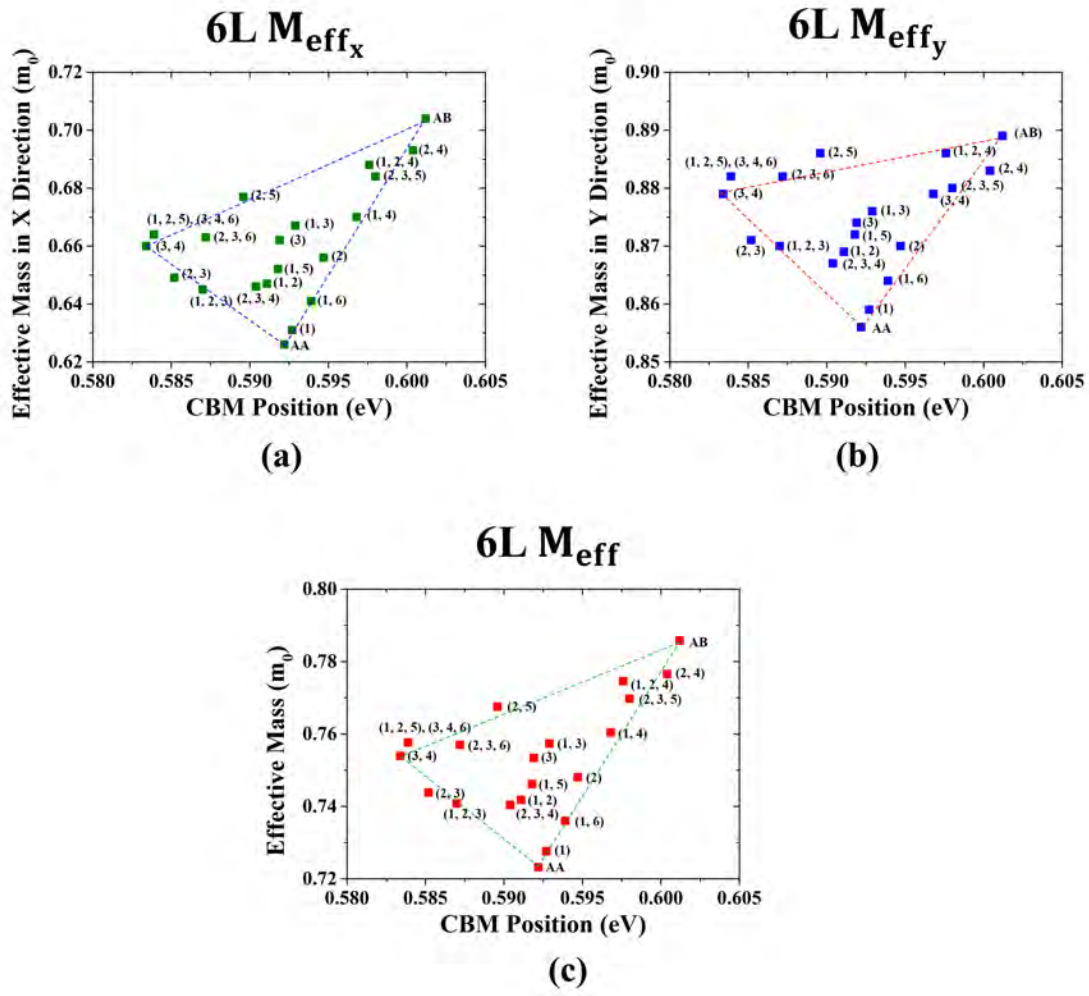

Figure 7.18: The Electron Effective Mass of All Possible Piling Orientations of 6L MoS_2. (a), the effective mass in X direction m_{eff_x}. (b), the effective mass in Y direction m_{eff_y}. (c), the total effective mass m_{eff}.

6L EAM cases, the m_{eff_x}, m_{eff_y} and m_{eff} shows very similar distribution in terms of the CBM energy. Under the circumstance, for the specific MoS_2 thickness, the variations of m_{eff_x}, m_{eff_y} and m_{eff} show great synchrony in terms of the geometry changing. Secondly, in each case, the AA MoS_2 always shows the smallest electron effective mass while the AB MoS_2 exhibits the largest effective mass. Finally, for each plot, a triangle region could be sketched out by connecting the top and bottom data points. To be noticed, no matter what the MoS_2 thickness it is, the AA and AB data points are always the two vertexes of the triangle region.

On the other hand, the simulation results presented by the fig-7.16 to fig-7.18 demonstrate that, although there is a strong correlation between the CBM position and the electron effective mass, but the CBM energy itself is not sufficient to fully describe the laws behind this correlation. The energy-effective mass triangle mentioned could be considered as a criterion to describe how far the CBM-effective mass correlation diverges from the ideal linear relationship. As shown in fig-7.16 (a) to (c), for 4L MoS_2 cases, the AA, 4L (1), 4L (2) and AB cases shows a linear pattern, while the 4L (1, 2) and 4L (2, 3) are the dispersed points. As shown in fig-7.17 and fig-7.18, the distribution of the data points is becoming more and more dispersed while the thickness of MoS_2 increasing. For 5L and 6L cases, more dispersed data points exist and the CBM-effective mass triangle becomes larger. It is very clear that, the data points beyond AA-AB curve provide counter-examples to the previous assumption: lower CBM means smaller effective mass. For example, as shown in fig-7.17 (a) to (c), the 5L (2, 3) configuration shows smaller CBM, but larger m_{eff_x}, m_{eff_y} and m_{eff}, compared with 5L AA MoS_2.

The simulation results presented in fig-7.16 to fig-7.18 demonstrates the synchrony of the m_{eff_x}, m_{eff_y} and m_{eff} variation. To further verify this synchrony, the scatter diagram of the m_{eff_x} and m_{eff_y} of the EAM cases has been plotted for 4-6L MoS_2. The m_{eff_x} is set as the X of the scatter diagram while the m_{eff_y} is set as the Y.

As shown in fig-7.19 (a), for 4L MoS_2, the EAM data points show a good linear

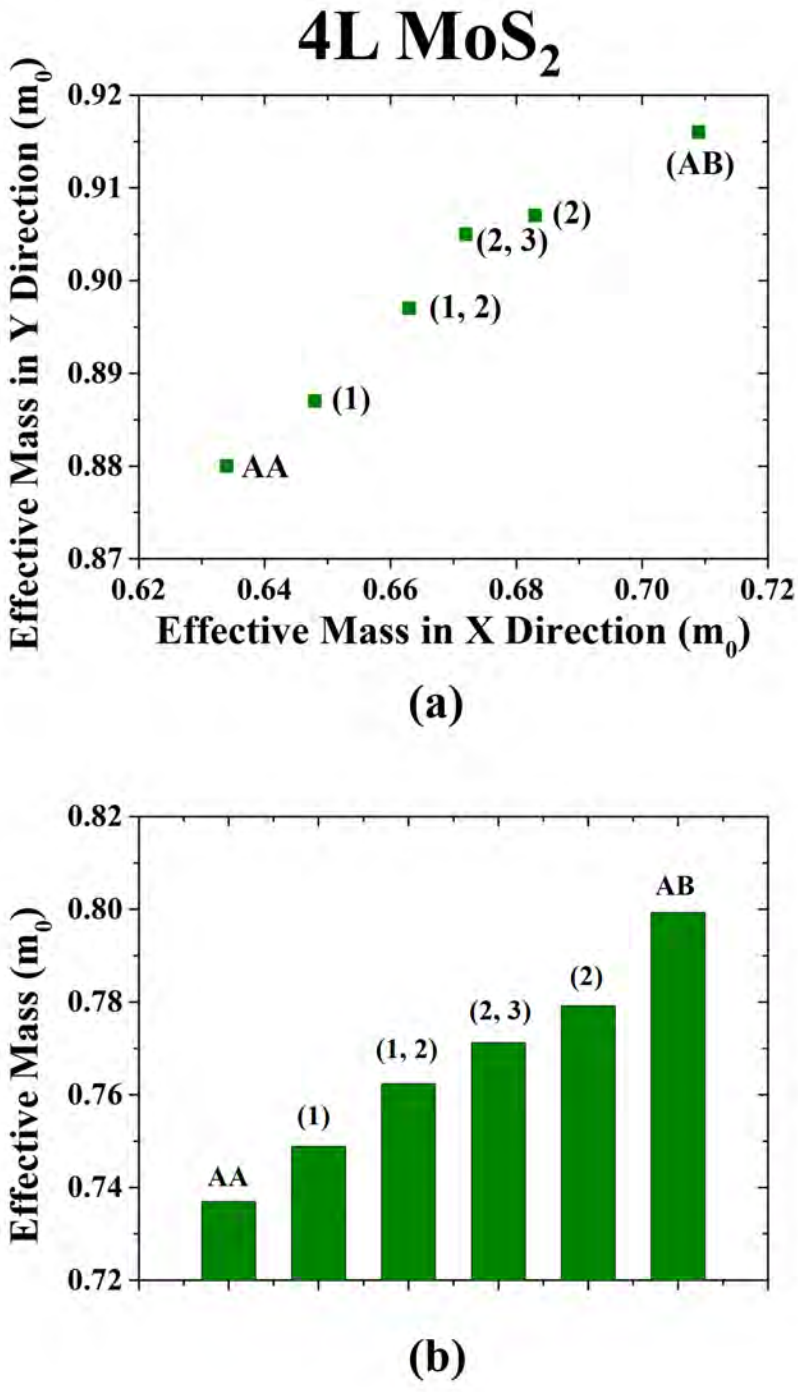

Figure 7.19: The Breakdown of the Electron Effective Mass of All Possible 4L Configurations. (a), the data point distribution in terms of the effective mass in X direction (m_{eff_x}) and the effective mass in Y direction (m_{eff_y}). (b), the bar chart of the total effective mass m_{eff}. The columns are arranged in an ascending order from the left to the right. The label on the top of each column denotes the corresponding configuration.

distribution. In this case, while a 4L MoS_2 film shows larger m_{eff_x} than other 4L films with different stacking orientations, it possesses a larger m_{eff_y} as well. The bar diagram of the m_{eff} provides with the scatter diagram supplementary results. As shown in fig-7.19 (b), the m_{eff} of 4L EAM cases are array in an ascending order. By comparing fig-7.19 (a) and (b), it is very clear that, for 4L EAM cases, the ascending order of the m_{eff} is in coincidence with the scatter diagram.

As shown in fig-7.20 and fig-7.21, the scatter diagram of 5L and 6L MoS_2 also shows a linear distribution, which is comparable to the 4L case. However, for 5L and 6L case, the data points between the AA and AB cases exhibit a scattered distribution. By comparison, the 6L case shows a more scattered distribution of data points than 5L case. This result matches the previous analysis. For 5L and 6L cases, the synchrony of the electron effective mass variation is broken due to the complicated geometry variation. As a result, as shown in fig-7.19 (b), fig-7.20 (b) and fig-7.22, the ascending trend of the electron effective mass m_{eff} of 6L MoS_2 cases is not as clear as 4L and 5L cases. As what is show by fig-7.22 (a) and (b), there are two flat regions in the bar diagram. In these flat regions, the MoS_2 configurations show very similar m_{eff} but different m_{eff_x} and m_{eff_y}.

The simulation results of 4-6L EAM cases clearly show that, the electron effective mass shows great dependence on the geometry of the MoS_2 sheets. Basically, on the one hand, systems with different symmetries lead to different solutions of the Schrödinger equation based on Bloch electron wave function. On the other hand, different piling orientations cause different interlayer interactions. All these factors will significantly modify the electron effective mass. To gain a comprehensive understanding, MP and EDP calculations have been performed.

7.5 Mulliken Population Analysis

The interlayer interaction of MoS_2 films will be modified by changing the MoS_2 piling orientation. This modification may explain the geometry dependence of the electron

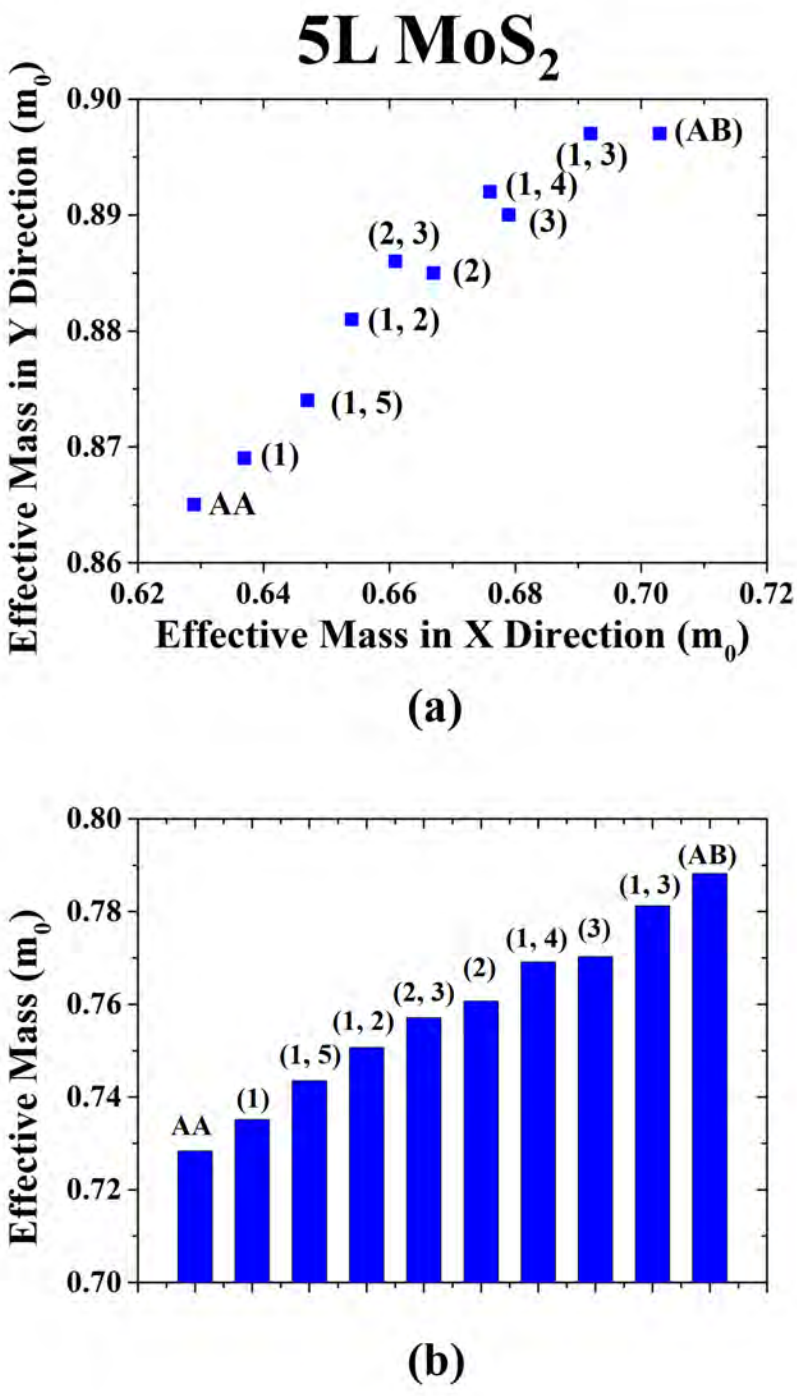

Figure 7.20: The Breakdown of the Electron Effective Mass of All Possible 5L Configurations. (a), the data point distribution in terms of the effective mass in X direction (m_{eff_x}) and the effective mass in Y direction (m_{eff_y}). (b), the bar chart of the total effective mass m_{eff}. The columns are arranged in an ascending order from the left to the right. The label on the top of each column denotes the corresponding configuration.

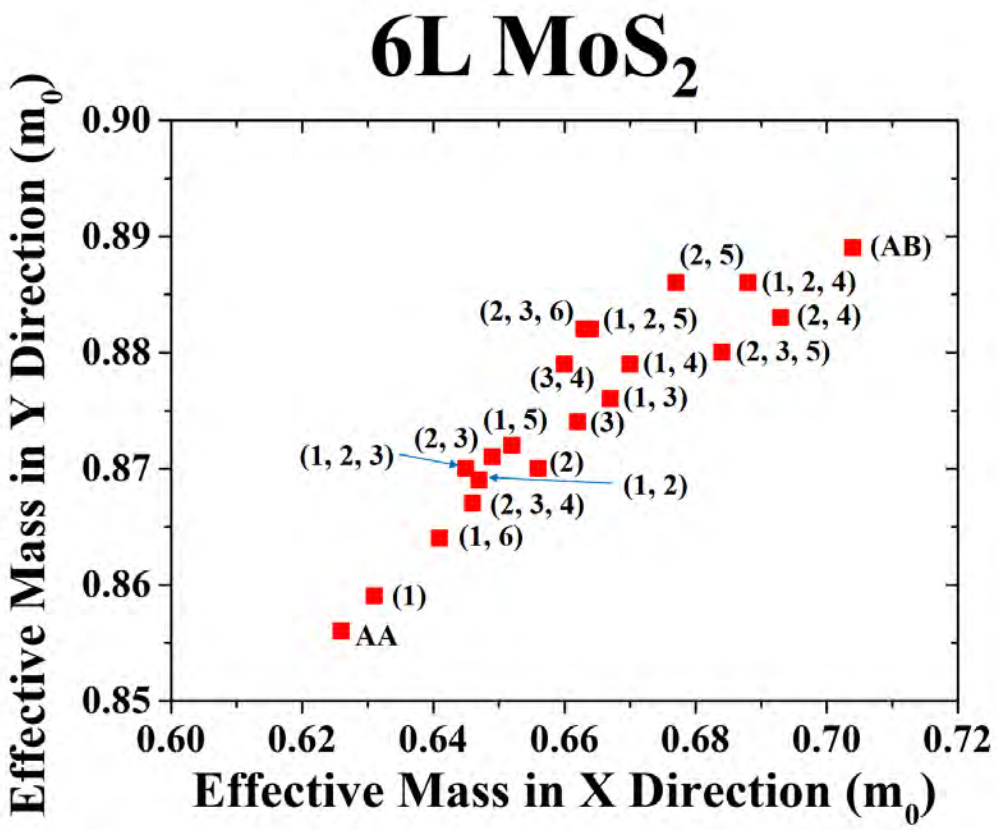

Figure 7.21: The Breakdown of the Electron Effective Mass of All Possible 6L Configurations. In the plot, the data point distribution in terms of the effective mass in X direction (m_{eff_x}) and the effective mass in Y direction (m_{eff_y}).

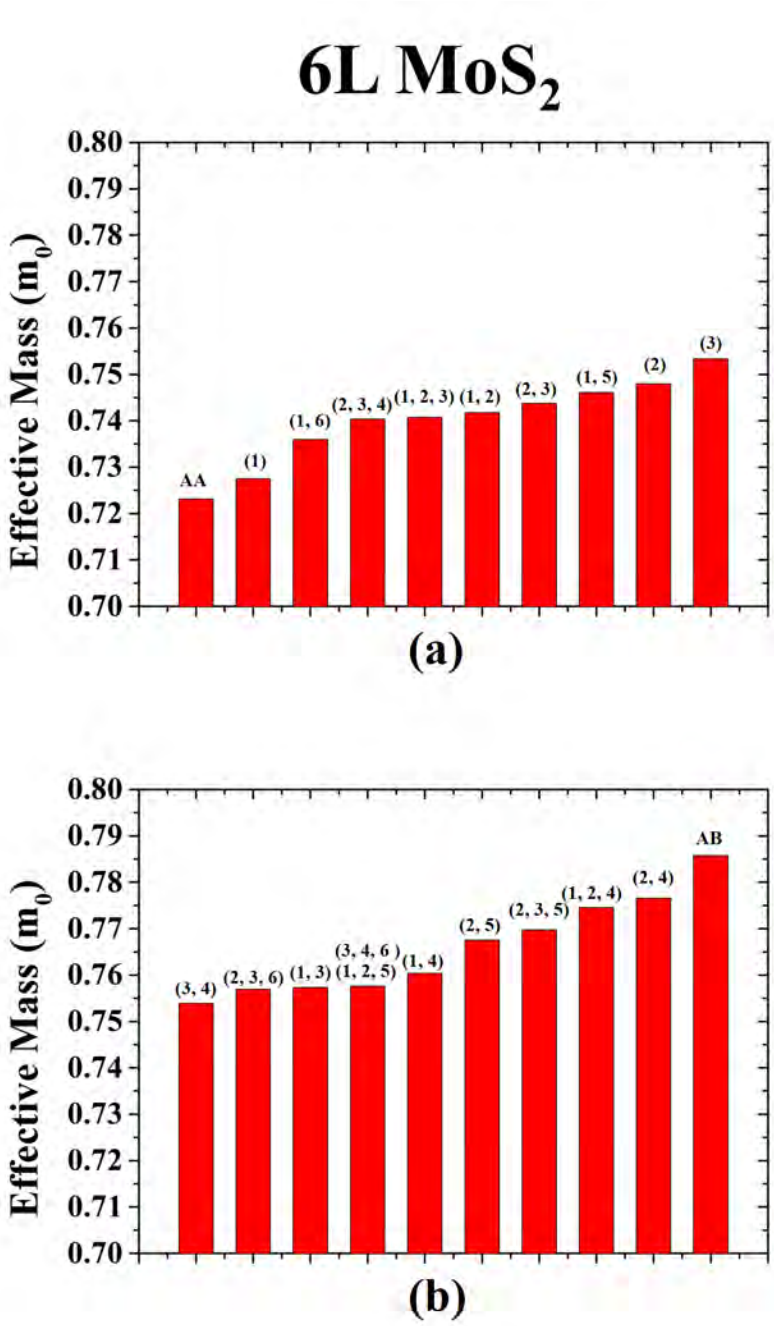

Figure 7.22: The Bar Chart of the Electron Effective Mass of All Possible 6L Configurations. (a), the first half of the bar chart. (b), the second half of the bar chart. The columns are arranged in an ascending order from the left to the right. The label on the top of each column denotes the corresponding configuration.

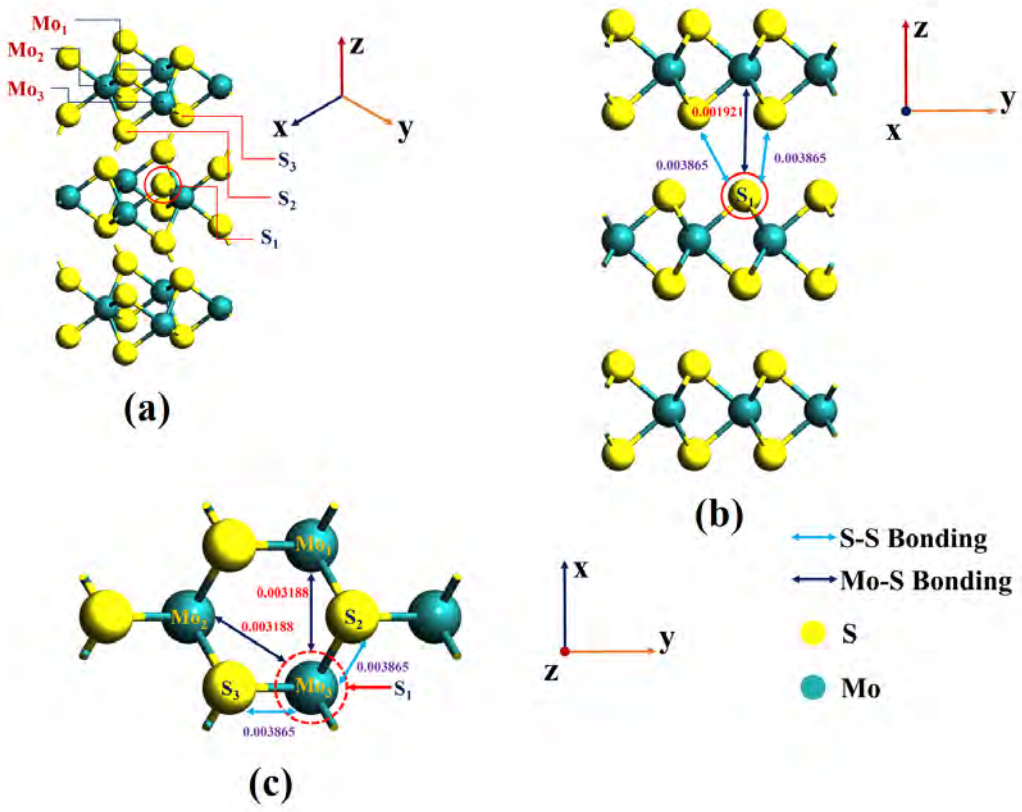

Figure 7.23: The MP Analysis of 3L AA MoS_2. In the plot, the 3D configuration and cross-section plots are provided. (a), the 3D configuration. (b), the cross-section plot of YZ plane (side view). (c), the cross-section plot of XY plane (top view). In each cross-section plot, the blue line denotes the bonding between S atoms and the navy blue line denotes the bonding between the Mo and S atoms. The Mo and S atoms investigated are labelled out in the figure by digit.

effective mass of MoS_2. To investigate the difference of the interfacial bonding condition between AA and AB configurations, the MP analysis has been conducted on 3L AA and AB MoS_2. The MP method is a powerful tool which provides us with an intuitive criterion to evaluate the strength of the electron bonding condition. Basically, a larger MP value of the specific bond indicates a stronger coupling between the relative atoms [61, 62].

As shown in fig-7.23 and fig-7.24, since the system is symmetric, only the bonding condition between the layer 1 and layer 2 is investigated in the analysis. One outer S atom in the layer 2 is chosen as the reference point, which is denoted as S_1. For each

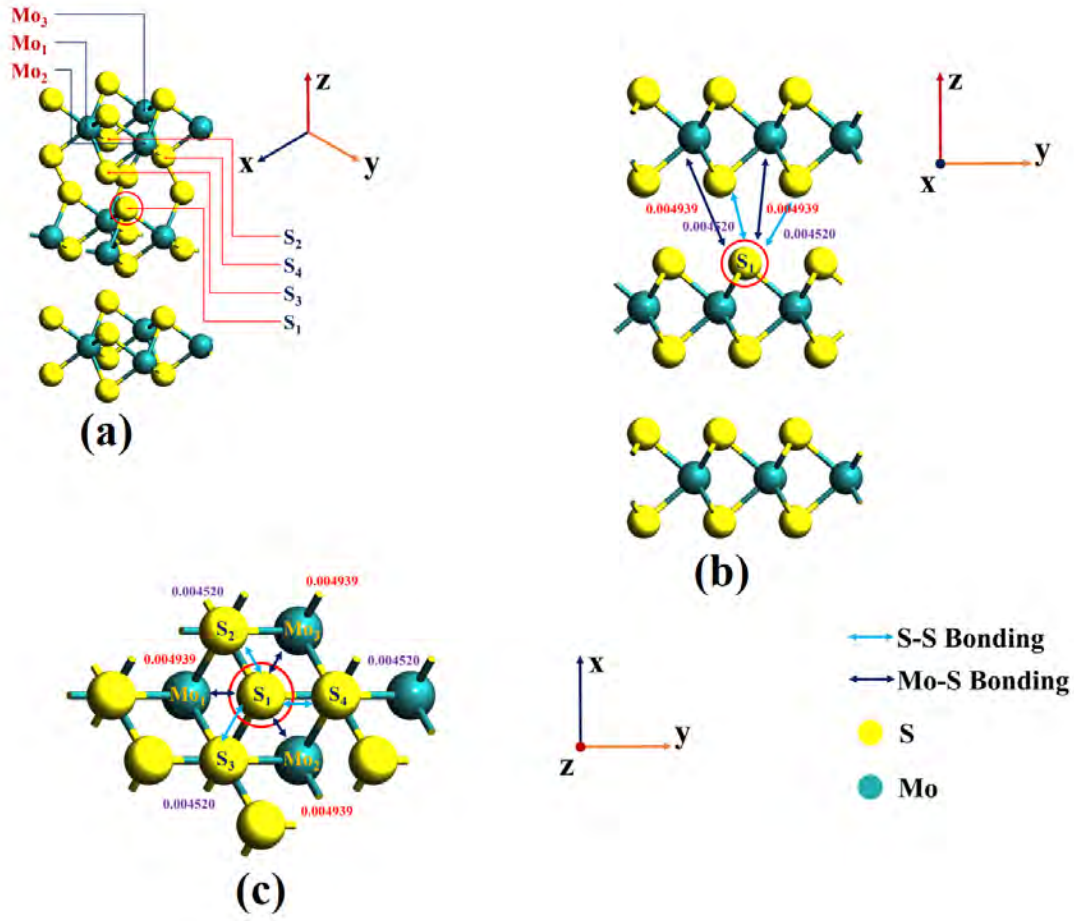

Figure 7.24: The MP Analysis of 3L AB MoS_2. In the plot, the 3D configuration and cross-section plots are provided. (a), the 3D configuration. (b), the cross-section plot of YZ plane (side view). (c), the cross-section plot of XY plane (top view). In each cross-section plot, the blue line denotes the bonding between S atoms and the navy blue line denotes the bonding between the Mo and S atoms. The Mo and S atoms investigated are labelled out in the figure by digit.

S and Mo atom in the layer 1 of the superlattice, the relative MP with the reference atom has been calculated. The atoms which show non-zero MP with the reference atom are labelled by digit, as what shown in fig-7.23 and fig-7.24. In the superlattice of AA MoS_2, there are 3 Mo atoms and 2 S atoms which have non-zero MP with S_1. In this case, atom S_1 just sits on the top of one labelled Mo atom. As for AB MoS_2, 3 Mo atoms and 3 S atoms show non-zero MP with S_1. Under the circumstances, S_1 sits on the hollow site and the distance between S_1 and the interacting Mo and S atoms is uniform. As shown in fig-7.23 (b), in the AA-stacking case, the MP of the Mo_3-S_1 bonding is 0.001921. To be noticed, the Mo_3 is the nearest interlayer Mo atom to the S_1. As for the two farther Mo atoms Mo_1 and Mo_2, both the MP of Mo_1-S_1 and Mo_2-S_1 bonding is 0.003188, since the two Mo atoms are at the same distance from the S_1. The MP between the reference atom and the two S atoms S_2 and S_3 is 0.003865. The MP results of AA MoS_2 shows that, the nearest Mo and S atoms have the weakest bonding. That's because of the electronegativity of the outer S atoms in layer 1 weaken the neighboring Mo-S bonding. As for AB MoS_2, the MP of the interlayer Mo-S bonding is 0.004939, while the MP of the interlayer S-S bonding is 0.004520. From the MP results we can see that, the MP of AB MoS_2 is larger than AA MoS_2, which indicates that AB MoS_2 films have a stronger interlayer interaction between the outer S and Mo atoms. To be noticed, a larger MP won't definitely lead to a larger average binding energy. As mentioned before, the average binding energy of AB MoS_2 is 0.12337 eV. For AA MoS_2 the average binding energy is 0.12379 eV. That is due to the cancellation between the repulsion of the interlayer S-S interaction and the attraction of the interlayer Mo-S interaction. In general, the MP simulation demonstrates that, the interlayer interaction in AA MoS_2 differs from which in AB MoS_2, as a result of the difference in the piling orientation. And this leads to the different spatial distribution of the EDP.

Table 7.5: The MP of 3L AA and AB MoS_2. In the table, for example, the S_1-Mo_1 denotes the bonding between the S_1 atom and Mo_1 atom. These atoms are labeled in the fig-7.7

3L AA Stacking		3L AB Stacking	
Bonding	MP	Bonding	MP
S_1-Mo_1	0.003188	S_1-Mo_1	0.004939
S_1-Mo_2	0.003188	S_1-Mo_2	0.004939
S_1-Mo_3	0.001921	S_1-Mo_3	0.004939
S_1-S_2	0.003865	S_1-S_2	0.004520
S_1-S_3	0.003865	S_1-S_3	0.004520
-	-	S_1-S_4	0.004520

7.6 Electrostatic Differential Potential

The EDP of 3L AA and AB MoS_2 intuitively presents the spatial distribution of the periodic electrostatic potential of the MoS_2 superlattice. The valuable information provided by the system EDP help us analyze the interlayer interaction and evaluate the Bloch wave function of the electrons. To give an overall outline of the potential distribution within the spatial region of the superlattice, in this chapter, the EDP results in X, Y and Z direction are calculated separately.

In X direction, the maximum and minimum of the EDP are 0.00847 V and -0.0108 V, yielding a barrier height of 0.0193 eV. To evaluate the scattering effect of these potential barriers, the FWHM is considered as a critical criterion. For electrons, the FWHM of the valley regions is the value should be investigated. As shown in fig-7.25, the FWHM of the potential barrier is given by X_2-X_1, which is 0.098 (fractional coordinate). The FWHM of the energy barrier for electrons is given by X_3-X_2, which is 0.070.

As shown in fig-7.26, for 3L AA MoS_2, the energy barrier height in Y direction is 0.0772 eV. As shown in fig-7.25 and fig-7.26, compared with the EDP in X direction,

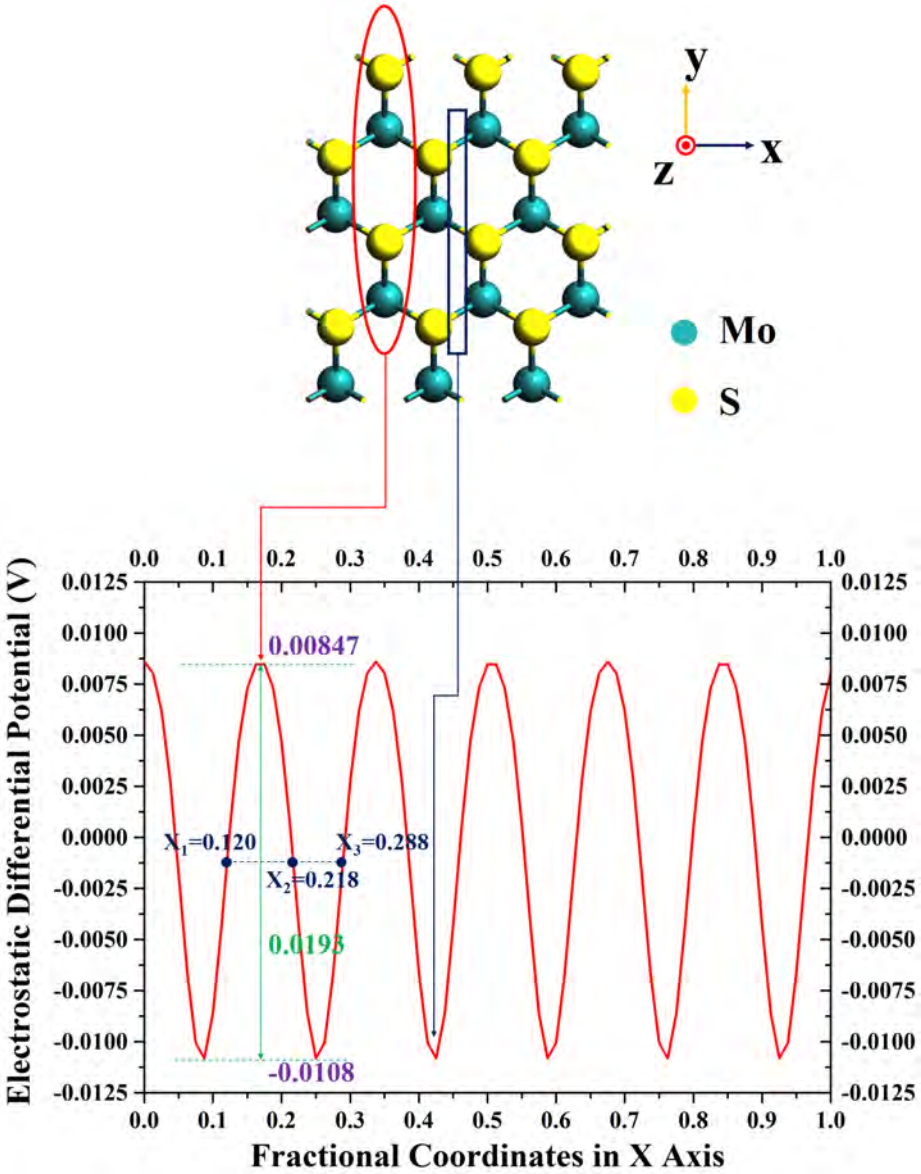

Figure 7.25: The EDP of 3L AA MoS_2 Projected in X Direction.

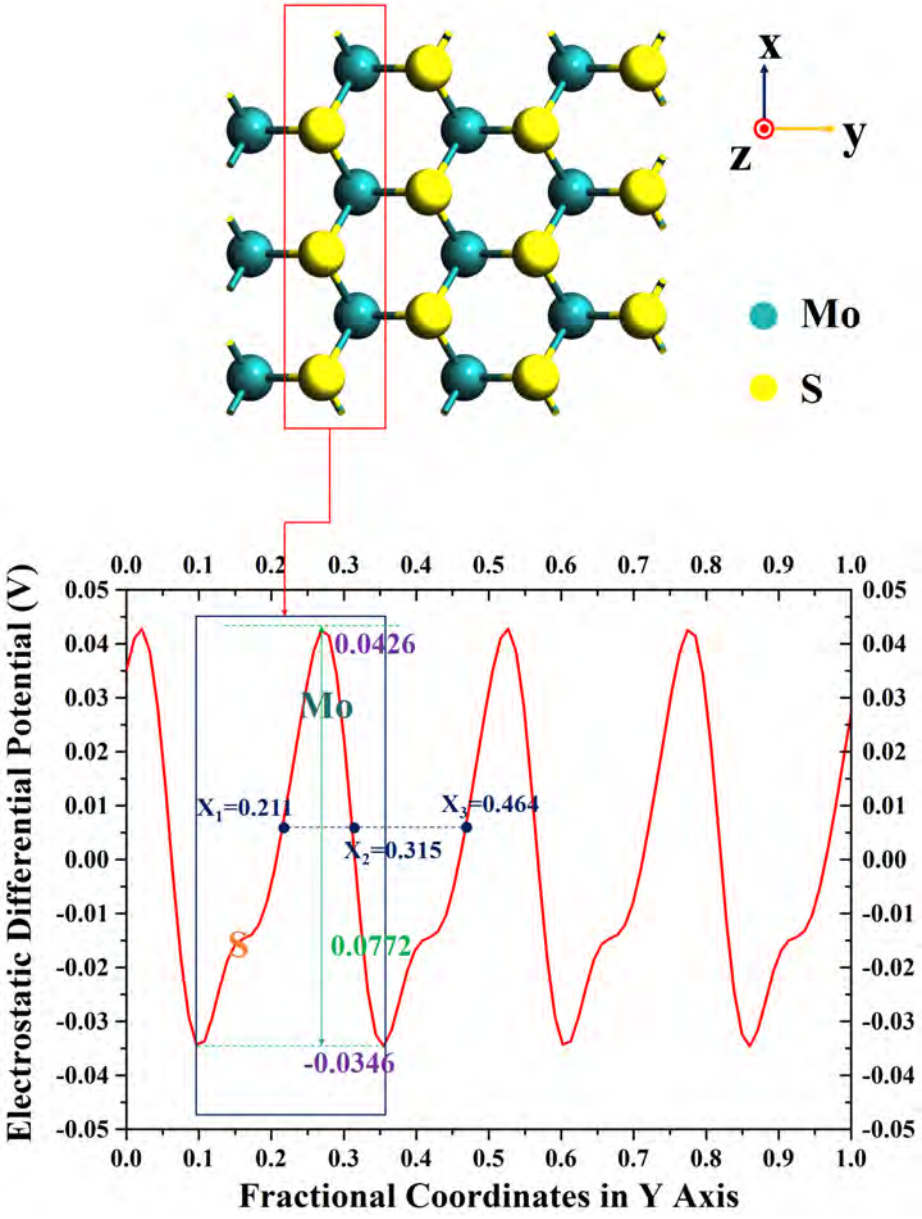

Figure 7.26: The EDP of 3L AA MoS_2 Projected in Y Direction.

on the one hand, the EDP in Y direction exhibits a different periodicity. On the other hand, in Y direction, the EDP contributed by S atoms does not fully overlap with the EDP contributed by Mo atoms, while in X direction, the EDP contributed by S atoms merges with the EDP of Mo atoms. Thus each valley region between the two peaks of the EDP in Y direction is partially occupied by a sub peak contributed by S electrostatic potential, which may increases the potential barrier width. As shown in fig-7.26, in Y direction, the FWHM of the potential barrier is 0.104, and the FWHM of the electron energy barrier is 0.149. The energy barrier height is 0.0772 eV. The EDP simulation intuitively shows that, for AA MoS_2, the barrier height and barrier width of the energy barrier of electrons in Y direction is much larger than X direction.

As shown in fig-7.27, for AB MoS_2, in X direction, the energy barrier height of electrons is 0.0193 eV. The FWHM of the potential barrier is 0.081, while the FWHM of the energy barrier of electrons is 0.085. In Y direction, the EDP of S atoms and the EDP of Mo atoms overlap with each other, and there is no sub peak in the valley region between EDP peaks. As shown in the fig-7.28, the barrier height of electrons is 0.104 eV. The FWHM of the potential barrier is 0.135. The FWHM of the energy barrier of electrons is 0.113.

Calculating the possibility of the electron passing through the potential barrier is a quantitative method to evaluate the strength of scattering effect of the lattice. The possibility T_B has the following relationship with the electron energy barrier [29]:

$$T_B \propto \exp\left(-4\pi \frac{\sqrt{2\ m\Delta V}}{h} W_B\right) \tag{7.5}$$

Where the ΔV is the barrier height, m is the mass of free electron, and the h is the Planck constant. The barrier width W_B in the equation 7.5 can be given by the FWHM of the electron energy. The equation 7.5 shows that, the T_B is determined by the factor α, which is defined by:

$$\alpha = \sqrt{\Delta V} \times\ W_B \tag{7.6}$$

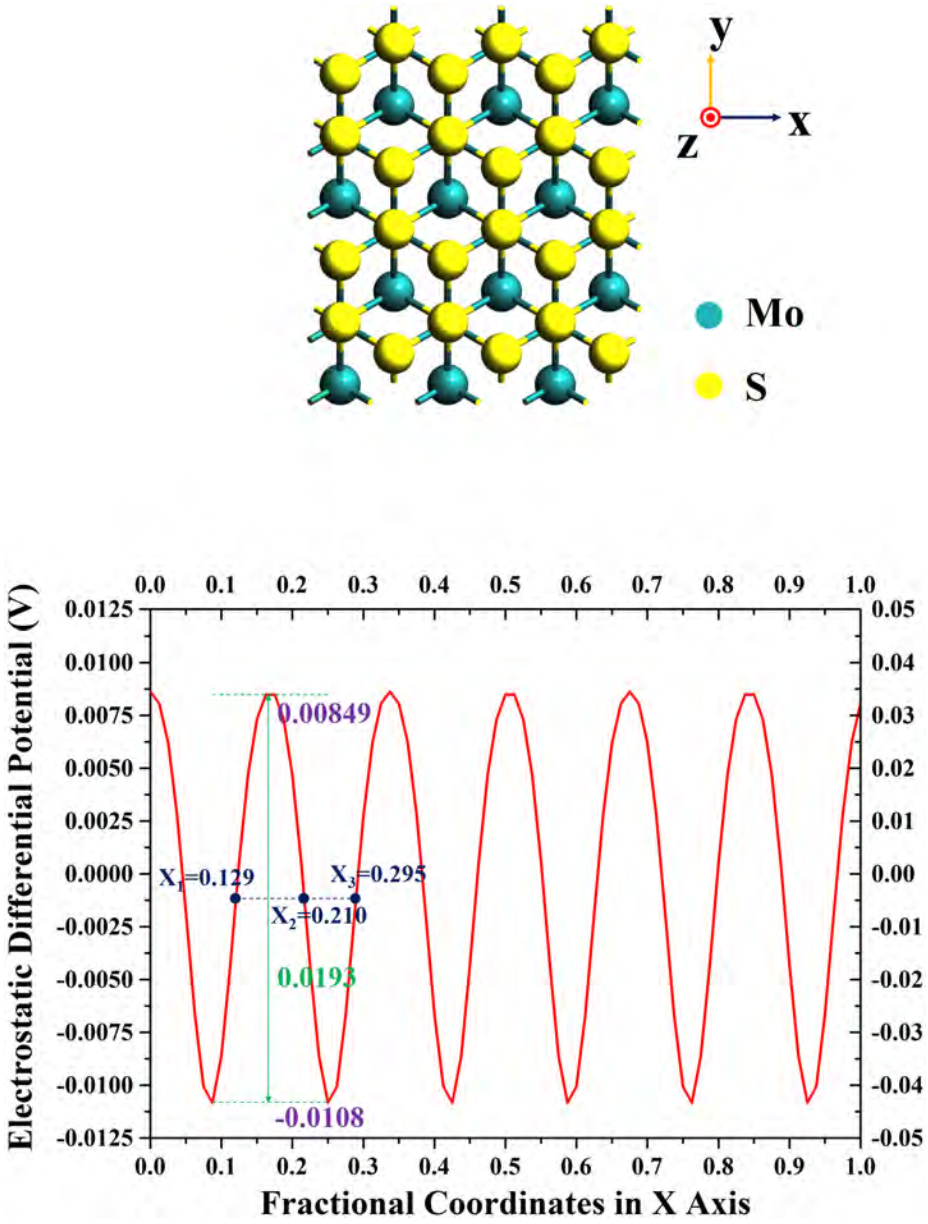

Figure 7.27: The Electrostatic Differential Potential (EDP) of 3L AB MoS_2 Projected in X Direction.

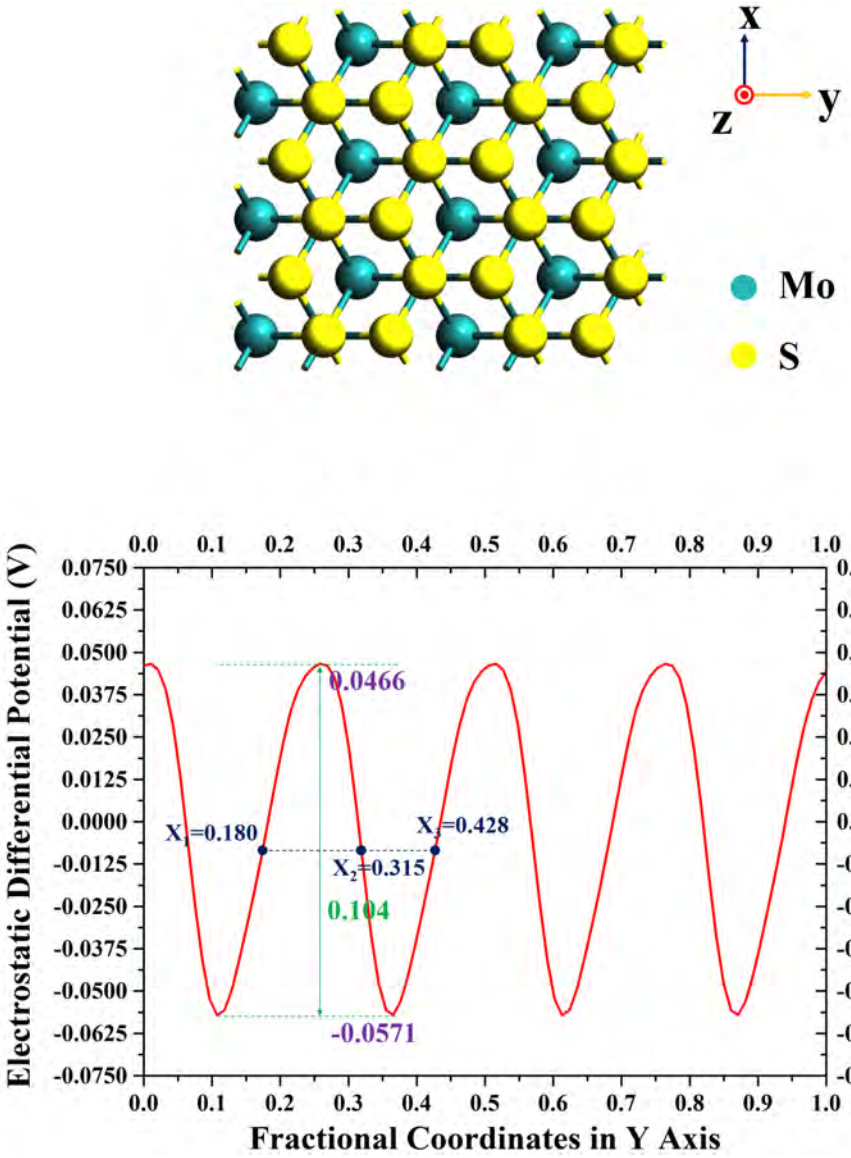

Figure 7.28: The EDP of 3L AB MoS_2 Projected in Y Direction.

A larger α indicates a smaller T_B, which means the electrons are faced with more scattering effects while travelling in this direction. For 3L AA MoS_2, the α is 0.00972 in X direction, and 0.0414 in Y direction. For 3L AB MoS_2, the α is 0.0113 in X direction, and 0.0435 in Y direction. The EDP analysis provides a proper explanation to the difference of the m_{eff_x} and m_{eff_y} between AA and AB MoS_2. Generally speaking, for both AA and AB MoS_2, the T_B in Y direction is smaller than the T_B in X direction, which indicates that the electron transportation is faced with larger scattering effect in Y direction than X direction. Thus the m_{eff_y} is larger than m_{eff_x}. On the other hand, the α in X and Y direction of AA MoS_2 is smaller than AB MoS_2. Thus the T_B in X and Y direction of AA MoS_2 is larger than AB MoS_2. That explains why the m_{eff_x} and m_{eff_y} of AA MoS_2 is smaller than AB MoS_2.

To gain a comprehensive understanding of the spatial EDP distribution of AA and AB MoS_2, the EDP in Z direction has also been calculated. As shown in fig-7.29 and fig-7.30, each of the Mo and S layers contributes to one specific peak in the EDP curve. The Mo layers contribute to the higher peaks in the curve, while the S layers contribute to the lower peaks. As mentioned in previous part, the MP analysis reveals that after rotating the second layer of 3L AA MoS_2 and turn the system into AB MoS_2, the Mo-S and S-S orbital couplings are enhanced by this geometry modification. This is also demonstrated by the EDP in Z direction. The fig-7.29 shows that, for 3L AA MoS_2, the Mo peaks range from 1.355 V to 1.356 V, which is very uniform. As for the S layers, compared with outer S peaks, the inner S peaks have higher EDP value, which are 0.244 V, 0.256 V, 0.257 V and 0.244 V. The outer two S peaks have the lowest EDP value, which is 0.224 V for both. The inner S peaks tend to have higher EDP value than outer S peaks since the inner S layers feel stronger interlayer interaction and coupling effect than the outer layers, according to the MP analysis. As for AB MoS_2, the center Mo peak has a EDP value of 1.411 V while both the outer two Mo peaks are 1.349 V. The EDP values of the inner S peaks are: 0.24 V, 0.314 V, 0.314 V and 0.24 V. The 3L AB MoS_2 shows higher inner EDP

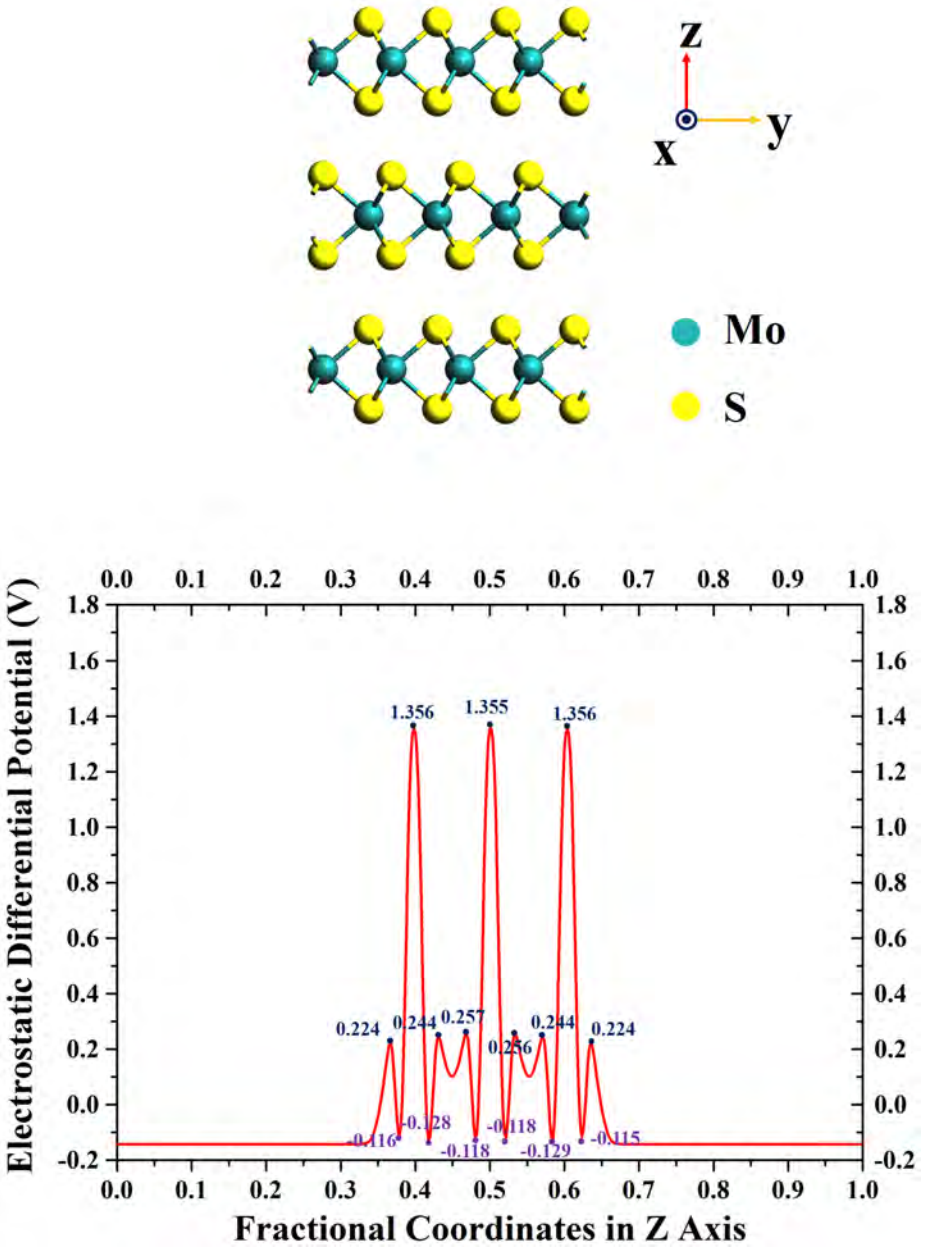

Figure 7.29: The EDP of 3L AA MoS_2 Projected in Z Direction.

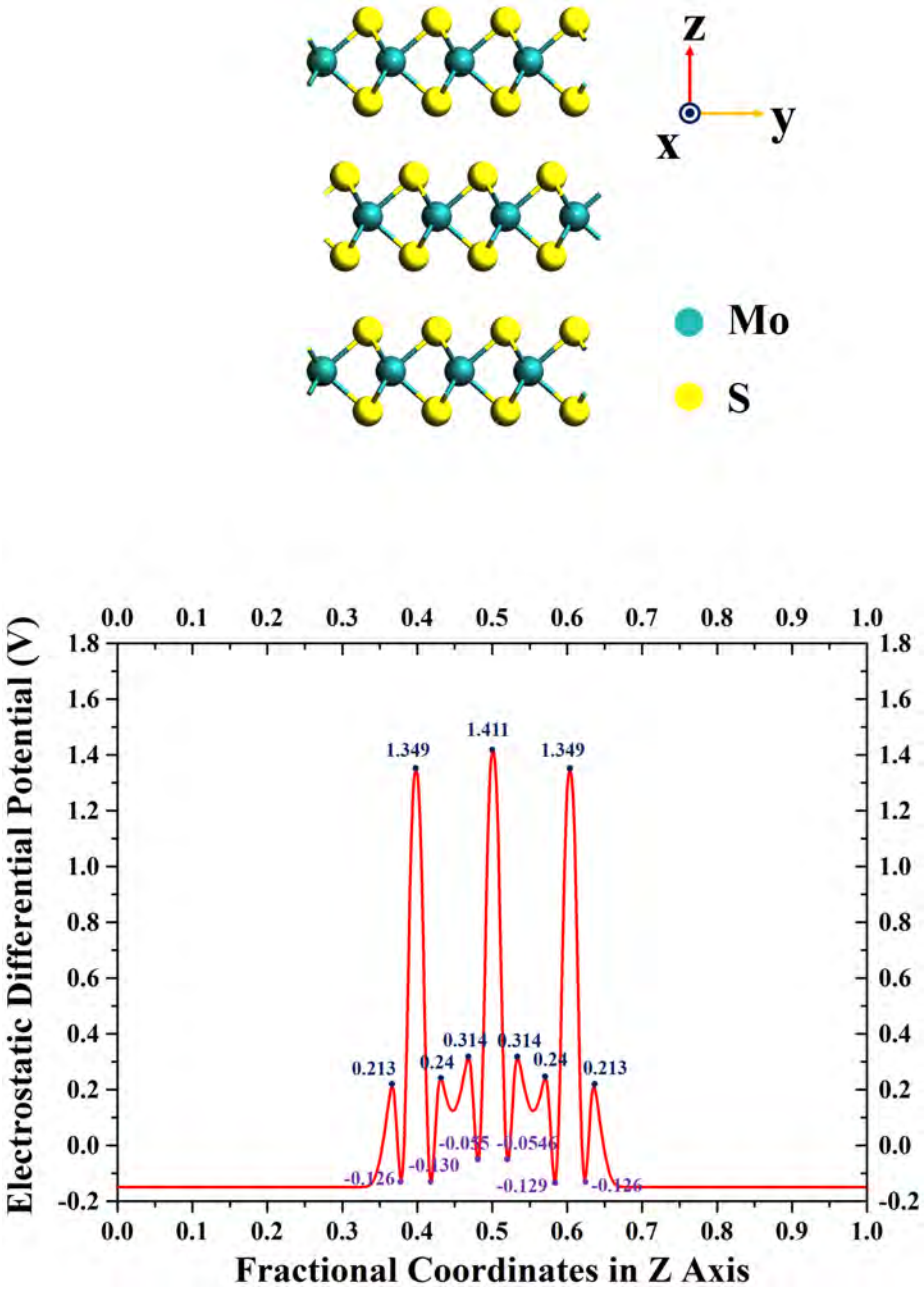

Figure 7.30: The EDP of 3L AB MoS_2 Projected in Z Direction.

peaks than AA MoS_2, which demonstrates the stronger coupling effect exists within the AB MoS_2. This matches the results of the MP analysis.

In summary, the EDP results of 3L AA and AB MoS_2 demonstrate the anisotropic distribution of the MoS_2 lattice electrostatic potential. According to the basic concepts of the Bloch Theorem [210], this anisotropic EDP distribution will cause the MoS_2 to possess anisotropic effective mass. For both 3L AA and AB MoS_2, the periodic potential barrier in Y direction is more difficult for electrons to travel through than that in X direction. In other words, while applying external electric or magnetic field, the electron movement will be faced with more scattering effect in Y direction. Thus both the AA and AB MoS_2 samples exhibit a larger m_{eff_y}. Compared with 3L AA MoS_2, the periodic potential barrier for the electrons in 3L AB MoS_2 is larger (harder to overcome) in both X and Y directions. As a result, the 3L AB MoS_2 shows larger m_{eff_x} and m_{eff_y} than 3L AA MoS_2. The simulation of the in-plane EDP distribution of 3L AA and AB MoS_2 provides us a reasonable explanation to the effective mass difference, while the EDP in Z direction along with the MP analysis results explain why AA and AB MoS_2 samples possess different in-plane EDP distributions. The MP simulation clearly shows that, the AB MoS_2 shows a stronger inter-layer interaction than AA MoS_2, which is also confirmed by the simulation results of the EDP projected in Z direction. This inter-layer interaction difference between AA and AB MoS_2 samples is mainly caused by the piling orientation difference. In general, the MoS_2 effective mass shows a strong correlation with the piling orientation. While the MoS_2 piling orientation is switched from AA to AB, on the one hand, the modification of the system geometry symmetry reorganizes the lattice potential distribution, which causes stronger scattering effect to the in-plane electron motion in AB MoS_2 while applying external electric or magnetic field. On the other hand, the inter-layer interaction is stronger in AB MoS_2, which also leads to a stronger scattering effect to the in-plane electron motion under external field. For these reasons, AB MoS_2 samples show larger effective mass compared with AA MoS_2.

7.7 conclusion

In this work, a comprehensive DFT study has been conducted on both AA and AB MoS_2. The bandstructure simulation results show that, both the AA and AB MoS_2 bandstructures show layer dependence. The bandgap energy decreases while the number of layer increasing. After 6 layers, this trend starts to saturate. Compared with AA MoS_2 bandstructure, the bandstructure of AB MoS_2 shows larger bandgap energy, smoother CBM band and further band degeneration generated by the broken symmetry, which verifies the correlation between the MoS_2 stacking orientation and the bandstructure. On the other hand, the bandstructure simulation also demonstrate that, compared with GGA method, the mGGA method brings about great correction to the bandgap energy value, which makes the simulation results more accurate. Since the effective mass of the electrons is the second order derivative of the band function, while the bandgap energy of MoS_2 decreasing with the number of layers increasing, as what is exhibited by the effective mass simulation, the effective mass of the electrons decreases. This trend is valid for both the AA and AB MoS_2. The electron effective mass simulation of mixed piling orientations shows that, among all the EAM cases, the AA MoS_2 shows the smallest effective mass while the AB MoS_2 possesses the largest effective mass. The data points distribution of all the 4-6L EAM cases further demonstrates that the electron effective mass of the MoS_2 shows a strong correlation with the MoS_2 piling orientation. To understand the piling orientation dependence of the MoS_2 electron effective mass, the MP and EDP analysis have been provided. The MP results demonstrate that, by changing the MoS_2 structure from AA stacking to AB stacking, the interlayer Van der Waals bonding is enhanced. This enhancement along with the modification of the lattice periodicity strengthen the electron scattering effect in X and Y direction in AB MoS_2, as shown in EDP simulation. Thus the AB MoS_2 exhibits larger m_{eff_x} and m_{eff_y} than AA MoS_2. Our computational work has demonstrated the correlation between the MoS_2 electronic

structure and MoS_2 geometry. While designing and fabricating the MoS_2 devices, it is crucial to achieve a good controllability over the thickness and the stacking orientation of the deposited MoS_2 thin films. To further explore this matter and find a resolution to the existing challenges, in the future, we would like to perform more simulations to dig out the laws behind the effective mass variation associated with the geometry modification. To work out the exact electron mobility, a relaxation time simulation will also be conducted in the future. We hope our computational work could help the progress of the MoS_2 FET optimization, and pave the way to the high-performance 2D electronic devices.

Chapter 8

Exploration of Novel Emergent Properties of Transition Metal Dichalcogenide Heterostructures

8.1 Transition Metal Dichalcogenide Heterostructures and Emergent Properties

2D materials have shown their advantages of forming heterostructures such as stacking ability, flexibility and zero dangling bonds on the surface. Efforts have been focused on novel 2D heterostructures in the past few years. The relative research has demonstrated that, the formation of the 2D heterostructure brings about novel electronic/optical properties [40–43]. These properties do not exist in any free-standing 2D constituent of the heterostructure alone, and they are referred to as emergent properties [39]. The emergent properties of the 2D heterostructures lead to both potentials and challenges. On the one hand, the emergent properties of 2D heterostructures broaden the application fields of 2D devices, leading to novel designs for quantum electronic and optics. On the other hand, it is difficult to predict the emergent properties. The well-defined Anderson's rule states that the conduction band offset of two adjacent semiconductor constituents in the heterostructure could be predicted by working out the difference in electron affinity. This rule could predict the traditional 3D heterostructures successfully. However, it has been demonstrated that, the band offset of 2D heterostructures does not follow the Anderson's rule [44].

To successfully predict and understand the emergent properties, a systematic computational work is necessary.

It is of our great interest to explore the channel designs beyond ML or multilayer MoS_2. Heterojunctions formed by ML 2D materials is a good start point. Graphene is an attractive choice for its large carrier mobility [15]. However, the zero bandgap energy limits its applications. Compared with graphene, TMDCs show finite bandgap, which could be transferred from indirect bandgap to direct band gap by reducing the number of layers to ML. Take MoX_2 and WX_2 (where X denotes S, Se or Te) as examples, the ML MoS_2 shows a 1.8 eV direct bandgap [17], while other ML TMDCs show direct bandgap with different bandgap energy: ML $MoSe_2$ 1.55 eV [211], ML $MoTe_2$ 1.1 eV [212], WS_2 2.0 eV [213] and WSe_2 1.65 eV [214]. Bulk TMDCs show indirect bandgap with smaller bandgap energy: bulk MoS_2 1.2 eV [16], bulk $MoSe_2$ 1.1 eV [215], bulk $MoTe_2$ 1.0 eV [212], bulk WS_2 1.4 eV [216] and bulk WSe_2 1.2 eV [217]. Unlike the TMDCs mentioned above, the WTe_2 is a class of semi-metallic material with very narrow bandgap [218]. The TMDC family members provide us with wide-range choices of bandgap energy and share close lattice parameters, thus they are promising candidates for the constituent layers of 2D heterostructures.

To precisely predict the band offset and understand the possible emergent properties of the TMDC heterostructures, a comprehensive and precise computational work is required. Some computational works have been provided in the past few years [219–221], but the simulation results are still in doubt. It is still an urgent need to develop a systematic DFT analysis method for our research work. To better understand the emergent properties of different TMDC combinations, in this work, we have performed a wide-range DFT study on the vertical abrupt heterostructures based on ML MX_2, where M denotes the Mo and W elements, while X represents S, Se and Te elements (M: W and Mo, X: S, Se and Te). We have built up the heterostructures covering all the combinations of ML MX_2. By using the DOS, projected bandstructure PBS and ED analysis, we have conducted a detailed investigation to

the TMDC heterostructures and predicted their electronic structures. We hope our work will provide useful predictions to guide our future designs and optimizations of 2D devices, and contribute the progress of modern electronics.

8.2 Methodology

8.2.1 Density Functional Theory Simulation Set-up

Our simulation is performed by applying the DFT method [132]. The Atomistix Toolkit [6] provides the pre-defined DFT packages. The GGA functional Perdew-Burke-Ernzerhof [134] is employed. To gain a good simulation accuracy for the systems which contain Se and Te element, instead of using HGH pseudo potential [141], the SG-15 pseudo potential is adopted [134]. The 16×16×1 Monkhorst-Pack k-point mesh is chosen to describe the systems with hexagonal lattice, while the 4×8×1 Monkhorst-Pack k-point mesh for the simple orthorhombic systems. As for the I-V simulation, the k-point sampling in c direction is increased to 24, thus makes the k-point sampling density in the transport direction (c direction) 800 $Å^{-1}$. A 30 Å vacuum buffer is added to the super lattice. The force tolerance is set as 0.005 eV/Å to fully relax the lattice in the geometry optimization. In the I-V simulation, the Green's function is employed to describe the equilibrium system, and the sparse Green's function is used to model the non-equilibrium system under the finite bias.

8.2.2 Geometry Set-up

The hexagonal lattice is employed for both bulk and ML MoS_2, $MoSe_2$, $MoTe_2$, WS_2 and WSe_2. In the 2H hexagonal MX_2 structure, the X atoms in one layer will sit on the top of the M atoms of adjacent layers. The WTe_2 normally shows 1-T metallic phase. In this case, the superlattice of the WTe_2 is in simple orthorhombic. After relaxation, the lattice parameters of the investigated TMDCs are extracted and listed in table-8.1. As shown in table-8.1, the a and b of the MoS_2 unit cell is 3.1857 Å, while the original value is 3.1604 Å, which is in coincidence with the reported computational

Table 8.1: The Optimized a and b Parameters of the Unit Cell of TMDCs.

	a [Å]	b [Å]
MoS_2	3.1857	3.1857
$MoSe_2$	3.3195	3.3195
$MoTe_2$	3.5905	3.5905
WS_2	3.1933	3.1933
WSe_2	3.3182	3.3182
WTe_2	3.4980	6.3380

results [208]. As for the $MoSe_2$ case, the a and b after relaxation is 3.3195 Å. The optimized a and b is 3.5905 Å for $MoTe_2$. For WX_2 cases, the optimized a and b of WS_2 and WSe_2 is 3.1933 Å and 3.3182 Å respectively. For the WTe_2 case, the optimized a and b is 3.498 Å and 6.338 Å.

After the geometry optimization, the relaxed ML TMDC structures are employed to construct the MX_2 heterostructures. Then the second geometry optimization is applied to these heterostructures. The in-plane lattice parameters listed in the table-8.1 demonstrate that, as a result of the differences of the in-plane valence bond length and radius of the atoms between TMDC materials, while constructing heterojunctions with distinctive MX_2 lattices, the lattice mismatch is inevitable.

The mean absolute strain is defined as the strain generated by matching interface A to interface B. This strain will be fully relaxed after the second geometry optimization, thus it is only exists in the system for initial guessing. However, the mean absolute strain could be a usable criterion to define the mismatch between the constituents of the junctions. Normally the mean absolute strain should be chosen carefullysince a system with a very large mean absolute strain may be degraded during the geometry optimization. The figure-8.1 and figure-8.2 show the typical examples of the defined ML TMDC heterojunctions. As shown in figure-8.1 (a), the two MX_2 materials with very close lattice parameters tend to form heterostructures with

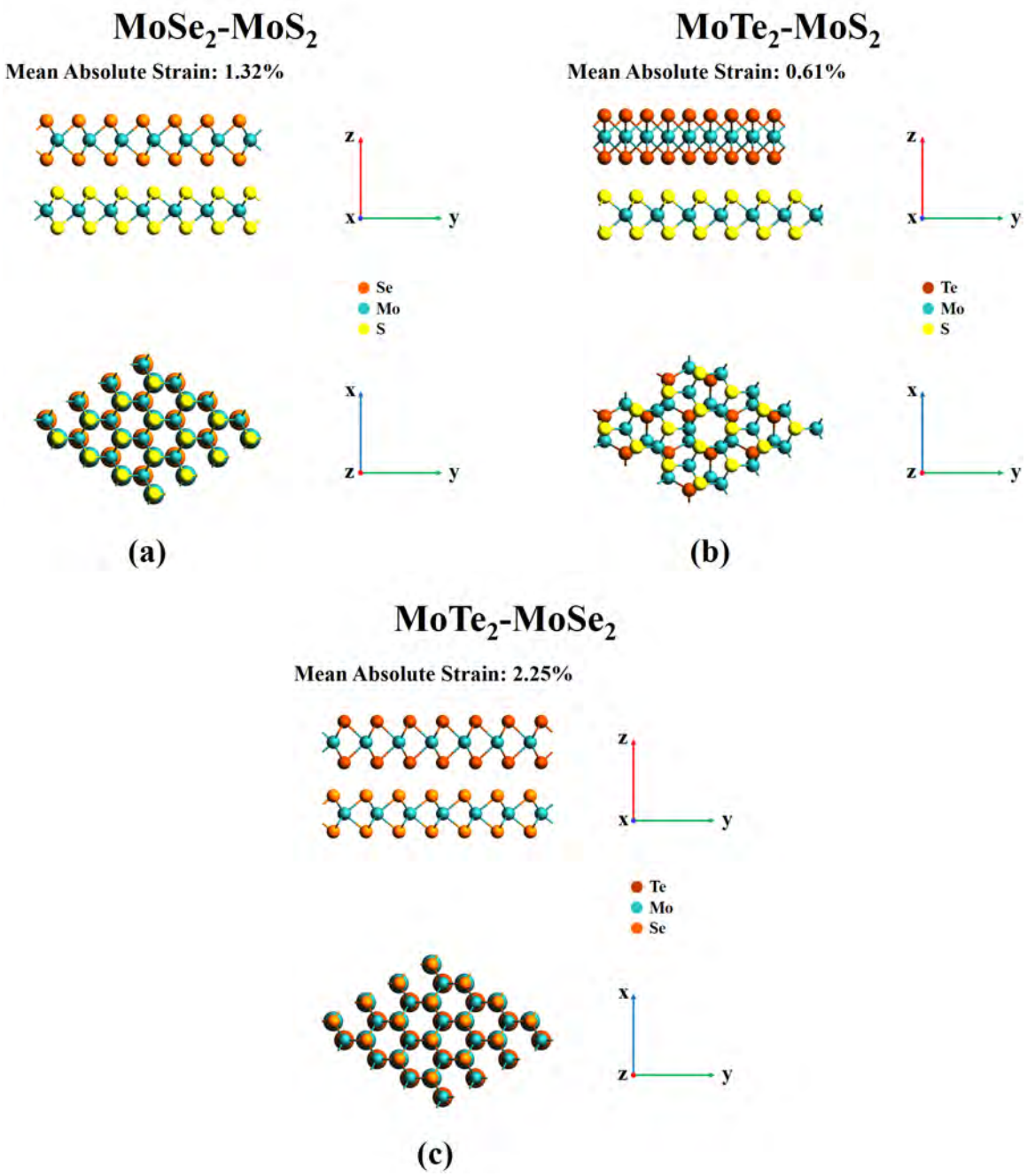

Figure 8.1: The Geometry Configuration of ML MX_2-MX_2 Heterojunctions. (a) MoS_2-$MoSe_2$ junction, (b) MoS_2-$MoTe_2$ junction, (c) $MoSe_2$-$MoTe_2$ junction.

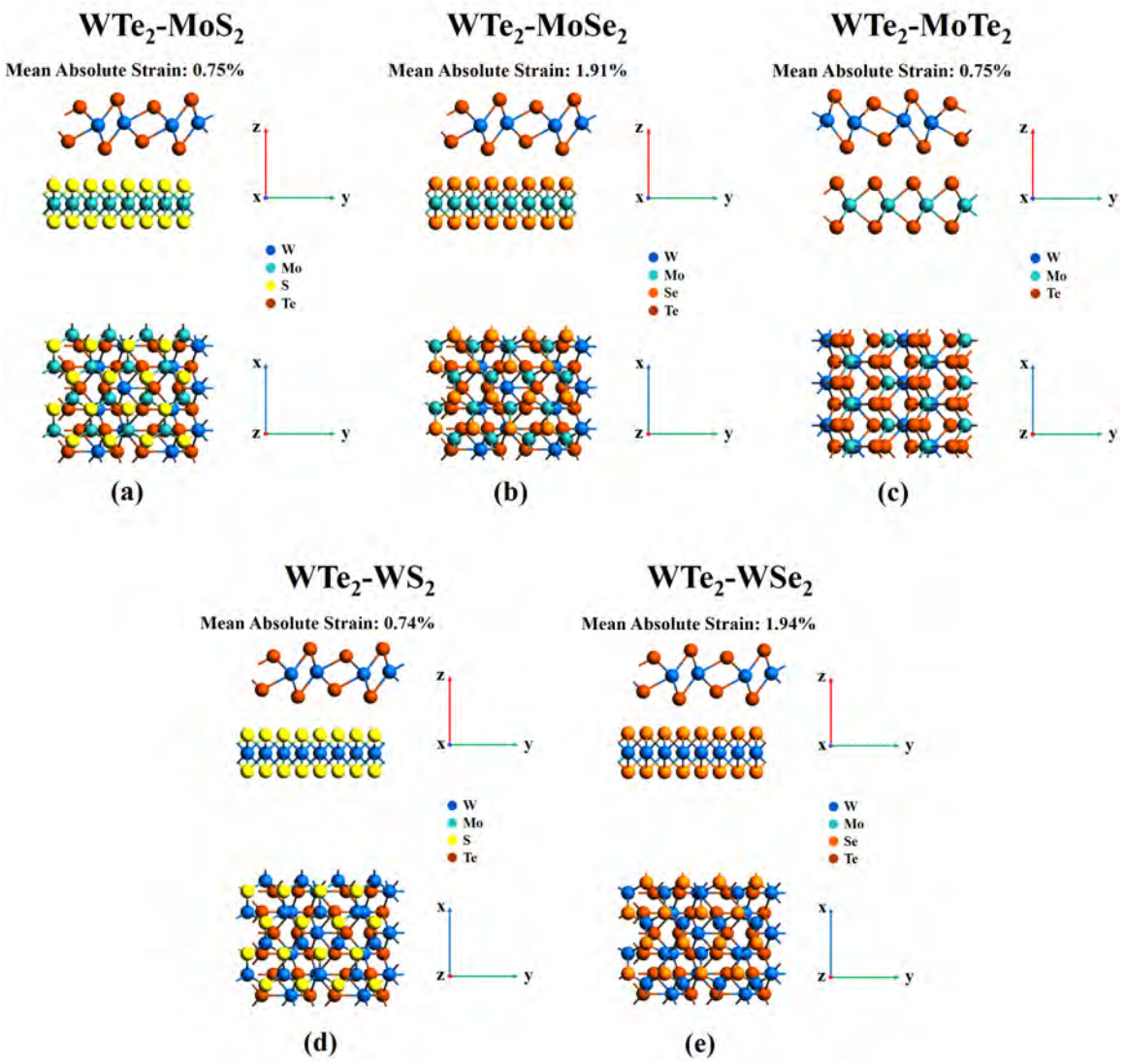

Figure 8.2: The Geometry Configuration of the TMDC Heterojunctions Consisting of ML Semiconducting MX_2 and ML WTe_2. (a)-(e) The side view and top view of the MoS_2-WTe_2 junction (a), $MoSe_2$-WTe_2 junction (b), $MoTe_2$-WTe_2 junction (c), WS_2-WTe_2 junction (d) and WSe_2-WTe_2 junction (e).

Table 8.2: The Mean Absolute Strain and Lattice Type of ML TMDC Heterojunctions.

Junction	Mean Absolute Strain	Lattice Type
(ML)MoS_2-(ML)$MoSe_2$	1.32%	Hexagonal
(ML)MoS_2-(ML)$MoTe_2$	0.61%	Hexagonal
(ML)$MoSe_2$-(ML)$MoTe_2$	2.25%	Simple Orthorhombic
(ML)MoS_2-(ML)WS_2	0.08%	Hexagonal
(ML)MoS_2-(ML)WSe_2	1.34%	Hexagonal
(ML)$MoSe_2$-(ML)WS_2	1.40%	Hexagonal
(ML)$MoSe_2$-(ML)WSe_2	0.02%	Hexagonal
(ML)$MoTe_2$-(ML)WS_2	1.14%	Hexagonal
(ML)$MoTe_2$-(ML)WSe_2	2.23%	Simple Orthorhombic
(ML)WS_2-(ML)WSe_2	1.42%	Hexagonal
(ML)MoS_2-(ML)WTe_2	0.75%	Simple Orthorhombic
(ML)$MoSe_2$-(ML)WTe_2	1.91%	Simple Orthorhombic
(ML)$MoTe_2$-(ML)WTe_2	0.75%	Simple Orthorhombic
(ML)WS_2-(ML)WTe_2	0.74%	Simple Orthorhombic
(ML)WSe_2-(ML)WTe_2	1.94%	Simple Orthorhombic

small mean absolute strain. ML MoS_2 (3.1857 Å) and ML $MoSe_2$ (3.3195 Å) form heterojunction with hexagonal superlattice. The mean absolute strain of (ML)MoS_2-(ML)$MoSe_2$ interface is only 1.32%. The mean absolute strain could be modified by altering the stacking orientation of the system or including more atoms in the superlattice. As shown in figure-8.1 (b), the mean absolute strain of the (ML)MoS_2-(ML)$MoTe_2$ interface is 0.61%, although the lattice parameter difference between the ML MoS_2 (3.1857 Å) and ML $MoTe_2$ (3.5905 Å) is large. That is because the super lattice of the (ML)MoS_2-(ML)$MoTe_2$ interface includes more atoms than other interfaces, which reduces the mean absolute strain. As shown in figure-8.2, the simple orthorhombic superlattice of the (ML)MX_2-(ML)WTe_2 heterojunctions exhibit small mean absolute strain. As shown in figure-8.2 (a), the mean absolute strain of the (ML)WTe_2-(ML)MoS_2 heterojuntion is 0.75 %. Adopting the simple orthorhombic superlattice and including more atoms in the superlattice reduce the mean absolute strain of the (ML)WTe_2-(ML)MoS_2 heterojuntion.

The mean absolute strain and lattice type of other TMDC heterojunctions are listed in table-8.2.

8.3 Electronic Structure of Thin Films

After the first geometry optimization, the bandstructure are simulated for both ML and bulk MX_2. The simulated bandgap energy of the ML and bulk MX_2 are shown in table-8.3. Specifically, the ML MoS_2 and WS_2 show larger bandgap energy, which are 1.795 eV and 1.903 eV respectively. The ML $MoTe_2$ shows the smallest bandgap energy among the ML semiconducting MX_2 investigated in this work, which is only 1.141 eV. ML WTe_2 shows a zero bandgap, which demonstrates that ML WTe_2 is a type of semimetal. For bulk semiconducting MX_2, the bandgap energy are reduced from 1.795 eV, 1.531 eV, 1.141 eV, 1.903 eV, 1.611 eV to 1.204 eV, 1.086 eV, 0.846 eV, 1.395 eV and 1.277 eV respectively, as shown in table-8.3.

The figure-8.3 sketches out the bandgap alignment of the ML MX_2. To give a

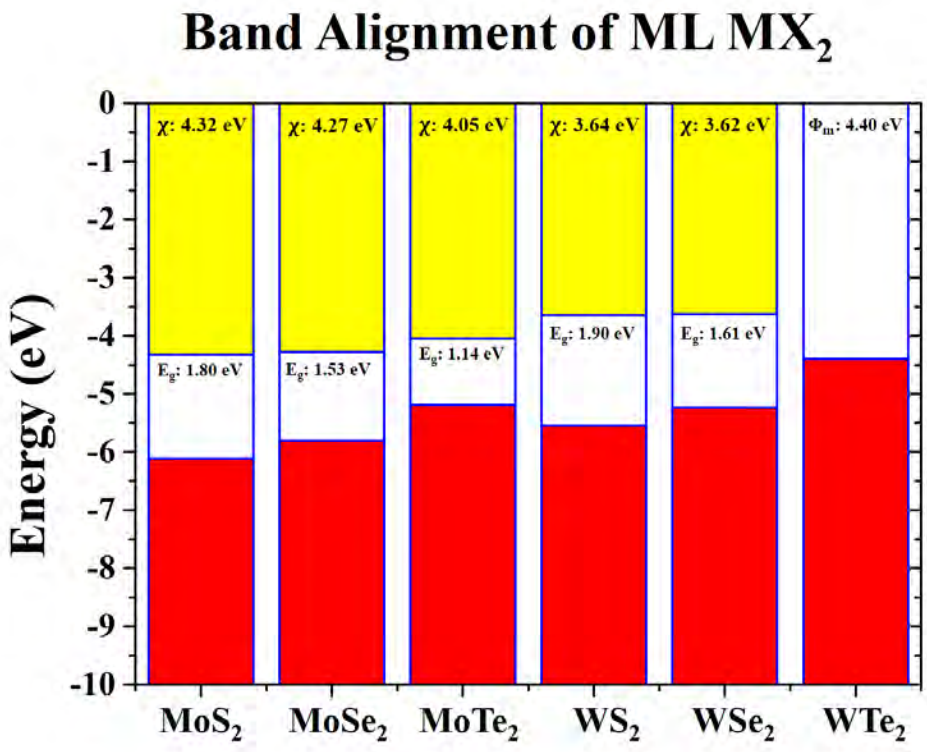

Figure 8.3: The Band Alignment Diagram of the ML MX_2. In the diagram, the yellow region denotes the conduction band and the red region denotes the valence band.The blank region in-between the red and yellow region represents the forbidden gap region.The bandgap energy E_g, the electron affinity χ and the workfunction of the ML WTe_2 Φ_m are labeled in the plot.

Table 8.3: The Bandgap Energy of Bulk MX_2, the Bandgap Energy of ML MX_2 and the ELectron Affinity of ML MX_2.In the table, the E_g is the bandgap energy while the χ is the electron affinity.

	Bulk E_g (eV)	ML E_g (eV)	ML χ (eV)
MoS_2	1.204	1.795	4.32
$MoSe_2$	1.086	1.531	4.27
$MoTe_2$	0.846	1.141	4.05
WS_2	1.395	1.903	3.64
WSe_2	1.277	1.611	3.62
WTe_2	0	0	-

comprehensive investigation of the characteristics of the ML MX_2 electronic structure, the electron affinity χ of the semiconducting ML MX_2 and the workfunction of the ML WTe_2 are also extracted by the simulation, which are labeled in the figure-8.3 and listed in table-8.3. The band alignment shown in figure-8.3 is under the condition before the contacting (the ML MX_2 films are free-standing in the case), and the vacuum level is set as the zero level. The simulated electron affinity χ is 4.32 eV for ML MoS_2, 4.27 eV for ML $MoSe_2$, 4.05 eV for ML $MoTe_2$, 3.64 eV for WS_2 and 3.62 eV for WSe_2. The simulated workfunction of WTe_2 is 4.40 eV. The extracted electron affinity of ML MoS_2 by using the SG-15 pseudo potential is larger than our previous results extracted by using HGH pseudo potential.

8.4 Electronic Structure of the Heterostructures

After the geometry optimization of the predefined heterostructures, the DOS and PBS simulations have been conducted to investigate the emergent properties of the ML TMDCs heterojunctions. Only the typical cases are presented.

8.4.1 Projected Bandstructure Simulation

The PBS simulation results of the (ML)MoS_2-(ML)$MoSe_2$ heterojunction is shown in figure-8.4. In the total BS of (ML)MoS_2-(ML)$MoSe_2$ heterojunction, which is shown in figure-8.4 (a), the bands labeled by blue color denote the bands contributed by ML $MoSe_2$, while the green bands are contributed by ML MoS_2.

As shown in figure-8.4 (b) and (c), according to the PBS simulation of the ML MoS_2 and $MoSe_2$ in the junction, the bandgap energy of the ML MoS_2 is reduced from 1.795 eV to 1.236 eV. The energy difference between the CBM and Fermi level ϕ_{n} is 0.316 eV, while the energy difference between the VBM and the Fermi level ϕ_{p} is 0.920 eV. The simulated results indicate that the ML MoS_2 in the junction is n-type doped after contacting with the ML $MoSe_2$. On the other hand, the bandgap energy of the ML $MoSe_2$ is reduced from 1.531 eV to 1.294 eV. The ϕ_{n} and ϕ_{p} of the

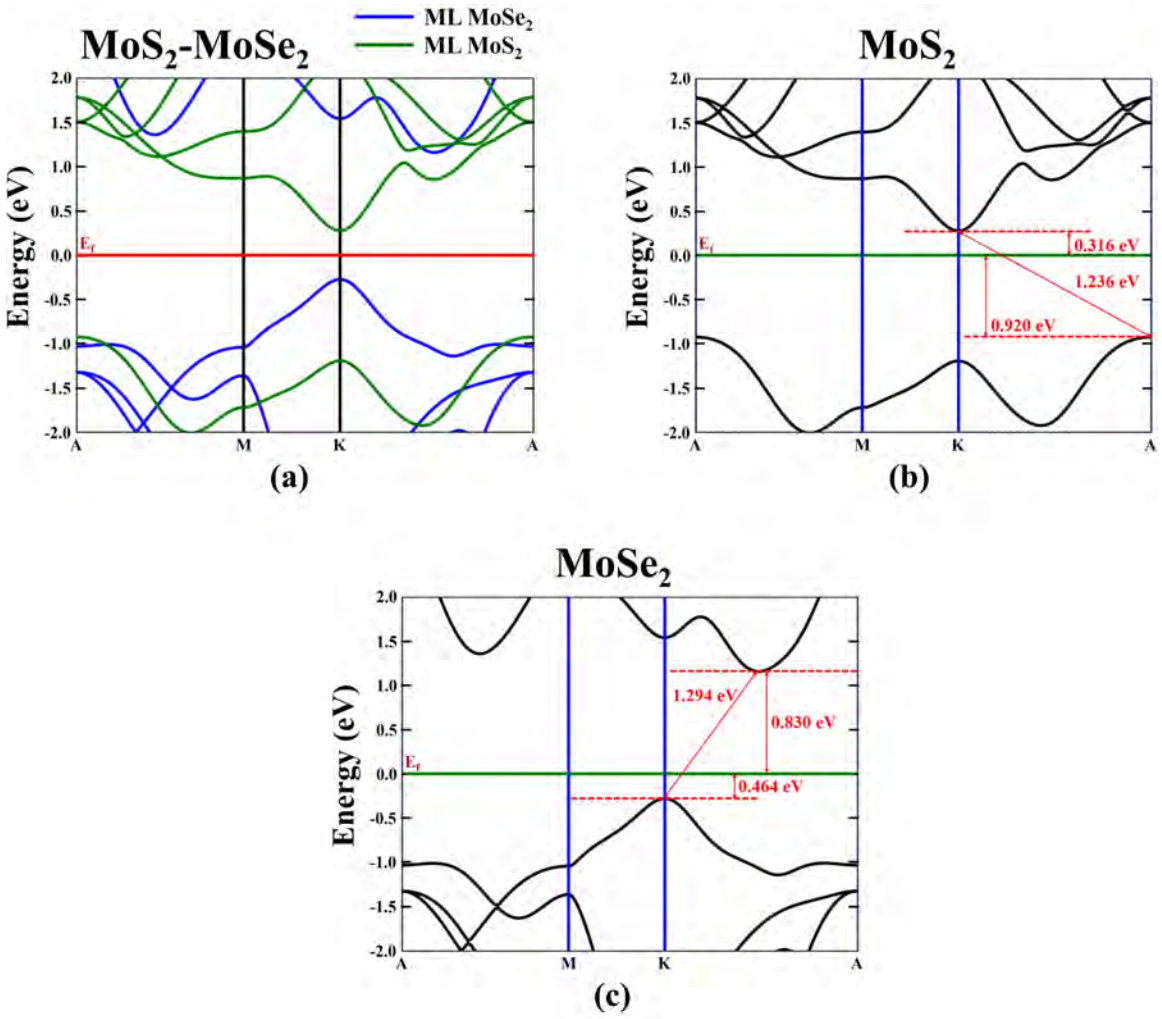

Figure 8.4: The Bandstructure and Projected Bandstructure of (ML)MoS_2-(ML)$MoSe_2$ Junction. (a) the bandstructure of (ML)MoS_2-(ML)$MoSe_2$ junction, (b) the projected bandstructure of the ML MoS_2 layer in the junction, (c) the projected bandstructure of the ML $MoSe_2$ layer in the junction.

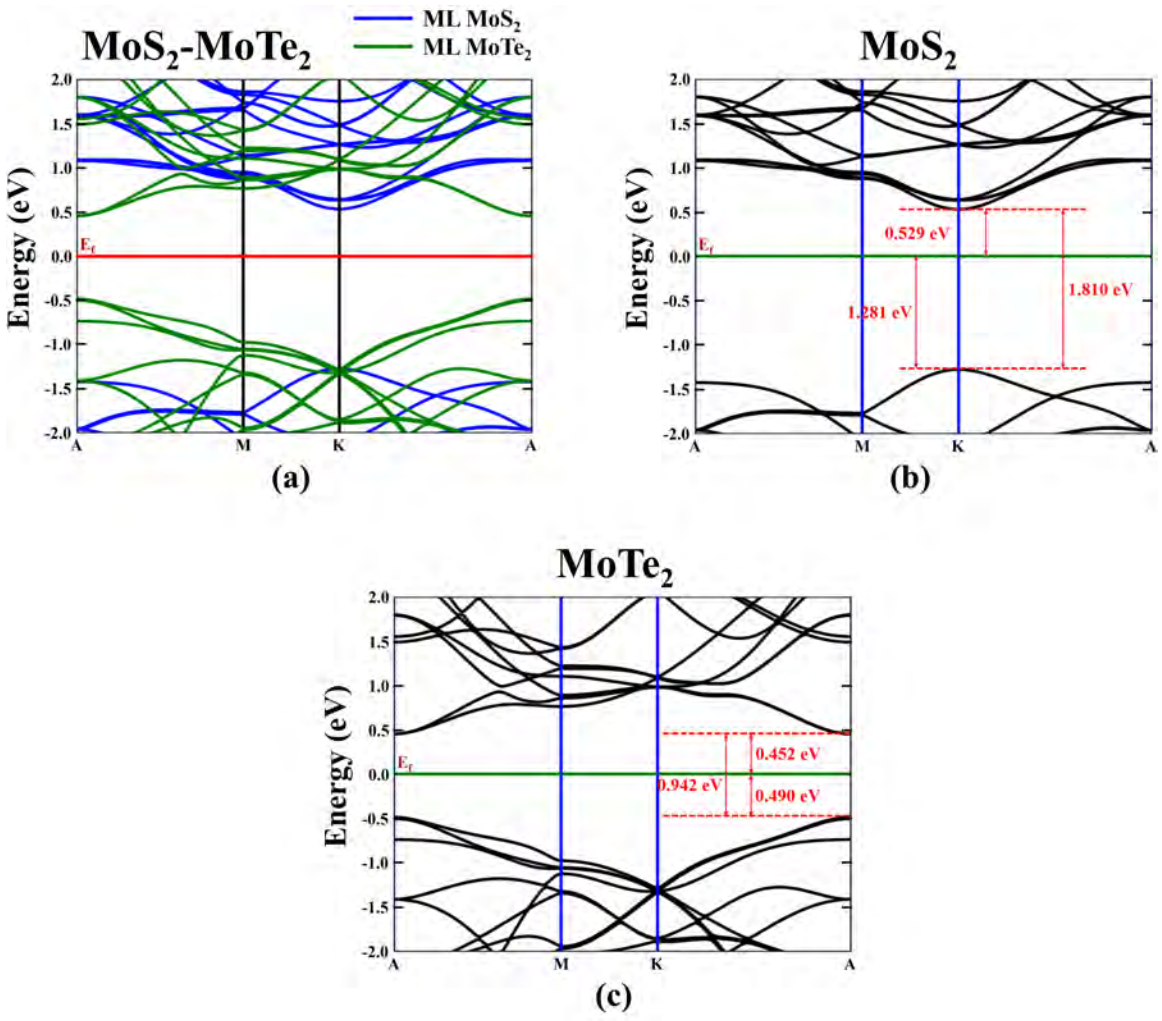

Figure 8.5: The Bandstructure and Projected Bandstructure of (ML)MoS_2-(ML)$MoTe_2$ Junction. (a) the bandstructure of (ML)MoS_2-(ML)$MoTe_2$ junction, (b) the projected bandstructure of the ML MoS_2 layer in the junction, (c) the projected bandstructure of the ML $MoTe_2$ layer in the junction.

ML $MoSe_2$ in the junction is 0.830 eV and 0.464 eV, indicating that the ML $MoSe_2$ is p-type doped.

As shown in figure-8.5 (b) and (c), the bandgap energy of the ML MoS_2 in (ML)MoS_2-(ML)$MoTe_2$ junction is 1.810 eV, which is very close to the bandgap energy of the intrinsic ML MoS_2 extracted by the previous simulation (1.795 eV). The ϕ_n of the ML MoS_2 is 0.529 eV, indicating that the ML MoS_2 is n-type doped. After forming the heterojunction, the bandgap of the ML $MoTe_2$ is reduced from 1.141 eV to 0.942

eV. The ϕ_n and ϕ_p of the ML $MoTe_2$ are 0.452 eV and 0.490 eV respectively. To be noticed, the bandgap of the ML $MoTe_2$ in the heterojunction is still direct bandgap, and the ϕ_n and ϕ_p of the ML $MoTe_2$ are close to each other. For this reason, it is concluded that after forming the (ML)MoS_2-(ML)$MoTe_2$ junction, the ML $MoTe_2$ preserves its intrinsic properties.

The PBS examples of the heterojunctions consisting of ML semiconducting MX_2 and ML WTe_2 are shown in figure-8.6 and figure-8.7. In the (ML)MoS_2-(ML)WTe_2 heterojunction, after contacting with ML WTe_2, the ML MoS_2 becomes n-type doped. As shown in figure-8.6, the ML MoS_2 in the (ML)MoS_2-(ML)WTe_2 heterojunction shows a ϕ_n of 0.561 eV. It also exhibits a 1.746 eV direct bandgap.

Contrarily, the ML $MoSe_2$ tends to show p-type electronic structure after contacting with ML WTe_2. As shown in figure-8.7, after contacting with ML WTe_2, the ML $MoSe_2$ in the (ML)$MoSe_2$-(ML)WTe_2 heterojunction shows a ϕ_p of 0.587 eV, while its bandgap energy is modified to 1.414 eV.

The BS and PBS results of all the investigated TMDC heterojunctions are listed in table-8.4 and table-8.5. The simulation results clearly show that, by employing different combinations of MX_2, heterojunctions with various emergent electronic properties could be created. Generally speaking, after forming the heterostructures, the electronic structure of the constituents will be modified, including band edge shifting, bandgap energy modification, introduced doping concentration and the direct bandgap to indirect bandgap transforming.

8.4.2 The Projected Bandstructure Analysis

To under stand the emergent properties extracted from the PBS simulations, the analysis of the bandstructure difference between the free-standing ML TMDCs and constituent ML TMDCs in heterojunctions has been employed. This comparison could provide us with intuitive and detailed information of the bandstructure variation. In this chapter, typical cases of ML TMDC heterojunctions are presented in

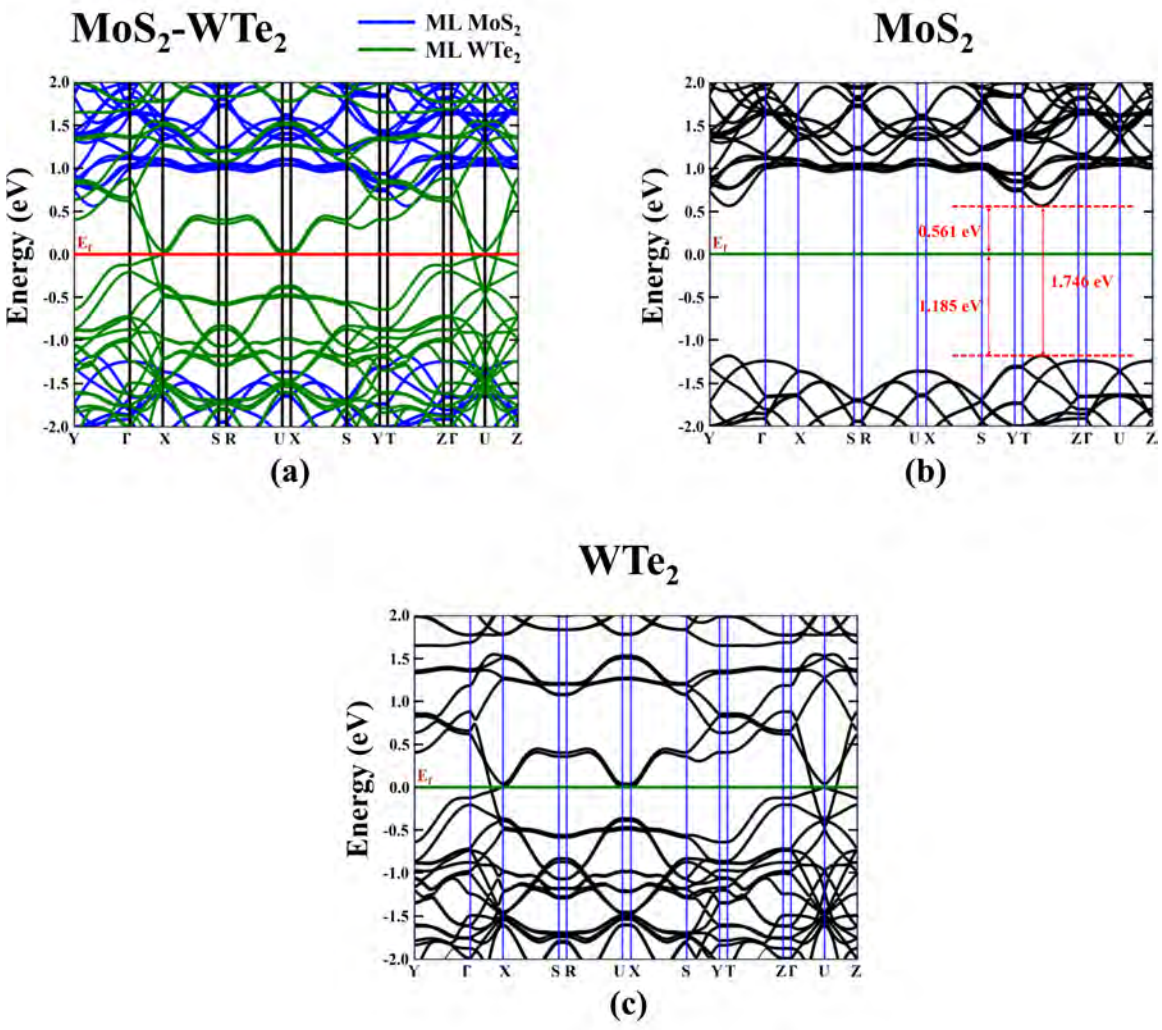

Figure 8.6: The Bandstructure and Projected Bandstructure of (ML)MoS_2-(ML)WTe_2 Junction. (a) the bandstructure of (ML)MoS_2-(ML)WTe_2 junction, (b) the projected bandstructure of the ML MoS_2 layer in the junction, (c) the projected bandstructure of the ML WTe_2 layer in the junction.

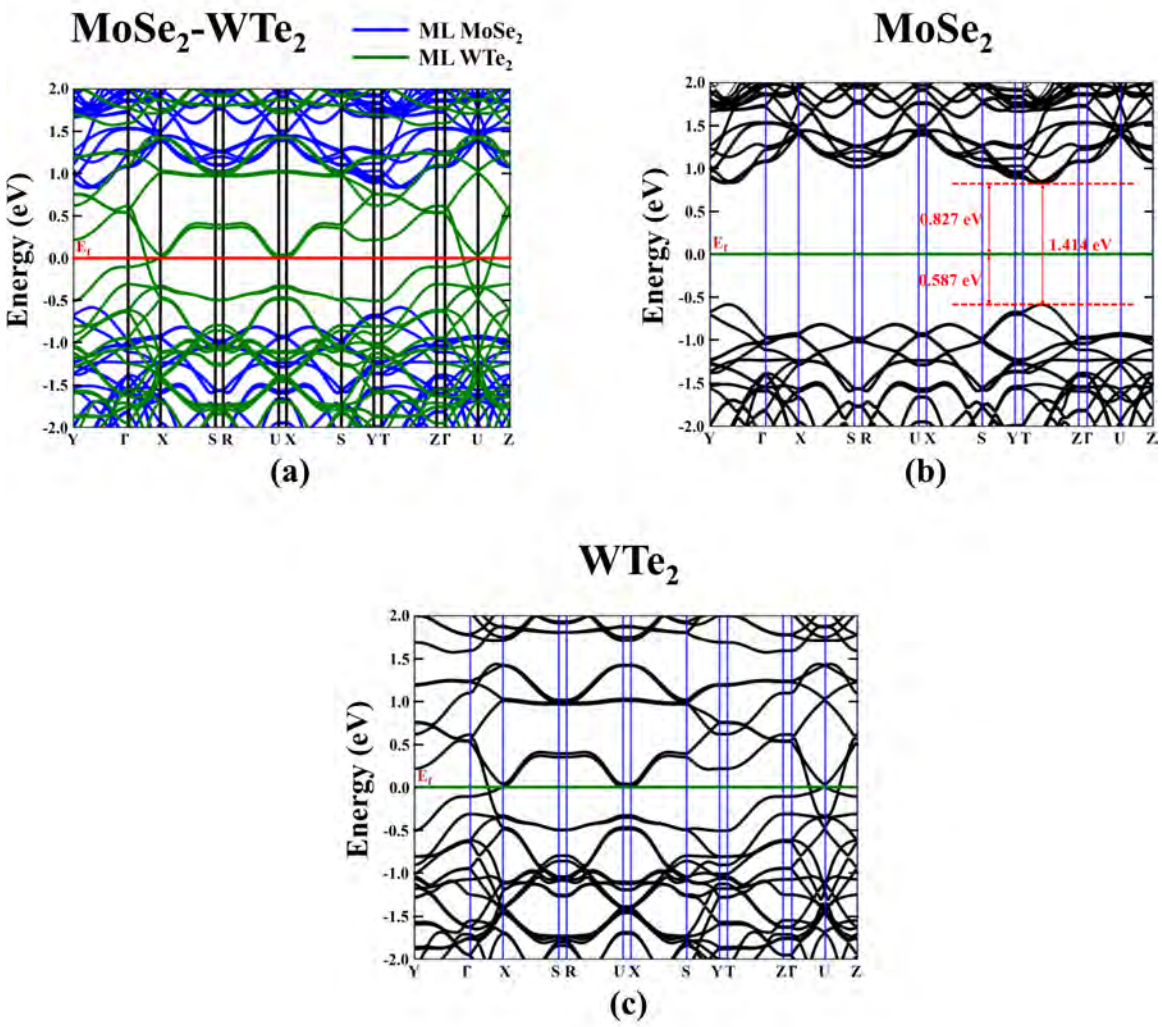

Figure 8.7: The Bandstructure and Projected Bandstructure of (ML)$MoSe_2$-(ML)WTe_2 Junction. (a) the bandstructure of (ML)$MoSe_2$-(ML)WTe_2 junction, (b) the projected bandstructure of the ML $MoSe_2$ layer in the junction, (c) the projected bandstructure of the ML WTe_2 layer in the junction.

Table 8.4: The Band Structure Parameters of ML TMDC Heterojunctions. In the table, the ϕ_n (eV) denotes the distance between CBM and Fermi level, the ϕ_p (eV) denotes the distance between VBM and Fermi level. The E_g (eV) is the bandgap energy of the constituent layer after forming heterojuntion.

	Constituent	ϕ_n (eV)	ϕ_p (eV)	E_g	Doping Type
MoS_2-$MoSe_2$	MoS_2	0.316	1.236	1.552	n
	$MoSe_2$	0.830	0.464	1.294	p
MoS_2-$MoTe_2$	MoS_2	0.529	1.281	1.810	n
	$MoTe_2$	0.452	0.490	0.942	intrinsic
$MoSe_2$-$MoTe_2$	$MoSe_2$	0.216	0.937	1.153	n
	$MoTe_2$	0.789	0.301	1.090	p
WS_2-WSe_2	WS_2	0.409	0.945	1.354	n
	WSe_2	1.094	0.419	1.513	p
MoS_2-WS_2	MoS_2	0.549	1.059	1.608	n
	WS_2	0.913	0.885	1.798	intrinsic
MoS_2-WSe_2	MoS_2	0.275	0.927	1.202	n
	WSe_2	1.157	0.279	1.436	p
$MoSe_2$-WS_2	$MoSe_2$	0.876	0.552	1.428	p
	WS_2	0.502	0.887	1.389	n
$MoSe_2$-WSe_2	$MoSe_2$	0.551	0.891	1.450	n
	WSe_2	0.842	0.688	1.530	p

Table 8.5: The Band Structure Parameters of ML TMDC Heterojunctions. In the table, the ϕ_n (eV) denotes the distance between CBM and Fermi level, the ϕ_p (eV) denotes the distance between VBM and Fermi level. The E_g (eV) is the bandgap energy of the constituent layer after forming heterojuntion.

	Constituent	ϕ_n (eV)	ϕ_p (eV)	E_g	Doping Type
$MoTe_2$-WS_2	$MoTe_2$	0.455	0.476	0.931	intrinsic
	WS_2	0.864	1.083	1.947	n
$MoTe_2$-WSe_2	$MoTe_2$	0.757	0.358	1.115	p
	WSe_2	0.311	0.846	1.157	n
MoS_2-WTe_2	MoS_2	0.561	1.185	1.746	n
	WTe_2	-	-	-	-
$MoSe_2$-WTe_2	$MoSe_2$	0.827	0.587	1.414	p
	WTe_2	-	-	-	-
$MoTe_2$-WTe_2	$MoTe_2$	0.619	0.399	1.018	p
	WTe_2	-	-	-	-
WS_2-WTe_2	WS_2	0.868	1.010	1.878	n
	WTe_2	-	-	-	-
WSe_2-WTe_2	WSe_2	1.084	0.407	1.491	p
	WTe_2	-	-	-	-

details.

As shown in figure-8.8 (a) and (c), after forming the heterojunction, both the ML MoS_2 and ML WS_2 exhibit band shifting at two k points: A (Γ) and K. As shown in figure-8.8 (a), for the ML MoS_2, the CBM and VBM at the K point shift down with 0.349 eV and 0.216 eV respectively, as compared to the intrinsic bandstructure of free-standing ML MoS_2. The valence band (VB) at the A point shifts down with 0.053 eV, which is much smaller than the shifting at A point. As a result, the VBM position is changed from the K point to the A point and the bandgap energy is reduced. The n-type doping is introduced to the ML MoS_2, as shown in figure-8.8 (b).

As for the ML WS_2 in the junction, the band shifting also occurs at the A point and the K point. At the K point, the VBM of the WS_2 shifts up for 0.067 eV while the CBM shift down with a smaller energy value of 0.039 eV. The VB at the A point shifts up for 0.093 eV. Since the VB at the A point does not go beyond the original VBM, thus the position of the VBM of the ML WS_2 bandstructure does not change and the bandgap remains direct bandgap.

The PBS analysis of the (ML)MoS_2-(ML)$MoSe_2$ heterojunction is shown in figure-8.9. The results show that, the bandstructure of the ML MoS_2 is modified by the band shifting of the CB and VB located at the K and A point. At the same time, the bandstructure of the ML $MoSe_2$ is modified by the band shifting at the K and Q point, where the Q point is defined as (0.17, 0.17, 0.2425) in k space. As shown in figure-8.9 (b), the ML MoS_2 in the junction shows n-type doping, as its CBM and VBM at the K point shift down while the VB at the A point shifts up. After forming the heterojunction, the bandgap of the ML MoS_2 in the junction is transformed from direct bandgap to indirect bandgap. The ML $MoSe_2$ in the junction shows p-type doping. For the ML $MoSe_2$ in the junction, the CBM and VBM shift up at the K point. At the Q point, the CB of the ML MSe_2 shifts down with a smaller energy compared with the band shifting located at the K point. As a result, the CBM is moved from the K point to Q point. Thus the bandgap of the $MoSe_2$ layer becomes

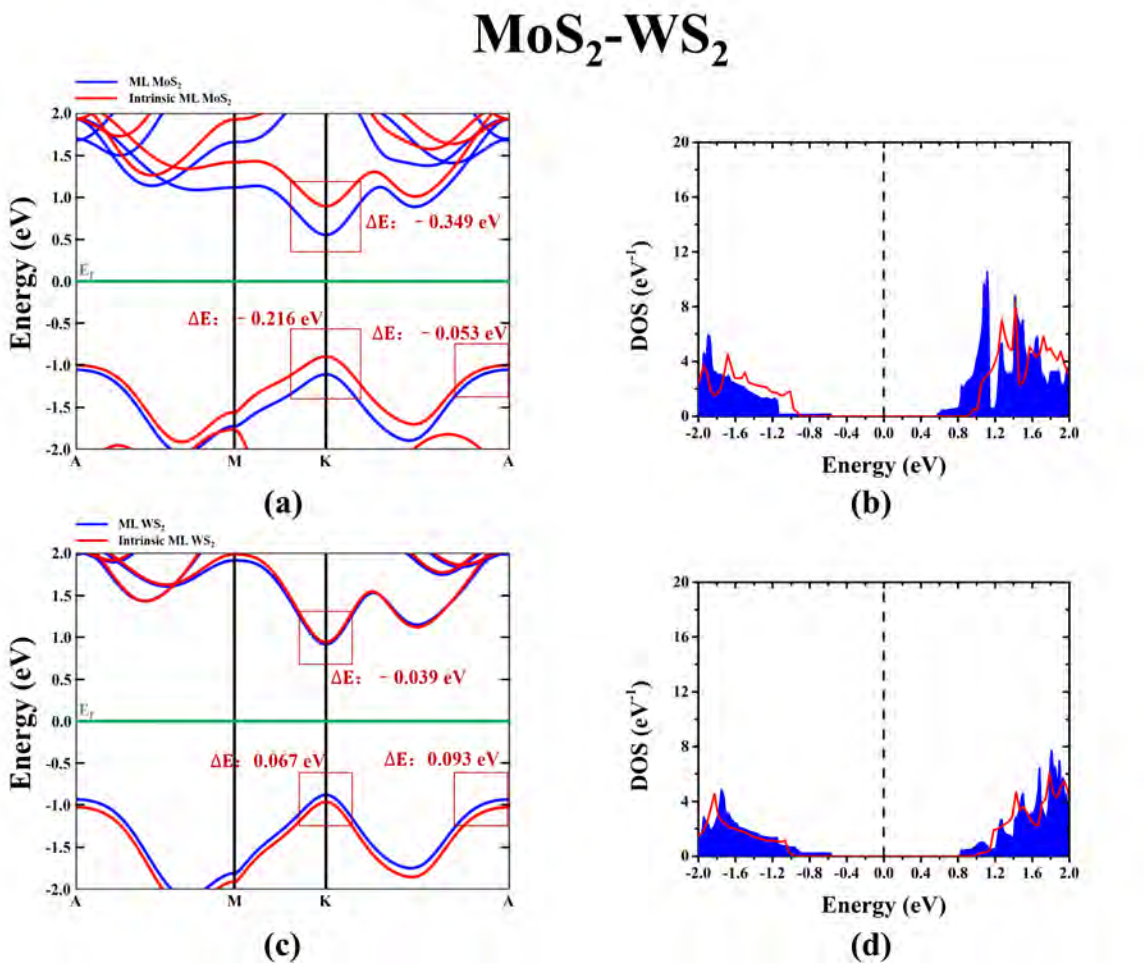

Figure 8.8: The Comparison between the PBS and PDOS of the Constituent Layers of the (ML)MoS_2-(ML)WS_2 Heterojunction, Free-Standing Intrinsic ML MoS_2 and WS_2. (a) the PBS of the ML MoS_2 in the heterojunction and free-standing ML MoS_2. (b) the PDOS of the ML MoS_2 in the heterojunction and free-standing ML MoS_2. (c) the PBS of the ML WS_2 in the heterojunction and free-standing ML WS_2. (d) the PDOS of the ML WS_2 in the heterojunction and free-standing ML WS_2. In the plot (a) and (c), the blue line denotes the bandstructure of the constituent layers in the heterojunction, while the red line denotes the bandstructure of the free-standing intrinsic ML TMDCs. In the plot (b) and (d), the blue colored region represents the PDOS of the heterojunction constituent layers while the red line refers the PDOS of the free-standing intrinsic TMDCs.

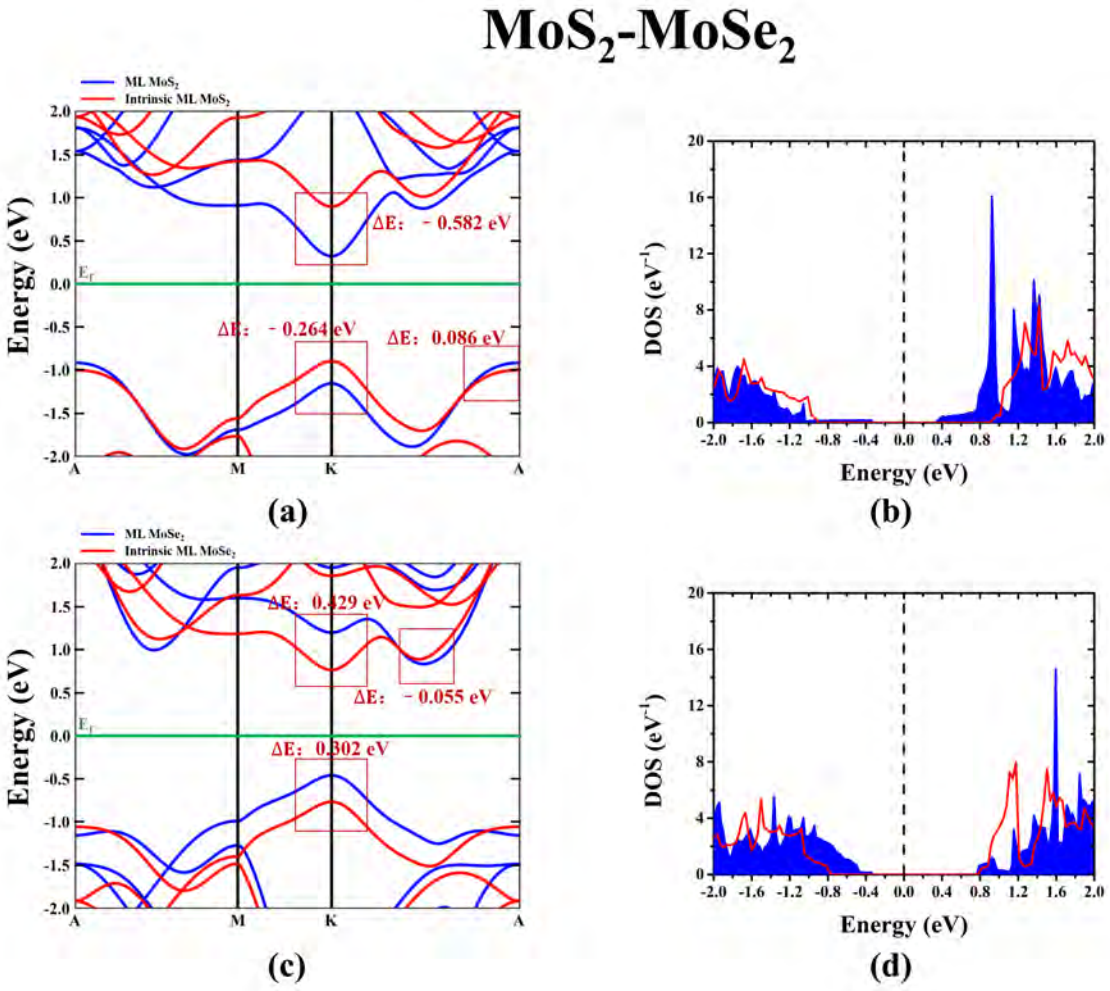

Figure 8.9: The Comparison between the PBS and PDOS of the Constituent Layers of the (ML)MoS_2-(ML)$MoSe_2$ Heterojunction, Free-Standing Intrinsic ML MoS_2 and $MoSe_2$. (a) the PBS of the ML MoS_2 in the heterojunction and free-standing ML MoS_2. (b) the PDOS of the ML MoS_2 in the heterojunction and free-standing ML MoS_2. (c) the PBS of the ML $MoSe_2$ in the heterojunction and free-standing ML $MoSe_2$. (d) the PDOS of the ML $MoSe_2$ in the heterojunction and free-standing ML $MoSe_2$. In the plot (a) and (c), the blue line denotes the bandstructure of the constituent layers in the heterojunction, while the red line denotes the bandstructure of the free-standing intrinsic ML TMDCs. In the plot (b) and (d), the blue colored region represents the PDOS of the heterojunction constituent layers while the red line refers the PDOS of the free-standing intrinsic TMDCs.

indirect.

The typical examples of the PBS of(ML)MX_2-(ML)WTe_2 (X: S, Se and Te) junctions are shown in figure-8.10 and figure-8.11.

As shown in figure-8.10, the ML MoS_2 in the (ML)MoS_2-(ML)WTe_2 junction becomes n-type after contacting with the ML WTe_2. In this case, the CBM located at α_1 point (which is between the Γ and X point) shifts towards the β_1 point (which is between the Y and Γ point), while the β_1 point is closer to the Fermi level. Meanwhile, the VBM also moves in the same direction as the CBM, from the α_2 point to β_2 point, as shown in the figure-8.10 (a). The band energy of the ML MoS_2 is reduced by 0.625 eV after contacting, as shown in the figure-8.10 (b). The shifting of the CBM and VBM of the ML MoS_2 is 0.337 eV and 0.288 eV respectively.

As shown in figure-8.11, after contacting with the ML WTe_2, the ML $MoSe_2$ becomes p-type. The PBS shows that, for (ML)$MoSe_2$-(ML)WTe_2 junction, the CBM and VBM of the ML $MoSe_2$ shift upwards from α_1 and α_2 to β_1 and β_2. The bandgap energy of the ML $MoSe_2$ is reduced by 0.241 eV.

After contacting with ML MoS_2 and $MoSe_2$, the ML WTe_2 remains semi-metallic, as shown in figure-8.10 (c) and figure-8.11 (c). The ML WTe_2 layer in the (ML)MoS_2-(ML)WTe_2 and (ML)$MoSe_2$-(ML)WTe_2 junctions show very similar bandstructure. The empty region between the X and Y point in the intrinsic bandstructure of the ML WTe_2 now is filled with bands.

The PBS analysis shows that, the bandstructure modification and introduced doping for the constituents of the heterojunctions are highly dependent on the interaction of the interfacial atoms. For example, according to the PBS results listed in table-8.4 and table-8.5, the ML MS_2 (M: Mo and W) in the (ML)MS_2-(ML)MSe_2 heterojunctions always show n-type doping, while the ML MSe_2 always shows p-type doping. Different interfacial atoms possess different reach-out electron orbitals, thus the localized states around several critical k points show different sensitivity to the interfacial interaction at the heterointerface. This difference leads to different shifting near the

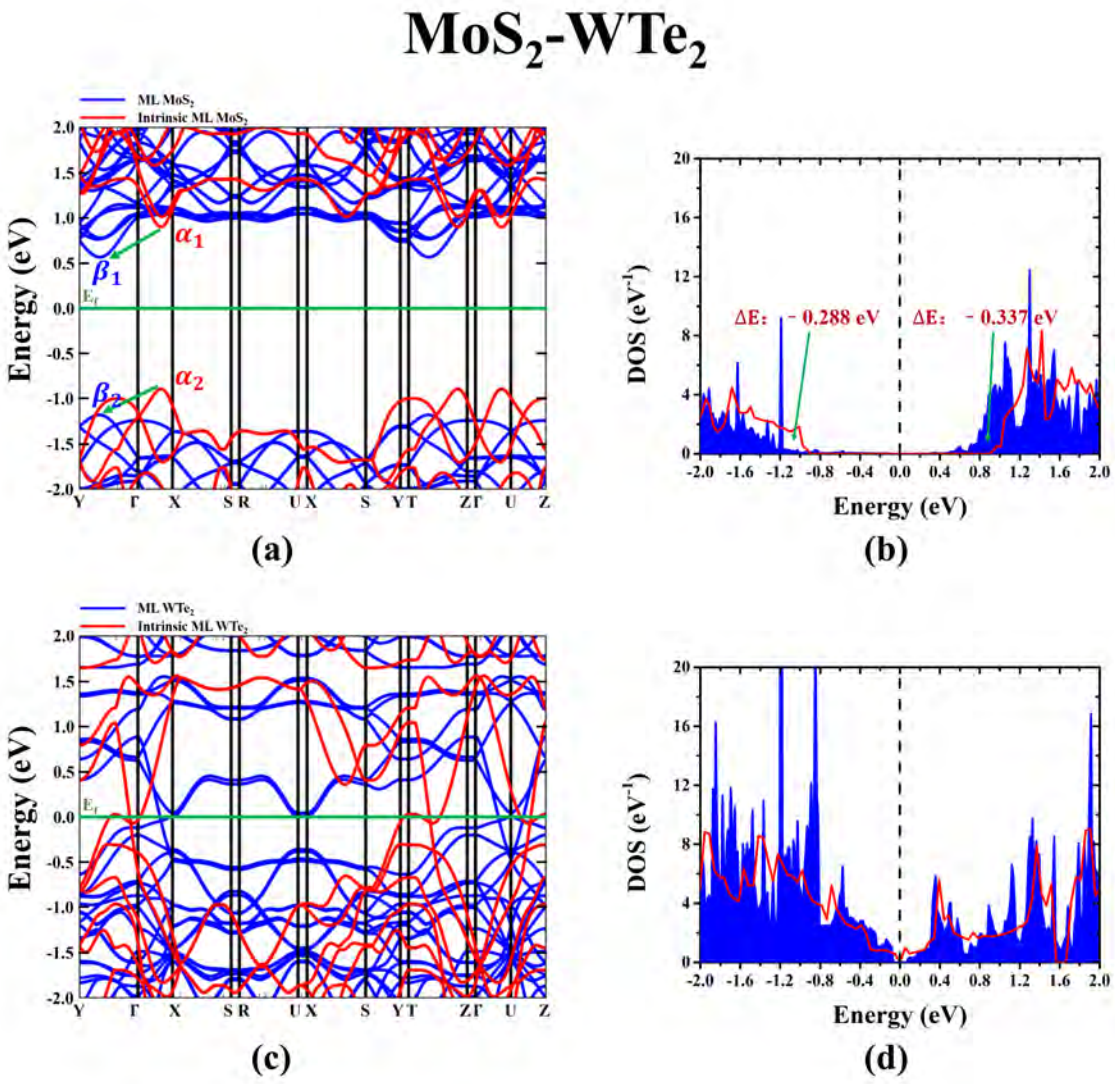

Figure 8.10: The Comparison between the PBS and PDOS of the Constituent Layers of the (ML)MoS_2-(ML)WTe_2 Heterojunction, Free-Standing Intrinsic ML MoS_2 and WTe_2. (a) the PBS of the ML MoS_2 in the heterojunction and free-standing ML MoS_2. (b) the PDOS of the ML MoS_2 in the heterojunction and free-standing ML MoS_2. (c) the PBS of the ML WTe_2 in the heterojunction and free-standing ML WTe_2. (d) the PDOS of the ML WTe_2 in the heterojunction and free-standing ML WTe_2. In the plot (a) and (c), the blue line denotes the bandstructure of the constituent layers in the heterojunction, while the red line denotes the bandstructure of the free-standing intrinsic ML TMDCs. In the plot (b) and (d), the blue colored region represents the PDOS of the heterojunction constituent layers while the red line refers the PDOS of the free-standing intrinsic TMDCs.

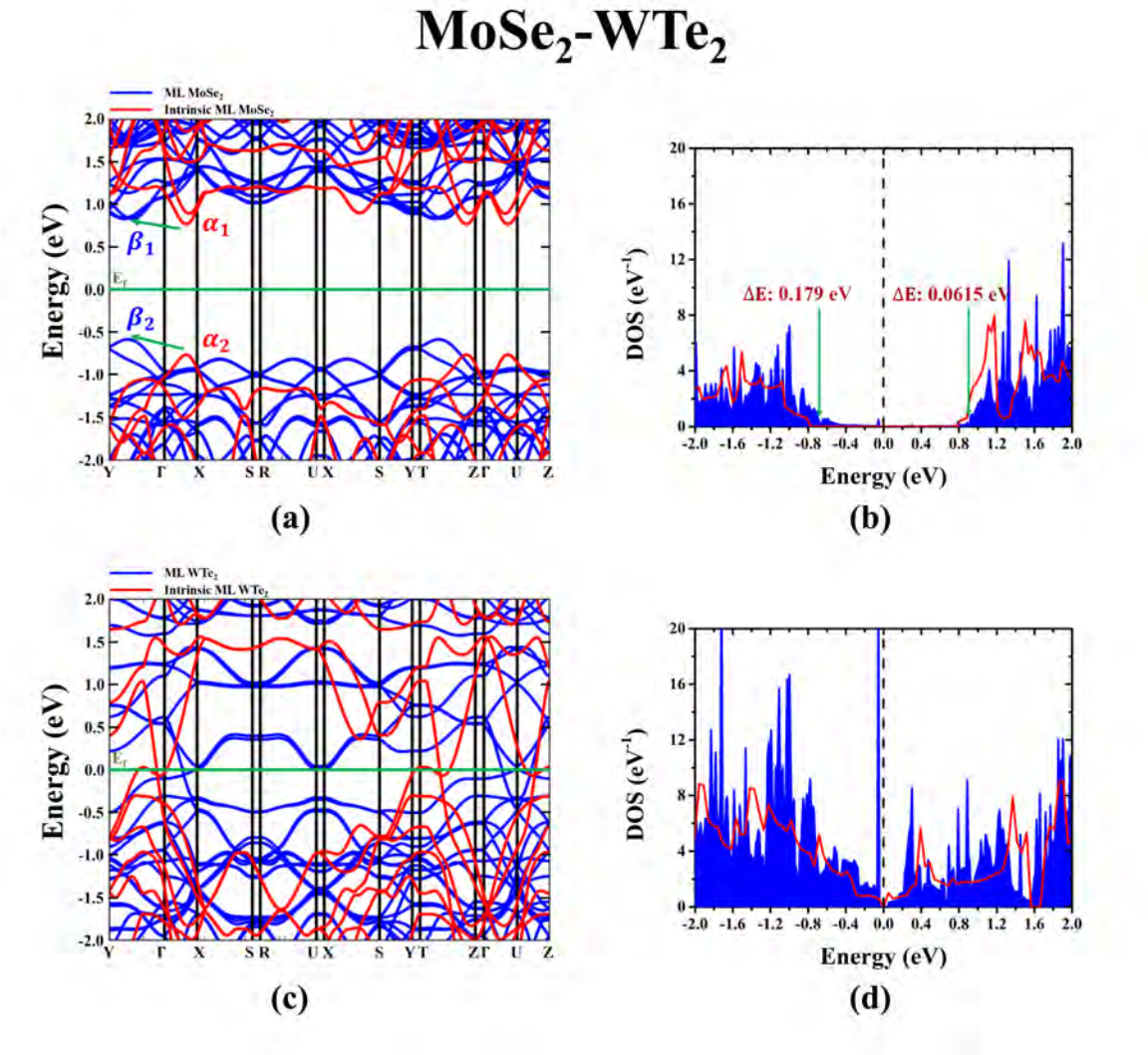

Figure 8.11: The Comparison between the PBS and PDOS of the Constituent Layers of the (ML)$MoSe_2$-(ML)WTe_2 Heterojunction, Free-Standing Intrinsic ML $MoSe_2$ and WTe_2. (a) the PBS of the ML $MoSe_2$ in the heterojunction and free-standing ML $MoSe_2$. (b) the PDOS of the ML $MoSe_2$ in the heterojunction and free-standing ML $MoSe_2$. (c) the PBS of the ML WTe_2 in the heterojunction and free-standing ML WTe_2. (d) the PDOS of the ML WTe_2 in the heterojunction and free-standing ML WTe_2. In the plot (a) and (c), the blue line denotes the bandstructure of the constituent layers in the heterojunction, while the red line denotes the bandstructure of the free-standing intrinsic ML TMDCs. In the plot (b) and (d), the blue colored region represents the PDOS of the heterojunction constituent layers while the red line refers the PDOS of the free-standing intrinsic TMDCs.

critical k points after the formation of the heterojunctions. The variation of the shifting in the respect of the k point in the same bandstructure causes the reduction of the bandgap energy and the transforming of the direct/indirect bandgap. To understand the emergent properties of the heterostructure, investigating the states contributed by the interfacial atoms and the interlayer interaction should be the main focus. It is of our great interest to investigate the band states weight in terms of the interfacial layer electron orbitals. However, the ATK does not provide such kind of tools. The relative simulation will be done in the future once we have the access to the resources.

8.5 Band Alignment

After the PBS simulation, the extracted band alignment intuitively sketches out the electronic structure of the TMDC heterostructures, which helps us gain a better point of view of the potential application fields of the TMDC heterostructures. For the band alignment, the zero energy level is set as the Fermi level. That is because after forming the hetero interface, the system is in equilibrium. The Fermi levels of the constituents are aligned to a single flat Fermi level. It is clear that, the band alignment for the semiconducting TMDC heterostructures could be divided into two groups: Type I, as shown in figure-8.12, and Type II, as shown in figure-8.13. The definition of each group is based on the relative position of the bands.

For Type I heterojunctions, as shown in figure-8.12, the bandgap of one constituent falls entirely into the bandgap of the other constituent. In this case, suppose the bandgap of the material 1 falls entirely into the bandgap of material 2, thus the $CB_1 \leqslant CB_2$, and $VB_1 \geqslant VB_2$, where the CB_1 and CB_2 are the positions of the conduction band edge, and VB_1 and VB_2 are the positions of the valence band edge. Specifically, the conduction band edge of the ML MoS_2 in the (ML)MoS_2-(ML)$MoTe_2$ heterojunction is 0.529 eV, which is larger than the conduction band edge of the ML $MoTe_2$ in the junction (0.452 eV). The valence band edge of the ML MoS_2 in the junction is located at -1.281 eV, while the valence band edge of the ML $MoTe_2$ is at

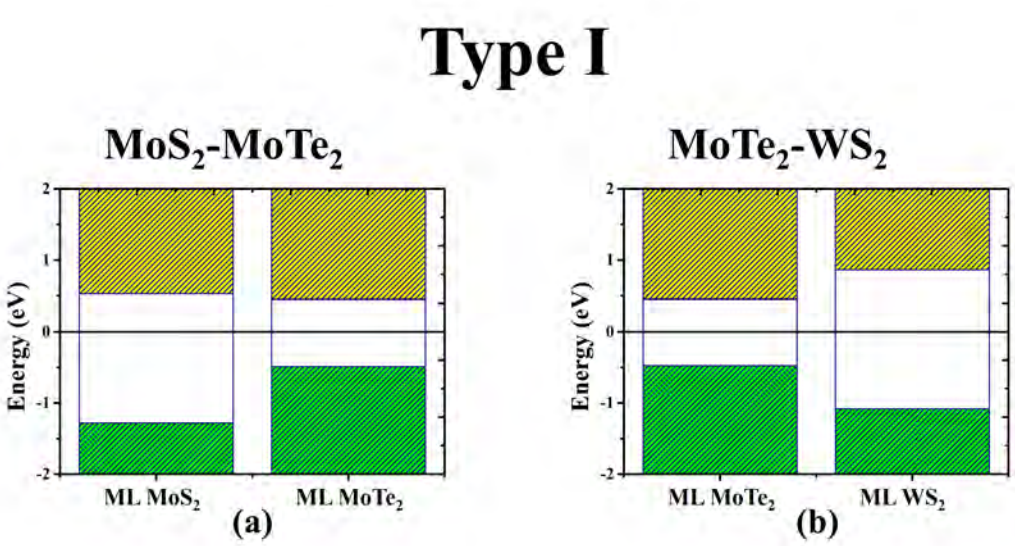

Figure 8.12: The Band Alignment of Type-I (ML)MX_2-(ML)MX_2 Heterojunctions. (a) (ML)MoS_2-(ML)$MoTe_2$ heterojunction. (b) (ML)$MoTe_2$-(ML)WS_2 heterojunction.

-0.490 eV. Thus the (ML)MoS_2-(ML)$MoTe_2$ heterojunction is Type I junction.

Most of the ML semiconducting TMDC heterostructures are Type II heterojunctions, as shown in figure-8.13. The Type II heterojunction is defined as the two bands of the two materials are staggered with each other. In this case, $CB_1<CB_2$, and $VB_1<VB_2<CB_1$. For example, as shown in figure-8.13 (a), for the (ML)MoS_2-(ML)$MoSe_2$ junction, the conduction band edge CB_1 and the valence band edge VB_1 of the MoS_2 is 0.316 eV and -0.920 eV, while the CB_2 and VB_2 of the $MoSe_2$ is 0.830 eV and -0.464 eV respectively. As shown in figure-8.13 (b), the conduction band edge CB_1 and valence band edge VB_1 of the ML MoS_2 in the (ML)MoS_2-(ML)WS_2 hetero junction is 0.549 eV and -1.059 eV. As for the ML WS_2 in the hetero junction, the conduction band edge CB_2 is 0.913 eV and the valence band edge VB_2 is -0.885 eV. Thus both the (ML)MoS_2-(ML)$MoSe_2$ and (ML)MoS_2-(ML)WS_2 junctions are the Type II hetero junction.

The Type I and Type II TMDC heterojunctions can be put adopted in wide range of electronic and optical applications. For example, the figure-8.15 (a) and (b) show

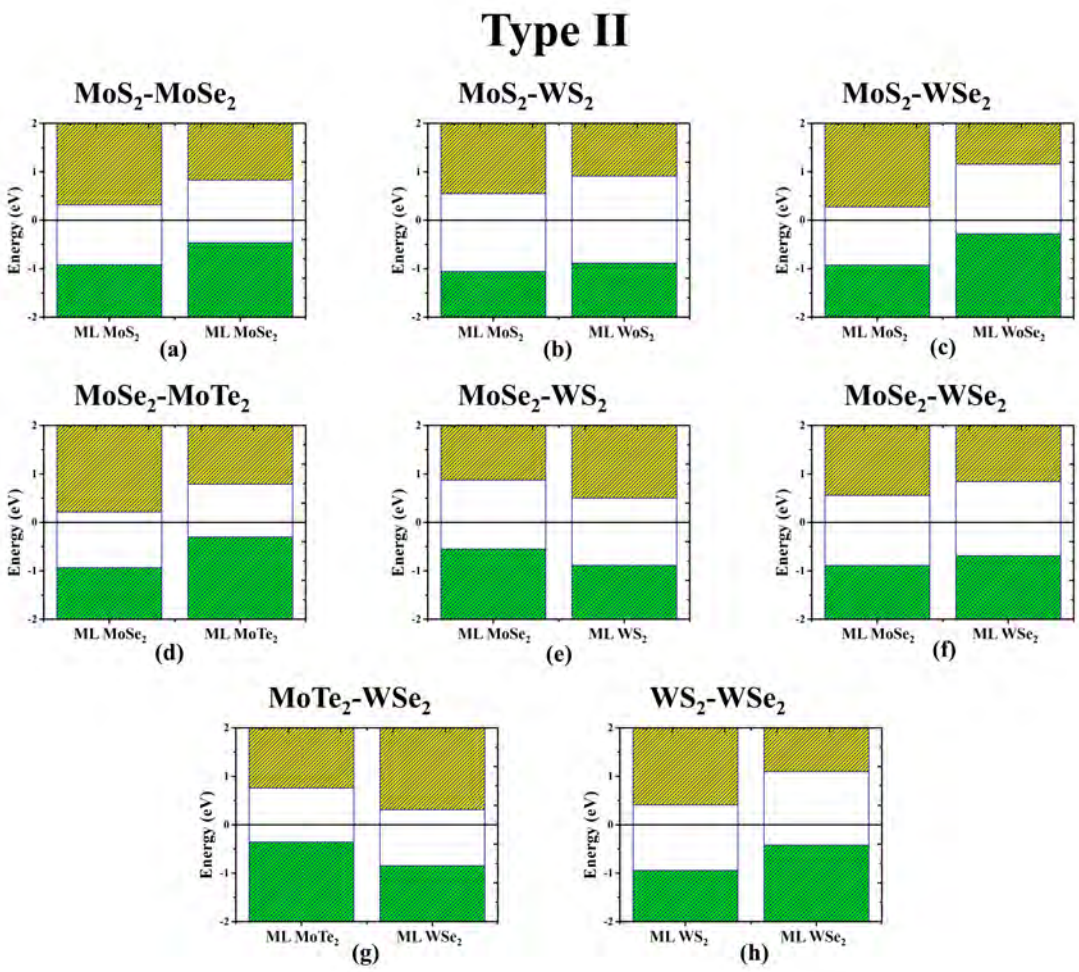

Figure 8.13: The Band Alignment of Type-II (ML)MX_2-(ML)MX_2 Heterojunctions. (a) (ML)MoS_2-(ML)$MoSe_2$ heterojunction. (b) (ML)MoS_2-(ML)WS_2 heterojunction. (c) (ML)MoS_2-(ML)WSe_2 heterojunction. (d) (ML)$MoSe_2$-(ML)$MoTe_2$ heterojunction. (e) (ML)$MoSe_2$-(ML)WS_2 heterojunction. (f) (ML)$MoSe_2$-(ML)WSe_2 heterojunction. (g) (ML)$MoTe_2$-(ML)WSe_2 heterojunction. (h) (ML)WS_2-(ML)WSe_2 heterojunction.

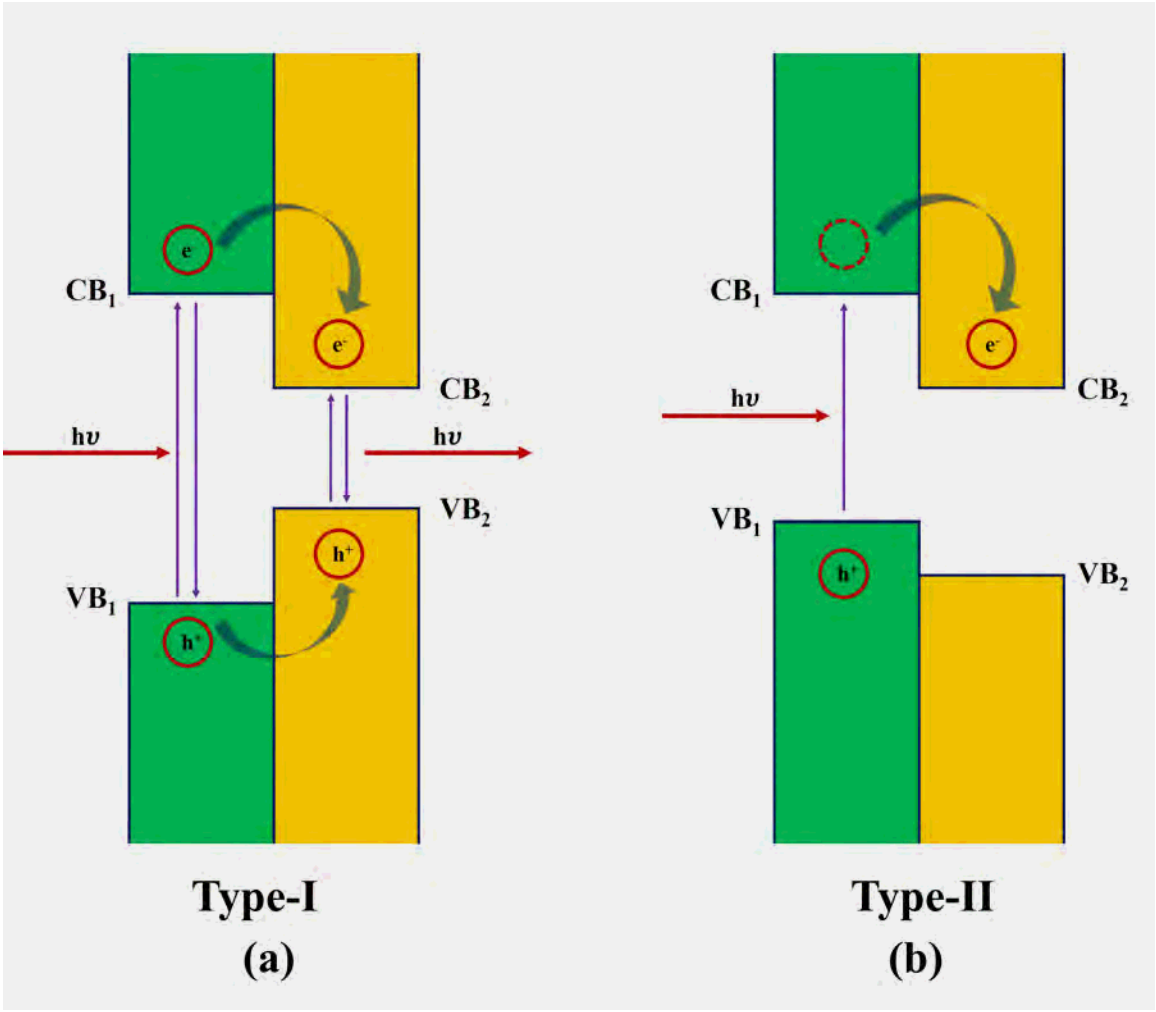

Figure 8.14: The Working Mechanism of the (ML)MX_2-(ML)MX_2 Heterojunctions under the Excitation. (a) The working mechanism of the Type-I heterojunctions. (b) The working mechanism of the Type-II heterojunctions.

the working mechanism of the Type I and Type II heterostructures under the incident light. The energy of the incident photons hυ is larger than the bandgap energy of material 1. For Type I hetero junctions, three phenomena with different mechanisms will happen: the excitation and recombination of the electrons and holes within the material 1, the hopping of the excited electrons and holes from the material 1 to material 2 and the recombination of the excited electron-hole pairs in the material 2. The recombination in material 2 will generate strong photoluminescence process. The figure-8.15 (a) demonstrates that, the Type I semiconducting TMDC heterostructures are promising candidates for photoluminescence. In the Type II hetero junctions, after the excitation, the excited electrons hop through the low-energy Van der Waals barrier into the adjacent material at the interface to achieve a lower energy state. The staggered structure of the hetero junctions provides a perfect reservoir for the excited electron-hole pairs. This unique bandstructure grants Type II TMDC heterostructures superior ability of separating the excited charge populations, which makes them suitable for photovoltaic applications.

The band alignment of the MX_2-WTe_2 junctions are shown in the figure-8.14. It is clear that, compared with the metal contacts W, Mo and Au discussed in the previous part, the ML WTe_2 adds less doping concentration to the ML MoS_2. The doping concentrations added to other semiconducting TMDC materials by ML WTe_2 is also very limited. At the same time, the bandgap shrinking for the semiconducting MX_2 after contacting with the ML WTe_2 is very tiny. This demonstrates that, as a semi-metallic electrode material, the WTe_2 shows superior ability of preserving the intrinsic properties of the contacting MX_2 materials. This is important for the application of the TMDC heterojunctions since the doping concentration introduced by the metallic contact will affect the functionality of the devices. The main disadvantage of the (ML)WTe_2-(ML)MX_2 contact is the large Schottky barrier height, as shown in figure-8.14. The Schottky barrier height ranging from 0.399 eV to 0.868 eV for different MX_2-WTe_2 junctions, which is extremely high compared with other

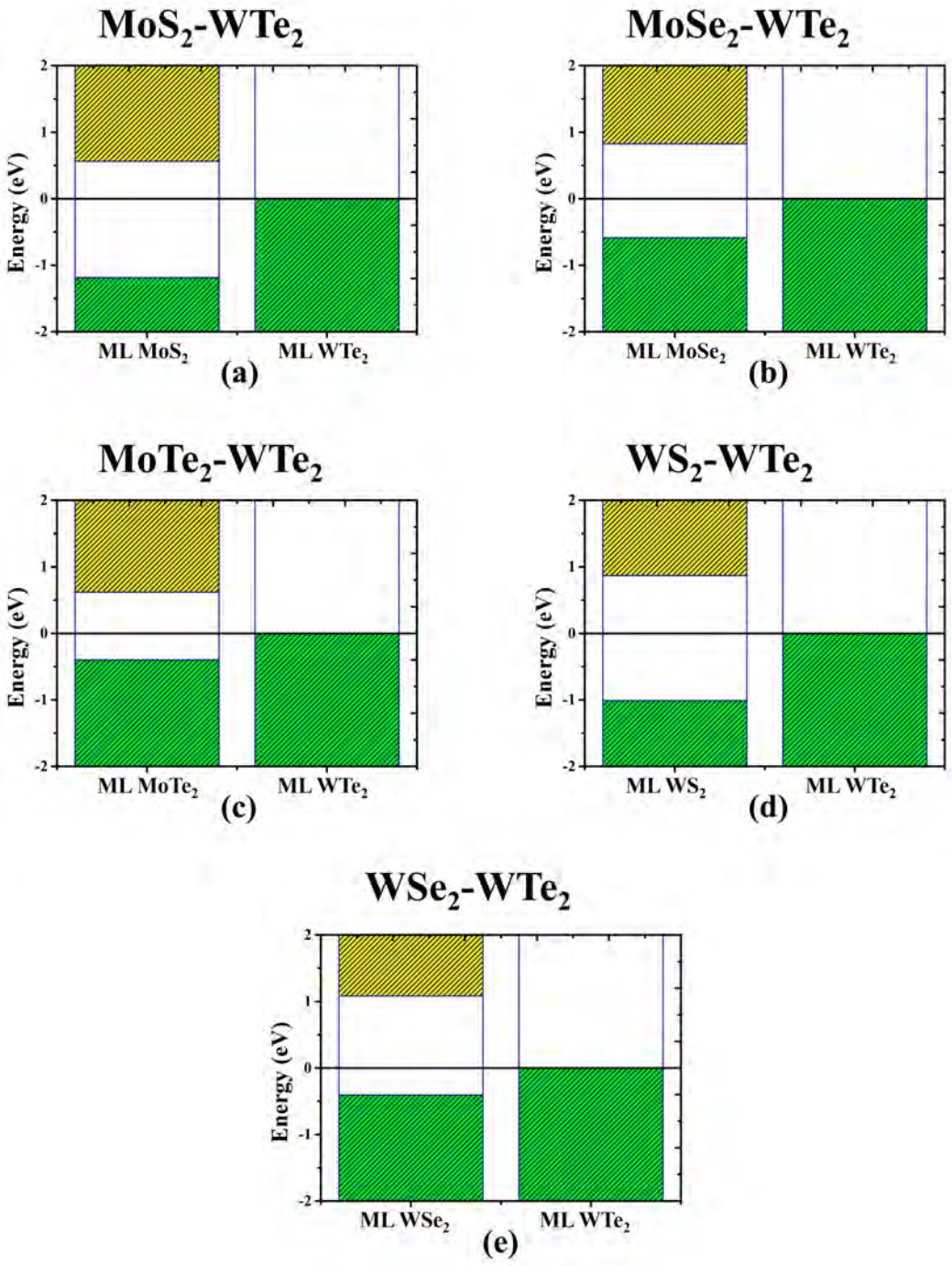

Figure 8.15: The Band Alignment of (ML)MX_2-(ML)WTe_2 Heterojunctions. (a) (ML)MoS_2-(ML)WTe_2 heterojunction. (b) (ML)$MoSe_2$-(ML)WTe_2 heterojunction. (c) (ML)$MoTe_2$-(ML)WTe_2 heterojunction. (d) (ML)WS_2-(ML)WTe_2 heterojunction. (e) (ML)WSe_2-(ML)WTe_2 heterojunction.

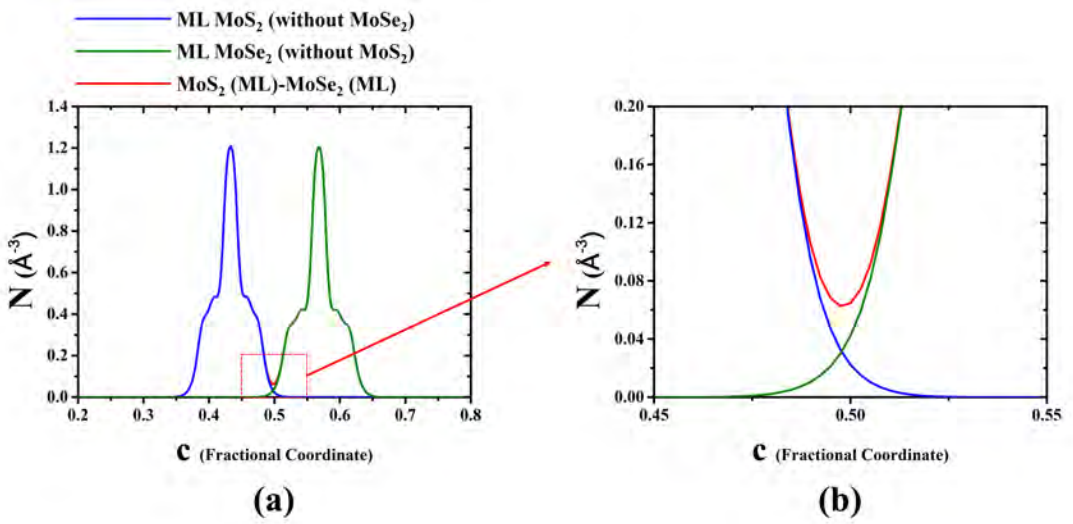

Figure 8.16: The Electron Density of (ML)MoS_2-(ML)$MoSe_2$ Junction. (a) The electron density of (ML)MoS_2-(ML)$MoSe_2$ Junction is projected onto the c axis (fractional coordinate). In the plot, the green and blue lines denote the electron density of the isolated ML MoS_2 and $MoSe_2$, while the red line denotes the total electron density of the junction. (b) the zoom-in plot of the electron density of the junction.

electrodes discussed in the previous chapters. It means that, to make good WTe_2 contacts, moderate n-type or p-type doping of the ML MX_2 layer is required.

8.5.1 The Electron Density Analysis

The electron density is a useful tool to describe the distribution of the electron orbitals. To understand the redistribution of the electron orbitals after the formation of the heterointerface, the electron density simulations are performed on the investigated ML TMDC heterojunctions.

As shown in figure-8.16, a test simulation has been conducted on theML)MoS_2-(ML)$MoSe_2$ heterojunction. In the test simulation, electron density of the ML MoS_2 (without the adjacent $MoSe_2$ layer), ML $MoSe_2$ (without the adjacent MoS_2 layer) and the (ML)MoS_2-(ML)$MoSe_2$ heterojunction are simulated and colored by blue, green and red respectively. The simulated electron density is normalized and projected to the c axis, which is in fractional coordinate. As shown in figure-8.16, the electron density of the isolated ML MoS_2 and ML $MoSe_2$ shows perfect overlapping with the

Table 8.6: The Interfacial ED Minimum and the Intefacial Electron Population of the TMDC Heterojunctions.

	Interfacial ED Minimum ($Å^{-3}$)	Intefacial Electron Population
MoS_2-$MoSe_2$	0.06245	0.08665
MoS_2-$MoTe_2$	0.04096	0.08203
MoS_2-WS_2	0.04359	0.07673
MoS_2-WSe_2	0.05106	0.07863
$MoSe_2$-$MoTe_2$	0.07262	0.10623
$MoSe_2$-WS_2	0.04398	0.07486
$MoSe_2$-WSe_2	0.05389	0.08021
$MoTe_2$-WS_2	0.03223	0.07629
$MoTe_2$-WSe_2	0.05919	0.10411
WS_2-WSe_2	0.03652	0.06754
MoS_2-WTe_2	0.03785	0.06797
$MoSe_2$-WTe_2	0.03763	0.06536
$MoTe_2$-WTe_2	0.04680	0.09320
WS_2-WTe_2	0.02916	0.05791
WSe_2-WTe_2	0.03290	0.06227

electron density of the (ML)MoS_2-(ML)$MoSe_2$ junction. The only exception is the electron density located at the heterointerface. The figure-8.16 (b) intuitively shows that, the electron density distribution of the (ML)MoS_2-(ML)$MoSe_2$ heterojunction at the heterointerface is exactly determined by the overlapping of the delocalized electron orbitals of the interfacial atoms. The delocalization of the interfacial electron orbitals and intralayer electron distribution indicates that, the emergent properties are mainly generated by the interaction between heterointerface atoms. Thus, it is of our great interest to explore the relationship between the emergent properties and interfacial electron populations.

The figure-8.17 and figure-8.18 show the ED analysis of the typical cases of TMDC

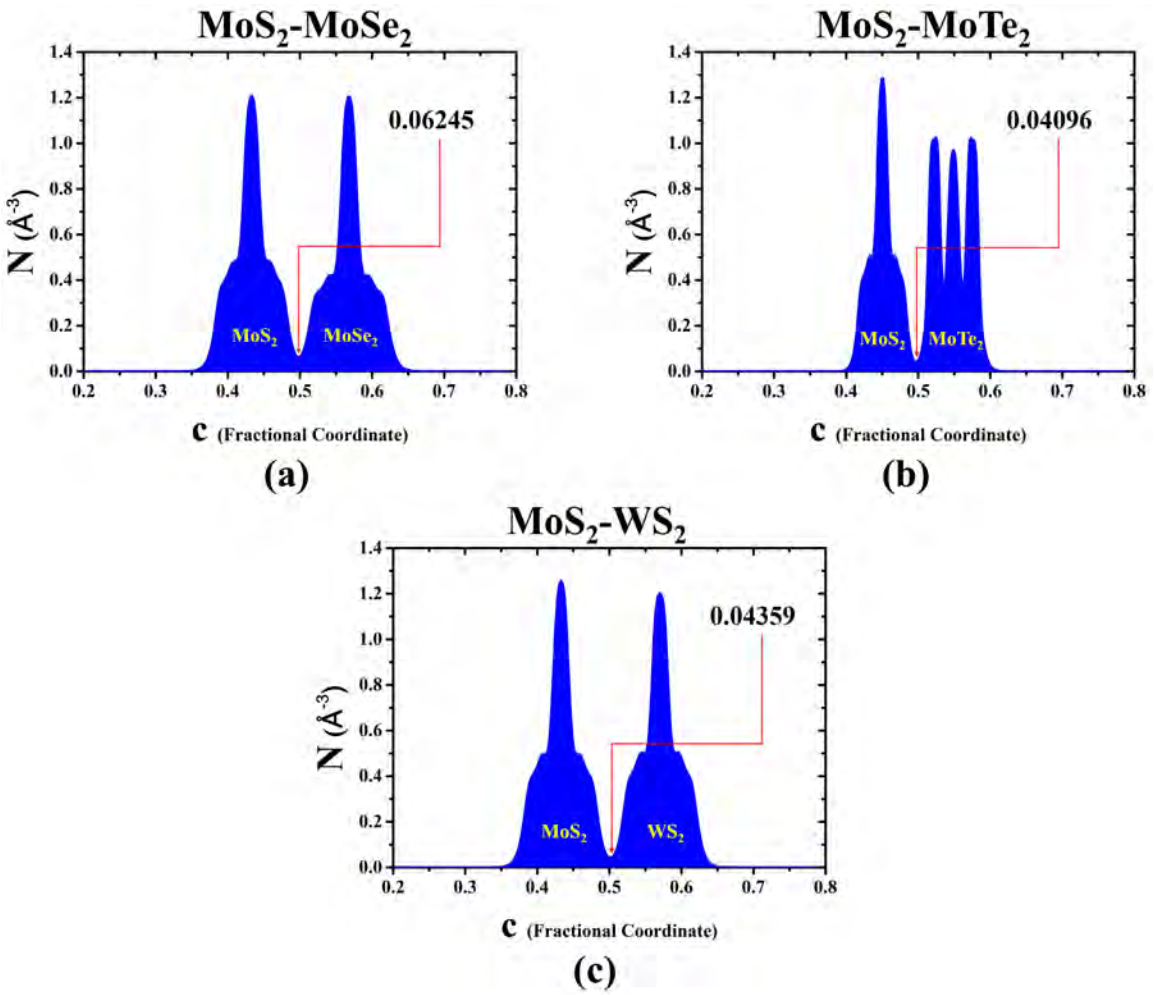

Figure 8.17: The Electron Density of (ML)MX_2-(ML)MX_2 Heterojunctions. (a) the electron density of (ML)MoS_2-(ML)$MoSe_2$ heterojunction, (b) the electron density of (ML)MoS_2-(ML)$MoTe_2$ heterojunction, (c) the electron density of (ML)MoS_2-(ML)WS_2 heterojunction.

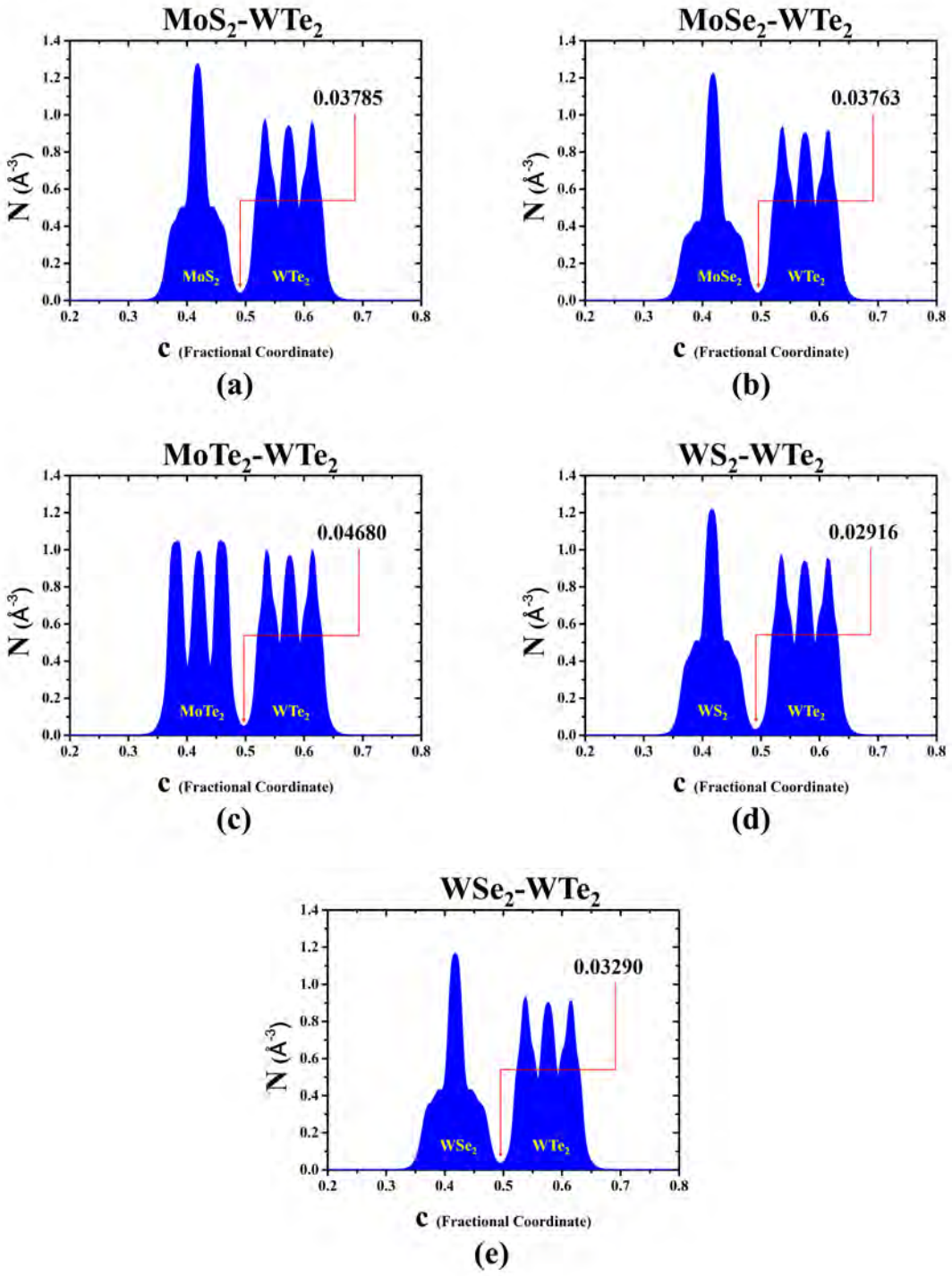

Figure 8.18: The Electron Density of (ML)MX_2-(ML)WTe_2 Heterojunctions. (a) the electron density of (ML)MoS_2-(ML)WTe_2 heterojunction, (b) the electron density of (ML)$MoSe_2$-(ML)WTe_2 heterojunction, (c) the electron density of (ML)$MoTe_2$-(ML)WTe_2 heterojunction, (d) the electron density of (ML)WS_2-(ML)WTe_2 heterojunction, (e) the electron density of (ML)WSe_2-(ML)WTe_2 heterojunction.

heterojuntions. To evaluate the interlayer electron orbital overlapping, the minimum point of the ED of the heterointerface region has been extracted and listed in table-8.6. As shown in figure-8.17 and table-8.6, the ED minimum of the heterointerface of semiconducting TMDC heterojunctions ranges from 0.03223 $Å^{-3}$ to 0.07262 $Å^{-3}$. Among the investigated semiconducting TMDC heterojunctions, the (ML)$MoSe_2$-(ML)$MoTe_2$ junction exhibits the largest interfacial ED minimum 0.07262 $Å^{-3}$, while the (ML)$MoTe_2$-(ML)WS_2 junction shows the smallest interfacial ED minimum 0.03223 $Å^{-3}$. Comparing with the previous BS and PBS results shown in table-8.4, the constituent layers of the (ML)$MoSe_2$-(ML)$MoTe_2$ junction show very distinct n-type or p-type doping. In the (ML)$MoTe_2$-(ML)WS_2 junction, the bandstructure characteristics of the ML $MoTe_2$ and ML WS_2 are very similar to their intrinsic properties. The ED simulation results indicate that the interlayer interaction in the (ML)$MoSe_2$-(ML)$MoTe_2$ junction is stronger than (ML)$MoTe_2$-(ML)WS_2 junction. This stronger interlayer interaction leads to a larger electron orbital delocalization in the (ML)$MoSe_2$-(ML)$MoTe_2$ junction. Thus the charge transfer in the (ML)$MoSe_2$-(ML)$MoTe_2$ junction is stronger than the (ML)$MoTe_2$-(ML)WS_2 junction, and more doping concentration is introduced to the constituent layers of the (ML)$MoSe_2$-(ML)$MoTe_2$ junction. For semiconducting TMDC heterojunctions, the heterointerface ED minimum provides good prediction to the strength of the interlayer charge transfer of the heterojunctions for most of the cases, except the (ML)MoS_2-(ML)$MoSe_2$ case. According to our simulation, the (ML)MoS_2-(ML)$MoSe_2$ junction shows a very large heterointerface ED minimum, but only a moderate amount of doping are introduced to the layers after the formation of the junction, which is smaller than several junctions with smaller heterointerface ED minimum such as (ML)MoS_2-(ML)WSe_2 junction.

As for the (ML)MX_2-(ML)WTe_2 junctions, as shown in figure-8.18 and table-8.6, the heterointerface ED minimum of these junctions ranges from 0.02916 $Å^{-3}$ to 0.04680 $Å^{-3}$. Among the (ML)MX_2-(ML)WTe_2 junctions, the (ML)$MoTe_2$-(ML)WTe_2

junction possesses the largest heterointerface ED minimum. The previous simulated results shown in table-8.5 demonstrate that, the ML $MoTe_2$ layer in the (ML)$MoTe_2$-(ML)WTe_2 junction shows largest introduced p-type doping concentration among all the (ML)MX_2-(ML)WTe_2 junctions. The (ML)WS_2-(ML)WTe_2 junction displays the smallest heterointerface ED minimum. According to the previous PBS results, the ML WS_2 is slightly doped after contacting with ML WTe_2, and only a small amount of n-type doping is added to the ML WS_2 in the junction. The ED minimum results match most of the (ML)MX_2-(ML)WTe_2 cases except the (ML)WSe_2-(ML)WTe_2 case. The heterointerface ED minimum of the (ML)WSe_2-(ML)WTe_2 junction is smaller than the ML $MoSe_2$ in (ML)$MoSe_2$-(ML)WTe_2 junction, but the introduced p-type doping of the ML WSe_2 is larger.

The heterointerface ED minimum does not include the factor of the interface distance and size of the superlattice. With a larger superlattice and interlayer distance, a TMDC heterojunction with smaller heterointerface ED minimum may have a larger absolute value of the interfacial delocalized electron population. To fix this issue, an integration over the heterointerface region is adopted to correct the heterointerface ED minimum. The integration gives the area under the ED curve. After translating the fractional coordinates to the Cartesian coordinates, the given integration reveals the absolute value of the delocalized interfacial electron populations. To define the interfacial region of the heterointerface, a peak finding based on the second derivative of the ED curve has been conducted and the two peaks which are closest to the interface are defined as the ED peak of the interfacial atoms. Suppose the left peak location c_1, the interfacial ED minimum coordinate c_2, and the right peak location c_3, the integration starts at the point $(c_1+c_2)/2$ and ends at point $(c_2+c_3)/2$. The calculated value times the c parameter of the supperlattice gives the absolute value of the heterointerface electron population projected onto the c axis. The heterointerface ED minimum and absolute heterointerface electron population of each junction are listed in the table-8.6.

By comparing the previous PBS results and corrected absolute interfacial electron population, it demonstrates that the interfacial electron population could partially predict the modification of the bandgap energy, ϕ_{n} and ϕ_{p}. Normally, a larger electron population at the heterointerface indicates larger introduced doping concentration and bandedge shifting of the constituent monolayers. The ED analysis also reveal the delocalization of the interfacial electron population, indicating that the polarization occurs after the formation of the heterojunction. However, there are exceptions. For example, the (ML)MoS_2-(ML)WSe_2 junction shows smaller heterointerface ED minimum and electron population compared with (ML)MoS_2-(ML)$MoSe_2$ junction. However, the bandedge shifting and introduced doping concentration of the ML MoS_2 and ML WSe_2 in the (ML)MoS_2-(ML)WSe_2 junction is larger than TMDCs in the (ML)MoS_2-(ML)$MoSe_2$ junction. Thus, the ED analysis alone could not predict the modification of electronic structures precisely.

8.6 Conclusion

In this work, we have conducted a comprehensive study of the TMDC heterojunctions consisting of ML MX_2 (M: Mo, W; X: S, Se, Te). We have studied all the possible combination of the MX_2 materials listed, and the investigation through the PBS simulation demonstrates that, The TMDC heterojunctions based on ML MX_2 show numerous emergent properties which are suitable for a wide range of applications. The band alignment demonstrates that, the semiconducting MX_2 materials able to form Type I and Type II heterojunctions. The ML WTe_2 is able to form n-type Schottky barrier with ML MoS_2 and ML WS_2, while forming p-type Schottky barrier with ML $MoSe_2$, ML $MoTe_2$ and ML WSe_2. The WTe_2 contact is able to preserve the intrinsic properties of the contacting semiconducting ML MX_2, but with a very large barrier height. This issue could be probably solved by doping the MX_2 layer. To understand the emergent properties, the ED, PBS and PDOS analysis have been conducted to the heterojunctions. The simulation results demonstrate that, the

electron density could be used to explain the strength of the band shifting. However, it could not be correlated with the simulation results perfectly. The PBS results show that, the interfacial atomic structure determines the emergent properties of the heterojunctions. However, due to the limitation of the simulation tools, we could not determine the contribution of different electron orbitals of the interfacial atoms. Hopefully we could be able to solve the problem in the future work.

Chapter 9

Summary and Future Works

In this thesis, a comprehensive study combining computational and experimental works have been conducted on the optimization of 2D MoS_2 FET. To find good Schottky/Ohmic contacts for MoS_2, metal contacts Au, Mo, W and 2D contact TiS_2 have been tested using DFT. To verify the simulated results, optimized back-to-back Au-MoS_2 Schottky contacts have been fabricated and tested. We have developed a novel I-V analysis method based on image force correction to analyze the extracted I-V characteristics of the Au-MoS_2 Schottky contacts. Applying a systematic DFT study on the MoS_2 effective mass, we have gained a better understanding of how the stacking orientation of multilayer MoS_2 thin films affects the effective mass of the channel. By performing a detailed DFT study on TMDC heterostructures, we have explored the novel emergent properties generated by forming ML TMDC heterojunctions. Our work demonstrates that the TMDC materials are able to form Type-I, Type-II and Schottky heterojuntions which are suitable for different electronic and optical applications. By optimizing and understanding the contacts and channel of 2D FETs, we step forward towards the next generation 2D electronic devices.

In chapter 4, we have investigated three different metal contacts Au, Mo and W for metal-(ML)MoS_2 Schottky contacts. Two different geometry configurations with one and two electrodes are used to extracted the Schottky barrier height of the tested contacts. We also implement a new technique using PLDOS and extracted

the lateral and vertical Schottky barrier height along with the built-in potential of the investigated contacts. It is observed that the Mo and W contacts show larger built-in potential as compared to Au. It means Mo and W contacts may show better rectification than Au contact. It is demonstrated that the Mo and W atoms form strong covalent bonding with the sulfur atoms in the ML MoS_2, which introduces large amount doping to the ML MoS_2 sheet and reduces the vertical Schottky barrier height of the Mo and W contacts. In this case the vertical Schottky barrier does not play an important role in the rectification. The PLDOS analysis of the two-electrode configurations reveals the lateral Schottky contacts of the three metals. It can be concluded that Mo and W form better Schottky contact with MoS_2 as compared to Au. Au is able to form Ohmic contact with MoS_2.

Since the metal contacts introduce strong metallization to the ML MoS_2, in chapter 5, we have explored novel Van der Waals contact material TiS_2. Our simulation demonstrates that, unlike most other contact materials, TiS_2 introduced p-type doping to the ML MoS_2. The weak Van der Waals bonding between the TiS_2 and MoS_2 preserves the intrinsic nature of ML MoS_2. The Schottky barrier of the TiS_2 contact is high for both electrons and holes in the intrinsic ML MoS_2 at the vertical interface. This barrier height can be reduced by either n-type or p-type doping of the ML MoS_2 channel. It is demonstrated that TiS_2 can form low-barrier-height contact with p-type doped ML MoS_2. The contact could be either Ohmic contact or Schottky barrier height, which depends on the p-type doping concentration of the ML MoS_2.

In chapter 6, multiple back-to-back Au-MoS_2 Schottky contacts have been fabricated and tested. The MoS_2 thickness ranges from a few monolayers to bulk. We demonstrate that the performance of the Au-MoS_2 contacts are improved dramatically after annealing process. Three models are implemented to analyze the I-V of the contacts, including TE model and SR model. It has been confirmed that the TE and SR models are not suitable to extract the Schottky barrier height of the back-to-back Schottky diodes because of the dual voltage drops. To solve this issue, we

have developed a novel mathematical model based on the image force correction. A 4-order polynomial fitting is applied and the Schottky barrier height of the contacts has been extracted. The extracted Schottky barrier height ranges from 0.134 eV to 0.272 eV.

In chapter 7, our simulation work demonstrates the geometry dependence of the electronic structure of MoS_2 films. In this work, MoS_2 films with AA, AB and hybrid stacking orientations have been investigated. Our simulation shows that as compared to AA MoS_2, AB MoS_2 shows larger bandgap energy, smoother conduction band and band degeneration, as a result of the broken symmetry. For both the AA and AB MoS_2, the electron effective mass decreases as the number of layers increasing. This trend saturates after 6 layers. The electron effective mass simulation for the MoS_2 films with mixed stacking orientations demonstrates the strong correlation between the electron effective mass and the stacking order of the MoS_2 film. It is demonstrated that, among all the cases, the AA MoS_2 shows the smallest effective mass while the AB MoS_2 possesses the largest electron effective mass. The MP and EDP simulation reveal that the interlayer Van der Waals bonding and periodicity of the intralayer lattice potential cause the effective mass difference between the MoS_2 films with different stacking orientations.

In chapter 8, we have conducted a comprehensive study of the TMDC heterojunctions consisting of ML MX_2 (M: Mo, W; X: S, Se, Te). The band alignment demonstrates that the semiconducting TMDC materials are able to form type I and type II heterojunctions which are suitable for photoluminescence and photovoltaic applications. The ML WTe_2 is able to form n-type Schottky contact with ML MoS_2 and WS_2, while forming p-type Schottky contact with ML $MoSe_2$, $MoTe_2$ and WSe_2. The ED, PDOS and PBS simulation help us understand the physics behind the emergent properties. It is demonstrated that the emergent properties correlate with the electron orbital coupling at the heterointerface. In most of the cases, a stronger coupling indicates larger band shifting of the constituent layers.

Despite the aspects discussed above for each chapter, there are still many factors that need to be taken into consideration, and there is space for the optimization of this research in the future. The contact optimization covers Au, Mo, W and TiS_2 in this work. There are still many promising candidates for the MoS_2 Schottky contacts. In the future, we would like investigate more metal and 2D semimetal contacts such as Ti and WTe_2. This would offer more choices to the design of our 2D devices. To verify the simulation results, we will further optimize our fabrication technique and fabricate top-gated Mo, W and Au Schottky contacts. If possible, we will implement asymmetric electrode design to avoid back-to-back contact structure. As for the effective mass study, we will study thicker MoS_2 samples and conduct a data mining study based on machine learning. The relaxation time simulation of the MoS_2 films is demanding. By upgrading our computational facilities we will conduct relaxation time simulation on the MoS_2 thin films with different stacking to extract the mobility variation associated with geometry modification. Heterojunctions with more complexity is also our future research goal. By modifying the junction thickness and stacking order, more emergent properties can be achieved. Our future goal is to design pure 2D FET devices with 2D hetero channels, 2D contact and 2D dielectric layer with the prediction of DFT simulation. We aim to develop a totally controllable method to fabricate the designed devices and conduct the characterization with proper technique. We hope our work could improve the performance of our 2D devices and put them in real applications.

Chapter 10

List of Acronyms

ICs Integrated Circuits ii

2D Two-Dimensional ii

TMDC Transition Metal Dichalcogenide ii

FETs Field-Effect Transistors ii

DFT Density Functional Theory ii

PLDOS Projected Local Density of States ii

ML Monolayer ii

MP Mulliken population iv

ED Electron Density iv

EDP Electrostatic Differential Potential iv

PBS Projected Bandstructure iv

ATK Atomistix ToolKit vi

MOSFETs Metal-Oxide-Semiconductor Field-Effect Transistors 1

Bibliography

[1] "Moore's law: Past, present, and future," *IEEE SPECTRUM*, 1997.

[2] T. Zanni, L. Clark, C. Gentle, S. Jones, and S. Lohokare, "Semiconductors: As the backbone of the connected world, the industry's future is bright," *KPMG Global Semiconductor Industry Outlook*, 2019.

[3] S. Sahay and M. J. Kumar, "Comprehensive analysis of gate-induced drain leakage in emerging fet architectures: Nanotube fets versus nanowire fets," *IEEE Access*, vol. 5, pp. 18 918–18 926, Sep. 2017, ISSN: 21693536. DOI: 10.1109/ACCESS.2017.2751518.

[4] N. Pandey, G. Pahwa, and Y. S. Chauhan, "Addressing source to drain tunneling in extremely scaled si-transistors using negative capacitance," *Solid-State Electronics*, vol. 186, Dec. 2021, ISSN: 00381101. DOI: 10.1016/j.sse.2021.108189.

[5] Q. Xie, J. Xu, and Y. Taur, "Review and critique of analytic models of mosfet short-channel effects in subthreshold," *IEEE Transactions on Electron Devices*, vol. 59, pp. 1569–1579, 6 2012, ISSN: 00189383. DOI: 10.1109/TED.2012.2191556.

[6] J. M. Soler, E. Artacho, J. D. Gale, A. García, J. Junquera, P. Ordejón, and D. Sánchez, "The siesta method for ab initio order-n materials simulation," *J. Phys.: Condens. Matter*, vol. 14, pp. 2745–2779, 2002.

[7] K. Boucart and A. M. Ionescu, "Length scaling of the double gate tunnel fet with a high-k gate dielectric," *Solid-State Electronics*, vol. 51, pp. 1500–1507, 11-12 Nov. 2007, ISSN: 00381101. DOI: 10.1016/j.sse.2007.09.014.

[8] B. Yu, L. Chang, S. Ahmed, H. Wang, S. Bell, C. Y. Yang, C. Tabery, C. Ho, Q. Xiang, T. J. King, J. Bokor, C. Hu, M. R. Lin, and D. Kyser, "Finfet scaling to 10 nm gate length," *Technical Digest - International Electron Devices Meeting*, pp. 251–254, 2002, ISSN: 01631918. DOI: 10.1109/IEDM.2002.1175825.

[9] A. Gnudi, S. Reggiani, E. Gnani, and G. Baccarani, "Analysis of threshold voltage variability due to random dopant fluctuations in junctionless fets," *IEEE Electron Device Letters*, vol. 33, pp. 336–338, 3 Mar. 2012, ISSN: 07413106. DOI: 10.1109/LED.2011.2181153.

[10] "Epitaxial growth of k-(al(x)ga(1-x))2o3 layers and superlattice heterostructures up to x = 0.48 on highly conductive al-doped zno thin-film templates by pulsed laser deposition," *Physica Status Solidi (B) Basic Research*, vol. 258, 2 Feb. 2021, ISSN: 15213951. DOI: 10.1002/pssb.202000359.

[11] "Dislocations, lattice slip, defects and rotated domains: The effect of a lattice misfit on supported thin-film metal oxides," *Physical Chemistry Chemical Physics*, vol. 2, pp. 5491–5499, 23 Dec. 2000, ISSN: 14639076. DOI: 10.1039/b006587k.

[12] "Large-scale production of size-controlled mos2 nanosheets by shear exfoliation," *Chemistry of Materials*, vol. 27, pp. 1129–1139, 3 Feb. 2015, ISSN: 15205002. DOI: 10.1021/cm5044864.

[13] R. Wu, Q. Tao, W. Dang, Y. Liu, B. Li, J. Li, B. Zhao, Z. Zhang, H. Ma, G. Sun, X. Duan, and X. Duan, "Van der waals epitaxial growth of atomically thin 2d metals on dangling-bond-free wse2 and ws2," *Advanced Functional Materials*, vol. 29, 12 Mar. 2019, ISSN: 16163028. DOI: 10.1002/adfm.201806611.

[14] H. W. Guo, Z. Hu, Z. B. Liu, and J. G. Tian, "Stacking of 2d materials," *Advanced Functional Materials*, vol. 31, 4 Jan. 2021, ISSN: 16163028. DOI: 10.1002/adfm.202007810.

[15] X. Du, I. Skachko, A. Barker, and E. Y. Andrei, "Approaching ballistic transport in suspended graphene," *Nature Nanotechnology*, vol. 3, pp. 491–495, 8 2008, ISSN: 17483395. DOI: 10.1038/nnano.2008.199.

[16] J. K. Ellis, M. J. Lucero, and G. E. Scuseria, "The indirect to direct band gap transition in multilayered mos2 as predicted by screened hybrid density functional theory," *Applied Physics Letters*, vol. 99, 26 Dec. 2011, ISSN: 00036951. DOI: 10.1063/1.3672219.

[17] Z. Y. Zhang, M. S. Si, Y. H. Wang, X. P. Gao, D. Sung, S. Hong, and J. He, "Indirect-direct band gap transition through electric tuning in bilayer mos2," *Journal of Chemical Physics*, vol. 140, 17 May 2014, ISSN: 00219606. DOI: 10.1063/1.4873406.

[18] J. Pu, Y. Yomogida, K. K. Liu, L. J. Li, Y. Iwasa, and T. Takenobu, "Highly flexible mos 2 thin-film transistors with ion gel dielectrics," *Nano Letters*, vol. 12, pp. 4013–4017, 8 Aug. 2012, ISSN: 15306984. DOI: 10.1021/nl301335q.

[19] B. Radisavljevic, A. Radenovic, J. Brivio, V. Giacometti, and A. Kis, "Single-layer mos2 transistors," *Nature Nanotechnology*, vol. 6, pp. 147–150, 3 2011, ISSN: 17483395. DOI: 10.1038/nnano.2010.279.

[20] Z. Wang, H. Xia, P. Wang, X. Zhou, C. Liu, Q. Zhang, F. Wang, M. Huang, S. Chen, P. Wu, Y. Chen, J. Ye, S. Huang, H. Yan, L. Gu, J. Miao, T. Li, X. Chen, W. Lu, P. Zhou, and W. Hu, "Controllable doping in 2d layered materials," *Advanced Materials*, vol. 33, 48 Dec. 2021, ISSN: 15214095. DOI: 10.1002/adma.202104942.

[21] V. P. Pham and G. Y. Yeom, "Recent advances in doping of molybdenum disulfide: Industrial applications and future prospects," *Advanced Materials*, vol. 28, pp. 9024–9059, 41 Nov. 2016, ISSN: 15214095. DOI: 10.1002/adma.201506402.

[22] H. Terrones, R. Lv, M. Terrones, and M. S. Dresselhaus, "The role of defects and doping in 2d graphene sheets and 1d nanoribbons," *Reports on Progress in Physics*, vol. 75, 6 Jun. 2012, ISSN: 00344885. DOI: 10.1088/0034-4885/75/6/062501.

[23] A. Lherbier, X. Blase, Y. M. Niquet, F. Triozon, and S. Roche, "Charge transport in chemically doped 2d graphene," *Physical Review Letters*, vol. 101, 3 Jul. 2008, ISSN: 00319007. DOI: 10.1103/PhysRevLett.101.036808.

[24] W. Cao, J. Kang, D. Sarkar, W. Liu, and K. Banerjee, "2d semiconductor fets - projections and design for sub-10 nm vlsi," *IEEE Transactions on Electron Devices*, vol. 62, pp. 3459–3469, 11 Sep. 2015, ISSN: 00189383. DOI: 10.1109/TED.2015.2443039.

[25] P. M. Das and M. Drndić, "In situ 2d mos2 field-effect transistors with an electron beam gate," *ACS Nano*, vol. 14, pp. 7389–7397, 6 Jun. 2020, ISSN: 1936086X. DOI: 10.1021/acsnano.0c02908.

[26] J. Kang, W. Liu, D. Sarkar, D. Jena, and K. Banerjee, "Computational study of metal contacts to monolayer transition-metal dichalcogenide semiconductors," *Physical Review X*, vol. 4, 3 2014, ISSN: 21603308. DOI: 10.1103/PhysRevX.4.031005.

[27] J. Kang, W. Liu, and K. Banerjee, "High-performance mos2 transistors with low-resistance molybdenum contacts," *Applied Physics Letters*, vol. 104, 9 Mar. 2014, ISSN: 00036951. DOI: 10.1063/1.4866340.

[28] N. Kaushik, A. Nipane, F. Basheer, S. Dubey, S. Grover, M. M. Deshmukh, and S. Lodha, "Schottky barrier heights for au and pd contacts to mos2," *Applied Physics Letters*, vol. 105, 11 Sep. 2014, ISSN: 00036951. DOI: 10.1063/1.4895767.

[29] H. Zhong, R. Quhe, Y. Wang, Z. Ni, M. Ye, Z. Song, Y. Pan, J. Yang, L. Yang, M. Lei, J. Shi, and J. Lu, "Interfacial properties of monolayer and bilayer mos2 contacts with metals: Beyond the energy band calculations," *Scientific Reports*, vol. 6, Mar. 2016, ISSN: 20452322. DOI: 10.1038/srep21786.

[30] J. Y. Kwak, J. Hwang, B. Calderon, H. Alsalman, N. Munoz, B. Schutter, and M. G. Spencer, "Electrical characteristics of multilayer mos2 fets with mos 2/graphene heterojunction contacts," *Nano Letters*, vol. 14, pp. 4511–4516, 8 Aug. 2014, ISSN: 15306992. DOI: 10.1021/nl5015316.

[31] K. Yang, J. R. East, and G. I. Haddad, "Numerical modeling of abrupt heterojunctions using a thermionic-field emission boundary condition," vol. 36, pp. 321–330, 3 1993.

[32] M. J. Tadjer, V. D. Wheeler, D. I. Shahin, C. R. Eddy, and F. J. Kub, "Thermionic emission analysis of tin and pt schottky contacts to beta-ga2o3," *ECS Journal of Solid State Science and Technology*, vol. 6, P165–P168, 4 2017, ISSN: 2162-8769. DOI: 10.1149/2.0291704jss.

[33] Y. J. Lin, "Origins of the temperature dependence of the series resistance, ideality factor and barrier height based on the thermionic emission model for n-type gallium nitride schottky diodes," *Thin Solid Films*, vol. 519, pp. 829–832, 2 Nov. 2010, ISSN: 00406090. DOI: 10.1016/j.tsf.2010.08.103.

[34] T. Li and G. Galli, "Electronic properties of mos2 nanoparticles," *Journal of Physical Chemistry C*, vol. 111, pp. 16 192–16 196, 44 Nov. 2007, ISSN: 19327447. DOI: 10.1021/jp075424v.

[35] C. Stern, S. Grinvald, M. Kirshner, O. Sinai, M. Oksman, H. Alon, O. E. Meiron, M. Bar-Sadan, L. Houben, and D. Naveh, "Growth mechanisms and electronic properties of vertically aligned mos2," *Scientific Reports*, vol. 8, 1 Dec. 2018, ISSN: 20452322. DOI: 10.1038/s41598-018-34222-z.

[36] N. N. Hieu, H. V. Phuc, V. V. Ilyasov, N. D. Chien, N. A. Poklonski, N. V. Hieu, and C. V. Nguyen, "First-principles study of the structural and electronic properties of graphene/mos2 interfaces," *Journal of Applied Physics*, vol. 122, 10 Sep. 2017, ISSN: 10897550. DOI: 10.1063/1.5001558.

[37] A. Mukhopadhyay, S. Kanungo, and H. Rahaman, "The effect of the stacking arrangement on the device behavior of bilayer mos2 fets," *Journal of Computational Electronics*, vol. 20, pp. 161–168, 1 Feb. 2021, ISSN: 15728137. DOI: 10.1007/s10825-020-01636-w.

[38] J. Yan, J. Xia, X. Wang, L. Liu, J. L. Kuo, B. K. Tay, S. Chen, W. Zhou, Z. Liu, and Z. X. Shen, "Stacking-dependent interlayer coupling in trilayer mos2 with broken inversion symmetry," *Nano Letters*, vol. 15, pp. 8155–8161, 12 Dec. 2015, ISSN: 15306992. DOI: 10.1021/acs.nanolett.5b03597.

[39] S. S. Lo, T. Mirkovic, C. H. Chuang, C. Burda, and G. D. Scholes, "Emergent properties resulting from type-ii band alignment in semiconductor nano heterostructures," *Advanced Materials*, vol. 23, pp. 180–197, 2 Jan. 2011, ISSN: 09359648. DOI: 10.1002/adma.201002290.

[40] J. Zhao, K. Cheng, N. Han, and J. Zhang, "Growth control, interface behavior, band alignment, and potential device applications of 2d lateral heterostructures," *Wiley Interdisciplinary Reviews: Computational Molecular Science*, vol. 8, 2 Mar. 2018, ISSN: 17590884. DOI: 10.1002/wcms.1353.

[41] C. J. Shih, Q. H. Wang, Y. Son, Z. Jin, D. Blankschtein, and M. S. Strano, "Tuning on-off current ratio and field-effect mobility in a mos2-graphene heterostructure via schottky barrier modulation," *ACS Nano*, vol. 8, pp. 5790–5798, 6 Jun. 2014, ISSN: 1936086X. DOI: 10.1021/nn500676t.

[42] Z. Li, R. Ye, R. Feng, Y. Kang, X. Zhu, J. M. Tour, and Z. Fang, "Graphene quantum dots doping of mos2 monolayers," *Advanced Materials*, vol. 27, pp. 5235–5240, 35 Sep. 2015, ISSN: 15214095. DOI: 10.1002/adma.201501888.

[43] D. Kaplan, Y. Gong, K. Mills, V. Swaminathan, P. M. Ajayan, S. Shirodkar, and E. Kaxiras, "Excitation intensity dependence of photoluminescence from monolayers of mos2 and ws2/mos2 heterostructures," *2D Materials*, vol. 3, 1 Jan. 2016, ISSN: 20531583. DOI: 10.1088/2053-1583/3/1/015005.

[44] Y. Si, H. Y. Wu, K. Yang, J. C. Lian, T. Huang, W. Q. Huang, W. Y. Hu, and G. F. Huang, "High-throughput computational design for 2d van der waals functional heterostructures: Fragility of anderson's rule and beyond," *Applied Physics Letters*, vol. 119, 4 Jul. 2021, ISSN: 00036951. DOI: 10.1063/5.0058156.

[45] K. Xu, Y. Xu, H. Zhang, B. Peng, H. Shao, G. Ni, J. Li, M. Yao, H. Lu, H. Zhu, and C. M. Soukoulis, "The role of anderson's rule in determining electronic, optical and transport properties of transition metal dichalcogenide heterostructures," *Physical Chemistry Chemical Physics*, vol. 20, pp. 30 351–30 364, 48 2018, ISSN: 14639076. DOI: 10.1039/c8cp05522j.

[46] C. H. Wann, K. Noda, T. Tanaka, M. Yoshida, and C. Hu, "A comparative study of advanced mosfet concepts," *IEEE TRANSACTIONS ON ELECTRON DEVICES*, vol. 43, 10 1996.

[47] R. K. Ratnesh, A. Goel, G. Kaushik, H. Garg, Chandan, M. Singh, and B. Prasad, "Advancement and challenges in mosfet scaling," *Materials Science in Semiconductor Processing*, vol. 134, Nov. 2021, ISSN: 13698001. DOI: 10.1016/j.mssp.2021.106002.

[48] D. J. Frank, R. H. Dennard, E. Nowak, P. M. Solomon, Y. Taur, and H. S. P. Wong, "Device scaling limits of si mosfets and their application dependencies," *Proceedings of the IEEE*, vol. 89, pp. 259–287, 3 2001, ISSN: 00189219. DOI: 10.1109/5.915374.

[49] R. Koh, "Buried layer engineering to reduce the drain-induced barrier lowering of sub-0.05 μm soi-mosfet," *Japanese Journal of Applied Physics Jpn. J. Appl. Phys*, vol. 38, pp. 2294–2299, 4B 1999.

[50] K. Takeuchi and M. Fukuma, "Effects of the velocity saturated region on mosfet characteristics," *IEEE Transactions on Electron Devices*, vol. 41, pp. 1623–1627, 9 1994, ISSN: 15579646. DOI: 10.1109/16.310116.

[51] A. Kumar, S. Bhushan, and P. K. Tiwari, "A threshold voltage model of silicon-nanotube-based ultrathin double gate-all-around (dgaa) mosfets incorporating quantum confinement effects," *IEEE Transactions on Nanotechnology*, vol. 16, pp. 868–875, 5 Sep. 2017, ISSN: 1536125X. DOI: 10.1109/TNANO.2017.2717841.

[52] A. Acovic, G. L. Rosa, and Y.-C. Sun, "A review of hot-carrier degradation mechanisms in mosfets," *Microelectronics Reliability*, vol. 36, pp. 845–869, 8 1996.

[53] K. S. Novoselov, A. K. Geim, S. V. Morozov, D Jiang, Y Zhang, S. V. Dubonos, I. V. Grigorieva, and A. A. Firsov, "Electric field effect in atomically thin carbon films," *Phys. Rev. Lett*, vol. 404, p. 3824, 2000. [Online]. Available: www.arXiv.org/quant-ph/.

[54] M. Chhowalla, H. S. Shin, G. Eda, L. J. Li, K. P. Loh, and H. Zhang, "The chemistry of two-dimensional layered transition metal dichalcogenide nanosheets," *Nature Chemistry*, vol. 5, pp. 263–275, 4 Apr. 2013, ISSN: 17554330. DOI: 10.1038/nchem.1589.

[55] Z. Q. Wang, T. Y. Lü, H. Q. Wang, Y. P. Feng, and J. C. Zheng, "Review of borophene and its potential applications," *Frontiers of Physics*, vol. 14, 3 Jun. 2019, ISSN: 20950470. DOI: 10.1007/s11467-019-0884-5.

[56] J. D. Caldwell, I. Aharonovich, G. Cassabois, J. H. Edgar, B. Gil, and D. N. Basov, "Photonics with hexagonal boron nitride," *Nature Reviews Materials*, vol. 4, pp. 552–567, 8 Aug. 2019, ISSN: 20588437. DOI: 10.1038/s41578-019-0124-1.

[57] M. Cetina, M. Jag, R. S. Lous, I. Fritsche, J. T. Walraven, R. Grimm, J. Levinsen, M. M. Parish, R. Schmidt, M. Knap, and E. Demler, "Ultrafast many-body interferometry of impurities coupled to a fermi sea," *Science*, vol. 354, pp. 96–99, 6308 Oct. 2016, ISSN: 10959203. DOI: 10.1126/science.aaf5134.

[58] A. Ramasubramaniam, D. Naveh, and E. Towe, "Tunable band gaps in bilayer transition-metal dichalcogenides," *Physical Review B - Condensed Matter and Materials Physics*, vol. 84, 20 Nov. 2011, ISSN: 10980121. DOI: 10.1103/PhysRevB.84.205325.

[59] H. J. Conley, B. Wang, J. I. Ziegler, R. F. Haglund, S. T. Pantelides, and K. I. Bolotin, "Bandgap engineering of strained monolayer and bilayer mos2," *Nano Letters*, vol. 13, pp. 3626–3630, 8 Aug. 2013, ISSN: 15306984. DOI: 10.1021/nl4014748.

[60] C. Hsu, R. Frisenda, R. Schmidt, A. Arora, S. M. de Vasconcellos, R. Bratschitsch, H. S. van der Zant, and A. Castellanos-Gomez, "Thickness-dependent refractive index of 1l, 2l, and 3l mos2, mose2, ws2, and wse2," *Advanced Optical Materials*, vol. 7, 13 Jul. 2019, ISSN: 21951071. DOI: 10.1002/adom.201900239.

[61] C. Li, X. Yan, W. Bao, S. Ding, D. W. Zhang, and P. Zhou, "Low subthreshold swing realization with contacts of graphene/h-bn/mos2 heterostructures in mos2 transistors," *Applied Physics Letters*, vol. 111, 19 Nov. 2017, ISSN: 00036951. DOI: 10.1063/1.4997226.

[62] K. Xu, Y. Zhao, Z. Lin, Y. Long, Y. Wang, M. Chan, and Y. Chai, "Doping of two-dimensional mos2 by high energy ion implantation," *Semiconductor Science and Technology*, vol. 32, 12 Oct. 2017, ISSN: 13616641. DOI: 10.1088/1361-6641/aa8ed3.

[63] J. M. Larson and J. P. Snyder, "Overview and status of metal s/d schottky-barrier mosfet technology," *IEEE Transactions on Electron Devices*, vol. 53, pp. 1048–1058, 5 May 2006, ISSN: 00189383. DOI: 10.1109/TED.2006.871842.

[64] A. Islam, J. Lee, and P. X. Feng, "All-dry transferred single- and few-layer mos2 field effect transistor with enhanced performance by thermal annealing," *Journal of Applied Physics*, vol. 123, 2 Jan. 2018, ISSN: 10897550. DOI: 10.1063/1.5008846.

[65] Y. Pan, K. Jia, K. Huang, Z. Wu, G. Bai, J. Yu, Z. Zhang, Q. Zhang, and H. Yin, "Near-ideal subthreshold swing mos2 back-gate transistors with an optimized ultrathin hfo2 dielectric layer," *Nanotechnology*, vol. 30, 9 Jan. 2019, ISSN: 13616528. DOI: 10.1088/1361-6528/aaf956.

[66] W. Bao, X. Cai, D. Kim, K. Sridhara, and M. S. Fuhrer, "High mobility ambipolar mos2 field-effect transistors: Substrate and dielectric effects," *Applied Physics Letters*, vol. 102, 4 Jan. 2013, ISSN: 00036951. DOI: 10.1063/1.4789365.

[67] M. W. Lin, L. Liu, Q. Lan, X. Tan, K. S. Dhindsa, P. Zeng, V. M. Naik, M. M. C. Cheng, and Z. Zhou, "Mobility enhancement and highly efficient gating of monolayer mos2 transistors with polymer electrolyte," *Journal of Physics D: Applied Physics*, vol. 45, 34 Aug. 2012, ISSN: 00223727. DOI: 10.1088/0022-3727/45/34/345102.

[68] D. Wu, Z. Zhang, D. Lv, G. Yin, Z. Peng, and C. Jin, "High mobility top gated field-effect transistors and integrated circuits based on chemical vapor deposition-derived monolayer mos2," *Materials Express*, vol. 6, pp. 198–204, 2 Apr. 2016, ISSN: 21585857. DOI: 10.1166/mex.2016.1289.

[69] X. X. Li, X. Y. Chen, J. X. Chen, G. Zeng, Y. C. Li, W. Huang, Z. G. Ji, D. W. Zhang, and H. L. Lu, "Dual-gate mos2 phototransistor with atomic-layer-deposited hfo2 as top-gate dielectric for ultrahigh photoresponsivity," *Nanotechnology*, vol. 32, 21 May 2021, ISSN: 13616528. DOI: 10.1088/1361-6528/abe2cc.

[70] Q. A. Vu, S. Fan, S. H. Lee, M. K. Joo, W. J. Yu, and Y. H. Lee, "Near-zero hysteresis and near-ideal subthreshold swing in h-bn encapsulated single-layer mos2 field-effect transistors," *2D Materials*, vol. 5, 3 Mar. 2018, ISSN: 20531583. DOI: 10.1088/2053-1583/aab672.

[71] O. Breitenstein and S. Rißland, "A two-diode model regarding the distributed series resistance," *Solar Energy Materials and Solar Cells*, vol. 110, pp. 77–86, 2013, ISSN: 09270248. DOI: 10.1016/j.solmat.2012.11.021.

[72] I. Meric, M. Y. Han, A. F. Young, B. Ozyilmaz, P. Kim, and K. L. Shepard, "Current saturation in zero-bandgap, top-gated graphene field-effect transistors," *Nature Nanotechnology*, vol. 3, pp. 654–659, 11 2008, ISSN: 17483395. DOI: 10.1038/nnano.2008.268.

[73] R. F. Frindt, "Single crystals of mos2 several molecular layers thick," *Journal of Applied Physics*, vol. 37, pp. 1928–1929, 4 1966, ISSN: 00218979. DOI: 10.1063/1.1708627.

[74] S. M. Shinde, K. P. Dhakal, X. Chen, W. S. Yun, J. Lee, H. Kim, and J. H. Ahn, "Stacking-controllable interlayer coupling and symmetric configuration of multilayered mos2," *NPG Asia Materials*, vol. 10, pp. 1–13, 2 2018, ISSN: 18844057. DOI: 10.1038/am.2017.226.

[75] Y. Yu, G. H. Nam, Q. He, X. J. Wu, K. Zhang, Z. Yang, J. Chen, Q. Ma, M. Zhao, Z. Liu, F. R. Ran, X. Wang, H. Li, X. Huang, B. Li, Q. Xiong, Q. Zhang, Z. Liu, L. Gu, Y. Du, W. Huang, and H. Zhang, "High phase-purity 1t'-mos2- and 1t'-mose2-layered crystals," *Nature Chemistry*, vol. 10, pp. 638–643, 6 Jun. 2018, ISSN: 17554349. DOI: 10.1038/s41557-018-0035-6.

[76] S. H. Mir, V. K. Yadav, J. K. Singh, and J. K. Singh, "Recent advances in the carrier mobility of two-dimensional materials: A theoretical perspective," *ACS Omega*, vol. 5, pp. 14 203–14 211, 24 Jun. 2020, ISSN: 24701343. DOI: 10.1021/acsomega.0c01676.

[77] T. T. T. Can, H. L. Ko, and W. S. Choi, "Ehd-jet patterned mos2 on a high-k dielectric for high mobility in thin film transistor applications," *Nanotechnology*, vol. 32, 24 Jun. 2021, ISSN: 13616528. DOI: 10.1088/1361-6528/abed05.

[78] K. Liu, X. Chen, P. Gong, R. Yu, J. Wu, L. Li, W. Han, S. Yang, C. Zhang, J. Deng, A. Li, Q. Zhang, F. Zhuge, and T. Zhai, "Approaching strain limit of two-dimensional mos2 via chalcogenide substitution," *Science Bulletin*, vol. 67, pp. 45–53, 1 Jan. 2022, ISSN: 20959281. DOI: 10.1016/j.scib.2021.07.010.

[79] A. Castellanos-Gomez, M. Poot, G. A. Steele, H. S. V. D. Zant, N. Agraït, and G. Rubio-Bollinger, "Elastic properties of freely suspended mos2 nanosheets," *Advanced Materials*, vol. 24, pp. 772–775, 6 Feb. 2012, ISSN: 15214095. DOI: 10.1002/adma.201103965.

[80] Y. S. Lin, R. Puthenkovilakam, and J. P. Chang, "Dielectric property and thermal stability of hfo2 on silicon," *Applied Physics Letters*, vol. 81, pp. 2041–2043, 11 Sep. 2002, ISSN: 00036951. DOI: 10.1063/1.1506207.

[81] W. Bao, X. Cai, D. Kim, K. Sridhara, and M. S. Fuhrer, "High mobility ambipolar mos2 field-effect transistors: Substrate and dielectric effects," *Applied Physics Letters*, vol. 102, 4 Jan. 2013, ISSN: 00036951. DOI: 10.1063/1.4789365.

[82] S. Kim, A. Konar, W. S. Hwang, J. H. Lee, J. Lee, J. Yang, C. Jung, H. Kim, J. B. Yoo, J. Y. Choi, Y. W. Jin, S. Y. Lee, D. Jena, W. Choi, and K. Kim, "High-mobility and low-power thin-film transistors based on multilayer mos2 crystals," *Nature Communications*, vol. 3, 2012, ISSN: 20411723. DOI: 10.1038/ncomms2018.

[83] S. Kim, A. Konar, W. S. Hwang, J. H. Lee, J. Lee, J. Yang, C. Jung, H. Kim, J. B. Yoo, J. Y. Choi, Y. W. Jin, S. Y. Lee, D. Jena, W. Choi, and K. Kim, "High-mobility and low-power thin-film transistors based on multilayer mos2 crystals," *Nature Communications*, vol. 3, 2012, ISSN: 20411723. DOI: 10.1038/ncomms2018.

[84] M. Amani, M. L. Chin, A. G. Birdwell, T. P. O'Regan, S. Najmaei, Z. Liu, P. M. Ajayan, J. Lou, and M. Dubey, "Electrical performance of monolayer mos2 field-effect transistors prepared by chemical vapor deposition," *Applied Physics Letters*, vol. 102, 19 May 2013, ISSN: 00036951. DOI: 10.1063/1.4804546.

[85] B. Radisavljevic and A. Kis, "Mobility engineering and a metal-insulator transition in monolayer mos2," *Nature Materials*, vol. 12, pp. 815–820, 9 2013, ISSN: 14764660. DOI: 10.1038/nmat3687.

[86] W. Liu, D. Sarkar, J. Kang, W. Cao, and K. Banerjee, "Impact of contact on the operation and performance of back-gated monolayer mos2 field-effect-transistors," *ACS Nano*, vol. 9, pp. 7904–7912, 8 Aug. 2015, ISSN: 1936086X. DOI: 10.1021/nn506512j.

[87] J. Jiang, Y. Zhang, A. Wang, J. Duan, H. Ji, J. Pang, Y. Sang, X. Feng, H. Liu, and L. Han, "Construction of high field-effect mobility multilayer mos2field-effect transistors with excellent stability through interface engineering," *ACS Applied Electronic Materials*, vol. 2, pp. 2132–2140, 7 Jul. 2020, ISSN: 26376113. DOI: 10.1021/acsaelm.0c00347.

[88] Y. Y. Illarionov, K. K. Smithe, M. Waltl, R. W. Grady, S. Deshmukh, E. Pop, and T. Grasser, "Annealing and encapsulation of cvd-mos2 fets with 1010on/off current ratio," *Device Research Conference - Conference Digest, DRC*, vol. 2018-June, Aug. 2018, ISSN: 15483770. DOI: 10.1109/DRC.2018.8442242.

[89] S. Deng, E. Gao, Z. Xu, and V. Berry, "Adhesion energy of mos2 thin films on silicon-based substrates determined via the attributes of a single mos2 wrinkle," *ACS Applied Materials and Interfaces*, vol. 9, pp. 7812–7818, 8 Mar. 2017, ISSN: 19448252. DOI: 10.1021/acsami.6b16175.

[90] J. Robertson, "High dielectric constant oxides," *EPJ Applied Physics*, vol. 28, pp. 265–291, 3 Dec. 2004, ISSN: 12860042. DOI: 10.1051/epjap:2004206.

[91] X. Li, X. Yin, L. Zhang, L. Cheng, and Y. Qi, "Mechanical and dielectric properties of porous si3n4-sio2 composite ceramics," *Materials Science and Engineering A*, vol. 500, pp. 63–69, 1-2 Jan. 2009, ISSN: 09215093. DOI: 10.1016/j.msea.2008.09.066.

[92] J. Xu, M. Wen, X. Zhao, L. Liu, X. Song, P. T. Lai, and W. M. Tang, "Effects of hfo2 encapsulation on electrical performances of few-layered mos2 transistor with ald hfo2 as back-gate dielectric," *Nanotechnology*, vol. 29, 34 Jun. 2018, ISSN: 13616528. DOI: 10.1088/1361-6528/aac853.

[93] A. A. Volinsky, N. R. Moody, and W. W. Gerberich, "Interfacial toughness measurements for thin films on substrates," *Acta Materialia*, vol. 50, pp. 441–466, 2002. [Online]. Available: www.elsevier.com/locate/actamat.

[94] Y. Pan, K. Jia, K. Huang, Z. Wu, G. Bai, J. Yu, Z. Zhang, Q. Zhang, and H. Yin, "Near-ideal subthreshold swing mos2 back-gate transistors with an optimized ultrathin hfo2 dielectric layer," *Nanotechnology*, vol. 30, 9 Jan. 2019, ISSN: 13616528. DOI: 10.1088/1361-6528/aaf956.

[95] Y. Guo, X. Wei, J. Shu, B. Liu, J. Yin, C. Guan, Y. Han, S. Gao, and Q. Chen, "Charge trapping at the mos2-sio2 interface and its effects on the characteristics of mos2 metal-oxide-semiconductor field effect transistors," *Applied Physics Letters*, vol. 106, 10 Mar. 2015, ISSN: 00036951. DOI: 10.1063/1.4914968.

[96] Y. Guo, X. Wei, J. Shu, B. Liu, J. Yin, C. Guan, Y. Han, S. Gao, and Q. Chen, "Charge trapping at the mos2-sio2 interface and its effects on the characteristics of mos2 metal-oxide-semiconductor field effect transistors," *Applied Physics Letters*, vol. 106, 10 Mar. 2015, ISSN: 00036951. DOI: 10.1063/1.4914968.

[97] Y. Y. Illarionov, G. Rzepa, M. Waltl, T. Knobloch, A. Grill, M. M. Furchi, T. Mueller, and T. Grasser, "The role of charge trapping in mos2/sio2 and mos2/hbn field-effect transistors," *2D Materials*, vol. 3, 3 Jul. 2016, ISSN: 20531583. DOI: 10.1088/2053-1583/3/3/035004.

[98] S. Ghatak, A. N. Pal, and A. Ghosh, "Nature of electronic states in atomically thin mos2 field-effect transistors," *ACS Nano*, vol. 5, pp. 7707–7712, 10 Oct. 2011, ISSN: 19360851. DOI: 10.1021/nn202852j.

[99] A. Sanne, R. Ghosh, A. Rai, H. C. Movva, A. Sharma, R. Rao, L. Mathew, and S. K. Banerjee, "Top-gated chemical vapor deposited mos2 field-effect transistors on si3n4 substrates," *Applied Physics Letters*, vol. 106, 6 Feb. 2015, ISSN: 00036951. DOI: 10.1063/1.4907885.

[100] D. J. Late, B. Liu, H. S. Matte, V. P. Dravid, and C. N. Rao, "Hysteresis in single-layer mos2 field effect transistors," *ACS Nano*, vol. 6, pp. 5635–5641, 6 Jun. 2012, ISSN: 19360851. DOI: 10.1021/nn301572c.

[101] A. K. Singh, R. G. Hennig, A. V. Davydov, and F. Tavazza, "Al2o3 as a suitable substrate and a dielectric layer for n-layer mos2," *Applied Physics Letters*, vol. 107, 5 Aug. 2015, ISSN: 00036951. DOI: 10.1063/1.4928179.

[102] T. Li, B. Wan, G. Du, B. Zhang, and Z. Zeng, "Electrical performance of multilayer mos2 transistors on high-k al2o3 coated si substrates," *AIP Advances*, vol. 5, 5 May 2015, ISSN: 21583226. DOI: 10.1063/1.4919800.

[103] H. Birey, "Thickness dependence of the dielectric constant and resistance of al2o3 films," *Journal of Applied Physics*, vol. 48, pp. 5209–5212, 12 1977, ISSN: 00218979. DOI: 10.1063/1.323603.

[104] C. D. Young, P. Zhao, P. Bolshakov-Barrett, A. Azcatl, P. K. Hurley, Y. Y. Gomeniuk, M. Schmidt, C. L. Hinkle, and R. M. Wallace, "(invited) evaluation of few-layer mos2 transistors with a top gate and hfo2 dielectric," *ECS Transactions*, vol. 75, pp. 153–162, 5 Aug. 2016, ISSN: 1938-5862. DOI: 10.1149/07505.0153ecst.

[105] J. Xu, M. Wen, X. Zhao, L. Liu, X. Song, P. T. Lai, and W. M. Tang, "Effects of hfo2 encapsulation on electrical performances of few-layered mos2 transistor with ald hfo2 as back-gate dielectric," *Nanotechnology*, vol. 29, 34 Jun. 2018, ISSN: 13616528. DOI: 10.1088/1361-6528/aac853.

[106] C. M. Smyth, R. Addou, S. McDonnell, C. L. Hinkle, and R. M. Wallace, "Contact metal-mos2 interfacial reactions and potential implications on mos2-based device performance," *Journal of Physical Chemistry C*, vol. 120, pp. 14 719–14 729, 27 Jul. 2016, ISSN: 19327455. DOI: 10.1021/acs.jpcc.6b04473.

[107] H. Yuan, G. Cheng, L. You, H. Li, H. Zhu, W. Li, J. J. Kopanski, Y. S. Obeng, A. R. H. Walker, D. J. Gundlach, C. A. Richter, D. E. Ioannou, and Q. Li, "Influence of metal-mos2 interface on mos2 transistor performance: Comparison of ag and ti contacts," *ACS Applied Materials and Interfaces*, vol. 7, pp. 1180–1187, 2 Jan. 2015, ISSN: 19448252. DOI: 10.1021/am506921y.

[108] Z. Li, X. Li, and J. Yang, "Comparative study on electronic structures of sc and ti contacts with monolayer and multilayer mos2," *ACS Applied Materials and Interfaces*, vol. 7, pp. 12 981–12 987, 23 Jun. 2015, ISSN: 19448252. DOI: 10.1021/acsami.5b02782.

[109] P. Chen, J. Xiang, H. Yu, J. Zhang, G. Xie, S. Wu, X. Lu, G. Wang, J. Zhao, F. Wen, Z. Liu, R. Yang, D. Shi, and G. Zhang, "Gate tunable mos2-black phosphorus heterojunction devices," *2D Materials*, vol. 2, 3 Jul. 2015, ISSN: 20531583. DOI: 10.1088/2053-1583/2/3/034009.

[110] Y. Deng, Z. Luo, N. J. Conrad, H. Liu, Y. Gong, S. Najmaei, P. M. Ajayan, J. Lou, X. Xu, and P. D. Ye, "Black phosphorus-monolayer mos2 van der waals heterojunction p-n diode," *ACS Nano*, vol. 8, pp. 8292–8299, 8 Aug. 2014, ISSN: 1936086X. DOI: 10.1021/nn5027388.

[111] K. Zhang, Y. Feng, F. Wang, Z. Yang, and J. Wang, "Two dimensional hexagonal boron nitride (2d-hbn): Synthesis, properties and applications," *Journal of Materials Chemistry C*, vol. 5, pp. 11 992–12 022, 46 2017, ISSN: 20507526. DOI: 10.1039/c7tc04300g.

[112] A. Laturia, M. L. V. de Put, and W. G. Vandenberghe, "Dielectric properties of hexagonal boron nitride and transition metal dichalcogenides: From monolayer to bulk," *npj 2D Materials and Applications*, vol. 2, 1 Dec. 2018, ISSN: 23977132. DOI: 10.1038/s41699-018-0050-x.

[113] G. H. Lee, Y. J. Yu, X. Cui, N. Petrone, C. H. Lee, M. S. Choi, D. Y. Lee, C. Lee, W. J. Yoo, K. Watanabe, T. Taniguchi, C. Nuckolls, P. Kim, and J. Hone, "Flexible and transparent mos2 field-effect transistors on hexagonal boron nitride-graphene heterostructures," *ACS Nano*, vol. 7, pp. 7931–7936, 9 Sep. 2013, ISSN: 19360851. DOI: 10.1021/nn402954e.

[114] Y. H. Lee, X. Q. Zhang, W. Zhang, M. T. Chang, C. T. Lin, K. D. Chang, Y. C. Yu, J. T. W. Wang, C. S. Chang, L. J. Li, and T. W. Lin, "Synthesis of large-area mos2 atomic layers with chemical vapor deposition," *Advanced Materials*, vol. 24, pp. 2320–2325, 17 May 2012, ISSN: 09359648. DOI: 10.1002/adma.201104798.

[115] D. Fu, X. Zhao, Y. Y. Zhang, L. Li, H. Xu, A. R. Jang, S. I. Yoon, P. Song, S. M. Poh, T. Ren, Z. Ding, W. Fu, T. J. Shin, H. S. Shin, S. T. Pantelides, W. Zhou, and K. P. Loh, "Molecular beam epitaxy of highly crystalline monolayer molybdenum disulfide on hexagonal boron nitride," *Journal of the American Chemical Society*, vol. 139, pp. 9392–9400, 27 Jul. 2017, ISSN: 15205126. DOI: 10.1021/jacs.7b05131.

[116] M. I. Serna, S. H. Yoo, S. Moreno, Y. Xi, J. P. Oviedo, H. Choi, H. N. Alshareef, M. J. Kim, M. Minary-Jolandan, and M. A. Quevedo-Lopez, "Large-area deposition of mos2 by pulsed laser deposition with in situ thickness control," *ACS Nano*, vol. 10, pp. 6054–6061, 6 Jun. 2016, ISSN: 1936086X. DOI: 10.1021/acsnano.6b01636.

[117] H. Samassekou, A. Alkabsh, M. Wasala, M. Eaton, and A. Walber, "Corrigendum: Viable route towards large-area 2d mos2 using magnetron sputtering," *2D Materials*, vol. 4, 3 Sep. 2017, ISSN: 20531583. DOI: 10.1088/2053-1583/aa78ac.

[118] Y. Shi, W. Zhou, A. Y. Lu, W. Fang, Y. H. Lee, A. L. Hsu, S. M. Kim, K. K. Kim, H. Y. Yang, L. J. Li, J. C. Idrobo, and J. Kong, "Van der waals epitaxy of mos2 layers using graphene as growth templates," *Nano Letters*, vol. 12, pp. 2784–2791, 6 Jun. 2012, ISSN: 15306984. DOI: 10.1021/nl204562j.

[119] L. Fei, S. Lei, W. B. Zhang, W. Lu, Z. Lin, C. H. Lam, Y. Chai, and Y. Wang, "Direct tem observations of growth mechanisms of two-dimensional mos2 flakes," *Nature Communications*, vol. 7, Jul. 2016, ISSN: 20411723. DOI: 10.1038/ncomms12206.

[120] Y. Hu, X. Zeng, T. Ren, S. Wu, W. Wang, Y. Zeng, G. Zhou, Z. Guo, W. Jin, S. Wang, Y. Xiao, and J. Lu, "Preparation of controllable-thickness 1t@2h-mos2 thin films by pulsed laser-induced synthesis and the selective separation of the 1t phase," *Journal of Materials Chemistry C*, vol. 6, pp. 11 651–11 658, 43 2018, ISSN: 20507526. DOI: 10.1039/c8tc03815e.

[121] J. H. Ahn, W. M. Parkin, C. H. Naylor, A. T. Johnson, and M. Drndić, "Ambient effects on electrical characteristics of cvd-grown monolayer mos2 field-effect transistors," *Scientific Reports*, vol. 7, 1 Dec. 2017, ISSN: 20452322. DOI: 10.1038/s41598-017-04350-z.

[122] H. F. Liu, S. L. Wong, and D. Z. Chi, "Cvd growth of mos2-based two-dimensional materials," *Chemical Vapor Deposition*, vol. 21, pp. 241–259, 10-12 Dec. 2015, ISSN: 15213862. DOI: 10.1002/cvde.201500060.

[123] M. Demirtaş, C. Odacı, Y. Shehu, N. K. Perkgöz, and F. Ay, "Layer and size distribution control of cvd-grown 2d mos2 using ald-deposited moo3 structures as the precursor," *Materials Science in Semiconductor Processing*, vol. 108, Mar. 2020, ISSN: 13698001. DOI: 10.1016/j.mssp.2019.104880.

[124] L. Tao, K. Chen, Z. Chen, W. Chen, X. Gui, H. Chen, X. Li, and J. B. Xu, "Centimeter-scale cvd growth of highly crystalline single-layer mos2 film with spatial homogeneity and the visualization of grain boundaries," *ACS Applied Materials and Interfaces*, vol. 9, pp. 12 073–12 081, 13 Apr. 2017, ISSN: 19448252. DOI: 10.1021/acsami.7b00420.

[125] L. H. Isherwood, G. Athwal, B. F. Spencer, C. Casiraghi, and A. Baidak, "Gamma radiation-induced oxidation, doping, and etching of two-dimensional mos2 crystals," *Journal of Physical Chemistry C*, vol. 125, pp. 4211–4222, 7 Feb. 2021, ISSN: 19327455. DOI: 10.1021/acs.jpcc.0c10095.

[126] M. H. Jeon, C. Ahn, H. U. Kim, K. N. Kim, T. Z. Lin, H. Qin, Y. Kim, S. Lee, T. Kim, and G. Y. Yeom, "Controlled mos2 layer etching using cf4 plasma," *Nanotechnology*, vol. 26, 35 Sep. 2015, ISSN: 13616528. DOI: 10.1088/0957-4484/26/35/355706.

[127] S. Xiao, P. Xiao, X. Zhang, D. Yan, X. Gu, F. Qin, Z. Ni, Z. J. Han, and K. K. Ostrikov, "Atomic-layer soft plasma etching of mos2," *Scientific Reports*, vol. 6, Jan. 2016, ISSN: 20452322. DOI: 10.1038/srep19945.

[128] T. N. Walter, N. Oliver, and S. E. Mohney, "Electron beam evaporated au islands as a nanoscale etch mask on few-layer mos2 and fabrication of top-edge hybrid contacts for field-effect transistors," *Nanotechnology*, vol. 32, 2 Jan. 2021, ISSN: 13616528. DOI: 10.1088/1361-6528/abbb4a.

[129] C. Lu and S. N. Mohammad, "Validity/invalidity of schottky-mott rules for schottky contacts to iii-v nitride semiconductor heterostructures," *Applied Physics Letters*, vol. 89, 16 2006, ISSN: 00036951. DOI: 10.1063/1.2358956.

[130] S. McDonnell, R. Addou, C. Buie, R. M. Wallace, and C. L. Hinkle, "Defect-dominated doping and contact resistance in mos2," *ACS Nano*, vol. 8, pp. 2880–2888, 3 Mar. 2014, ISSN: 1936086X. DOI: 10.1021/nn500044q.

[131] W. H. Chae, J. D. Cain, E. D. Hanson, A. A. Murthy, and V. P. Dravid, "Substrate-induced strain and charge doping in cvd-grown monolayer mos2," *Applied Physics Letters*, vol. 111, 14 Oct. 2017, ISSN: 00036951. DOI: 10.1063/1.4998284.

[132] A. K. Rajagopal and J Callaway, "Inhomogeneous electron gas," *PHYSICAL REVIEW B*, vol. 7, pp. 1912–1919, 5 1973.

[133] G Seifert, D Porezag, and T. H. Frauenheim, "Calculations of molecules, clusters, and solids with a simplified lcao-dft-lda scheme," *International Journal of Quantum Chemistry*, vol. 58, pp. 185–192, 1996.

[134] J. P. Perdew, K. Burke, and M. Ernzerhof, "Generalized gradient approximation made simple," *Physical Review Letters*, vol. 77, 18 1996.

[135] A. Janotti and C. G. V. D. Walle, "Native point defects in zinc oxide," *Physical Review B - Condensed Matter and Materials Physics*, vol. 76, 16 Oct. 2007, ISSN: 10980121. DOI: 10.1103/PhysRevB.76.165202.

[136] J. P. Perdew, W. Yang, K. Burke, Z. Yang, E. K. Gross, M. Scheffler, G. E. Scuseria, T. M. Henderson, I. Y. Zhang, A. Ruzsinszky, H. Peng, J. Sun, E. Trushin, and A. Görling, "Understanding band gaps of solids in generalized kohn-sham theory," *Proceedings of the National Academy of Sciences of the United States of America*, vol. 114, pp. 2801–2806, 11 Mar. 2017, ISSN: 10916490. DOI: 10.1073/pnas.1621352114.

[137] J. P. Perdew, S. Kurth, A. Zupan, and P. Blaha, "Accurate density functional with correct formal properties: A step beyond the generalized gradient approximation," *PHYSICAL REVIEW B*, vol. 82, 12 1999.

[138] R. Neumann, R. h. Nobes, and N. C. Handy, "Exchange functionals and potentials," *Molecular Physics*, vol. 87, pp. 1–36, 1 1996, ISSN: 13623028. DOI: 10.1080/00268979600100011.

[139] F. Tran, J. Doumont, P. Blaha, M. A. Marques, S. Botti, and A. P. Bartók, "On the calculation of the bandgap of periodic solids with mgga functionals using the total energy," *Journal of Chemical Physics*, vol. 151, 16 Oct. 2019, ISSN: 00219606. DOI: 10.1063/1.5126393.

[140] N Troullier and J. L. Martins, "Efficient pseudopotentials for plane-wave calculations. ii. operators for fast iterative diagonalization," *PHYSICAL REVIEW B*, vol. 43, 11 1991.

[141] S Goedecker, M Teter, and J Hutter, "Separable dual-space gaussian pseudopotentials," *PHYSICAL REVIEW B*, vol. 54, 3 1996.

[142] G. Prandini, A. Marrazzo, I. E. Castelli, N. Mounet, and N. Marzari, "Precision and efficiency in solid-state pseudopotential calculations," *npj Computational Materials*, vol. 4, 1 Dec. 2018, ISSN: 20573960. DOI: 10.1038/s41524-018-0127-2.

[143] K. F. Garrity, J. W. Bennett, K. M. Rabe, and D. Vanderbilt, "Pseudopotentials for high-throughput dft calculations," *Computational Materials Science*, vol. 81, pp. 446–452, 2014, ISSN: 09270256. DOI: 10.1016/j.commatsci.2013.08.053.

[144] C. N. R. Rao, S. Natarajan, A. Choudhury, S Neeraj, and A. A. Ayi, "Aufbau principle of complex open-framework structures of metal phosphates with different dimensionalities," 2001. DOI: 10.1021/ar000135. [Online]. Available: https://pubs.acs.org/sharingguidelines.

[145] R. A. Evarestov and V. P. Smirnov, "Modification of the monkhorst-pack special points meshes in the brillouin zone for density functional theory and hartree-fock calculations," *Physical Review B - Condensed Matter and Materials Physics*, vol. 70, pp. 1–4, 23 2004, ISSN: 1550235X. DOI: 10.1103/PhysRevB.70.233101.

[146] H. Li, Q. Zhang, C. C. R. Yap, B. K. Tay, T. H. T. Edwin, A. Olivier, and D. Baillargeat, "From bulk to monolayer mos2: Evolution of raman scattering," *Advanced Functional Materials*, vol. 22, pp. 1385–1390, 7 Apr. 2012, ISSN: 1616301X. DOI: 10.1002/adfm.201102111.

[147] K. S. Novoselov, A. Mishchenko, A. Carvalho, and A. H. C. Neto, "2d materials and van der waals heterostructures," *Science*, vol. 353, 6298 Jul. 2016, ISSN: 10959203. DOI: 10.1126/science.aac9439.

[148] V. Singh, D. Joung, L. Zhai, S. Das, S. I. Khondaker, and S. Seal, "Graphene based materials: Past, present and future," *Progress in Materials Science*, vol. 56, pp. 1178–1271, 8 Oct. 2011, ISSN: 00796425. DOI: 10.1016/j.pmatsci.2011.03.003.

[149] Y. Zhang, T. T. Tang, C. Girit, Z. Hao, M. C. Martin, A. Zettl, M. F. Crommie, Y. R. Shen, and F. Wang, "Direct observation of a widely tunable bandgap in bilayer graphene," *Nature*, vol. 459, pp. 820–823, 7248 Jun. 2009, ISSN: 00280836. DOI: 10.1038/nature08105.

[150] K. He, C. Poole, K. F. Mak, and J. Shan, "Experimental demonstration of continuous electronic structure tuning via strain in atomically thin mos2," *Nano Letters*, vol. 13, pp. 2931–2936, 6 Jun. 2013, ISSN: 15306984. DOI: 10.1021/nl4013166.

[151] S. Mouri, Y. Miyauchi, and K. Matsuda, "Tunable photoluminescence of monolayer mos2 via chemical doping," *Nano Letters*, vol. 13, pp. 5944–5948, 12 Dec. 2013, ISSN: 15306984. DOI: 10.1021/nl403036h.

[152] Y. Ma, Y. Dai, M. Guo, C. Niu, Y. Zhu, and B. Huang, "Evidence of the existence of magnetism in pristine vx2 monolayers (x = s, se) and their strain-induced tunable magnetic properties," *ACS Nano*, vol. 6, pp. 1695–1701, 2 Feb. 2012, ISSN: 19360851. DOI: 10.1021/nn204667z.

[153] M. Buscema, M. Barkelid, V. Zwiller, H. S. V. D. Zant, G. A. Steele, and A. Castellanos-Gomez, "Large and tunable photothermoelectric effect in single-layer mos2," *Nano Letters*, vol. 13, pp. 358–363, 2 Feb. 2013, ISSN: 15306984. DOI: 10.1021/nl303321g.

[154] K. K. Kam and B. A. Parkinson, "Detailed photocurrent spectroscopy of the semiconducting group vi transition metal dichalcogenides," *J. Phys. Chem*, vol. 86, p. 463, 1982. [Online]. Available: https://pubs.acs.org/sharingguidelines.

[155] K. F. Mak, C. Lee, J. Hone, J. Shan, and T. F. Heinz, "Atomically thin mos2: A new direct-gap semiconductor," *Physical Review Letters*, vol. 105, 13 Sep. 2010, ISSN: 00319007. DOI: 10.1103/PhysRevLett.105.136805.

[156] M Pepper, "Metal-semiconductor contacts," *Physics in Technology*, 1974.

[157] H. Yuan, G. Cheng, L. You, H. Li, H. Zhu, W. Li, J. J. Kopanski, Y. S. Obeng, A. R. H. Walker, D. J. Gundlach, C. A. Richter, D. E. Ioannou, and Q. Li, "Influence of metal-mos2 interface on mos2 transistor performance: Comparison of ag and ti contacts," *ACS Applied Materials and Interfaces*, vol. 7, pp. 1180–1187, 2 Jan. 2015, ISSN: 19448252. DOI: 10.1021/am506921y.

[158] S. McDonnell, R. Addou, C. Buie, R. M. Wallace, and C. L. Hinkle, "Defect-dominated doping and contact resistance in mos2," *ACS Nano*, vol. 8, pp. 2880–2888, 3 Mar. 2014, ISSN: 1936086X. DOI: 10.1021/nn500044q.

[159] C. Gong, L. Colombo, R. M. Wallace, and K. Cho, "The unusual mechanism of partial fermi level pinning at metal-mos2 interfaces," *Nano Letters*, vol. 14, pp. 1714–1720, 4 Apr. 2014, ISSN: 15306992. DOI: 10.1021/nl403465v.

[160] Y. L. Huang, Y. Chen, W. Zhang, S. Y. Quek, C. H. Chen, L. J. Li, W. T. Hsu, W. H. Chang, Y. J. Zheng, W. Chen, and A. T. Wee, "Bandgap tunability at single-layer molybdenum disulphide grain boundaries," *Nature Communications*, vol. 6, Feb. 2015, ISSN: 20411723. DOI: 10.1038/ncomms7298.

[161] H. J. Conley, B. Wang, J. I. Ziegler, R. F. Haglund, S. T. Pantelides, and K. I. Bolotin, "Bandgap engineering of strained monolayer and bilayer mos2," *Nano Letters*, vol. 13, pp. 3626–3630, 8 Aug. 2013, ISSN: 15306984. DOI: 10.1021/nl4014748.

[162] S. Grimme, J. Antony, S. Ehrlich, and H. Krieg, "A consistent and accurate ab initio parametrization of density functional dispersion correction (dft-d) for the 94 elements h-pu," *Journal of Chemical Physics*, vol. 132, 15 Apr. 2010, ISSN: 00219606. DOI: 10.1063/1.3382344.

[163] W. R. Wadt and P. J. Hay, "Ab initio effective core potentials for molecular calculations. potentials for main group elements na to bi," *The Journal of Chemical Physics*, vol. 82, pp. 284–298, 1 1985, ISSN: 00219606. DOI: 10.1063/1.448800.

[164] X. Hai, J. Tahir-Kheli, and W. A. Goddard, "Accurate band gaps for semiconductors from density functional theory," *Journal of Physical Chemistry Letters*, vol. 2, pp. 212–217, 3 Feb. 2011, ISSN: 19487185. DOI: 10.1021/jz101565j.

[165] J. M. Crowley, J. Tahir-Kheli, and W. A. Goddard, "Resolution of the band gap prediction problem for materials design," *Journal of Physical Chemistry Letters*, vol. 7, pp. 1198–1203, 7 Apr. 2016, ISSN: 19487185. DOI: 10.1021/acs.jpclett.5b02870.

[166] M. D. Segall, R. Shah, C. J. Pickard, and M. C. Payne, "Population analysis of plane-wave electronic structure calculations of bulk materials," *PHYSICAL REVIEW B*, vol. 54, 23 1996.

[167] M. D. Segall, C. J. Pickard, R. Shah, and M. C. Payne, "Population analysis in plane wave electronic structure calculations," *Molecular Physics*, vol. 89, pp. 571–577, 2 Oct. 1996, ISSN: 13623028. DOI: 10.1080/002689796173912.

[168] H. Schmidt, S. Wang, L. Chu, M. Toh, R. Kumar, W. Zhao, A. H. C. Neto, J. Martin, S. Adam, B. Özyilmaz, and G. Eda, "Transport properties of monolayer mos2 grown by chemical vapor deposition," *Nano Letters*, vol. 14, pp. 1909–1913, 4 Apr. 2014, ISSN: 15306992. DOI: 10.1021/nl4046922.

[169] L. J. Sham, M Schluter, B. I. Aboratories, M. Hill, and N. Jersey, "Physical review letters density-functional theory of the energy gay," *PHYSICAL REVIEW LETTERS*, vol. 51, 1983.

[170] S. W. Han, H. Kwon, S. K. Kim, S. Ryu, W. S. Yun, D. H. Kim, J. H. Hwang, J. S. Kang, J. Baik, H. J. Shin, and S. C. Hong, "Band-gap transition induced by interlayer van der waals interaction in mos2," *Physical Review B - Condensed Matter and Materials Physics*, vol. 84, 4 Jul. 2011, ISSN: 10980121. DOI: 10.1103/PhysRevB.84.045409.

[171] X. W. Wang, C. T. Chan, K. M. Ho, and W Weber, "Role of surface-state nesting in the incommensurate reconstruction of mo(001)," vol. 16, 1988. DOI: 10.7.

[172] M Posternak and H Krakauer, "Self-consistent electronic structure of surfaces: Surface states and surface resonances on w(001)," *PHYSICAL REVIEW B*, vol. 21, p. 15, 1980.

[173] H. B. Michaelson, "The work function of the elements and its periodicity," *Journal of Applied Physics*, vol. 48, pp. 4729–4733, 11 1977, ISSN: 00218979. DOI: 10.1063/1.323539.

[174] M. C. Toroker, D. K. Kanan, N. Alidoust, L. Y. Isseroff, P. Liao, and E. A. Carter, "First principles scheme to evaluate band edge positions in potential transition metal oxide photocatalysts and photoelectrodes," *Physical Chemistry Chemical Physics*, vol. 13, pp. 16 644–16 654, 37 Oct. 2011, ISSN: 14639076. DOI: 10.1039/c1cp22128k.

[175] S. K. Pradhan, B. Xiao, and A. K. Pradhan, "Enhanced photo-response in p-si/mos2 heterojunction-based solar cells," *Solar Energy Materials and Solar Cells*, vol. 144, pp. 117–127, Jan. 2016, ISSN: 09270248. DOI: 10.1016/j.solmat.2015.08.021.

[176] B. Cho, J. Yoon, S. K. Lim, A. R. Kim, D. H. Kim, S. G. Park, J. D. Kwon, Y. J. Lee, K. H. Lee, B. H. Lee, H. C. Ko, and M. G. Hahm, "Chemical sensing of 2d graphene/mos2 heterostructure device," *ACS Applied Materials and Interfaces*, vol. 7, pp. 16 775–16 780, 30 Aug. 2015, ISSN: 19448252. DOI: 10.1021/acsami.5b04541.

[177] H. Nan, Z. Wu, J. Jiang, A. Zafar, Y. You, and Z. Ni, "Improving the electrical performance of mos2 by mild oxygen plasma treatment," *Journal of Physics D: Applied Physics*, vol. 50, 15 Mar. 2017, ISSN: 13616463. DOI: 10.1088/1361-6463/aa5c6a.

[178] H. J. Sung, D. H. Choe, and K. J. Chang, "The effects of surface polarity and dangling bonds on the electronic properties of monolayer and bilayer mos2 on alpha-quartz," *New Journal of Physics*, vol. 16, Nov. 2014, ISSN: 13672630. DOI: 10.1088/1367-2630/16/11/113055.

[179] X. Cui, G. H. Lee, Y. D. Kim, G. Arefe, P. Y. Huang, C. H. Lee, D. A. Chenet, X. Zhang, L. Wang, F. Ye, F. Pizzocchero, B. S. Jessen, K. Watanabe, T. Taniguchi, D. A. Muller, T. Low, P. Kim, and J. Hone, "Multi-terminal transport measurements of mos2 using a van der waals heterostructure device platform," *Nature Nanotechnology*, vol. 10, pp. 534–540, 6 Jun. 2015, ISSN: 17483395. DOI: 10.1038/nnano.2015.70.

[180] J. Pu, Y. Yomogida, K. K. Liu, L. J. Li, Y. Iwasa, and T. Takenobu, "Highly flexible mos2 thin-film transistors with ion gel dielectrics," *Nano Letters*, vol. 12, pp. 4013–4017, 8 Aug. 2012, ISSN: 15306984. DOI: 10.1021/nl301335q.

[181] H. Liu and P. D. Ye, "Mos2 dual-gate mosfet with atomic-layer-deposited al2o3 as top-gate dielectric," *IEEE Electron Device Letters*, vol. 33, pp. 546–548, 4 Apr. 2012, ISSN: 07413106. DOI: 10.1109/LED.2012.2184520.

[182] Y. Zhan, Z. Liu, S. Najmaei, P. M. Ajayan, and J. Lou, "Large-area vapor-phase growth and characterization of mos2 atomic layers on a sio2 substrate," *Small*, vol. 8, pp. 966–971, 7 Apr. 2012, ISSN: 16136810. DOI: 10.1002/smll.201102654.

[183] H. Wang, L. Yu, Y. H. Lee, Y. Shi, A. Hsu, M. L. Chin, L. J. Li, M. Dubey, J. Kong, and T. Palacios, "Integrated circuits based on bilayer mos2 transistors," *Nano Letters*, vol. 12, pp. 4674–4680, 9 Sep. 2012, ISSN: 15306984. DOI: 10.1021/nl302015v.

[184] A. J. Cho, S. Yang, K. Park, S. D. Namgung, H. Kim, and J. Y. Kwon, "Multi-layer mos2 fet with small hysteresis by using atomic layer deposition al2o3 as gate insulator," *ECS Solid State Letters*, vol. 3, 10 2014, ISSN: 21628750. DOI: 10.1149/2.0111409ssl.

[185] L. Yu, D. El-Damak, S. Ha, X. Ling, Y. Lin, A. Zubair, Y. Zhang, Y. H. Lee, J. Kong, A. Chandrakasan, and T. Palacios, "Enhancement-mode single-layer cvd mos2 fet technology for digital electronics," *Technical Digest - International Electron Devices Meeting, IEDM*, vol. 2016-February, pp. 32.3.1–32.3.4, Feb. 2015, ISSN: 01631918. DOI: 10.1109/IEDM.2015.7409814.

[186] J. Gao, D. Nandi, and M. Gupta, "Density functional theory - projected local density of states - based estimation of schottky barrier for monolayer mos2," *Journal of Applied Physics*, vol. 124, 1 Jul. 2018, ISSN: 10897550. DOI: 10.1063/1.5030538.

[187] X. Han, J. Lin, J. Liu, N. Wang, and D. Pan, "Effects of hexagonal boron nitride encapsulation on the electronic structure of few-layer mos2," *Journal of Physical Chemistry C*, vol. 123, pp. 14 797–14 802, 23 Jun. 2019, ISSN: 19327455. DOI: 10.1021/acs.jpcc.9b02549.

[188] J. Yoon, W. Park, G. Y. Bae, Y. Kim, H. S. Jang, Y. Hyun, S. K. Lim, Y. H. Kahng, W. K. Hong, B. H. Lee, and H. C. Ko, "Highly flexible and transparent multilayer mos2 transistors with graphene electrodes," *Small*, vol. 9, pp. 3295–3300, 19 Oct. 2013, ISSN: 16136810. DOI: 10.1002/smll.201300134.

[189] Y. Liu, H. Wu, H. C. Cheng, S. Yang, E. Zhu, Q. He, M. Ding, D. Li, J. Guo, N. O. Weiss, Y. Huang, and X. Duan, "Toward barrier free contact to molybdenum disulfide using graphene electrodes," *Nano Letters*, vol. 15, pp. 3030–3034, 5 May 2015, ISSN: 15306992. DOI: 10.1021/nl504957p.

[190] H. G. Shin, H. S. Yoon, J. S. Kim, M. Kim, J. Y. Lim, S. Yu, J. H. Park, Y. Yi, T. Kim, S. C. Jun, and S. Im, "Vertical and in-plane current devices using nbs2/n-mos2 van der waals schottky junction and graphene contact," *Nano Letters*, vol. 18, pp. 1937–1945, 3 Mar. 2018, ISSN: 15306992. DOI: 10.1021/acs.nanolett.7b05338.

[191] H. J. Chuang, B. Chamlagain, M. Koehler, M. M. Perera, J. Yan, D. Mandrus, D. Tománek, and Z. Zhou, "Low-resistance 2d/2d ohmic contacts: A universal approach to high-performance wse2, mos2, and mose2 transistors," *Nano Letters*, vol. 16, pp. 1896–1902, 3 Mar. 2016, ISSN: 15306992. DOI: 10.1021/acs.nanolett.5b05066.

[192] L. Xie, M. Liao, S. Wang, H. Yu, L. Du, J. Tang, J. Zhao, J. Zhang, P. Chen, X. Lu, G. Wang, G. Xie, R. Yang, D. Shi, and G. Zhang, "Graphene-contacted ultrashort channel monolayer mos2 transistors," *Advanced Materials*, vol. 29, 37 Oct. 2017, ISSN: 15214095. DOI: 10.1002/adma.201702522.

[193] S Paul, A Ghosh, T Sato, al, M. F. A. Fattah, M. R. Amin, M. Mallmann, W Drubet, I Schafer, and M Skibowski, "The experimental band structure of occupied and unoccupied states of titanium dichalcogenides," *J. Phys*, vol. 20, pp. 4201–4212, 1987.

[194] Y. Yukimasa and K. Motizuki, "Electron-lattice interactions and lattice instabilities of 1t-vse2, 1t-crse2 and 1t-tis2.," *J. Phys. Soc. Jpn.*, vol. 51, 2107–2115, 1982.

[195] J. Chen, Z. L. Tao, and S. L. Li, "Lithium intercalation in open-ended tis2 nanotubes," *Angewandte Chemie - International Edition*, vol. 42, pp. 2147–2151, 19 May 2003, ISSN: 14337851. DOI: 10.1002/anie.200250573.

[196] Y. Fujii, A. Miura, N. C. Rosero-Navarro, Y. Mizuguchi, C. Moriyoshi, Y. Kuroiwa, M. Higuchi, and K. Tadanaga, "Reaction mechanism of feps3 electrodes in all-solid-state lithium secondary batteries using sulfide-based solid electrolytes," *Journal of The Electrochemical Society*, vol. 165, A2948–A2954, 13 2018, ISSN: 0013-4651. DOI: 10.1149/2.0191813jes.

[197] A. J. Huckaba, S. Gharibzadeh, M. Ralaiarisoa, C. Roldán-Carmona, N. Mohammadian, G. Grancini, Y. Lee, P. Amsalem, E. J. Plichta, N. Koch, A. Moshaii, and M. K. Nazeeruddin, "Low-cost tis2 as hole-transport material for perovskite solar cells," *Small Methods*, vol. 1, p. 1 700 250, 10 Oct. 2017. DOI: 10.1002/smtd.201700250.

[198] R. Verrelli, A. Black, R. Dugas, D. Tchitchekova, A. Ponrouch, and M. R. Palacin, "Steps towards the use of tis2 electrodes in ca batteries," *Journal of The Electrochemical Society*, vol. 167, p. 070 532, 7 Jan. 2020, ISSN: 0013-4651. DOI: 10.1149/1945-7111/ab7a82.

[199] M. Lickleder, G. Cha, R. Hahn, and P. Schmuki, "Ordered nanotubular titanium disulfide (tis2) structures: Synthesis and use as counter electrodes in dye sensitized solar cells (dsscs)," *Journal of The Electrochemical Society*, vol. 166, H3009–H3013, 5 2019, ISSN: 0013-4651. DOI: 10.1149/2.0031905jes.

[200] L. Wang, J. Zou, S. Chen, G. Zhou, J. Bai, P. Gao, Y. Wang, X. Yu, J. Li, Y. S. Hu, and H. Li, "Tis2 as a high performance potassium ion battery cathode in ether-based electrolyte," *Energy Storage Materials*, vol. 12, pp. 216–222, May 2018, ISSN: 24058297. DOI: 10.1016/j.ensm.2017.12.018.

[201] S. Ferhat, C. Domain, J. Vidal, D. Noël, B. Ratier, and B. Lucas, "Flexible thermoelectric device based on tis2(ha(x)) n-type nanocomposite printed on paper," *Organic Electronics*, vol. 68, pp. 256–263, May 2019, ISSN: 15661199. DOI: 10.1016/j.orgel.2019.02.031.

[202] R. Chaudhary, K. Patel, R. K. Sinha, S. Kumar, and P. K. Tyagi, "Potential application of mono/bi-layer molybdenum disulfide (mos2) sheet as an efficient transparent conducting electrode in silicon heterojunction solar cells," *Journal of Applied Physics*, vol. 120, 1 Jul. 2016, ISSN: 10897550. DOI: 10.1063/1.4955071.

[203] H Rashid, K. S. Rahman, M. I. Hossain, N Tabet, F. H. Alharbi, and N Amin, "Prospects of molybdenum disulfide (mos2) as an alternative absorber layer material in thin film solar cells from numerical modeling," *Chalcogenide Letters*, vol. 11, pp. 397–403, 8 2014.

[204] A. Rai, H. C. Movva, A. Roy, D. Taneja, S. Chowdhury, and S. K. Banerjee, "Progress in contact, doping and mobility engineering of mos2: An atomically thin 2d semiconductor," *Crystals*, vol. 8, 8 Aug. 2018, ISSN: 20734352. DOI: 10.3390/cryst8080316.

[205] J. Suh, T. E. Park, D. Y. Lin, D. Fu, J. Park, H. J. Jung, Y. Chen, C. Ko, C. Jang, Y. Sun, R. Sinclair, J. Chang, S. Tongay, and J. Wu, "Doping against the native propensity of mos2: Degenerate hole doping by cation substitution," *Nano Letters*, vol. 14, pp. 6976–6982, 12 Dec. 2014, ISSN: 15306992. DOI: 10.1021/nl503251h.

[206] J. He, K. Hummer, and C. Franchini, "Stacking effects on the electronic and optical properties of bilayer transition metal dichalcogenides mos2, mose2, ws2, and wse2," *Physical Review B - Condensed Matter and Materials Physics*, vol. 89, 7 Feb. 2014, ISSN: 10980121. DOI: 10.1103/PhysRevB.89.075409.

[207] A. Yan, C. S. Ong, D. Y. Qiu, C. Ophus, J. Ciston, C. Merino, S. G. Louie, and A. Zettl, "Dynamics of symmetry-breaking stacking boundaries in bilayer mos2," *Journal of Physical Chemistry C*, vol. 121, pp. 22 559–22 566, 40 Oct. 2017, ISSN: 19327455. DOI: 10.1021/acs.jpcc.7b08398.

[208] C. Ataca, M. Topsakal, E. Aktürk, and S. Ciraci, "A comparative study of lattice dynamics of three- and two-dimensional mos2," *Journal of Physical Chemistry C*, vol. 115, pp. 16 354–16 361, 33 Aug. 2011, ISSN: 19327447. DOI: 10.1021/jp205116x.

[209] A. Mukhopadhyay, S. Kanungo, and H. Rahaman, "The effect of the stacking arrangement on the device behavior of bilayer mos2 fets," *Journal of Computational Electronics*, vol. 20, pp. 161–168, 1 Feb. 2021, ISSN: 15728137. DOI: 10.1007/s10825-020-01636-w.

[210] N. Yamamoto, "Generalized bloch theorem and chiral transport phenomena," *Physical Review D - Particles, Fields, Gravitation and Cosmology*, vol. 92, 8 Oct. 2015, ISSN: 15502368. DOI: 10.1103/PhysRevD.92.085011.

[211] B. K. Choi, M. Kim, K. H. Jung, J. Kim, K. S. Yu, and Y. J. Chang, "Temperature dependence of band gap in mose2 grown by molecular beam epitaxy," *Nanoscale Research Letters*, vol. 12, 2017, ISSN: 1556276X. DOI: 10.1186/s11671-017-2266-7.

[212] C. Quan, M. He, C. He, Y. Huang, L. Zhu, Z. Yao, X. Xu, C. Lu, and X. Xu, "Transition from saturable absorption to reverse saturable absorption in mote2 nano-films with thickness and pump intensity," *Applied Surface Science*, vol. 457, pp. 115–120, Nov. 2018, ISSN: 01694332. DOI: 10.1016/j.apsusc.2018.06.245.

[213] D. Bocharov, S. Piskunov, Y. F. Zhukovskii, and R. A. Evarestov, "Ab initio calculations on the electronic structure and photocatalytic properties of two-dimensional ws2(0001) nanolayers of varying thickness," *Physica Status Solidi - Rapid Research Letters*, vol. 13, 1 Jan. 2019, ISSN: 18626270. DOI: 10.1002/pssr.201800253.

[214] Y. Wang, S. Zhao, Y. Wang, D. A. Laleyan, Y. Wu, B. Ouyang, P. Ou, J. Song, and Z. Mi, "Wafer-scale synthesis of monolayer wse2: A multi-functional photocatalyst for efficient overall pure water splitting," *Nano Energy*, vol. 51, pp. 54–60, Sep. 2018, ISSN: 22112855. DOI: 10.1016/j.nanoen.2018.06.047.

[215] S. Tongay, J. Zhou, C. Ataca, K. Lo, T. S. Matthews, J. Li, J. C. Grossman, and J. Wu, "Thermally driven crossover from indirect toward direct bandgap in 2d semiconductors: Mose2 versus mos2," *Nano Letters*, vol. 12, pp. 5576–5580, 11 Nov. 2012, ISSN: 15306984. DOI: 10.1021/nl302584w.

[216] S. Qiao, H. Yang, Z. Bai, G. Peng, and X. Zhang, "Identifying the number of ws2 layers via raman and photoluminescence spectrum," *Advances in Engineering Research*, vol. 141, 2017.

[217] H. Zhou, C. Wang, J. C. Shaw, R. Cheng, Y. Chen, X. Huang, Y. Liu, N. O. Weiss, Z. Lin, Y. Huang, and X. Duan, "Large area growth and electrical properties of p-type wse2 atomic layers," *Nano Letters*, vol. 15, pp. 709–713, 1 Jan. 2015, ISSN: 15306992. DOI: 10.1021/nl504256y.

[218] P. K. Das, D. D. Sante, F. Cilento, C. Bigi, D. Kopic, D. Soranzio, A. Sterzi, J. A. Krieger, I. Vobornik, J. Fujii, T. Okuda, V. N. Strocov, M. B. Breese, F. Parmigiani, G. Rossi, S. Picozzi, R. Thomale, G. Sangiovanni, R. J. Cava, and G. Panaccione, "Electronic properties of candidate type-ii weyl semimetal wte2. a review perspective," *Electronic Structure*, vol. 1, 1 Mar. 2019, ISSN: 25161075. DOI: 10.1088/2516-1075/ab0835.

[219] G. C. Constantinescu and N. D. Hine, "Energy landscape and band-structure tuning in realistic mos2/mose2 heterostructures," *Physical Review B - Condensed Matter and Materials Physics*, vol. 91, 19 May 2015, ISSN: 1550235X. DOI: 10.1103/PhysRevB.91.195416.

[220] N. Lu, H. Guo, L. Wang, X. Wu, and X. C. Zeng, "Van der waals trilayers and superlattices: Modification of electronic structures of mos2 by intercalation," *Nanoscale*, vol. 6, pp. 4566–4571, 9 May 2014, ISSN: 20403372. DOI: 10.1039/c4nr00783b.

[221] L. Kou, T. Frauenheim, and C. Chen, "Nanoscale multilayer transition-metal dichalcogenide heterostructures: Band gap modulation by interfacial strain and spontaneous polarization," *Journal of Physical Chemistry Letters*, vol. 4, pp. 1730–1736, 10 May 2013, ISSN: 19487185. DOI: 10.1021/jz400668d.